

AD-A243 049



DTIC  
S  
c  
J

AFOSR-90-0002

2

## STRENGTH AND MICROSTRUCTURE OF CERAMICS

BRIAN R. LAWN

Ceramics Division  
National Institute of Standards and Technology  
Gaithersburg, MD 20899

With S.J. Bennison, H.M. Chan, P. Chantikul, J. Kelly, S. Lathabai, N.P. Padture, M.J. Readey, J. Rödel, J.L. Runyan, M.R. Stoudt

Final Technical Report  
FY 90-91

AFOSR Contract Nos. ISSA-90-0003 and ISSA-91-0002  
NIST Project No. 852-2464

for

Air Force Office of Scientific Research  
Bolling Air Force Base  
Washington, DC 20332

October 1991

91-16556



Approved for public release;  
distribution unlimited.

91 11 20 038

AIR FORCE OFFICE OF SCIENTIFIC RESEARCH  
NOTICE  
THIS REPORT  
APPROVED  
DISSEMINATION  
GROSS PRICE  
STIMFO PRICE

REPORT DOCUMENTATION PAGE			Form Approved OMB No 0704-0188	
<small>Public reporting burden for this collection of information is estimated to average 1 hour per response, including the time for reviewing instructions, searching existing data sources, gathering and maintaining the data needed, and completing and reviewing the collection of information. Send comments regarding this burden estimate or any other aspect of this collection of information, including suggestions for reducing this burden, to Washington Headquarters Services, Directorate for Information Operations and Reports, 1215 Jefferson Davis Highway, Suite 1204, Arlington, VA 22202-4302, and to the Office of Management and Budget, Paperwork Reduction Project (0704-0188), Washington, DC 20503.</small>				
1. AGENCY USE ONLY (Leave blank)	2. REPORT DATE November 1990	3. REPORT TYPE AND DATES COVERED <i>Final Report</i> <del>Technical Report</del> - FY90 <i>10-1-89-9-30-91</i>		
4. TITLE AND SUBTITLE  "Strength and Microstructures of Ceramics"		5. FUNDING NUMBERS NIST Project No. 852-2464  AFOSR Contract Nos. ISSA-90-0003 91-0002  <i>61102 F 2304/A2</i>		
6. AUTHOR(S)  Brian R. Lawn				
7. PERFORMING ORGANIZATION NAME(S) AND ADDRESS(ES) National Institute of Standards & Technology Materials Science and Engineering Laboratory Building 223, Room A347 Gaithersburg, MD 20899		8. PERFORMING ORGANIZATION REPORT NUMBER		
9. SPONSORING / MONITORING AGENCY NAME(S) AND ADDRESS(ES) Air Force Office of Scientific Research Bolling Air Force Base Washington, DC 20332		10. SPONSORING MONITORING AGENCY REPORT NUMBER  <i>AFOSR ISSA 90-0003</i> <i>AFOSR - ISSA-91 0002</i>		
11. SUPPLEMENTARY NOTES				
12a. DISTRIBUTION / AVAILABILITY STATEMENT  Unlimited		12b. DISTRIBUTION CODE		
13. ABSTRACT (Maximum 200 words)  Results of a program on the toughness properties of monophase and two-phase ceramics that toughen by bridging are presented. Fracture mechanics models describing this behavior, in the particular context of strength, are developed. Results of strengths tests confirming the essential predictions of the theory are presented. Innovative processing routes suggested by the models are shown to lead to two-phase composites with impressive flaw insensitivity.				
14. SUBJECT TERMS			15. NUMBER OF PAGES 169	
			16. PRICE CODE	
17. SECURITY CLASSIFICATION OF REPORT  Unclassified	18. SECURITY CLASSIFICATION OF THIS PAGE  Unclassified	19. SECURITY CLASSIFICATION OF ABSTRACT  Unclassified	20. LIMITATION OF ABSTRACT	

## STRENGTH AND MICROSTRUCTURE OF CERAMICS

	<i>Page</i>
<b>INTRODUCTION</b>	iii
<b>PUBLICATIONS</b>	
1. "The Role of Crystallization of an Intergranular Glassy Phase in Determining Grain Boundary Residual Stresses in Debased Aluminas" N.P. Padture, H.M. Chan, B.R. Lawn and M.J. Readey <i>Tailored Interfaces in Composites</i> , Mater. Res. Soc., Pittsburgh, PA, Vol. 170, p. 245, 1990.	1
2. "Role of Grain Size in the Strength and R-Curve Properties of Alumina" P. Chantikul, S.J. Bennison and B.R. Lawn <i>J. Am. Ceram. Soc.</i> 73 2419 (1990).	7
3. "In Situ Measurements of Bridged Crack Interfaces in the SEM" J. Rödel, J. Kelly and B.R. Lawn <i>J. Am. Ceram. Soc.</i> 73 3313 (1990).	15
4. "A Loading Device for Fracture Testing of Compact Tension Specimens in the Scanning Electron Microscope" J. Rödel, J.F. Kelly, M.R. Stoudt and S.J. Bennison <i>Scanning Microscopy</i> 5 29 (1991).	21
5. "Fundamental Condition for Existence of Microcrack Clouds in Monophase Ceramics" B.R. Lawn <i>J. European Ceram. Soc.</i> 7 17 (1991).	28
6. "Cyclic Fatigue from Frictional Degradation at Bridging Grains in Alumina" S. Lathabai, J. Rödel and B.R. Lawn <i>J. Am. Ceram. Soc.</i> 74 1340 (1991).	32
7. "Microstructure, Toughness Curves and Mechanical Properties of Alumina Ceramics" S.J. Bennison, J. Rödel, S. Lathabai, P. Chantikul, B.R. Lawn <i>Toughening Mechanisms in Quasi-Brittle Materials</i> , Kluwer Academic Publishers, Dordrecht, The Netherlands, p. 209, 1991.	41
8. "Flaw Tolerant $Al_2O_3$ - $Al_2TiO_5$ Composites" N.P. Padture, H.M. Chan, S.J. Bennison, J.L. Runyan, J. Rödel and B.R. Lawn <i>Advanced Composite Materials</i> , American Ceramic Society, Ohio, Vol. 19, p. 715, 1991.	68



A-1

9. "Fabrication of Flaw-Tolerant Aluminum-Titanate-Reinforced Alumina" 75  
J.L. Runyan and S.J. Bennison  
J. Europ. Ceram. Soc. 7 93 (1991).
10. "Crack Closure Forces in Ceramics: Characterization and Formation" 82  
J. Rödel  
J. Europ. Ceramic Society, in press.
11. "Influence of Grain Size and Degree of Crystallization of Intergranular Glassy Phase on the Mechanical Behaviour of a Debased Alumina" 129  
N.P. Padture and H.M. Chan  
J. Mater. Sci. 26 2711 (1991)
12. "On the Constrained Crystallization of Synthetic Anorthite" 134  
N.P. Padture and H.M. Chan  
J. Mater. Research, in press.

## INTRODUCTION

This two-year program has been concerned with the role of microstructure in the toughness and strength properties of flaw-tolerant ceramics, i.e. ceramics with strong R-curves. The R-curve is crucial to the utility of monophase ceramics and multiphase composites in applications where high toughness and flaw tolerance is paramount. Our group has sought to identify and analyze the interrelations between R-curve processes and materials characteristics, to establish reliable design criteria, and to tailor new, superior ceramics with maximum resistance to damage accumulation and degradation. A key aspect of our approach has been to establish strong links between properties and processing, fracture mechanics experimentation and modelling, materials design and characterization. The results of these studies are summarized in the appended publications [1-12].

An important part of the fracture mechanics experimentation has been *in situ* observations of grain-localized bridging in elementary ceramics (e.g. aluminas) and two-phase composites, using a device that locates inside an SEM. Our studies have helped to determine the underlying micromechanics of the bridging process. We are able to monitor crack growth in ceramics with remote control from outside the SEM in various loading modes, including cyclic. Specific aspects of this work is described in appended papers [3,4]. A general review of the *in situ* experiments is given in Ref. 10.

Work on cyclic fatigue has revealed a strength degradation with time, due to progressive bridge degradation. The *in situ* device has been useful in identifying a mechanism for this degradation. Sliding grains at bridging points generate very high stresses which produce wear products, leading to reduction in the contact friction. This reduces the shielding, and hence the strength. Results and fracture mechanics modelling of this process are presented in Ref. [6].

The most crucial element of our program is the role of microstructure in the R-curve. With the bridging mechanism identified and understood, fracture mechanics models have been developed by our group. These models incorporate the essential elements of the microstructure

into the underlying constitutive stress-separation function for the grain pullout. They allow one to predict the special role of the microstructural scaling, especially grain size, on the R-curve and strength. A systematic experimental study on alumina ceramics over a wide range of grain sizes confirms the basic predictions of the model, and explains previous mysteries concerning observed strength vs grain size relations [2,11]. On the other hand, incorporation of small additive phases at the grain boundaries has a relatively small effect on the properties [1,11,12].

Another important variable in the bridging fracture mechanics is the level of internal residual stress from thermal expansion anisotropy. The bridging models tell us that such stresses should augment the frictional tractions responsible for the toughening. We have fabricated two-phase alumina/aluminum-titanate ceramics, for which the expansion mismatch is uncommonly high [8,9]. This material exhibits extraordinary flaw insensitivity, i.e. strength which are virtually independent of starting flaw size.

Work is proceeding on this last exciting new area of properties-processing research.

## THE ROLE OF CRYSTALLIZATION OF AN INTERGRANULAR GLASSY PHASE IN DETERMINING GRAIN BOUNDARY RESIDUAL STRESSES IN DEBASED ALUMINAS

NITTIN P. PADTURE<sup>1</sup>, HELEN M. CHAN<sup>1</sup>, BRIAN R. LAWN<sup>2</sup> and MICHAEL J. READEY<sup>3</sup>

<sup>1</sup>Department of Materials Science and Engineering, Whitaker Lab # 5, Lehigh University, Bethlehem, PA 18015

<sup>2</sup>Ceramics Division, Bldg. # 223, National Institute of Standards and Technology, Gaithersburg, MD 20899

<sup>3</sup>Coors Ceramics Company, 17750, 32nd Avenue, Golden, CO 80401

### ABSTRACT

The influence of microstructure on the crack resistance (R-curve) behavior of a commercial debased alumina containing large amounts of glassy phase (28 vol %) has been studied using the Indentation-Strength test. The effect of two microstructural variables, viz. grain size and the nature of the intergranular second phase (glassy or crystalline) has been evaluated. Crystallization of the intergranular glass was carried out in order to generate residual stresses at the grain boundaries, which have been shown to enhance R-curve behavior in ceramic materials. Enhancement of the R-curve behavior was observed with the increase in grain size. However, no effect of the nature of the intergranular second phase on the R-curve behavior, in small and large grain materials, was observed. The results from characterization of these materials using various analytical techniques is presented, together with possible explanations for the observed effects.

### INTRODUCTION

Recently several researchers [1 to 4] have reported considerable increase in toughness of debased (liquid-phase-sintered) aluminas, containing 10 to 30 vol % intergranular glass, by crystallization of the glass via simple heat-treatments. However, it should be noted that the toughness measurements in the above studies were performed at single crack length values, whereas recent work has shown that many alumina ceramics show increase in toughness with crack length, i.e. crack resistance or R-curve behavior [5 to 10]. The effect of crack resistance has been attributed to the phenomenon of microstructural grain-localized bridging of the crack, in the wake of its tip, and is very sensitive to the microstructure of the material [5, 11]. In the present study we have set out to evaluate the effect of grain size and crystallization of the intergranular glass on the mechanical properties (R-curve behavior) of these materials over a wide range of crack lengths.

The grains bridging the crack, in non-cubic polycrystalline ceramics, have been postulated to be clamped in the matrix by compressive residual stresses generated during cooling from processing temperatures, due to thermal expansion anisotropy present in these materials [12]. These residual stresses play an important role in the bridging phenomenon. The grain size of the polycrystalline ceramic is also known to influence R-curve behavior of these materials [7,13].

Indentation-strength [7, 8] is a very convenient way of monitoring R-curve behavior in ceramic materials. Bending over of the fracture stress versus indentation load curve at the low indentation load end is a direct consequence of R-curve behavior exhibited by the material, and gives rise to a region where the fracture stress is independent of the indentation load (and hence crack size) [15, 16]. An important implication of R-curve behavior, therefore, is that it suggests a degree of flaw tolerance, which is very useful in terms of engineering design. R-curve behavior also has great significance in the wear properties of materials, since this is governed by fracture characteristics at low flaw sizes. More recently it has been postulated that R-curve behavior increases the Weibull modulus of ceramic materials which exhibit such behavior [17,

18].

The purpose of this study was to determine the separate and combined influence(s) of grain size and second phase crystallinity on the R-curve behavior of debased ceramics. The material chosen was Coors AD85 alumina containing about 28 vol % glass. This material was subjected to carefully designed heat-treatments so as to increase the grain size and increase residual stresses at the grain boundaries by crystallization of the intergranular glass. It was envisaged that in doing so, it would be possible to enhance R-curve behavior in these materials.

## EXPERIMENTAL

About 300 samples of AD85 alumina in the form of disks (25mm dia x 3mm) were obtained from Coors Ceramic Company. A series of heat-treatments was carefully devised in order to produce four sets of samples of differing microstructures. Tables I and II show the details of the heat-treatments and the resulting microstructures respectively. The denotation S or L refers to small or large grain size respectively, and C or G refers to crystalline or glassy second phase respectively.

Table I Various heat-treatments, AD85 subjected to.

<u>Material</u>	<u>Heat-treatments</u>	<u>Purpose</u>
AD85-S-G	a) As-received	-
AD85-S-C	a) 1400°C for 6 hours, quenched	Homogenize intergranular glass
	b) 1150°C for 130 hours	Crystallize intergranular glass
AD85-L-G	a) 1550°C for 250 hours	Increase grain size
AD85-L-C	b) 1200°C for 130 hours	Crystallize the intergranular glass

Table II Microstructural aspects of AD85 after the heat-treatments.

<u>Material</u>	<u>Grain size</u>	<u>Intergranular phase</u>
AD85-S-G	3µm	Glassy
AD85-S-C	3µm	80% crystalline
AD85-L-G	18µm	Glassy
AD85-L-C	18µm	80% crystalline

Specimens for Transmission Electron Microscopy (TEM) were prepared from the above samples using a dimpler and then ion-beam milling until perforation. TEM investigation was performed on a Phillips EM 400T at an accelerating voltage of 120 keV. Chemical composition of the intergranular glass was determined using Scanning Transmission Electron Microscopy (STEM) and Energy Dispersive Spectroscopy of x-rays (EDS) on the same instrument. Samples were prepared for Scanning Electron Microscopy (SEM) by polishing sections to 1µm grade followed by thermal etching at 1500 °C for 15 minutes.

Mechanical testing of AD85-S-G, AD85-S-C, AD85-L-G and AD85-L-C was carried out as follows. About 50 disk samples of each were polished to 1µm grade on the prospective tensile side. A Vickers indentation was made at the center of the polished surface with loads varying from 2 to 300 N. Some samples were left unindented. The samples were broken in biaxial flexure using the 3-point support and punch fixture. Details of this particular method of mechanical testing have been described elsewhere [7].



## RESULTS AND DISCUSSION

Table III shows the composition of the intergranular glass of AD85-S-G samples after homogenization heat-treatment, as determined by STEM and EDS. This is an average of many different spectra obtained from different regions of the sample. The compositions were observed to be fairly consistent, which implies that the glassy phase is homogeneous. The composition obtained agrees closely with that determined by Weiderhorn et al. [19] for AD85 with the same heat-treatment. Using this composition as the basis, the heat-treatment given in table I was devised. Figure 1 show SEM micrographs of AD85-S-G (grain size  $3\mu\text{m}$ ) and AD85-L-G (grain size  $18\mu\text{m}$ ). Figures 2 and 3 show TEM micrographs of AD85-S-G and AD85-S-C showing glassy and crystalline intergranular phases respectively. The grain size did not change appreciably during crystallization heat-treatment. The crystalline intergranular phase in AD85-S-C was observed to be mostly anorthite. With this composition it was not possible to achieve 100% crystallinity, thus pockets of residual glassy phase were observed at the triple points.

Table III Average composition of the intergranular glass in AD85.

<u>Oxide</u>	SiO <sub>2</sub>	Al <sub>2</sub> O <sub>3</sub>	MgO	CaO	BaO
<u>Wt%</u>	56.5	27.5	2.1	8.6	5.3

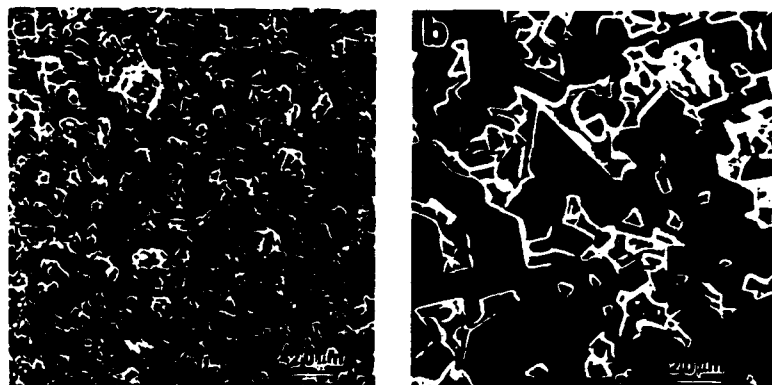


Figure 1 SEM Secondary electron images of polished and etched sections of AD85 aluminas  
a) AD85-S-G (fine grained material) , b) AD85-L-G (coarse grained material).



Figure 2 TEM bright field image of AD85-S-G showing intergranular glassy pockets (A-Alumina, G- Glass).

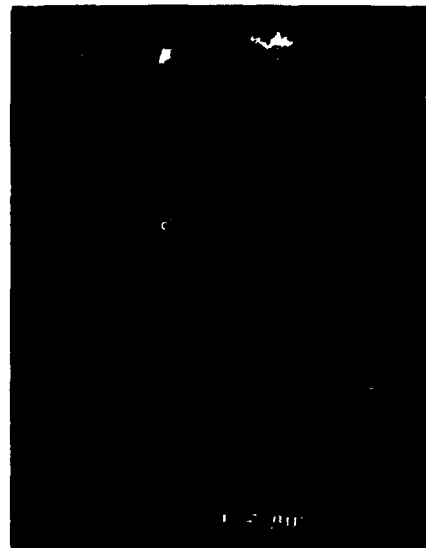


Figure 3 TEM bright field image of AD85-S-C showing crystalline intergranular phase (A-Alumina, C- Crystalline).

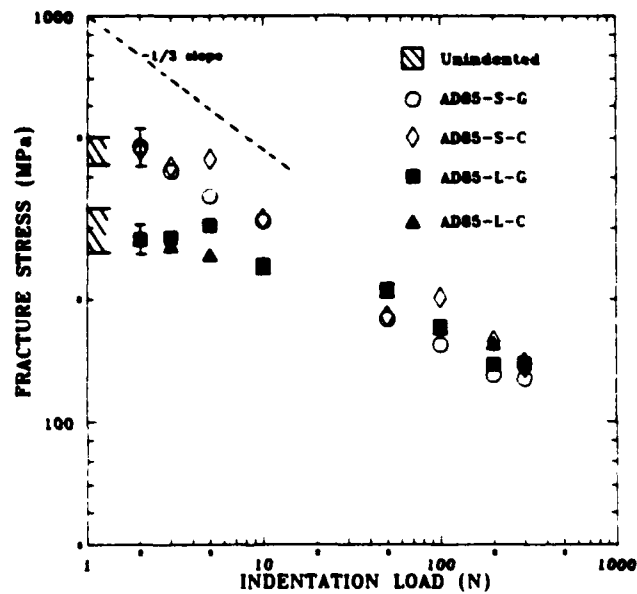


Figure 4 Plot of indentation load versus fracture stress for four different materials, derived from AD85. The error bars for all the data are shown in the left. The hatched region represents failures from natural flaws.

Figure 4 shows indentation load versus fracture stress for AD85-S-G, AD85-S-C, AD85-L-G, and AD85-L-C. It can be seen that all the data essentially falls on two graphs corresponding to 1) fine grained materials (AD85-S-G and AD85-S-C) and 2) coarse grained materials (AD85-L-G and AD85-L-C). It can be clearly seen that coarse grain aluminas show much more pronounced R-curve behavior than fine grain aluminas.

Because the curves for materials with glassy and crystalline intergranular phases show similar behavior, this indicates marginal or no effect of crystallization on the R-curve properties of these materials. The effect of grain size on the R-curve behavior, however, is much more marked, and this is in agreement with results obtained by Cook et al. [7] for single phase aluminas, and Bennison et al. [20] for debased aluminas. Given that grain-bridging processes must be dependent on the residual stresses in the grain boundary regions, the lack of effect of crystallization on the R-curve behavior is somewhat surprising.

Possible explanations for the lack of effect of crystallization of the intergranular glass are thought to be as follows:

1. Stress relaxation by residual glass
2. Fracture through the residual glass
3. Stress relaxation by high temperature deformation (twinning) of anorthite.

Work is currently underway to determine which of the above mechanisms (if any) are correct [21].

## CONCLUSIONS

The major conclusions from the above study can be summarized as follows:

1. The effect of grain size on the R-curve behavior predominates.
2. Crystallization of the intergranular glass has relatively little or no effect on the R-curve behavior of AD85. Possible explanations attributing to the observed behavior have been described above.
3. An important conclusion can however be drawn from the observed behavior. Coors AD85 can be subjected to prolonged heat-treatment cycles up to 1200°C without having any significant effect on room temperature mechanical properties (pertaining to fast crack growth). This property of AD85 can be very useful in prolonged high temperature structural applications and in metallization applications imparting heat-treatment tolerance along with flaw tolerance.

## ACKNOWLEDGEMENTS

The authors wish to thank Dr. S. J. Bennison for many useful discussions.

## REFERENCES

1. N.A. Travitzky, D.G. Brandon and E.Y. Gutmanas, *Mater. Sci. Eng.*, **21**, 65-70 (1985).
2. N.A. Travitzky, D.G. Brandon and E.Y. Gutmanas, *Mater. Sci. Eng.*, **21**, 77-86 (1985).
3. Y. Yeshurun, Z. Rosenberg, N.A. Travitzky and D.G. Brandon, *Mater. Sci. Eng.*, **21**, 71-75 (1985).
4. W.A. Zdaniewski and H.P. Kirchner, *Adv. Ceram. Mater.*, **1**, 99-103 (1986).
5. R. Knehans and R. Steinbrech, *J. Mater. Sci. Letters*, **1**, 327-329 (1982).
6. R.W. Steinbrech, R. Knehans and W. Schaarwachter, *J. Mater. Sci.*, **18**, 265-270 (1983).

7. R.F. Cook, B.R. Lawn and C.J. Fairbanks, J. Amer. Ceram. Soc., 68, 604-615 (1985).
8. R. F. Cook, B. R. Lawn, and C. J. Fairbanks, J. Amer. Ceram. Soc. 68, 616-623, (1985).
9. M. V. Swain, J. Mater. Sci. Letters, 5, 1313-1315 (1986).
10. F. Duerler, R. Knehs and R. W. Steinbrech, J. de Physique, C1, 617-621 (1986).
11. P.L. Swanson, C.J. Fairbanks, B.R. Lawn, Y-W. Mai and B.J. Hockey, J. Amer. Ceram. Soc., 70, 279-289 (1987).
12. S. J. Bennison and B. R. Lawn, Acta Metall., 37, 2659-2671, (1989).
13. P. Chanikul, S. J. Bennison and B. R. Lawn, J. Amer. Ceram. Soc., to be published.
14. Y-W. Mai and B. R. Lawn, J. Amer. Ceram. Soc., 70, 289- 294 (1987).
15. R.F. Cook, C.J. Fairbanks, Y-W. Mai and B.R. Lawn, J. Mater. Res., 2, 345-356 (1987).
16. S. J. Bennison and B. R. Lawn, J. Mater. Sci., 2, 3169-3175 (1989).
17. R. F. Cook and D. R. Clarke, Acta Metall., 36, 555-562 (1988).
18. D. K. Shetty and J-S. Wang, J. Amer. Ceram. Soc., 72, 1158-1162 (1989).
19. S.M. Wiederhorn, B.J. Hockey and R.F. Krause Jr., Ceramic Microstructures '86, edited by J. Pask and A.G. Evans (Plenum Publishing Company, New York, 1988) pp. 795-806.
20. S.J. Bennison, H. M. Chan and B.R. Lawn, J. Amer. Ceram. Soc., 72, 677-679 (1989).
21. N. P. Padture, H. M. Chan, B. R. Lawn and M. J. Readey, J. Amer. Ceram. Soc., to be published.

## Role of Grain Size in the Strength and R-Curve Properties of Alumina

Prapaipan Chantikul,\* Stephen J. Bennison,\*<sup>‡</sup> and Brian R. Lawn\*

Ceramics Division, National Institute of Standards and Technology, Gaithersburg, Maryland 20899

An investigation of the interrelationships between strength, crack-resistance (*R*-curve) characteristics, and grain size for alumina ceramics has been carried out. Results of indentation-strength measurements on high-density aluminas with uniform grain structures in the size range 2 to 80  $\mu\text{m}$  are presented. A theoretical fit to the data, obtained by adjusting parameters of a constitutive frictional-pullout relation in a grain-bridging model, allows determination of the critical microstructural parameters controlling the *R*-curve behavior of these aluminas. The primary role of grain size in the toughness characteristic is to determine the scale of grain pullout at the bridged interface. It is shown that the strength properties are a complex function of the bridged microstructure, governed at all but the finest grain sizes by the stabilizing effect of the *R*-curve. The analysis confirms the usual negative dependence of strength on grain size for natural flaws that are small relative to the grain size, but the dependence does not conform exactly to the  $-1/2$  power predicted on the basis of classical "Griffith-Orowan" flaws. The analysis provides a self-consistent account of the well-documented transition from "Orowan" to "Petch" behavior. [Key words: grain size, strength, *R*-curve, alumina, bridging.]

### 1. Introduction

THE influence of grain size on the strength of intrinsically brittle solids, particularly of aluminas and other noncubic ceramics, has been well documented.<sup>1-14</sup> Generally, the strength is observed to decline with coarsening of the grain structure. An understanding of the strength/grain-size dependence is an important element in the microstructural design of structural ceramics.

The earliest nonempirical accounts of the observed trends<sup>9</sup> were based on the simplistic Griffith concept of spontaneous failure from a dominant flaw. If it is assumed that the intrinsic flaw scales with grain size and that the toughness is single-valued, a so-called "Orowan" relation ensues in which the strength is proportional to the inverse square root of grain size.<sup>15</sup> Most data can be force-fitted reasonably well with this relation down to "intermediate" grain sizes (10 to 40  $\mu\text{m}$  in alumina), at which point the size dependence is markedly reduced.<sup>9,10</sup> This latter region is manifested as a secondary, "Petch" branch of low slope and nonzero intercept on a strength versus (grain size)<sup>-1/2</sup> diagram.<sup>16</sup> Various interpreta-

tions of the transition have been proposed: a precursor "microplasticity" stage in crack initiation from the flaw<sup>9,10</sup> (from literal adaptations of the original metals-based Hall-Petch model); the stabilizing influence of local (machining, thermal expansion mismatch) residual stresses in the flaw extension<sup>10,17</sup>; the dominance of extrinsic (e.g., machining) flaws in the small-grain-size region,<sup>10,12</sup> with any microstructural dependence attributable to a monocrystal-to-polycrystal increase in the crack resistance.<sup>10,17,18</sup> A common feature of these proposals is that the supporting evidence cited is invariably circumstantial: i.e., the evolution of the critical flaw to final instability is never observed directly. Indeed, there is a persistent school of thought that dismisses all of the above explanations, suggesting instead that (with proper attention to distributions in grain size) the fine-grain region can be represented adequately by an Orowan relation with simple grain-size-independent, extrinsic flaw cutoff.<sup>14</sup>

Central to the continuing debate are the issues of non-unique toughness and crack stability. In the early 1980s efforts were made to construct broad-based models which took into account both these factors.<sup>20-22</sup> Those models used empirical functions to represent a monocrystal-polycrystal transition in toughness and thereby predicted a stable region of crack growth prior to failure. Again, little or no attempt was made to confirm the models with direct experimental observations of flaw micromechanics. The lack of definitive experiments on materials with well-characterized toughness/crack-size properties and properly controlled flaws has not helped to resolve the debate.<sup>14,19,23</sup>

More recently, direct evidence for departures from single-valued toughness in polycrystalline ceramics, predominantly in aluminas<sup>24-29</sup> but also in other (noncubic) materials, has become available. (Typically, for an alumina of grain size  $\approx 20 \mu\text{m}$ , the toughness increases from a value of  $\approx 2$  to 6  $\text{MPa} \cdot \text{m}^{1/2}$  over a crack extension  $\approx 5 \text{ mm}$ .) This rising toughness, termed "*R*-curve" (or "*T*-curve") behavior, becomes more pronounced as the grain size increases.<sup>26,27</sup> Further studies using controlled indentation flaws in alumina<sup>30-35</sup> demonstrate that the *R*-curve strongly stabilizes crack growth, such that the critical flaw may extend several times its original dimension prior to failure.<sup>31</sup> In situ observations of the indentation flaws (as well as of other well-defined crack geometries) during applied loading unequivocally identify the underlying cause of this stabilization as crack-interface bridging by interlocked grains behind the crack tip.<sup>31,34</sup> These same observations reveal that the crack first propagates through one or two grain diameters and then arrests ("pop-in"), and thereafter grows erratically during the prefailure growth.<sup>31</sup> The failure condition shows strong departures from Griffith behavior, with a pronounced tendency for the strength to become independent of indentation load in the small-flaw domain ("flaw tolerance").<sup>30,33,35,36</sup>

Theoretical fracture mechanics treatments of the crack-bridging process have been developed on the basis of frictional grain pullout.<sup>32,33,36</sup> The most recent analysis<sup>36</sup> makes a special effort to incorporate essential elements of the microstructure into the fundamental constitutive relation for the pullout, especially the role of thermal expansion anisotropy

R. Cook—contributing editor

Manuscript No. 197864. Received December 21, 1989; approved May 2, 1990.

Presented at the 92nd annual Meeting of the American Ceramic Society, Dallas, TX, April, 1990.

Supported by a grant from the U.S. Air Force Office of Scientific Research.

\*Member, American Ceramic Society.

<sup>‡</sup>Guest Scientist, on leave from the Physics Department, Faculty of Science, Chulalongkorn University, Bangkok, Thailand BKK10330.

<sup>§</sup>Guest Scientist, on leave from the Department of Materials Science and Engineering, Lehigh University, Bethlehem, PA 18015.

stresses in augmenting grain-boundary friction. The model is thereby able to account for the observed tendency to more pronounced *R*-curves with coarsening microstructure. More appropriately, it has the necessary ingredients for a universal characterization of the grain-size dependence of strength, over a broad spectrum of flaw sizes (subgrain to multigrain) and types ("natural" as well as indentation).<sup>36</sup> Interestingly, the predicted dependence for natural flaws in the coarse-grained region can be significantly less than the power  $-1/2$  of Griffith-Orowan. A preliminary comparison with some literature data on alumina appeared to substantiate this predicted departure from ideal behavior.<sup>36</sup>

In the present study we investigate the interrelationship between strength and grain size in greater depth. Indentation-strength experiments are conducted on high-density aluminas with uniform grain structures in the size range 2 to 80  $\mu\text{m}$ . The surfaces of the specimens are finely polished to minimize the intrusion of extrinsic flaws. It is confirmed that strength is a multiregion function of grain size, governed at all but the finest microstructures ( $\leq 5 \mu\text{m}$  in our alumina) by the stabilizing effect of the *R*-curve. Analysis of the data in terms of the grain-bridging model provides a self-consistent account of the strength properties. For very small flaws the negative grain-size dependence of strength indeed differs (if only slightly) from power  $-1/2$ ; for very large flaws the dependence is the same in the coarse-grain region, somewhat lower but still negative in the intermediate-grain region, and is actually predicted to become slightly positive in the fine-grain region. A fit of the grain-bridging model to the data, obtained by adjusting microstructural quantities in the constitutive frictional pullout law, allows deconvolution of the critical *R*-curve parameters for the alumina.

## II. Experimental Procedure

### (1) Preparation of Alumina Specimens

A fabrication procedure based on the Lucalox<sup>1</sup> process<sup>37,38</sup> was used to produce high-density, single-phase  $\alpha\text{-Al}_2\text{O}_3$  specimens with homogeneous, equiaxed grain structures. Powder preparation was carried out in class A-100 clean-room conditions. Ultra-high-purity  $\text{Al}_2\text{O}_3$  powder<sup>1</sup> was doped with trace MgO (Mg/Al = 500 at. ppm, i.e., below the solid solubility limit for Mg in  $\text{Al}_2\text{O}_3$  at the firing temperatures used below)<sup>39</sup> by addition of a magnesium nitrate solution in methanol. The slurry was continuously stirred during drying and then deagglomerated by crushing. Disks 25 mm in diameter and 5 mm in thickness were fabricated by uniaxial pressing at 50 MPa using a high-purity graphite die, punch, and spacer assembly. Removal of any textural defects associated with nonhydrostatic pressures was achieved by subsequent wet-bag isostatic pressing at 350 MPa. A green density  $\approx 55\%$  of the theoretical limit was attained by this procedure.

The green disks were packed in loose powder of identical composition in high-purity alumina crucibles for heat treatment. Two firing stages were employed. The first consisted of calcining at 1150°C in air for 24 h followed by sintering at 1550°C for 30 min (MoSi<sub>2</sub> resistance furnace). This yielded specimens of  $\geq 99\%$  density with 1.8- $\mu\text{m}$  grain size. The second stage involved postsintering heat treatments under reducing conditions ( $\text{N}_2$  gas, graphite-element furnace), in separate batches at prescribed hold times and at temperatures between 1550° and 1800°C. This promoted grain growth, producing specimens in the grain-size range 2 to 80  $\mu\text{m}$ . All heating cycles were carried out at a maximum heating/cooling rate of 500°C/h.

Sample specimens from each batch were subjected to microstructural characterization. Densities were measured by the

Archimedes method using water as the immersion medium.<sup>40</sup> Surfaces were prepared for optical microscopy by diamond polishing to 1  $\mu\text{m}$ . The microstructures were revealed by thermal etching (air, 1550°C, 12 min) and the grain diameters measured using the linear intercept technique.<sup>41</sup> Unetched specimens were examined in transmitted light for the incidence of spontaneous microcracking.

### (2) Indentation-Strength Testing

Prior to testing, each remaining disk was machined to a thickness of 2.5 mm and the prospective tensile face diamond-polished to a 1- $\mu\text{m}$  finish. Most specimens were indented at their face centers with a Vickers diamond pyramid at contact loads between 0.2 and 200 N. Some were left unindented as controls. All indentations were made in laboratory ambient and allowed to stand for 10 min. Biaxial strength tests were then made using a flat circular punch (4-mm diameter) on a three-point support (15-mm diameter).<sup>42</sup> A drop of silicone oil was placed onto the indentations prior to testing, and failure times were kept below 20 ms, to minimize effects from moisture-assisted kinetic crack growth. "Inert" strengths were calculated from the breaking loads and specimen dimensions using thin-plate formulas.<sup>42</sup> Special care was taken to examine all specimens after failure in the optical microscope to verify the contact site as the origin of failure. Breaks that did not pass through the indentations were incorporated into the data pool for unindented controls.

Optical and scanning electron microscopy was also used to examine the fracture surfaces to determine the relative amounts of intergranular and transgranular cracking.

## III. Experimental Results

### (1) Characterization of Microstructure and Fracture Surfaces

Figure 1 shows representative microstructures of two aluminas, at opposite extremes of grain size. The grain structures are equiaxed and of narrow size distribution (maximum diameter  $<$  twice mean diameter—"Hillert's criterion"<sup>43</sup>), as is appropriate to an investigation of a size effect. Such equiaxed structures may be taken as circumstantial evidence for the lack of any intergranular glassy phases.<sup>44</sup> The defect population in Fig. 1 appears to consist predominantly of surface-intersected pores at triple-point junctions (seen to better advantage in Fig. 1(B)) and occasional grain pullouts due to polishing (e.g., at upper right in Fig. 1(A)). The small scale of the defects indicates that we have attained high density: actual measurements yield  $\geq 99\%$  of theoretical density at all grain sizes.

The translucence of our materials also allowed the internal flaw population to be investigated in the bulk material, using transmitted light. Figure 2 is an example. Small pores are again evident on a substantial fraction of the triple-point sites. Such pores can be effective sources of grain-facet cracking and are thereby believed to constitute a principal component of the intrinsic flaw population in our materials. More apparent are extended microcracks, on the order of two to three grain-facet dimensions, which have generated spontaneously under the action of local thermal expansion anisotropy stresses during the processing. The first incidence of such microcracks was observed at grain sizes as low as 35  $\mu\text{m}$ , beyond which the number density increased markedly with coarsening of the microstructure.

Figure 3 shows fracture surfaces of the same aluminas in Fig. 1, after biaxial strength testing. These micrographs reveal a mixture of fracture modes,  $\approx 70\%$  intergranular and  $\approx 30\%$  transgranular in our aluminas. This represents a somewhat larger proportion of transgranular mode than noted in our previous studies using a commercial alumina, which was characterized by a distinctly less uniform grain structure.<sup>30,31</sup>

<sup>1</sup>Polymers Product Division, General Electric Co., Pittsfield, MA.  
<sup>2</sup>AKP-HP grade (99.995% pure, 0.5- $\mu\text{m}$  crystallites), Sumitomo Chemical America, New York.

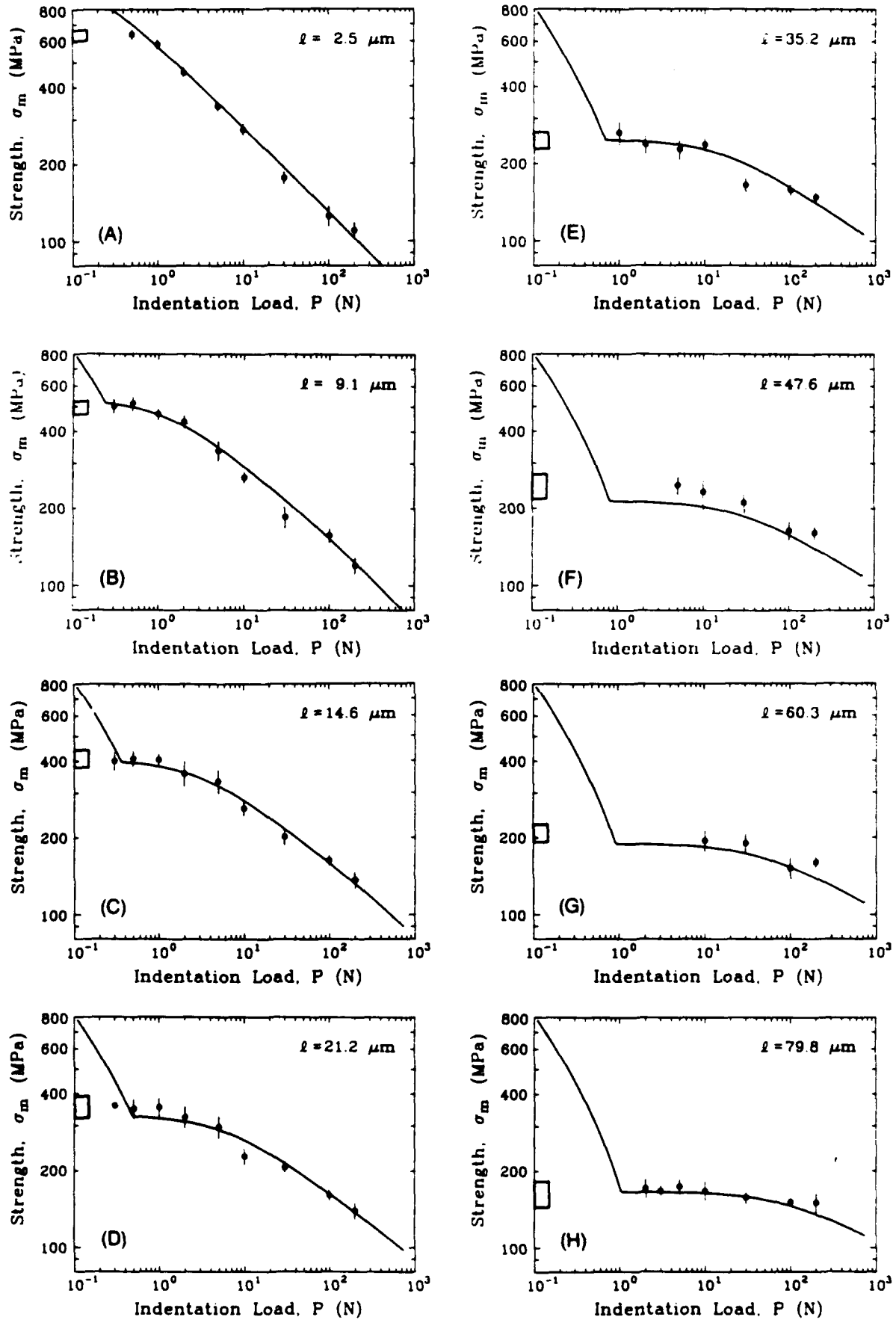


Fig. 4. Plots of inert strength  $\sigma_m$ , versus indentation load  $P$ , for aluminas of grain size (A)  $\ell = 2.5 \mu\text{m}$ , (B)  $\ell = 9.1 \mu\text{m}$ , (C)  $\ell = 14.6 \mu\text{m}$ , (D)  $\ell = 21.2 \mu\text{m}$ , (E)  $\ell = 35.2 \mu\text{m}$ , (F)  $\ell = 47.6 \mu\text{m}$ , (G)  $\ell = 60.3 \mu\text{m}$ , and (H)  $\ell = 79.8 \mu\text{m}$ . Curves are best fit from bridging model in Sections IV and V.

strength plateau is lower, but stronger (i.e., persists over a greater range of contact load), at larger grain sizes. One may also note a disposition for the data sets at any two grain sizes to cross each other at some point along the load axis. We shall discuss these trends in relation to transitions from Orowan to Petch behavior in Section V.

#### IV. Theory

We summarize here the essence of the grain-bridging theory of R-curve (T-curve) and strength characteristics in monophase ceramics as it pertains to grain size.<sup>36</sup> It is implicit in this endeavor that the principle of similitude applies to our materials, i.e., that the microstructure scales geometrically with grain size.

##### (1) Grain-Bridging and T-Curve (R-Curve)

Begin by defining a general stress intensity factor condition for the equilibrium of a crack subject to an applied tensile loading field,  $K_a(c)$ , a flaw-localized residual nucleation field,  $K_r(c)$ , and a microstructure-associated field,  $K_\mu(c)$ .<sup>32,48,49</sup> Equilibrium obtains when the net crack-tip field,  $K_\sigma(c)$ , just balances the toughness associated with the creation of (intergranular or transgranular) surfaces,  $T_0$ :

$$K_\sigma(c) = K_a(c) + K_r(c) + K_\mu(c) = T_0 \quad (1)$$

This requirement can be restated by considering  $K_a$  and  $K_r$  as part of the net applied mechanical field,  $K_A$ , and  $K_\mu = -T_\mu$  as part of the internal toughness,  $T$ , i.e.

$$\begin{aligned} K_A(c) &= K_a(c) + K_r(c) \\ &= T_0 + T_\mu(c) = T(c) \end{aligned} \quad (2)$$

The toughness function  $T(c)$  constitutes the so-called T-curve, the K-field equivalent of the R-curve.

Our principal aim is to express  $T_\mu(c)$  in terms of grain size and other microstructural variables.<sup>36</sup> The stress-separation micromechanics are assumed to be governed by thermal expansion mismatch stresses, which "clamp" the interlocking bridging grains into the matrix. (We have already noted the manifestations of such internal stresses in relation to the microcracks in Fig. 2.) As the crack walls move apart, the bridging grains debond along the constrained boundary facets and then slide out against frictional tractions at these boundaries until final "rupture" at some critical strain.<sup>31,34</sup> Ignoring the debond stage (which consumes relatively little energy<sup>36</sup>), the constitutive relation between the closure stress  $p$  and (half) crack-opening displacement  $u$  may be written<sup>32,36</sup>

$$p(u) = p_M(1 - u/u_\ell) \quad (3)$$

where  $p_M$  is the maximum resistance stress (at  $u = 0$ ) and  $2u_\ell$  is the wall-wall displacement at bridge-matrix disengagement (at  $p = 0$ ). For geometrically similar microstructures, these last two quantities may be determined more explicitly in terms of the grain size  $\ell$ :<sup>36</sup>

$$2u_\ell = \epsilon_r \ell \quad (4a)$$

$$p_M = (4\epsilon_r \mu \sigma_R)(1 - 1/2\alpha_d^2) \quad (4b)$$

with bridge rupture strain  $\epsilon_r$ , coefficient of sliding friction  $\mu$ , magnitude of internal stress  $\sigma_R$ , and ratio of bridge-spacing to grain-size  $\alpha_d = d/\ell$  all scale-independent parameters. Schematic plots of the constitutive relation are given for different grain sizes in Fig. 5. Note that  $\ell$  enters the formalism exclusively through the grain pullout distance  $u_\ell$ , and not through the closure stress  $p_M$ .

Now consider the evolution of a half-penny crack, radius  $c$ , through the microstructure, Fig. 6. The solution for  $T_\mu(c)$  may be subdivided into three domains.<sup>36</sup>

(A) *Small Cracks:* ( $c < d$ ), no bridge intersections. The crack is assumed to initiate in a region of local matrix tensile

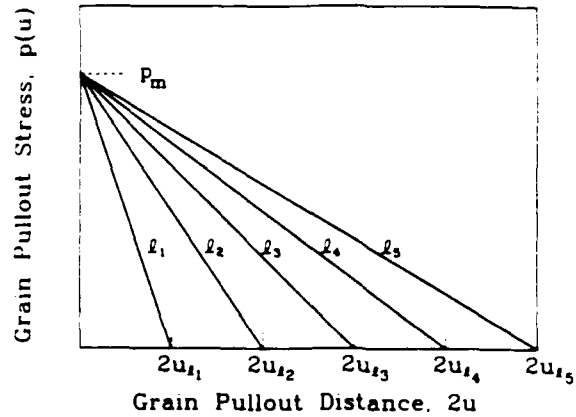


Fig. 5. Schematic plots of constitutive relation Eq. (3) for different grain sizes ( $\ell_1 < \ell_2 < \ell_3 < \ell_4 < \ell_5$ ). Note that pullout distance  $u_\ell$  in Eq. (4a) scales linearly with grain size  $\ell$ , but that corresponding stress  $p_M$  in Eq. (4b) is completely independent of  $\ell$ .

residual stress, assumed uniform at  $+\sigma_R$ , whence

$$T_\mu(c) = -\psi \sigma_R c^{1/2} \quad (5)$$

with  $\psi$  a geometry coefficient.

(B) *Intermediate Cracks:* ( $c \geq d$ ,  $0 \leq 2u \leq \epsilon_r \ell$ ), bridges intersected. There are two contributions in this region,  $T_\mu(c) = T'_\mu(c) + T''_\mu(c)$ . The first is a persistent, opening post-intersection component from the tensile stress  $+\sigma_R$  in (A); a Green's function integration yields

$$T'_\mu(c) = -\psi \sigma_R c^{1/2} [1 - (1 - \alpha_d^2 \ell^2 / c^2)^{1/2}] \quad (6)$$

The second is a countervailing closing component due to the bridging tractions in Eq. (3). One may use the J-integral to determine the corresponding crack resistance component  $R''_\mu$  in terms of crack-opening displacements.<sup>30</sup>

$$\begin{aligned} J_\mu &= 2 \int_0^{u_z} p(u) du \\ &= 2p_M u_z (1 - u_z/\epsilon_r \ell) = R''_\mu(u_z) \end{aligned} \quad (7)$$

where the displacement  $u_z = u_z(c)$  at the edge of the bridging zone (i.e., point of first bridge intersection at  $c = d = \alpha_d \ell$ , Fig. 6) may be evaluated separately from the approximate

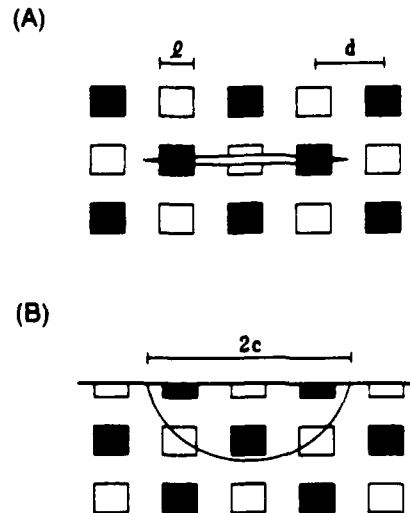


Fig. 6. Schematic of growth of pennylike crack in bridging field: (A) side view, (B) projection view. (Open squares are out-of-plane bridging grains.)



## Sneddon crack profile relation

$$u_z(c) = (\psi K_A/E')[(c^2 - \alpha_d^2 \ell^2)/c]^{1/2} \quad (8)$$

to give  $R_\mu^*(c)$ . The toughness  $T_\mu^*$  may be related to the crack resistance  $R_\mu^*$  by eliminating  $J_A$  and  $K_A$  from the equivalent equilibrium relations  $J_A = T_0^2/E' + R_\mu^*$  and  $K_A = T_0 + T_\mu^*$  (Eq. (2)) via  $J_A = K_A^2/E'$ :<sup>50</sup>

$$T_\mu^*(c) = [E'R_\mu^*(c)]^{1/2} \{ [1 + T_0^2/E'R_\mu^*(c)]^{1/2} - [T_0^2/E'R_\mu^*(c)]^{1/2} \} \quad (9)$$

Equation (9) is an implicit function in  $T_\mu^*$ , so Eqs. (2) and (7) to (9) must be solved simultaneously.<sup>50</sup>

(C) **Large Cracks:** ( $c \gg d$ ,  $2u_z \geq \epsilon_t \ell$ ), bridging zone translates with crack, and  $T_\mu = T_\mu' + T_\mu^*$  becomes invariant with crack size.

We shall consider the explicit form of  $T(c)$  in specific relation to our aluminas later. For the present we simply emphasize that the contribution to the toughness from the local matrix tensile residual stress is negative (Eqs. (5) and (6)) and thereby diminishes the stability at small crack sizes, whereas the contribution from the frictional pullout is positive (Eq. (9)) and strongly enhances the stability at large crack sizes.<sup>32,35</sup> It is these opposite tendencies at extremes of crack size that account for the spontaneous initiation and arrest of the microcracks in Fig. 2.

(2) **Flaws and Strength Characteristics**

Now consider the evolution of flaws through the bridging field under the action of a uniform applied stress  $\sigma_a$ , corresponding to a stress-intensity factor<sup>30,33</sup>

$$K_a = \psi \sigma_a c^{1/2} \quad (10)$$

so that Eq. (2) transposes to

$$\sigma_a(c) = (1/\psi c^{1/2})[T(c) - K_a(c)] \quad (11)$$

The strength response may then be determined by properly applying the crack instability condition  $d\sigma_a(c)/dc \geq 0$  (equivalent to  $dK_a(c)/dc \geq dT(c)/dc$ <sup>49</sup>). In relation to Griffith flaws ( $T = T_0 = \text{const}$ ,  $K_a = 0$ ), for which Eq. (11) reduces to a single, monotonically diminishing branch, the stabilizing influence of the  $T(c)$  and  $K_a(c)$  fields is manifest as maxima in the  $\sigma_a(c)$  function.<sup>33,36</sup> Ultimate failure at  $\sigma_a = \sigma_m$  corresponds to the greatest of these maxima.

It remains to specify the quantities  $K_a$  in Eq. (11) and initial sizes  $c$ , for the flaw types of interest. For the controlled Vickers flaws used to obtain the data in Fig. 4, we have<sup>45,51</sup>

$$K_a = \chi P/c^{3/2} \quad (12)$$

with  $P$  the indentation load and  $\chi$  an elastic-plastic contact coefficient;  $c$  is then determined by the condition  $\sigma_a = 0$  in Eq. (11). For the grain-facet processing flaws which determine the *intrinsic* strength characteristics, we simply set  $K_a = 0$ . According to the observations in Section III(1), the initial size of these flaws is on the order of one grain facet but, to allow conservatively for the possibility of preexisting extended microcracks (Fig. 2), we assume one bridge spacing,  $c = \alpha_d \ell$ . Finally, for *extrinsic* flaws we again set  $K_a = 0$ ; in this case the values of  $c$  are to be specified independently.

V. **Analysis of Alumina Data in Terms of Bridging Model**

Now let us apply the theory of the previous section to obtain fits to the data in Fig. 4 and thence to determine the  $T$ -curves for our aluminas. We do this by choosing initial values for the microstructural parameters and then adjusting these parameters using an iterative algorithm.

(1) **Regression Algorithm**

We begin by specifying first values for the material and geometrical parameters in the strength formulation, using estimates from a previous analysis on a commercial alumina.<sup>36</sup>

Some of these parameters are regarded as invariants in the regression: geometry coefficient  $\psi = 1.24$  (penny cracks),<sup>42</sup> Young's modulus  $E' = 409$  GPa, and indentation flaw parameter  $\chi = 0.018$  ("pure" alumina).<sup>33</sup> Other starting parameters are treated as adjustable:  $T_0 = 2.5$  MPa  $\cdot$  m<sup>1/2</sup> for the grain-boundary toughness and  $\sigma_R = 155$  MPa for the internal stress; bridge rupture strain  $\epsilon_t = 0.14$  and (normalized) bridge spacing  $\alpha_d = 1.5$ ; and friction coefficient  $\mu = 1.8$ .

The regression algorithm for best fitting the  $\sigma_m(P)$  data is based on a matrix search routine:<sup>33,36</sup> (i) compute trial  $T$ -curve based on starting values of parameters; (ii) evaluate function  $\sigma_a(c)$  in Eq. (11), using all individual (rather than mean) test points, at each indentation load and grain size for which experimental data are available; (iii) determine the inert strength  $\sigma_m$  as the largest maximum in each such  $\sigma_a(c)$  function; (iii) compare predicted strengths with measured values for each set of parameters, and evaluate the net variance in  $\sigma_m$  over all loads and grain sizes; (iv) adjust the floating parameters ( $T_0, \sigma_R, \epsilon_t, \alpha_d, \mu$ ), with increasing refinement in the increment size in successive iterations, and thence determine the parameter set with minimum variance.

(2) **Data Fits and Deconvolution of  $T$ -Curves**

The best fit to the strength data for our alumina corresponds to the following material parameters:  $T_0 = 2.75$  MPa  $\cdot$  m<sup>1/2</sup>,  $\sigma_R = 380$  MPa,  $\epsilon_t = 0.040$ ,  $\alpha_d = 1.0$ , and  $\mu = 1.6$ ; the standard deviation in  $\sigma_m$  over all data is 17 MPa. This parameter fit is represented by the solid curves in Fig. 4. (Compared with the above starting values from our earlier data fit, we may note an increase in  $T_0$  and  $\sigma_R$ , a decrease in  $\epsilon_t$ .) It can be seen that the theory accounts for the major grain-size dependencies in the indentation-strength data sets, particularly the relative positions and widths of the plateaus and the crossover tendencies. For ready comparison, the curves for the various grain sizes are plotted on the composite diagram of Fig. 7.

Deconvoluted  $T$ -curves resulting from the parameter fit are shown in Fig. 8. The strongly decreasing toughness with crack extension at small crack sizes (negative branch) reflects the high level of local (thermal expansion anisotropy) tensile stress acting on the flaw. After the first bridge intersection at  $c = \alpha_d \ell$  the toughness curves rise markedly (positive branch), especially for the coarser grain structures, reflecting the scaling effect in the grain pullout length. It is this rising por-

<sup>52</sup>Strictly,  $\psi$  should be a function of the ratio of crack length to specimen thickness. In our experiments the maximum crack size at failure was  $\approx 0.5$  mm, i.e., about 20% of the specimen thickness, which leads to a maximum error of  $\approx 7\%$ .<sup>52</sup> This error is considerably smaller than the shifts in strength values from grain size to grain size in Fig. 4 and is neglected here.

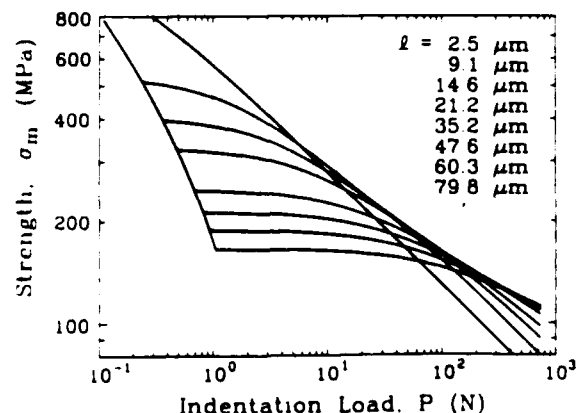


Fig. 7. Composite plot of best-fit  $\sigma_m(P)$  curves for the aluminas in Fig. 4. Note tendency for curves at different grain size to cross over at intermediate indentation loads.

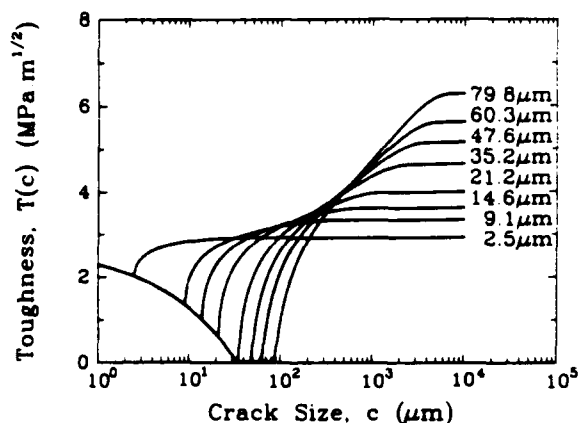


Fig. 8. Toughness curves for aluminas of grain sizes, deconvoluted from theoretical fits in Fig. 7.

tion of the curves that largely determines the strength properties. A flaw which becomes unstable at applied load  $K_A = K_A = \psi \sigma_a c^{1/2}$  (Eq. (10)) on the negative branch just to the left of the minimum propagates unstably and arrests on the positive branch; this accounts for the "pop-in" behavior observed experimentally.<sup>31</sup> The particular curve for which the condition  $c = \alpha_d \ell$  coincides with the abscissa ( $K_A = T = 0$  in Eq. (2)) determines the critical grain size for spontaneous pop-in; from Fig. 8 we estimate  $\ell = 30 \mu\text{m}$  for our alumina, consistent with the first observation of microcracking in Fig. 2.

From the parameter fits in Fig. 4 we determine the strength/grain-size characteristic for intrinsic flaws ( $K_i = 0$ ) shown in Fig. 9. Recall our assumption of an initial size  $c_i = \alpha_d \ell$  for such flaws; in fact, the computed strength curve is insensitive to wide variations in this initial flaw size,<sup>36</sup> as befits a truly intrinsic property. The predicted curve has a slope close to, but not exactly,  $-1/2$ ; nor, indeed, is the curve linear on the logarithmic plot. Note that only the data point corresponding to the very smallest grain size deviates significantly from this curve, suggesting that the stabilizing influence of the  $T(c)$  function exerts a controlling influence in all but the finest microstructures.

## VI. Discussion

The bridging model accounts for the main features of the indentation strength-load response for our aluminas. It explains, in particular, the flaw tolerance qualities apparent in the data of Fig. 4 and thereby accentuates the inadequacy of the simple Griffith flaw concept. It is no longer valid to consider toughness  $T$  as a material constant (although the intrinsic

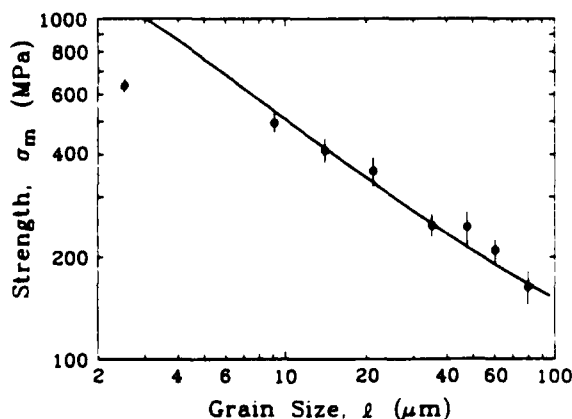


Fig. 9. Strength versus grain size for alumina. Data points are breaks from specimens without indentations; solid curve is prediction for intrinsic, microstructure-controlled flaws using indentation-strength parameters from fits in Fig. 4.

sic grain-boundary toughness  $T_0$  is invariant) or the critical flaw size at final instability to be proportional to grain size: the stabilizing influence of the  $T$ -curve fundamentally and dramatically transforms the micromechanics of failure.

We noted the capacity of the bridging theory to fit all the major trends in the alumina indentation-strength data of Fig. 4, over the entire range of grain sizes covered. Because there are several adjustable parameters involved in this fit, the "agreement" cannot be taken as "proof" of the model.<sup>36</sup> The validity of the bridging concept rests with the direct observations of crack evolution reported elsewhere.<sup>31</sup> Once "calibrated", the formalism allows us to quantify the role of grain size (as well as other microstructural variables) in the strength characteristics. Thus we recall that the grain-size exponent in the strength curve for intrinsic flaws in Fig. 9 is close, but not exactly equal, to the value  $-1/2$  for ideal Griffith flaws: there is nothing in the bridging theory to suggest that this exponent should necessarily assume any universal value or indeed that the relation should be power law at all.

In this context it is interesting to compare the fit to the present alumina data with the earlier fit to a commercial alumina.<sup>36</sup> There, a forced power-law fit yielded an exponent closer to  $-1/2$ . Two experimental observations distinguish our material from that used in the earlier study: the microstructure is considerably more uniform in size and shape (the commercial material showed evidence of some abnormal grain growth), and the fracture mode has a stronger transgranular component. This may be correlated with the relatively high grain-boundary toughness  $T_0$  and internal residual stress  $\sigma_R$ , and low bridge rupture strain  $\epsilon_r$ , indicators of grain boundaries which are less susceptible to debonding, hence pullout. Here is an example where an element of control in microstructural development could be counterproductive: comparative examination of the indentation-strength data sets confirms that the present materials have less pronounced  $T$ -curves and are therefore less flaw tolerant. The implication is that inhomogeneity and nonuniformity in the microstructure, e.g., elongate grains (to increase  $u_r$  in Eq. (4a)<sup>36</sup>), may actually be desirable features from the structural standpoint.

The bridging model also provides insights into the role of flaw states in the Orowan-Petch transition referred to in Section I. To illustrate, we replot from Fig. 9 the strength data for unindented surfaces as a function of inverse square root grain size in Fig. 10. Included in Fig. 10 are the corresponding predicted responses for intrinsic flaws (solid curve,  $K_i = 0$ ,  $c_i = \alpha_d \ell$ ) and extrinsic flaws (dashed curve,  $K_e = 0$ ,  $c_e$  as

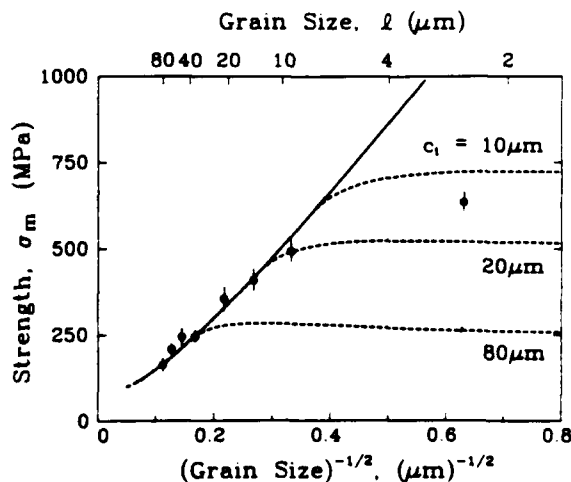


Fig. 10. Similar to Fig. 9, but with abscissa replotted as inverse square root of grain size, with data points again for unindented specimens and solid curve for intrinsic flaws. Also included as dashed curves are predictions for extrinsic flaws of specified initial size  $c_i$ . Note insensitivity of strength to flaw characteristics in large-grain-size domain.

specified). We note that the dashed and solid curves merge in the large grain-size (Orowan) domain. The insensitivity of the predictions to any assumptions concerning type or size of initial flaw in this domain (attributable to the  $T$ -curve stabilization) indicates a failure condition determined exclusively by material properties. Note again that the solid curve is not exactly linear in this region, as would obtain if true Griffith-Orowan behavior were to prevail.<sup>46</sup> On the other hand, in the small-grain-size (Petch) domain the strengths are highly flaw sensitive, and the dashed curves diverge substantially from the Orowan branch, the more so as  $c$ , increases. On passing into this region, the extrinsic flaws become increasingly larger than their microstructural counterparts and thereby traverse the upper reaches of the  $T$ -curves in Fig. 8 where precursor stable crack growth prior to failure no longer occurs.<sup>32,48</sup> We note that only one of the data points in Fig. 10, that at the finest grain size ( $\ell = 2.5 \mu\text{m}$ ), appears to fall into the extrinsic domain: this result implies an initial flaw size  $c_i \approx 15 \mu\text{m}$  for our polished surfaces. For the larger extrinsic flaws, the dashed curves in Fig. 10 pass through a slight maximum at fine grain sizes (i.e., into a region in which  $\sigma_m$  actually increases with respect to  $\ell$ ), reflecting the crossover to positive dependence of steady-state toughness on grain size at right in Fig. 8.

The results of the present study have some intriguing implications concerning microstructural design for improved structural materials. We have already alluded to the potential for engineering grain-boundary structures (as they affect  $T_0$ ,  $\sigma_R$ ,  $\epsilon_t$ , etc.) and grain texture (elongate grains) to impart respectable toughness properties to otherwise inherently brittle single-phase ceramics.<sup>36</sup> Perhaps the most far-reaching conclusion to emerge from the analysis is the relatively benign role of processing flaws in ceramics with strong  $T$ -curve behavior. The relentless elimination of every last defect, as advocated by some,<sup>14,53–55</sup> is not necessarily the ultimate in processing strategies.

Our study has focused on alumina, for which the mechanism of toughening is bridging grain pullout. However, we would emphasize that similar grain-size dependencies are to be expected in any material which exhibits  $T$ -curve ( $R$ -curve) behavior, e.g., whether due to incorporated second phases (e.g., fibers, whiskers), phase transformations, microcrack cloud formation, or any other subsidiary energy-dissipative process. This is not to preclude the possibility of ceramics without an  $R$ -curve, e.g., single-phase cubic ceramics, exhibiting an Orowan-Petch transition; but there the Orowan branch can no longer be defined exclusively by material properties and requires additional detailed specification of the intrinsic-flaw micromechanics.

**Acknowledgments:** The authors acknowledge discussions on different aspects of this work with several colleagues, including T.-J. Chuang, R. F. Cook, E. R. Fuller, Jr., Y.-W. Mai, and D. B. Marshall. We are also grateful to S. Darby for assistance with specimen preparation.

## References

- I. B. Cutler, "Strength Properties of Sintered Alumina in Relation to Porosity and Grain Size," *J. Am. Ceram. Soc.*, **40** [1] 20–23 (1957).
- F. P. Knudsen, "Dependence of Mechanical Strength of Brittle Polycrystalline Specimens on Porosity and Grain Size," *J. Am. Ceram. Soc.*, **42** [8] 376–87 (1959).
- W. B. Crandall, D. H. Chung, and T. J. Grav, "The Mechanical Properties of Ultra-Fine Hot-Pressed Alumina," pp. 349–76 in *Mechanical Properties of Engineering Ceramics*, Edited by W. W. Krieger and H. Palmour III, Interscience Publishers, New York, 1961.
- R. J. Charles and R. R. Shaw, "Delayed Failure of Polycrystalline and Single-Crystal Alumina," General Electric Report No. 62-RL-3081 M, 1962.
- R. M. Spriggs and T. Vasilos, "Effect of Grain Size on Transverse Bend Strength of Alumina and Magnesia," *J. Am. Ceram. Soc.*, **46** [5] 224–28 (1963).
- R. M. Spriggs, J. B. Mitchell, and T. Vasilos, "Mechanical Properties of Pure, Dense Aluminum Oxide as a Function of Temperature and Grain Size," *J. Am. Ceram. Soc.*, **47** [7] 323–27 (1964).
- E. M. Passmore, R. M. Spriggs, and T. Vasilos, "Strength-Grain Size-Porosity Relations in Alumina," *J. Am. Ceram. Soc.*, **48** [1] 1–7 (1965).
- D. B. Binnis and P. Popper, "Mechanical Properties of Some Commercial Alumina Ceramics," *Proc. Br. Ceram. Soc.*, **6**, 71–82 (1966).
- S. C. Carniglia, "Reexamination of Experimental Strength-vs-Grain Size Data for Ceramics," *J. Am. Ceram. Soc.*, **55** [5] 243–49 (1972).
- R. W. Rice, "Strength/Grain Size Effects in Ceramics," *Proc. Br. Ceram. Soc.*, **20**, 205–57 (1972).
- A. G. Evans and G. Tappin, "Effects of Microstructure on the Stress to Propagate Inherent Flaws," *Proc. Br. Ceram. Soc.*, **20**, 275–97 (1972).
- R. E. Tressler, R. A. Langensiepen, and R. C. Bradt, "Surface-Finish Effects on Strength vs Grain Size Relations in Polycrystalline  $\text{Al}_2\text{O}_3$ ," *J. Am. Ceram. Soc.*, **57** [5] 226–27 (1974).
- E. Dörre and H. Hübner, *Alumina: Processing, Properties and Applications*, Ch. 3, Springer-Verlag, New York, 1984.
- N. McN. Alford, K. Kendall, and J. D. Birchall, "Strength/Microstructure Relation in  $\text{Al}_2\text{O}_3$  and  $\text{TiO}_2$ ," *Adv. Ceram. Mater.*, **3** [2] 113–17 (1988).
- E. Orowan, "Fracture and Strength of Solids," *Rep. Prog. Phys.*, **12**, 186–232 (1948).
- N. J. Petch, "Cleavage Strength of Polycrystals," *J. Iron Steel Inst., London*, **174** [1] 25–28 (1953).
- R. W. Rice, S. W. Freiman, R. C. Pohanka, J. J. Mecholsky, Jr., and C. C. Wu, "Microstructural Dependence of Fracture Mechanics Parameters in Ceramics," pp. 849–76 in *Fracture Mechanics of Ceramics*, Vol. 4, Edited by R. C. Bradt, D. P. H. Hasselman, and F. F. Lange, Plenum Press, New York, 1978.
- R. W. Rice, S. W. Freiman, and J. J. Mecholsky, "Dependence of Strength-Controlling Fracture Energy on the Flaw Size to Grain Size Ratio," *J. Am. Ceram. Soc.*, **63** [3–4] 129–36 (1980).
- V. D. Krstic, "Grain-Size Dependence of Fracture Stress in Anisotropic Brittle Solids," *J. Mater. Sci.*, **23** [1] 259–66 (1988).
- J. P. Singh, A. V. Virkar, D. K. Shetty, and R. S. Gordon, "Strength-Grain Size Relations in Polycrystalline Ceramics," *J. Am. Ceram. Soc.*, **62** [3–4] 179–83 (1979).
- A. G. Evans, "Dimensional Analysis of the Grain-Size Dependence of Strength," *J. Am. Ceram. Soc.*, **63** [1–2] 115–16 (1980).
- A. V. Virkar, D. K. Shetty, and A. G. Evans, "Grain-Size Dependence of Strength," *J. Am. Ceram. Soc.*, **64** [3] C-56–C-57 (1981).
- R. W. Rice and D. Lewis, "Limitations and Challenges in Applying Fracture Mechanics to Ceramics," pp. 659–76 in *Fracture Mechanics of Ceramics*, Vol. 5, Edited by R. C. Bradt, A. G. Evans, D. P. H. Hasselman, and F. F. Lange, Plenum Press, New York, 1983.
- H. Hübner and W. Jillek, "Sub-Critical Crack Extension and Crack Resistance in Polycrystalline Alumina," *J. Mater. Sci.*, **12** [1] 117–25 (1977).
- R. Knehan and R. W. Steinbrech, "Memory Effect of Crack Resistance During Slow Crack Growth in Notched  $\text{Al}_2\text{O}_3$  Bend Specimens," *J. Mater. Sci. Lett.*, **1** [8] 327–29 (1982).
- R. W. Steinbrech, R. Knehan, and W. Schaarwächter, "Increase of Crack Resistance During Slow Crack Growth in  $\text{Al}_2\text{O}_3$  Bend Specimens," *J. Mater. Sci.*, **18** [10] 265–70 (1983).
- R. Knehan and R. W. Steinbrech, "Effect of Grain Size on the Crack Resistance Curves of  $\text{Al}_2\text{O}_3$  Bend Specimens," pp. 613–19 in *Science of Ceramics*, Vol. 12, Edited by P. Vincenzini, Ceramurgia, Imola, Italy, 1984.
- M. V. Swain, "R-Curve Behavior in a Polycrystalline Alumina Material," *J. Mater. Sci. Lett.*, **5** [12] 1313–15 (1986).
- R. W. Steinbrech and O. Schmenkel, "Crack-Resistance Curves of Surface Cracks in Alumina," *J. Am. Ceram. Soc.*, **71** [5] C-271–C-273 (1988).
- R. F. Cook, B. R. Lawn, and C. J. Fairbanks, "Microstructure-Strength Properties in Ceramics: I. Effect of Crack Size on Toughness," *J. Am. Ceram. Soc.*, **68** [11] 604 (1985).
- P. L. Swanson, C. J. Fairbanks, B. R. Lawn, Y.-W. Mai, and B. J. Hockey, "Crack-Interface Grain Bridging as a Fracture Resistance Mechanism in Ceramics: I. Experimental Study on Alumina," *J. Am. Ceram. Soc.*, **70** [4] 279–89 (1987).
- Y.-W. Mai and B. R. Lawn, "Crack-Interface Grain Bridging as a Fracture Resistance Mechanism in Ceramics: II. Theoretical Fracture Mechanics Model," *J. Am. Ceram. Soc.*, **70** [4] 289–94 (1987).
- R. F. Cook, C. J. Fairbanks, B. R. Lawn, and Y.-W. Mai, "Crack Resistance by Interfacial Bridging: Its Role in Determining Strength Characteristics," *J. Mater. Res.*, **2** [3] 345–56 (1987).
- P. L. Swanson, "Crack-Interface Traction: A Fracture-Resistance Mechanism in Brittle Polycrystals," pp. 135–55 in *Advances in Ceramics*, Vol. 22, Fractography of Glasses and Ceramics, American Ceramic Society, Columbus, OH, 1988.
- S. J. Bannison and B. R. Lawn, "Flaw Tolerance in Ceramics with Rising Crack-Resistance Characteristics," *J. Mater. Sci.*, **24** [9] 3169–75 (1989).
- S. J. Bannison and B. R. Lawn, "Role of Interfacial Grain-Bridging Sliding Friction in the Crack-Resistance and Strength Properties of Nontransforming Ceramics," *Acta Metall.*, **37** [10] 2659–71 (1989).
- R. L. Coble, "Sintering of Crystalline Solids—II. Experimental Test of Diffusion Models in Porous Compacts," *J. Appl. Phys.*, **32** [5] 793–99 (1961).
- S. J. Bannison and M. P. Harmer, "A History of the Role of MgO in the Sintering of  $\alpha\text{-Al}_2\text{O}_3$ ," *Ceramic Transactions*, Vol. 7, Sintering of Advanced Ceramics, Edited by C. A. Handwerker, J. E. Blendell, and W. A. Kayser.

<sup>46</sup>At very large grain sizes the strength is actually predicted to fall to zero, corresponding to unlimited unstable extension of the intrinsic flaws. Material compacts with microstructures on this scale will tend to fail spontaneously on cooling from the processing temperature.

American Ceramic Society, Westerville, OH, 1989.

<sup>39</sup>S. K. Roy and R. L. Coble, "Solubilities of Magnesia, Titania, and Magnesium Titanate in Aluminum Oxide," *J. Am. Ceram. Soc.*, **5** [1] 1-6 (1968).

<sup>40</sup>E. C. M. Pennings and W. Grellner, "Precise Nondestructive Determination of the Density of Porous Ceramics," *J. Am. Ceram. Soc.*, **72** [2] 1268-70 (1989).

<sup>41</sup>J. C. Wurst and J. A. Nelson, "Lineal Intercept Technique for Measuring Grain Size in Two-Phase Polycrystalline Ceramics," *J. Am. Ceram. Soc.*, **55** [2] 109 (1972).

<sup>42</sup>D. B. Marshall, "An Improved Biaxial Flexure Test for Ceramics," *Am. Ceram. Soc. Bull.*, **59** [5] 551-53 (1980).

<sup>43</sup>M. Hillert, "Theory of Normal and Abnormal Grain Growth," *Acta Metall.*, **13** [3] 227-38 (1965).

<sup>44</sup>C. A. Bateman, S. J. Bennison, and M. P. Harmer, "Mechanism for the Role of Magnesia in the Sintering of Alumina Containing Small Amounts of a Liquid Phase," *J. Am. Ceram. Soc.*, **72** [7] 1241-44 (1989).

<sup>45</sup>D. B. Marshall and B. R. Lawn, "Residual Stress Effects in Sharp-Contact Cracking: I. Indentation Fracture Mechanics," *J. Mater. Sci.*, **14** [9] 2001-12 (1979).

<sup>46</sup>D. B. Marshall, B. R. Lawn, and P. Chantikul, "Residual Stress Effects in Sharp-Contact Cracking: II. Strength Degradation," *J. Mater. Sci.*, **14** [9] 2225 (1979).

<sup>47</sup>B. R. Lawn, "The Indentation Crack as a Model Indentation Flaw," pp. 1-25 in *Fracture Mechanics of Ceramics*, Vol. 5. Edited by R. C. Bradt,

A. G. Evans, D. P. H. Hasselman, and F. F. Lange. Plenum Press, New York, 1983.

<sup>48</sup>Y.-W. Mai and B. R. Lawn, "Crack Stability and Toughness Characteristics in Brittle Materials," *Annu. Rev. Mater. Sci.*, **16**, 415-39 (1986).

<sup>49</sup>B. R. Lawn and T. R. Wilshaw, *Fracture of Brittle Solids*; Ch. 3. Cambridge University Press, London, U.K., 1975.

<sup>50</sup>R. F. Cook, "Transient Fracture Resistance in the Weak Toughening Limit," pp. 2747-55, in *Advances in Fracture Research*, I.C.F. 7. Edited by K. Salama, R. Ravi-Chandra, D. M. R. Taplin, and P. Rama-Rao. Pergamon Press, New York, 1989.

<sup>51</sup>B. R. Lawn, A. G. Evans, and D. B. Marshall, "Elastic/Plastic Indentation Damage in Ceramics: The Median/Radial Crack System," *J. Am. Ceram. Soc.*, **63** [9-10] 574-81 (1980).

<sup>52</sup>J. C. Newman, Jr., and I. S. Raju, "An Empirical Stress-Intensity Factor Equation for the Surface Crack," *Eng. Fract. Mech.*, **15**, 185-92 (1981).

<sup>53</sup>F. F. Lange, "Processing-Related Fracture Origins: I. Observations in Sintered and Isostatically Hot-Pressed  $\text{Al}_2\text{O}_3/\text{ZrO}_2$  Composites," *J. Am. Ceram. Soc.*, **66** [6] 396-98 (1983).

<sup>54</sup>F. F. Lange and M. Metcalf, "Processing-Related Fracture Origins: II. Agglomerate Motion and Cracklike Internal Surface Caused by Differential Sintering," *J. Am. Ceram. Soc.*, **66** [6] 398-406 (1983).

<sup>55</sup>F. F. Lange, B. I. Davies, and I. A. Aksay, "Processing-Related Fracture Origins: III. Differential Sintering of  $\text{ZrO}_2$  Agglomerates in  $\text{Al}_2\text{O}_3/\text{ZrO}_2$  Composite," *J. Am. Ceram. Soc.*, **66** [6] 407 (1983). □

## In Situ Measurements of Bridged Crack Interfaces in the Scanning Electron Microscope

Jürgen Rödel,\* James F. Kelly,\* and Brian R. Lawn\*

Ceramics Division, National Institute of Standards and Technology, Gaithersburg, Maryland 20899

A device for in situ SEM examination of crack propagation during loading of compact tension specimens is described, with a specific demonstration on an alumina ceramic. The device facilitates direct qualitative observations of the inception and subsequent frictional pullout of grain-localized bridges at the crack interface. Quantitative data on the bridging mechanism are obtained from measurements of the crack-opening displacements behind the crack tip. The crack profile is found to be closer to linear than parabolic at the bridged interface. Deconvolution of these crack-opening data allow for an evaluation of the closure tractions operative at the crack walls within the bridging zone, and thence the *R*-curve. [Key words: scanning electron microscopy, cracks, bridging, pullout, toughness.]

### I. Introduction

THE achievement of respectable fracture toughness in brittle ceramics necessitates the incorporation of crack-tip shielding agents like frontal-zone phase transformations<sup>1</sup> or microcracking,<sup>2</sup> crack-interface fiber pullout,<sup>3</sup> or interlocking grain sliding.<sup>4,5</sup> A proper understanding of the constitutive micromechanics of such processes can be gained only by direct observation of the crack shielding zone at the microstructural level during loading (and unloading, where applicable). In aluminas, for instance, in situ optical microscopy has been used to identify crack-interface grain bridging as the primary cause of *R*-curve toughening,<sup>4,6</sup> a mechanism that had passed unnoticed in previous, conventional post-mortem surface fractography. But while those studies have led to working microstructural constitutive relations for *R*-curve modeling of crack-interface bridging in simple monophase ceramics,<sup>5,7</sup> finer elements of the restraining mechanisms remain obscure. Optical microscopy is severely limited in its capacity to discern critical details of grain pullout and detachment. It is even more restrictive as a quantitative tool: in typical microstructures the crack-wall separations at the bridged interface are on the order of 1  $\mu\text{m}$  or less.

Accordingly, we have custom-designed a device for in situ crack observations in the scanning electron microscope (SEM). Previous SEM straining fixtures for tensile specimens or bend bars<sup>8-10</sup> have demonstrated the feasibility of the approach. Our device allows one to follow the progress of crack propagation at relatively high magnification in compact tension specimens with externally controlled loading, and thence to gain quantitative insight into the underlying *R*-curve processes.

R. F. Cook—contributing editor

Manuscript No. 197881. Received December 20, 1989; approved June 22, 1990.

Presented at the 92nd Annual Meeting of the American Ceramic Society, Dallas, TX, April 25, 1990 (Basic Science and Engineering Ceramics Divisions, Paper No. 2-JXX-90).

Supported by the U.S. Air Force Office of Scientific Research.

\*Member, American Ceramic Society.

\*On leave from the Department of Materials Science and Engineering, Lehigh University, Bethlehem, PA.

In this paper we briefly describe the fixture and illustrate its potential by tests on a polycrystalline alumina with demonstrated *R*-curve characteristics. Micrographs depicting the evolution of interlocking grain sites are presented as illustrations of the capacity to resolve essential microstructural detail at the bridged crack interface. Crack-opening displacement (COD) measurements are made along the bridging zone during the crack evolution. Corresponding bridging stresses in the crack wake are deconvoluted from these measurements, as functions of both COD and crack-plane coordinate. From these functions, we determine the *R*-curve characteristics for our particular material/geometry system.

### II. SEM Crack Propagation Studies

#### (1) SEM Device

Essential details of the SEM crack propagation device are shown in the schematic of Fig. 1. The device allows remote electronic application and monitoring of the applied load. Extension of a piezoelectric translator T delivers an opening force to the specimen S via pivot arms P and loading arms L. The P arms are connected to the L arms by ball-bearing joints and to the base of the device by pin joints for maximum flexibility. A load cell C mounted in one of the L arms measures the transmitted force. The piezoelectric translator is activated by a high-voltage amplifier which, in conjunction with a function generator, allows application of any prescribed load-time function (including, potentially, cyclic). The device operates effectively as a "soft" machine: that is, crack extension occurs under nearly constant load.

The entire fixture is housed within the chamber of an SEM.<sup>†</sup> Crack-interface events during externally controlled loading

<sup>†</sup>Amray 1830, Amray, Inc., Bedford, MA.

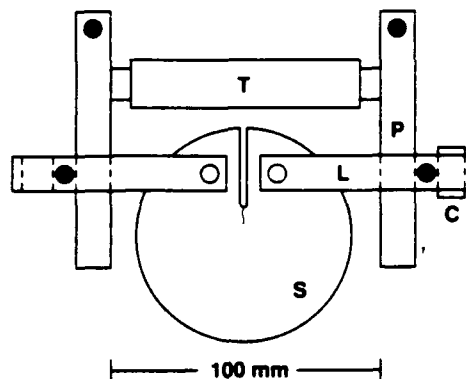


Fig. 1. Schematic of device for in situ SEM observations of fracture specimen under load: (T) piezoelectric translator, (C) load cell, (P) pivot arms, (L) loading arms, (S) specimen. Solid circles indicate joints between pivot arms and loading arms and between pivot arms and base.

can be viewed in real time and are routinely taped on a video recording unit for closer study.

A more detailed description of the unit will be given elsewhere.<sup>11</sup>

## (2) Crack Propagation Specimens

Alumina disks 4 mm thick and 100 mm in diameter were prepared by hot-pressing fine powder (nominal particle size 0.5  $\mu\text{m}$ ),<sup>2</sup> without additives, at 1650°C for 3 h at 35 MPa under vacuum. The pressed material was nonporous (>99.9% density), and the microstructure was equiaxed with a grain size of 11  $\mu\text{m}$ . The disks were ground to 1-mm thickness and the prospective viewing surface polished with diamond paste to 1- $\mu\text{m}$  finish.

Notches were sawed and loading holes drilled in the disks to form compact-tension specimens. The distance from the load points to the crack plane was 7 mm and from the line of the loading arms to the initial notch tip 15 mm. The notch root radius was 150  $\mu\text{m}$ . To enhance stability in the initial crack extension the notch was cut at an angle 28° to the surface in quasi-chevron geometry, i.e., so that the tip extended some 2 mm farther on the unpolished side. A Vickers indentation starter crack of diameter  $\approx 240$   $\mu\text{m}$  (load 50 N) was then placed in the polished surface with its center 200  $\mu\text{m}$  in front of the notch, in alignment with the notch plane. This starter crack was made to pop in some 300  $\mu\text{m}$  beyond the indentation center in a preliminary load cycle. The notch was then resawed through the indentation, leaving a precrack  $\approx 100$   $\mu\text{m}$  long. After the first crack propagation run through  $\approx 2$  mm (i.e., through to the end of the chevron) the specimen was removed and resawed, for second and third runs.

Some soda-lime glass specimens were also prepared to similar dimensions, as non-R-curve controls. After the notch was sawed, these specimens were annealed for 1 h at 550°C to remove residual stresses.

Specimens were gold coated before testing in the SEM. The evolution of bridging grains at selected sites in the crack wake was followed as the crack tip advanced. Video recordings were made along the interfaces at each of the fully propagated cracks for profile measurements. The COD measurements themselves were made only in well-behaved regions, e.g., at grain facets oriented normal to the load axis and located away from any secondary cracking around bridging sites. The cracks were rendered highly visible in the secondary electron mode by edge charging. This charging limited the absolute resolution of surface-surface separations to about 70 nm, although relative measurements could be made to better than 30 nm.

## III. Results

### (1) Qualitative Observations of Bridging Sites

General observations in our alumina confirm the basic conclusions from earlier studies with optical microscopy.<sup>4,6</sup> Crack extension occurred in a discontinuous fashion, at load increments from 5 to 15 N, but remained essentially stable during the entire loading, to a maximum level of  $\approx 300$  N. The fracture mode was predominantly intergranular. Active grain bridges were observed along the entire crack trace and over the entire propagation distance. No indication of a microcrack-cloud zone was observed, even though secondary cracking of grain facet dimensions adjoining the primary crack interface was readily discernible (see below).

Specific examples of SEM observations in the alumina are shown in Figs. 2 and 3. Figure 2 shows a bridging site in the crack wake some 1300  $\mu\text{m}$  behind the tip. That associated wake closure forces must be operative is immediately appar-



Fig. 2. SEM micrograph showing grain-bridging element at crack interface 1260  $\mu\text{m}$  behind the crack tip. Note resolution of crack-opening displacement.

ent from the severe disruption of individual grains at and around the bridge sites. The capacity to resolve and measure CODs is also clear from this micrograph.

Figure 3 depicts successive views of a second region, at two stages in the applied loading. The distances of this region behind the crack tip at these two stages are 660  $\mu\text{m}$  in Fig. 3(a)



Fig. 3. SEM micrographs showing another grain-bridging element at crack interface at two stages in the loading, (a) 660 and (b) 1190  $\mu\text{m}$  behind the crack tip. P and S denote frictional contact points.

<sup>2</sup>Sumitomo AKP-HP grade (99.995% pure, 0.5  $\mu\text{m}$  crystallites), Sumitomo Chemical America, New York, N.Y.

and 1190  $\mu\text{m}$  in Fig. 3(b). Two persistent contact points, at P and S, are indicated. At some load between (a) and (b) frictional tractions at P have opened up a network of secondary microfractures adjoining both sides of the primary crack interface. At S a single secondary microfracture has developed in the large grain at right prior to (a). Note that this latter microfracture has closed significantly between (a) and (b), indicating a falloff of the frictional tractions. The grain at S may conveniently be viewed as a fixed-end cantilever beam whose deflection reflects the magnitude of the internally applied friction force.

By contrast, the cracks in the soda-lime glass propagated relatively smoothly, but at a steady rate (typically,  $\approx 1 \mu\text{m} \cdot \text{s}^{-1}$ ) at fixed load, indicating the presence of slow crack growth even under vacuum.<sup>12</sup> Reducing the applied load on the specimen by about 5% was sufficient to bring the crack system to equilibrium.

## (2) Quantitative Measurements of Crack-Opening Displacements

CODs,  $2u(x)$ , were measured for our specimens, with  $x$  the distance behind the crack tip as indicated in the schematic of Fig. 4. Figures 5 and 6 show results from repeated crack propagation runs on the glass controls and the alumina, respectively.

The near-tip profiles for stress-free crack surfaces are usually represented by the Irwin  $K$ -field plane-strain displacement relation<sup>13</sup>

$$u(x) = (8x/\pi)^{1/2} K_A / E' \quad (1)$$

where  $E' = E/(1 - \nu^2)$  in plane strain,  $E$  is Young's modulus (400 GPa for alumina and 70 GPa for glass),  $\nu$  is Poisson's ratio (taken as 0.25 for both materials), and  $K_A$  is the applied stress-intensity factor. Equation (1) may be expected to remain a reasonable approximation for nonbridged cracks extending from sufficiently long notches ( $\Delta c \ll c_0$ , Fig. 4). A parabolic data fit may therefore be used to determine  $K_A$ .<sup>14</sup> For the glass in Fig. 5 a profile corresponding to  $K_A = 0.56 \text{ MPa} \cdot \text{m}^{1/2}$  (i.e., a little below the reported value  $0.7 \text{ MPa} \cdot \text{m}^{1/2}$  for crack propagation at velocity  $1 \mu\text{m} \cdot \text{s}^{-1}$  under vacuum<sup>12</sup>) passes through the data.

For alumina in Fig. 6, on the other hand, no such fit is possible with a single value of  $K_A$ . Bridging tractions in this material appear to have a strong modifying influence on the crack profile. The solid curve through the data is a theoretical fit allowing for this influence, to be described in Section III(3). We see that the profile in this material is closer to linear than parabolic. Included as the dashed curves in

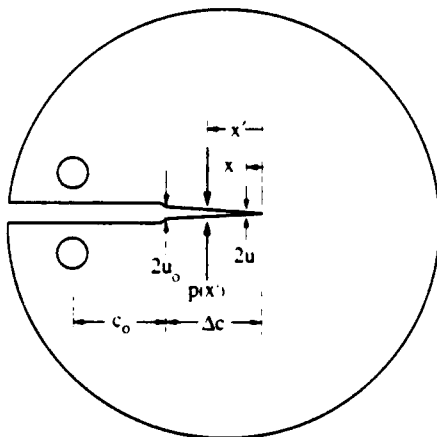


Fig. 4. Schematic of compact-tension specimen. Notch length  $c_0$ , crack extension  $\Delta c$ . Crack profile measured by COD  $2u$  at distance  $x$  behind crack tip,  $2u_0$  at crack mouth. Bridging tractions  $p(x')$  act to restrain crack.

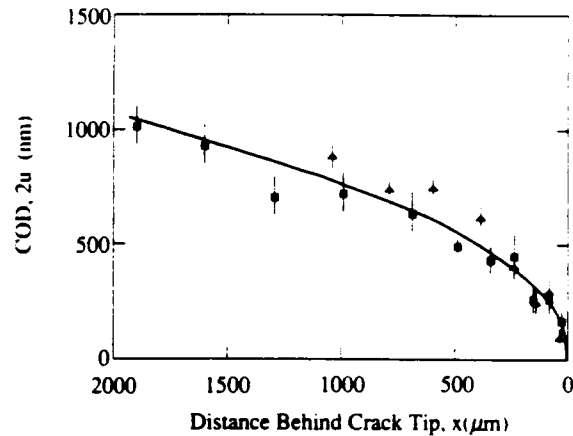


Fig. 5. Measured COD at crack interface in soda-lime glass, for compact-tension specimen ( $\Delta c = 1.9 \text{ mm}$ ). Different symbols designate separate crack runs. Error bars represent systematic uncertainty in COD measurement. Curve is Irwin parabola from Eq. (1) at  $K_A = 0.56 \text{ MPa} \cdot \text{m}^{1/2}$ .

Fig. 6 are asymptotic parabolas according to Eq. (1) with  $K_A = 4.6 \text{ MPa} \cdot \text{m}^{1/2}$  at the crack mouth (notch tip) (evaluated from the externally measured load using a stress-intensity factor solution for compact tension specimens at  $\Delta c = 1.0 \text{ mm}$ ) and  $2.0 \text{ MPa} \cdot \text{m}^{1/2}$  at the crack tip (corresponding to the grain-boundary toughness,  $T_0$  for alumina<sup>5</sup>).

We reiterate that the COD data in Figs. 5 and 6 correspond to measurements along the crack plane at stationary crack length ( $\Delta c = 1.9 \text{ mm}$ ). Alternatively, one may monitor the COD at the stationary notch tip as a function of variable crack extension  $\Delta c$ . Results of such measurements for the alumina are presented in Fig. 7.

## (3) Numerical Calculation of Closure Stresses in the Crack Wake

We indicated above that the crack profile in alumina deviates from the standard parabolic profile because of bridging tractions effective at the crack walls. The profile may thereby be used to compute the magnitude of these bridging tractions via an integral equation for continuum slit cracks.<sup>17,18</sup> In the limit of small bridging zones ( $\Delta c = 1.9 \text{ mm} \ll c = 22 \text{ mm}$ )

<sup>14</sup>Using the formula for standard circular specimens,<sup>15</sup> but with a correction factor allowing for nonstandard load-point positions from a general solution for rectangular specimens.<sup>16</sup>

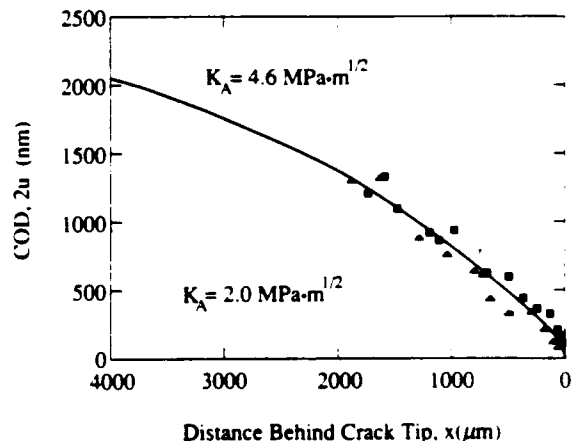


Fig. 6. Measured COD at crack interface in alumina, compact-tension specimen ( $\Delta c = 1.9 \text{ mm}$ ). Fitted profile (solid curve) from Eq. (2), Irwin parabolas for  $K_A = 4.6 \text{ MPa} \cdot \text{m}^{1/2}$  and  $T_0 = 2 \text{ MPa} \cdot \text{m}^{1/2}$  (dashed curves) from Eq. (1).

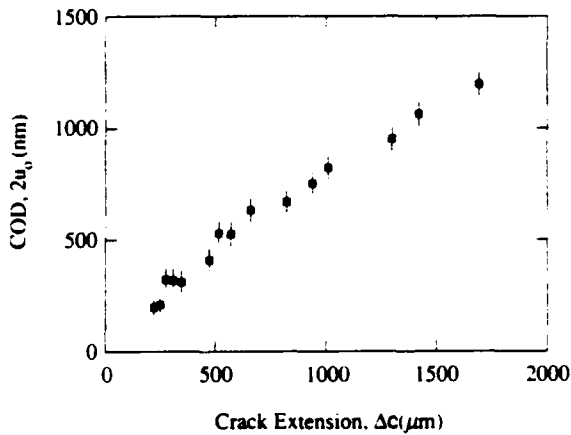


Fig. 7. COD at crack mouth as a function of crack extension for alumina compact-tension specimen.

the profile may be approximated by the Barenblatt relation<sup>17</sup> for cracks under applied stress

$$u(x) = (8x/\pi)^{1/2} K_A/E' - (2/\pi E') \times \int_0^{\Delta c} p(x') \ln [(x'^{1/2} + x^{1/2})/(x'^{1/2} - x^{1/2})] dx' \quad (2)$$

with  $x$  a field point at which the displacement is to be evaluated and  $x'$  a source point for the stresses  $p(x')$ .

The problem now consists of finding a solution for a stress function  $p(x')$  consistent with the measured profile in Fig. 6. Generally, Eq. (2) is analytically untractable, so numerical analysis is required. To facilitate such an analysis, the stress function was taken to have the empirical "tail-like" form<sup>5,7</sup>

$$p(x') = p_M(1 - x'/\Delta c_n)^n \quad (3)$$

with  $p_M$  the peak stress,  $\Delta c_n$  the bridging zone size at steady rate, and  $n$  an exponent. Note that this function has limiting values  $p = p_M$  at  $x' = 0$  ( $u = 0$ ) and  $p = 0$  at  $x' = \Delta c_n$  ( $u = u_0$ ), and that  $n$  will generally be expected to vary with  $\Delta c$ . Starting with initial estimates from Ref. 7 for  $p_M$  and  $\Delta c_n$  at  $n = 1$  for an alumina with our grain size, iterative parametric adjustments were made to the stress function in Eq. (3) until the calculated crack profile  $u(x)$  in Eq. (2) deviated from the (smoothed-out) data set in Fig. 6 by less than a prescribed amount (30 nm) at any position  $x$ . This procedure yielded final values  $p_M = 70$  MPa,  $\Delta c_n = 2.5$  mm, and  $n = 2.5$  for the half-chevron crack at  $\Delta c = 1.9$  mm. The ensuing  $u(x)$  function is represented as the smooth curve in Fig. 6.

Figure 8(a) plots the appropriately calibrated stress function  $p(x')$  in Eq. (3). The closure stresses decay from  $\approx 70$  MPa at the crack tip to  $\approx 2$  MPa at the crack mouth (notch tip). The corresponding stress-separation function  $p(u)$  in Fig. 8(b) is obtained in conjunction with Eq. (2). The crack-opening displacement at the notch tip corresponding to  $\Delta c = 1.9$  mm is  $2u_0 = 1300$  nm.

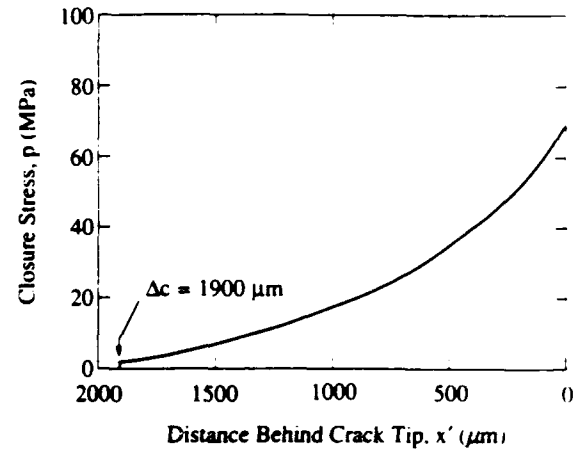
#### (4) Calculations of the Crack-Tip Shielding Toughness and the R-Curve

Given the calibrated stress functions  $p(x')$  and  $p(u)$ , we may calculate the shielding contribution to the toughness.

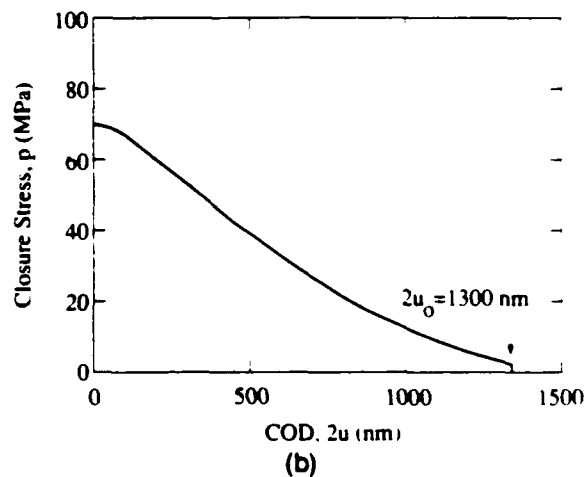
Let us do this first for the crack of fixed size  $\Delta c = 1.9$  mm ( $2u_0 = 1300$  nm) in Fig. 6. We may do this in two ways:

(A) *Stress-Intensity Factor*: The material toughness consists of superposable contributions from the intrinsic (grain boundary) cohesive forces,  $T_0$ , and the extrinsic microstructural shielding,  $T_\mu$ . At equilibrium, the net toughness balances the applied  $K$ -field:<sup>19</sup>

$$K_A = T = T_0 + T_\mu \quad (4)$$



(a)



(b)

Fig. 8. Bridging stress functions: (a)  $p(x')$  for compact-tension crack and (b) corresponding  $p(u)$ , for alumina. Note cutoff in plots at  $\Delta c = 1.9$  mm,  $2u_0 = 1.3$   $\mu$ m, indicating limits of crack size over which COD data were obtained in our experiments. Dashed line in (b) is evaluation from indentation-strength data on other aluminas.<sup>25</sup>

The shielding term may be determined from the Green's function relation<sup>13</sup>

$$T_\mu = (2/\pi)^{1/2} \int_0^{\Delta c} p(x') dx'/x'^{1/2} \quad (5)$$

Numerical integration gives  $T_\mu = 2.6$  MPa  $\cdot$  m<sup>1/2</sup> for  $\Delta c = 1.9$  mm. This result compares with the value  $T_\mu = K_A - T_0 = 4.6 - 2.0 = 2.6$  MPa  $\cdot$  m<sup>1/2</sup> from the asymptotic curves in Fig. 6.<sup>9</sup>

(B) *Mechanical-Energy Release Rate*: The equilibrium relation Eq. (4) may be alternatively expressed as a balance between the applied mechanical-energy-release rate,  $G_A$ , and the net crack-resistance energy,  $R$ :

$$G_A = R = R_0 + R_\mu \quad (6)$$

The shielding term is readily found from<sup>19,20</sup>

$$R_\mu = 2 \int_0^{u_0} p(u) du \quad (7)$$

Numerical integration gives  $R_\mu = 41.8$  J  $\cdot$  m<sup>-2</sup>. The values

<sup>25</sup>Note that application of Eq. (5) to compute  $T_\mu$  at any other  $\Delta c$  would strictly require reevaluation of Eq. (3), specifically  $n$ , at that specific  $\Delta c$ .



thus obtained can be checked for self-consistency through the equivalence relations<sup>21</sup>

$$G_A = K_A^2/E' \quad (8a)$$

$$R_0 = T_0^2/E' \quad (8b)$$

Eliminating  $G_A$  and  $K_A$  using Eqs. (4) and (6), and inserting the above value of  $R_u$  obtained from Eq. (7) along with the previously cited  $E'$  and  $T_0$  for our alumina, we obtain  $T_u = (T_0^2 + E' R_u)^{1/2} = T_0 = 2.7 \text{ MPa} \cdot \text{m}^{1/2}$ , which compares with the value 2.6 from Eq. (4).

Now let us consider how we may determine the  $R$ -curve from the above analysis. From Eq. (7),  $R_u$ , hence  $R$ , may be evaluated directly as the area under the  $p(u)$  curve in Fig. 8(b). Numerical integration yields the function  $R(u)$  in Fig. 9(a). This result may be converted to the more familiar  $R$ -curve function  $R(\Delta c)$  using the data points from Fig. 7. That function is plotted in Fig. 9(b). Note that since  $p(u)$  is an intrinsic material function,  $R(u)$  is a unique quantity for our alumina; but  $R(\Delta c)$ , insofar as it may be dependent on the crack-profile relation  $u(\Delta c)$ , is specific to our crack geometry.

#### IV. Discussion

We have sought to demonstrate that useful qualitative and quantitative information concerning the micromechanics of crack-tip shielding by grain bridging in monophase ceramics can be gained from in situ observations in the SEM. The most immediate outcome from our crack-interface observations on alumina is the confirmed existence of such bridging, shown pictorially in Figs. 2 and 3 and graphically in Fig. 9. Such

observations usefully reinforce earlier inferences as to the efficacy of bridging as a toughening mechanism from the classic wake sawcut experiments of Knehan and Steinbrech.<sup>22</sup> They also allow us to make useful inferences concerning the micromechanics of grain pullout: recall our description of secondary fractures (fortuitous "internal load cells") in Fig. 3, indicative of a falloff in frictional force with increasing crack-wall separation.

Our results in Fig. 6 also show that (within experimental scatter) the crack profile at the bridged interface is closer to linear than parabolic. This is in keeping with studies on bridged cracks in fiber-reinforced cementitious composites.<sup>23</sup> An empirical linear COD relation is therefore probably most appropriate for incorporation into fracture mechanics models of bridging zones for  $R$ -curve ( $T$ -curve) analysis.<sup>5,7,24</sup>

It will be noted that evaluation of the equilibrium crack profile in Eq. (2) requires specification of  $K_A$  for the half-chevron crack.  $K_A$  determines the scale of the shielding zone displacement field, thereby avoiding the necessity of making COD measurements in the notch region. Alternatively, one could eliminate  $K_A$  altogether from Eq. (2) by substitution of Eqs. (4) and (5):

$$u(x) = (8x/\pi)^{1/2} T_0/E' + (4/\pi E') \int_0^x p(x') \{(x/x')^{1/2} - \frac{1}{2} \ln [(x'^{-1/2} + x^{1/2})/(x'^{-1/2} - x^{1/2})]\} dx' \quad (9)$$

so that, given only the intrinsic toughness term  $T_0$ , one may compute the profile without having to evaluate the applied stress-intensity factor. This is a special advantage in those cases where the macroscopic crack geometry is ill-defined. It must be reiterated that the validity of Eq. (9) is contingent on satisfaction of the small-scale bridging zone approximation,  $\Delta c \ll c$ , and therefore contains no specific information on the profile in the far field.

These considerations open the way to evaluation of  $T_0$  from the COD data. In cases (like ours) where intergranular fracture dominates, this quantity relates to the basic surface and grain-boundary energies,  $\gamma_s$  and  $\gamma_{GB}$ , via  $T_0 = [(2\gamma_s + \gamma_{GB}) E']^{1/2}$ ; the relative values of  $\gamma_{GB}$  and  $\gamma_s$  (among other things) determine whether a crack will or will not remain along an intergranular path (and hence preserve the most favorable conditions for bridge formation). Access to  $T_0$  is restricted in conventional precrack test procedures because pop-in generally starts the system well up the  $R$ -curve. In principle,  $T_0$  should be determinable from the lower bound of the data in Fig. 6, which reflects COD measurements taken within two or three grains behind the crack tip (i.e., within a typical bridge spacing). Thus in Fig. 6 we are able to estimate  $T_0 = 2.0 \text{ MPa} \cdot \text{m}^{1/2}$  for our alumina. In our case experimental scatter limits the accuracy of this approach, but optimization of the SEM resolution may provide useful estimates in materials with stronger  $R$ -curves.

Perhaps the most consequential result from the COD data in Figs. 6 and 7 is the evaluation of the bridging stress functions  $p(u)$  and  $p(x')$ . Notwithstanding the fact that our parametric fitting procedure is constrained by the empirical relation in Eq. (3), the data confirm the existence of a "tail-dominated" constitutive relation, Fig. 8; i.e., maximum restraint at the crack tip, with near-linear falloff along the crack-wake interface. Our  $p(u)$  function may be compared with an independent, indirect determination from indentation-strength data on other aluminas, shown as the dashed line in Fig. 8.<sup>25</sup> The present evaluation indicates a substantially greater toughening due to bridging; the discrepancy may reflect material-to-material variations and/or uncertainties in deconvoluting the indentation data.<sup>25</sup> Once  $p(u)$  is established, the  $R$ -curve can be determined from Eqs. (6) and (7). The ensuing  $R(u)$  and  $R(\Delta c)$  functions in Figs. 9(a) and (b) show an initial sharp rise from  $\approx 10 \text{ J} \cdot \text{m}^{-2}$  at small crack

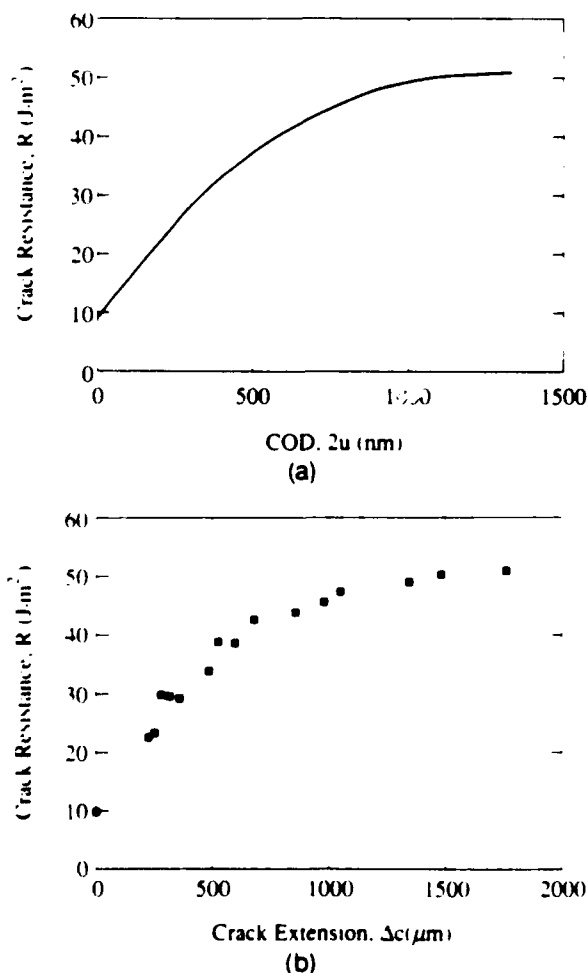


Fig. 9. Crack-resistance curves: (a)  $R(u)$  and (b)  $R(\Delta c)$  for compact-tension crack ( $\Delta c = 1.9 \text{ mm}$ ) for alumina.

openings (or extensions), to an asymptotic plateau  $\approx 50 \text{ J} \cdot \text{m}^{-2}$  at large openings (extensions). (The true plateau value could not be obtained in this study, because the crack size range covered in Figs. 6 and 7 did not extend beyond the range of the bridging zone.)

It is important to acknowledge possible sources of systematic error in the stress-function and  $R$ -curve evaluations in Figs. 8 and 9. In using Eq. (2) we have ignored the influence of finite notch length and outer specimen dimensions in our quasi-chevron configuration. Detailed analyses show that boundary effects can be significant in determining displacement profiles in the compact-tension geometry, especially with short notches.<sup>26</sup> Also, we have not addressed the possible influence of path deflections (with their connotation of shear modes) on the normal crack displacements.

The present study has focused on a monophase ceramic with moderate grain size. Our device would appear to be potentially even more useful for ceramics with coarser microstructures and multiphase composites, where the toughening events are more dramatic and the  $R$ -curves more pronounced. Also, attention has been given only to monotonic loading. Observations in cyclic loading could provide useful clues as to fatigue mechanisms, which remain obscure in ceramic materials. Fatigue might be especially important in materials with strong  $R$ -curve behavior, due to cumulative damage to bridges on repeated unloading. COD measurements at the crack mouth (or some other stationary point of interest at the crack interface) could provide a quantitative measure of any such degradation with number of cycles.

## V. Conclusions

(i) A device for in situ investigation of crack interfaces in the SEM has been described.

(ii) Micrographic evidence for evolution of bridging grains in alumina has been presented.

(iii) COD measurements as a function of both the distance from the crack tip and crack extension have been analyzed for alumina. The data provide a measure of the crack-tip shielding from bridging.

(iv) The bridging stress functions  $p(u)$  and  $p(x')$  have been computed self-consistently from the crack profile measurements.

(v) Crack-resistance functions  $R(u)$  and  $R(\Delta c)$  have been evaluated from the stress functions.

**Acknowledgments:** We are indebted to S. J. Bennison and M. R. Stoudt for help in the design of the fracture device, to B. N. Cox for discussions on the bridged-crack profile, and to E. R. Fuller for assistance with the numerical calculation.

## References

<sup>1</sup>R. M. McMeeking and A. G. Evans, "Mechanics of Transformation Toughening in Brittle Materials," *J. Am. Ceram. Soc.*, **65** [5] 242–46 (1982).

<sup>2</sup>M. Rühle, A. G. Evans, R. M. McMeeking, P. G. Charalambides, and J. W. Hutchinson, "Microcrack Toughening in Alumina/Zirconia," *Acta Metall.*, **35** [11] 2701–10 (1987).

<sup>3</sup>D. B. Marshall and A. G. Evans, "Failure Mechanisms in Ceramic-Fiber/Ceramic-Matrix Composites," *J. Am. Ceram. Soc.*, **68** [5] 225–31 (1985).

<sup>4</sup>P. L. Swanson, C. J. Fairbanks, B. R. Lawn, Y.-W. Mai, and B. J. Hockey, "Crack-Interface Grain Bridging as a Fracture Resistance Mechanism in Ceramics: I. Experimental Study on Alumina," *J. Am. Ceram. Soc.*, **70** [4] 279–89 (1987).

<sup>5</sup>Y.-W. Mai and B. R. Lawn, "Crack-Interface Grain Bridging as a Fracture Resistance Mechanism in Ceramics: II. Theoretical Fracture Mechanics Model," *J. Am. Ceram. Soc.*, **70** [4] 289–94 (1987).

<sup>6</sup>P. L. Swanson, "Crack-Interface Traction: A Fracture-Resistance Mechanism in Brittle Polycrystals," pp. 135–55 in *Advances in Ceramics*, Vol. 22, Fractography of Glasses and Ceramics, American Ceramic Society, Westerville, OH, 1988.

<sup>7</sup>S. J. Bennison and B. R. Lawn, "Role of Interfacial Grain-bridging Sliding Friction in the Crack-Resistance and Strength Properties of Nontransforming Ceramics," *Acta Metall.*, **37** [10] 2659–71 (1989).

<sup>8</sup>A. Nagy, J. B. Campbell, and D. L. Davidson, "High-Temperature, Cyclic Loading Stage for the Scanning Electron Microscope," *Rev. Sci. Instrum.*, **55** [5] 776–82 (1984).

<sup>9</sup>H. Frei and G. Grathwohl, "Development of a Piezotranslator-based Bending Device for In Situ SEM Investigations of High-Performance Ceramics," *J. Phys. E*, **22** [8] 589–93 (1989).

<sup>10</sup>H. Kodama, H. Sakamoto, and T. Miyoshi, "Silicon Carbide Monofilament Reinforced Silicon Nitride or Silicon Carbon Matrix Composites," *J. Am. Ceram. Soc.*, **72** [4] 551–58 (1989).

<sup>11</sup>J. Rödel, J. F. Kelly, M. R. Stoudt, and S. J. Bennison, "A Loading Device for Fracture Testing of Compact Tension Specimen in the SEM," to be published in *Scanning Electron Microsc.*

<sup>12</sup>S. M. Wiederhorn, H. Johnson, A. M. Diness, and A. H. Heuer, "Fracture of Glass in Vacuum," *J. Am. Ceram. Soc.*, **57** [8] 336–41 (1974).

<sup>13</sup>G. R. Irwin, "Fracture," pp. 551–94 in *Handbuch der Physik*, Vol. 6, Springer-Verlag, Berlin, 1958.

<sup>14</sup>E. Sommer, "Experimental Determination of Stress Intensity Factor by COD Measurements," pp. 331–47 in *Mechanics of Fracture*, Vol. 7, Edited by G. C. Sih, Nijhoff Publishers, The Hague, Netherlands, 1981.

<sup>15</sup>Annual Book of ASTM Standards, Vol. 3.01, E-399-83; pp. 480–504 American Society for Testing and Materials, Philadelphia, PA, 1989.

<sup>16</sup>H. Tada, P. C. Paris, and G. R. Irwin, *The Stress Analysis Handbook*, Ch. 2, Paris Productions (and Del Research Corp.), St. Louis, MO, 1985.

<sup>17</sup>G. I. Barenblatt, "The Mathematical Theory of Equilibrium Cracks in Brittle Fracture," *Adv. Appl. Mech.*, **7**, 55–129 (1962).

<sup>18</sup>I. N. Sneddon and M. Lowengrub, *Crack Problems in the Classical Theory of Elasticity*, Wiley, New York, 1969.

<sup>19</sup>Y.-W. Mai and B. R. Lawn, "Crack Stability and Toughness Characteristics in Brittle Materials," *Annu. Rev. Mater. Sci.*, **16**, 415–39 (1986).

<sup>20</sup>J. R. Rice, "Mathematical Analysis in the Mechanics of Fracture," pp. 191–311 in *Fracture II*, Edited by H. Liebowitz, Academic Press, New York, 1968.

<sup>21</sup>B. R. Lawn and T. R. Wilshaw, *Fracture of Brittle Solids*, Ch. 6, Cambridge University Press, London, 1975.

<sup>22</sup>R. Knehan and R. W. Steinbrech, "Memory Effect of Crack Resistance during Slow Crack Growth in Notched  $\text{Al}_2\text{O}_3$  Bend Specimens," *J. Mater. Sci. Lett.*, **1** [8] 327–29 (1982).

<sup>23</sup>B. Cotterell and Y.-W. Mai, "Modelling Crack Growth in Fibre-Reinforced Cementitious Materials," *Mater. Forum*, **11**, 341–51 (1988).

<sup>24</sup>R. M. L. Foote, Y.-W. Mai, and B. Cotterell, "Crack Growth Resistance Curves in Strain-Softening Materials," *J. Mech. Phys. Solids*, **34** [6] 593 (1986).

<sup>25</sup>P. Chantikul, S. J. Bennison, and B. R. Lawn, "Role of Grain Size in the Strength and  $R$ -Curve Properties of Alumina," *J. Am. Ceram. Soc.*, **73** [8] 2419–27 (1990).

<sup>26</sup>B. N. Cox and D. B. Marshall, "Stable and Unstable Solutions for Bridged Cracks in Various Specimens: unpublished work." □

A LOADING DEVICE FOR FRACTURE TESTING OF COMPACT  
TENSION SPECIMENS IN THE SCANNING ELECTRON MICROSCOPE

Jürgen Rödel<sup>1</sup>, James F. Kelly\*, Mark R. Stoudt and Stephen J. Bennison<sup>1</sup>

Ceramics Division  
National Institute of Standards and Technology  
Gaithersburg, MD 20899

1. Guest Scientist on leave from the Department of Materials Science  
and Engineering, Lehigh University, Bethlehem, PA 18015.

(Received for publication May 26, 1990, and in revised form October 12, 1990)

Abstract

A loading device for performing fracture experiments on compact tension specimens in the SEM has been designed. Its key elements are a piezoelectric translator for applying controlled displacements to the loading points on the specimen and a load cell to measure applied loads. The effective transmission of displacement from the piezoelectric driver to the specimen was found to be the major mechanical design problem. The peripheral equipment includes a function generator and a high voltage amplifier that drives the piezoelectric translator as well as a video overlay and standard video equipment to record the image continuously during the course of the experiment. A case study on alumina describes qualitative observations on the toughening mechanism, crack-interface bridging, operating in this material. Quantitative information pertaining to the closure stresses associated with this toughening mode can be obtained by measuring the crack profile.

**KEY WORDS:** Scanning electron microscopy, cracks, crack profile, in-situ, fracture toughness, microstructure, alumina

\*Address for correspondence:  
James F. Kelly,  
National Institute of Standards and Technology  
Bldg. 223, Rm. A256  
Gaithersburg, MD 20899  
Phone No. (301) 975-5794

Introduction

The science of fractography, viz. the postmortem observation of features associated with fracture, is an important element of any investigation into mechanical behavior of materials [12]. Fractography embodies a variety of techniques which can provide invaluable insights into fracture modes, loading histories and the role of microstructure in failure for a range of different materials.

The postmortem nature of fractography, however, ultimately places a restriction on its utility. Events influencing fracture which leave no visible traces after specimen failure go undetected. A case in point is the phenomenon of crack-interface bridging which is responsible for rising crack resistance (R-curve) behavior in many monolithic ceramics such as aluminum oxide [9,11,15,16]. In this mechanism, intact grains well behind the primary crack tip bridge the crack walls, shield it from the applied stress intensity field ( $K_I$ ) and lead to increased crack resistance (toughness) with crack extension; after failure the bridges have been destroyed. Identification of grain bridging has only been attained through careful in situ studies of crack growth using optical microscopy [16]. Recognition that the toughness behavior of many ceramic systems may be determined by grain bridging and other wake-associated mechanisms [6] has highlighted the importance of in situ observations of fracture events.

The aim of the present work is to develop a fixture for in situ testing of materials in the scanning electron microscope (SEM). The superior resolution afforded by the SEM provides two significant advantages over existing optically based systems. First, greater detail of crack - microstructure interactions, such as grain bridging, can be obtained. Such information is critical to the development of models describing the toughening and R-curve properties of ceramics [4]. Second, quantitative information on the stress intensity fields (K-fields) can be gained from direct measurements of crack profiles. In the case of ceramics, crack opening displacements typically range from 0  $\mu\text{m}$  (at the crack tip) to 1-2  $\mu\text{m}$  (at the crack mouth) and, as such, cannot be readily

measured by optical techniques.

A number of SEM-based testing systems have been described before, designed for tensile loading of test bars [5], four-point bending [8], double torsion [17] and wedge-loaded DCB-type specimen [19]. Special requirements, in particular the ability to measure the propagation and the profile of long cracks, necessitated the development of a loading stage for compact tension specimens. Profile measurements of long cracks in particular, allow a calculation of the stress-separation function [14], which is the key material characteristic determining R-curve behavior [4].

In this paper a design for such an SEM-based testing system is presented. Mechanical, electrical and imaging requirements are described, and results from a case study of crack growth in aluminum oxide are detailed to demonstrate the capabilities of the loading stage.

#### Instrument Design

The fracture device was designed for use in an AMRAY<sup>1</sup> SEM<sup>2</sup>. This particular instrument offers the advantage of a large specimen chamber (more than 30 cm in each dimension) and allows easy access to the SEM stage which is connected to the door and therefore swings out when the chamber is opened.

For this case study tests were run at 20 kV accelerating voltage with the sample surface perpendicular to the beam.

#### Mechanical Considerations

The specimen geometry of choice is compact tension (round or rectangular) according to the ASTM E 399 specification [1]. This geometry was chosen for several reasons. First, the stress intensity solutions for the applied stress field ( $K_I$ ) are available. Second, for materials, like alumina, which experience closure forces due to crack-interface bridging in the crack wake [15,16], the additional requirement, that the crack be long compared to the bridging zone, can be satisfied with this geometry. Then  $K_I$  values can readily be calculated from measurements of the applied load and crack length. Third, the crack path is stable [2] (shows no deviation from a straight line). Fourth, disk-shaped specimens are readily prepared using conventional ceramics processing.

Figure 1 shows schematically the loading stage and Figure 2 is a photograph of the fixture. The heart of the device is a

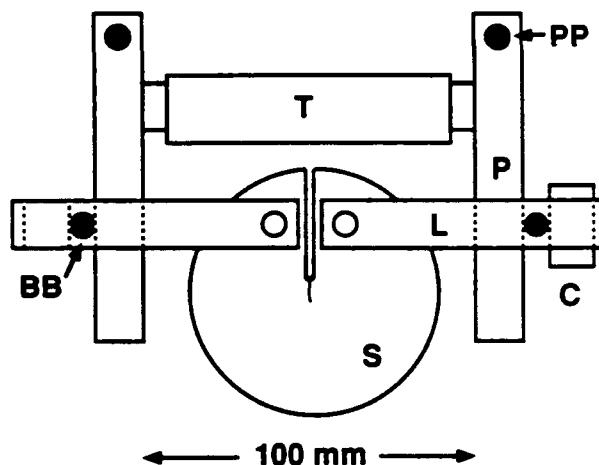


Figure 1. Schematic of device for in situ SEM observations of compact tension specimen. T = piezoelectric translator, C = load cell, P = pivot arms, L = loading arms, PP = pivot point, BB = ball bearing and S = specimen.

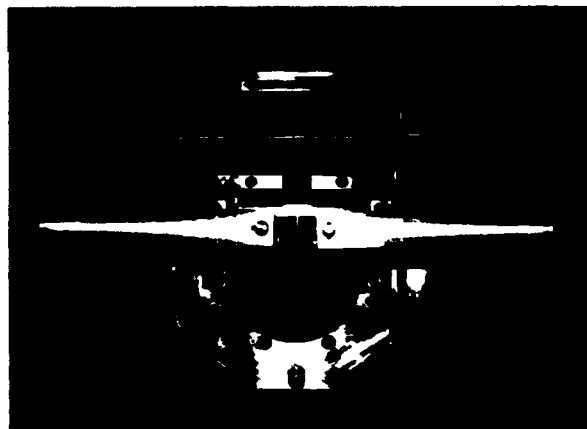


Figure 2. Photograph of the loading device containing disk compact tension specimen.

piezoelectric translator (T)<sup>3</sup> (see also [8]) capable of displacements up to 85  $\mu\text{m}$  and maximum force of 1,000 N when a voltage of 1 kV is applied. The force is transmitted to the specimen via a system of two pivot arms (P) and two loading arms (L). The pivot arms rotate on pivot points (PP) which are rigidly attached to a rectangular baseplate. The loading arms

<sup>1</sup> AMRAY 1830, Amray Inc., Bedford, MA.

<sup>2</sup> Certain commercial equipment are identified in this paper in order to adequately specify the experimental procedure. Such identification does not imply recommendation or endorsement by the NIST, nor does it imply that the equipment identified is necessarily the best available for the purpose.

<sup>3</sup> PI Model P-245.50, Physik Instrumente, D7571 Waldbronn, FRG.

connect to the pivot arms via two ball bearings (BB) which allow rotational alignment of the system and prevent the application of bending moments to the specimen. A strain gauge load cell<sup>4</sup> is placed in one loading arm and allows monitoring of the applied load between 0 and 2,300 N.

The primary mechanical design requirement is the efficient transmission of displacement from the piezoelectric translator to the specimen. Losses in displacement due to the compliance of the loading train are minimized by constructing the elements from (non-magnetic) stainless steel and fabricating the pivot points to tolerances of  $\sim 25 \mu\text{m}$ . Despite these precautions displacement losses were considerable in our early designs. The final arrangement, presented in Figure 1, places the piezoelectric translator between the pivot points (PP) and the load application points (BB) to the loading arm (L). At first glance this may appear to give a poor mechanical advantage, with the force applied through the piezoelectric translator being reduced to 40% at the loading arms. However, the design ensures that sufficient displacement is available at the crack mouth to drive cracks in ceramics of this specimen geometry. Specimens are also routinely prestressed with two screws, which link the piezoelectric translator to the pivot arms, before placing the loading device into the SEM chamber. The load transmission characteristics result in mechanical testing effectively in a constant load mode [2] due to the stored elastic energy in the loading train.

If the loading stage is used for cyclic loading applications, a slight specimen shift is noticeable. This displacement was less than  $6 \mu\text{m}$ .

#### Electrical Considerations

The supply voltage for the piezoelectric translator, and the supply and signal voltages for the load cell (5V power supply and standard voltmeter) are connected into the specimen chamber via three electrically isolated BNC type feedthroughs mounted on a side port of the SEM. The piezoelectric translator is driven by a high voltage amplifier<sup>5</sup> which, when fed with a function generator, affords application of controlled (e.g. cyclic) loading. The relatively large capacitance (113 nF) of the translator in combination with the low current output of the power supply (1.8 mA) places an upper bound on the range of available frequencies ( $\approx 2 \text{ Hz}$ ).

<sup>4</sup> Sensotech, LFH-71, Sensotech, Columbus, OH 43212.

<sup>5</sup> PI Model P-263, Physik Instrumente, D7517 Waldbronn, FRG.

<sup>6</sup> VT0232 Video Text Overlay, Linkam Scientific Instruments Ltd., Tadworth, UK.

#### Imaging requirements

The physical characteristics of the compact tension test fixture along with the requirement for real time imaging act to limit the image resolution in three ways: increased working distance, reduced vibrational stability, and higher specimen current. The piezoelectric driver and raised pivot rods require operating at a working distance of  $30 \text{ mm}$  to avoid contacting the secondary electron detector and the final lens. Since the best resolution obtained on this microscope is  $5 \text{ nm}$  at the minimum working distance of  $5 \text{ mm}$ , this increase in working distance alone decreases the secondary image resolution by a factor of about six. Additionally, the requisite stiffness for transmitting the load from the driver, through the loading and pivot arms, to the test specimen with minimal flexure of the arms, necessitates a large mass of nearly two kilograms which must be supported by the SEM stage. This increased load on the stage, together with the requirement that the test specimen be minimally constrained, significantly increases the vibrational sensitivity of the system. An improvement of the fixture support has been achieved by bolting the fixture to the SEM stage in addition to having the standard pin support. The third factor influencing the electron spot size is the beam current. A compromise between resolution and the ability to follow crack propagation in real time resulted in the use of a  $200 \mu\text{m}$  final aperture with the condenser lens adjusted to give a beam current of  $100 \text{ pA}$ . The combination of these operating conditions limits the resolution of the secondary image to approximately  $70 \text{ nm}$ .

Prior to full crack formation, highly polished, gold-coated specimen surfaces provide little contrast for secondary electron imaging. The charging of newly exposed non-coated material subsequent to crack extension, however, provides a readily detectable secondary electron signal. For more complex microstructures, backscattered electron imaging has proven useful in identifying the crack path relative to specific microstructural phases or grain boundaries. However, the relatively slow response time of the solid state backscatter electron detector, requiring scan times of at least  $30 \text{ s/frame}$  make this mode impractical for live time monitoring of crack propagation.

The rapid scan mode of the AMRAY Model 1830 SEM operates at a scan rate of  $5 \text{ frames/s}$ . The selected signal is processed through an integral  $512$  by  $512$  pixel frame buffer which displays the image at a standard TV rate of  $30 \text{ frames/s}$ . This capability for continuous display at TV rate enables the direct recording of the secondary image using a video cassette recorder (VCR). The SEM image is superimposed with the load cell output voltage using a video text overlay<sup>6</sup>. Photographic recording via instant film can also be done, either directly from the frame buffer, or by bypassing the buffer to obtain an increased line density in the recorded image.

### Case Study

We proceed to illustrate the capabilities of the fracture device by discussing some results from a case study on crack propagation in alumina.

An alumina disk, 4 mm thick and with a diameter of 100 mm, was prepared by hot pressing alumina powder<sup>7</sup> for 3 hours at 1650°C under a uniaxial pressure of 35 MPa. The pressed slab was found to be pore-free with an average grain size of 11  $\mu\text{m}$ . It was then ground to 1 mm thickness and polished with diamond pastes of grade 15  $\mu\text{m}$  down to 1  $\mu\text{m}$ . A compact tension specimen was machined by drilling holes for the loading arms and cutting a notch. The stability of the sample with respect to crack propagation was enhanced by extending the notch at an angle of 28° to the specimen surface, which gave the geometry of a quasi-chevron notch, with the notch being extended about 2 mm on the unpolished (lower) surface. A Vickers hardness indentation ( $P = 50 \text{ N}$ ) was placed about 200  $\mu\text{m}$  in front of the notch on the polished surface. The radial cracks emanating from the elastic-plastic zone in the direction of the notch were then extended under tension with the loading device placed on an optical microscope. Subsequently, the indented region was cut out to leave a precrack of about 100  $\mu\text{m}$  length. After the first crack propagation run (for  $\approx 2 \text{ mm}$ ) the specimen was removed and resawn again, for second and third runs. Etching to reveal the microstructure of the specimen was purposely avoided, since cracks following a grain boundary groove are difficult to detect in the crack tip region.

Crack propagation under applied tensile loading in the SEM was found to be stable in the quasi-chevron region. The load was increased until crack extension occurred (typically for 10 - 50  $\mu\text{m}$ ) and the crack arrested again. The required loading increments for crack instability to occur were found to be between 5 and 15 N with the total applied loading in the range between 200 and 300 N.

Microscopical observations during crack extension are classified here into two categories: events at the crack tip and events in the crack wake. In the first category, the mode of crack propagation, discontinuous in nature, in contrast to slow crack growth in glass in high vacuum [18], can be monitored. The occurrence of subsidiary cracking - either secondary cracking or microcracking in a zone [7] - can also be followed while the crack passes through a given region in the material. Microcracking in particular has been a focal point of recent considerations and has been invoked as one of the possible toughening mechanisms in ceramics [6]. The R-curve in alumina, in particular, was originally

attributed to this mechanism [13]. With the resolution now available using the loading device in the SEM, the creation of microcracks (of lengths down to at least one grain facet and openings down to about 50 nm) can be detected. No such microcracking was observed in the particular alumina studied in this case.

Observations of the crack wake focus on bridge evolution [14]. A bridge is here defined as any microstructural element connecting the crack faces which gives rise to a closure force. An example is given in Fig. 3 a,b with a closure force across the crack surfaces being applied at A. This force causes the secondary crack at location B to open. With further crack propagation the opening of the primary crack increases, the closure force diminishes and the secondary crack at B closes (Fig. 3b). Note also the creation of a new secondary crack at position C in Fig. 3b. Observations such as the one described help understand the origin of closure forces in the crack wake. The crack opening displacement of secondary cracks as a function of the opening of the primary crack can be utilized to measure the relative closure stress at given regions while the crack propagates through the material [14].

The existence of closure forces in the crack wake can further be demonstrated and, in fact, numerically evaluated by measuring the crack opening (COD) as a function of distance from the crack tip [3].

Crack opening displacements are measured by imaging cracks at a magnification of 30,000, taping the image and, after the experiment, measuring the opening from the video monitor. In ceramics we are typically concerned with crack opening displacements in the range of 50 to 2000 nm. Since standard optical techniques are not able to provide this type of resolution, SEM techniques are required. An accuracy of about 70 nm is currently obtained, although relative measurements can be made to 30 nm precision.

An example of three such measurements is given in Fig. 4 for the alumina studied. The profile is found to be linear in first approximation, which is in contrast to the parabolic profile of cracks with stress-free surfaces [10]. Closure forces arising from discrete bridges are commonly combined in a continuum description to give a continuous closure stress acting on the crack faces. This closure stress can be given as a function of distance from the crack tip [3], and, more fundamentally, as a function of the local crack opening displacement. If this description is used, the experimentally obtained profile can be related through an integral equation [14] to the closure force as a function of distance from the crack tip.

An additional route to obtaining quantitative information on the micromechanics of microstructural elements in the crack wake is given by recording crack opening displacements during loading/unloading. These measurements give further insight about the nature of the closure forces (frictional, elastic). In the

<sup>7</sup> Sumitomo AKP-HP grade (99.99% pure, 0.5  $\mu\text{m}$  crystallites), Sumitomo Chemical America, New York, NY.

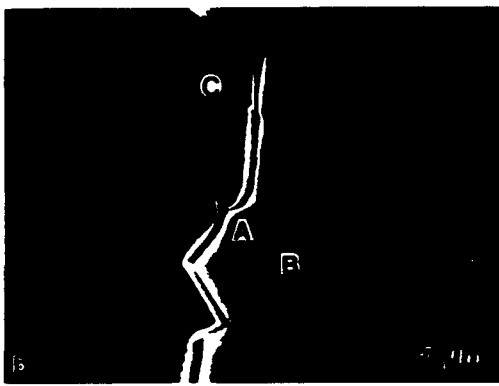
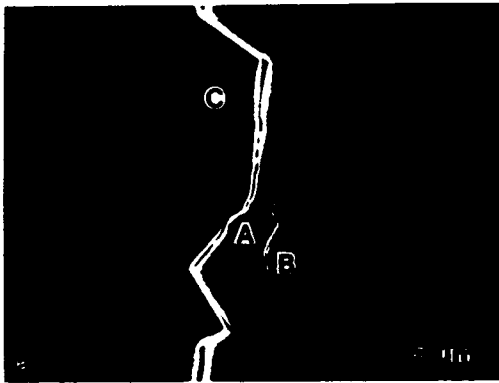


Figure 3. SEM micrographs of region showing closure force at A and secondary cracks at B and C; a) 330 μm behind the crack tip and b) after further loading the crack grows and the region is now 660 μm behind the crack tip.

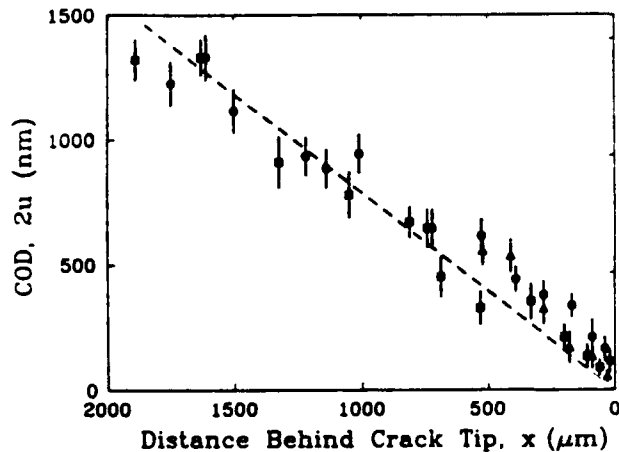


Figure 4. Examples of measured crack opening displacements as function of distance from the crack tip. Different symbols designate different runs; dashed line gives empirical linear fit.

case of the alumina studied, complete closure at a residual applied force was found. An example of a microstructural element bridging the crack faces of an equilibrated crack and a closed crack (in this case, no applied loading) is given in Fig. 5 a,b. The crack in Fig. 5b is virtually invisible and can only be visualized by following the trace of grains released from their original positions.

The case study on alumina thus demonstrates the use of the loading stage and the ability to gain valuable qualitative and quantitative information on the micromechanics operative in the crack wake and, possibly, at the crack tip. The experimental observations focus on the occurrence of microcracks or grain bridging (in other cases this might be fiber, whisker or ductile ligament bridging). Quantitative measurements focus on the crack opening displacement as a function of either applied load or distance from the crack tip.

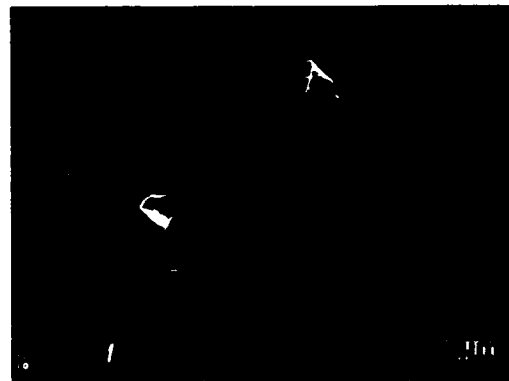


Figure 5. SEM micrographs of areas 1000 μm behind the crack tip showing grain release from the specimen surface; a) maximum applied load corresponding to crack equilibrium, b) zero applied load.

### Future Opportunities

The loading device in its current developmental stage is well suited for in situ studies of toughening mechanisms such as grain bridging, ductile ligament or whisker toughening as well as microcrack toughening.

Future advancements are sought in the areas of specimen geometry, and mode of applied loading.

In order to use K-field solutions for the standard geometries (ASTM), it is necessary to propagate a crack through a constant-thickness region. The preliminary aid of a quasi-chevron geometry should therefore be eliminated.

In situ observations during cyclic fatigue are currently under way. The evolution of bridges after given numbers of cycles can be monitored. The closure forces in the crack wake after cyclic loading can also be obtained by evaluating the crack opening displacements.

Further modifications of the fracture device are envisioned to provide the capability of compressive loading and therefore, also compression - compression fatigue. This would then allow inclusion of 4 - pt. bend fixtures as an additional option. A separate biaxial flexure stage is currently under construction. This new device will make it possible to test indentation cracks and will thus give an opportunity to investigate short vs. long crack behavior in the SEM.

### Summary

A fracture device which allows in situ observations of crack propagation in brittle solids under tensile loading has been described. It affords the opportunity to study the micromechanics of microstructural elements, which, acting as an ensemble, effect an increase in toughness over samples without special toughening features. The ability to measure applied load, crack opening and crack length makes the loading stage more than an in situ device for qualitative observations, but allows its use as a universal fracture testing machine. Quantitative measurements of the crack opening displacement allow evaluation of the closure stresses acting in the crack wake and enable a further characterization of the closure stress. Future opportunities include cyclic fatigue testing, compressive loading and biaxial flexure.

### Acknowledgements

We are indebted to Brian R. Lawn for suggesting this project and continued discussions. We also wish to thank Michael A. Hall for his excellent machining work. Funding was provided by the U.S. Air Force Office of Scientific Research.

### References

- [1] American Society for Testing and Materials. (1989). E-399-83. pp. 506-508. A.S.T.M. Philadelphia.
- [2] Atkins AM, Mai Y-W. (1985). Elastic and plastic fracture. pp. 198-219. Ellis Harwood Limited.
- [3] Barenblatt GI. (1962). The mathematical theory of equilibrium cracks in brittle fracture. Adv. Appl. Mech. 7 55-129.
- [4] Bennison SJ, Lawn BR. (1989). Role of interfacial grain-bridging sliding friction in the crack-resistance and strength properties of nontransforming ceramics. Acta metall. 37 [10] 2659-2671.
- [5] Davidson DL, Nagy A. (1978). A low-frequency cyclic-loading stage for the SEM. J. Phys. E: Sci. Instrum. 11 207-210.
- [6] Evans AG. (1990). Perspective on the development of high-toughness ceramics. J. Am. Ceram. Soc. 73 [2] 187-206.
- [7] Evans AG, Faber KT. (1984). Crack-growth resistance of microcracking brittle materials. J. Am. Ceram. Soc. 67 [4] 255-260.
- [8] Frei H, Grathwohl G. (1989). Development of a piezotranslator-based bending device for in situ SEM investigations on high-performance ceramics. J. Phys. E: Sci. Instrum. 22 589-593.
- [9] Hübner H, Jillek W. (1977). Subcritical crack extension and crack resistance in polycrystalline alumina. J. Mat. Sci. 12 117-125.
- [10] Irwin GRI. (1958). Fracture. Handbuch der Physik. 6,551-590.
- [11] Knehan R, Steinbrech R. Memory effect of crack resistance during slow crack growth in notched  $Al_2O_3$  bend specimens. J. Mat. Sci. Lett. 1,327-329.
- [12] Rice RW. (1988). Perspective on fractography. In: Fractography of glasses and ceramics. Varner JR, Frechette VD, Eds. pp. 3-53.
- [13] Rice RW, Freiman SW. (1981). Grain-Size Dependence of Fracture Energy in Ceramics: II, A Model for Noncubic Materials. J. Am. Ceram. Soc. 64 [6] 350-354.
- [14] Rödel J, Kelly JF, Lawn BR. (1990). In situ measurements of crack interfaces in the SEM. J. Am. Ceram. Soc. in press.
- [15] Swanson PL. (1988). Crack-interface traction: A fracture-resistance mechanism in brittle polycrystals. In: Fractography of glasses and ceramics. Varner JR, Frechette VD. Eds. pp. 135-155.
- [16] Swanson PL, Fairbanks CJ, Lawn BR, Mai Y-W, Hockey BJ. (1987). Crack-interface grain bridging as a fracture resistance mechanism in ceramics: I, Experimental Study on Alumina. J. Am. Ceram. Soc. 70 [4] 279-288.
- [17] Tait RB, Garrett GG. (1986). Direct observation of fracture in brittle materials in the SEM using a double torsion testing technique. Scanning 8,129-138.



[18] Wiederhorn SM, Johnson H, Diness AM, Heuer AH. (1974). Fracture of glass in vacuum. J. Am. Ceram. Soc. 57 [8] 336-341.

[19] Wu CC, Rice RW, Becher PF. (1981). The character of cracks in fracture toughness measurements of ceramics. In: Fracture mechanics methods for ceramics, rocks and concrete. ASTM STP 745, Freiman SW, Fuller ER. Eds. pp. 127-140.

#### Discussion with Reviewers

D.L. Davidson: If material is (virtually) elastic why doesn't COD vary with the square root of the distance behind tip (rather than distance behind the tip)? Crack bridging would be more convincing if a variation in COD were illustrated (Why not a graph of COD from Fig. 3?). This may be done in [14] but that's not accessible.

Authors: Elastic simply means non-permanent deformation. A parabolic profile describes cracks with stress-free crack walls, a non-parabolic profile points to forces applied at the crack walls, not necessarily affecting the elastic behavior of the material. Crack openings can only be meaningfully measured where no secondary cracking occurs. The resolution of our method is also not good enough to measure the effect of just one bridge, which might affect the crack opening by only a few nanometers. The closure stresses, however, are far reaching and, taken cumulatively, can be evaluated using a profile measurement [14]. Alternatively, the opening of a secondary crack at a bridge site can also give information about the closure stress [14].

H. Mueller: Can the crack jumping or slipping process be related to microstructure? Is it likely that the advancing crack was inhibited at grain boundaries or is it likely that the grain interiors contained inhomogeneities (even though appearing homogeneous) to account for the crack stick-slip behavior? Can the molecular configuration of the alumina account for this behavior?

Authors: Discontinuous crack advancement is related to variabilities in the microstructure, like variability in the local stresses, the grain boundary toughness, etc.

H. Mueller: Mention is made for obtaining quantitative information by recording COD during loading/reloading. This is essentially the procedure used for determining fracture toughness via chevron-notched methodology which is now well established. With the loading device described herein, it does seem possible to record load vs COD thereby providing a means to determine a plane strain fracture toughness. Has any consideration been given to relating the load vs COD plots to microstructure via SEM analysis. With this in mind, the chevron-notch geometry can therefore be beneficial instead of what is stated as preliminary and intended for

elimination.

Authors: The methodology mentioned does not lend itself easily to measurement of R-curve behavior. Detailed mathematical calculations of the relevant R-curves from the crack profile for this material can be found in [14].

H. Mueller: The presence of residual stresses can be compressive and tensile in nature. Mention is made of crack closure stresses which are likely due to compressive residual stresses. In the case of residual tensile stresses, can it be thought that crack opening stresses may instead be generated along the crack? If this is so, crack weakening instead of crack toughening would be operative.

Authors: The residual compressive and tensile stresses perpendicular to the crack plane indeed average out to zero. The residual stresses related to bridge formation (enhanced secondary cracking, clamping of grains etc.) allow for the generation of closure stresses.

H. Mueller: Was an angle of 28° critical for obtaining crack propagation stability? If a chevron angle of about 9 1/2° was used instead and extended to about 6 mm on the unpolished disc surface, there would have been no need to remove the samples to resaw after a crack was grown to 2 mm. If 28° was optimal, a thicker sample size of about 3 mm could also have been used to grow cracks to 6 mm in length within the quasi chevron-notched region without stopping to remove and resaw the samples.

Authors: The angle of 28° was rather arbitrarily chosen. Since the area of bridged crack walls has to be kept identical from experiment to experiment, the identical chevron geometry has to be used and the suggestion is not applicable.

H. Mueller: The COD vs distance from the crack tip plot shown in Figure 4 is apparently without crack bridging mechanisms being included. If crack bridging is included within regions along the crack, how would a typical COD vs distance plot be characterized? One might think that a parabolic profile or some other decreasing profile would be depicted in this situation and that a linear profile would be depicted with a stress-free surface (just the opposite of that mentioned).

Authors: From standard fracture mechanics theory we know [3,10]: Stress-free crack surfaces lead to a parabolic profile. Figure 4 includes crack bridging (not parabolic).

# Fundamental Condition for the Existence of Microcrack Clouds in Monophase Ceramics

Brian R. Lawn

Ceramics Division, National Institute of Standards and Technology, Gaithersburg, Maryland 20899, USA

(Received 23 April 1990; revised version received 3 July 1990; accepted 23 July 1990)

## Abstract

Conditions for the existence of a microcrack cloud about a primary crack front in monophase polycrystalline ceramics are examined. With the assumption that microcracks initiate from sub-facet flaws, and that these flaws scale with the grain size, an expression is derived for the cloud radius. The cloud radius diminishes rapidly with grain size, from unlimited dimensions at the critical size for spontaneous, general microcracking to sub-grain level at some fraction of the critical size. The corresponding grain-size 'window' is dependent on the flaw size but is restrictively small for typical monophase ceramics.

An einphasigen polykristallinen keramischen Werkstoffen werden die Bedingungen zur Ausbildung einer Zone von Mikrorissen um die primäre Rißfront untersucht. Eine Gleichung zur Berechnung des Radius dieser Zone wird abgeleitet. Dabei wird von der Annahme ausgegangen, daß die Mikrorisse von Gefügeteclern herrühren und daß diese Fehler mit der Korngröße zunehmen. Der Radius dieser Zone nimmt mit der Korngröße rasch ab. Der Maximalwert eines 'unendlichen' Radius liegt bei einer kritischen Korngröße, bei der im gesamten Gefüge spontane Mikrorißbildung eintritt. Der Minimalwert beträgt nur einen Bruchteil der kritischen Größe und ist kleiner als die Korngröße. Der entsprechende Korngrößenbereich hängt von der Fehlergröße ab, ist aber für typische einphasige keramische Werkstoffe sehr eng.

On a examiné les conditions d'existence d'un nuage de microfissures au voisinage d'un front de fissure primaire dans les céramiques cristallines monophasées. En supposant que les microfissures sont

initiales par des défauts subsurfaciques et que ces défauts sont proportionnels à la taille de grains on peut établir une expression du rayon de ce nuage. Ce rayon diminue rapidement avec la taille des grains, allant d'une dimension infinie pour une taille critique de microfissuration générale spontanée à une dimension subgranulaire pour une taille inférieure à la taille critique. La 'fenêtre' de taille de grains correspondante dépend de la taille du défaut mais est étroite pour les céramiques monophasées typiques.

Frontal-zone microcracking has been proposed as a mechanism of toughening<sup>1-5</sup> and consequent source of R-curve behaviour<sup>5</sup> in polycrystalline ceramics. In principle, individual microcracks can be activated at incipient sources, e.g. sub-facet grain-boundary flaws, in the field of a primary crack. The primary-crack stresses may be augmented by internal residual tensile stresses from differential thermal expansion or elastic mismatch. In relieving these tensile stresses, the fully developed microcracks remain irreversibly open, typically over several grain dimensions, thereby imposing a dilatant closure field on the primary crack.<sup>5</sup>

The issue of microcracking involves two fundamental questions: (i) Under what conditions will a microcrack cloud exist? (ii) Given that such a cloud does exist, what is the extent of toughening? The second of these questions has been frequently addressed, the first rarely. Thus the vast majority of studies presume the existence of a microcrack cloud. After all, above a critical grain size, many non-cubic ceramics do exhibit general, spontaneous microcracking throughout the material. However, definitive experimental supporting evidence for microcrack cloud zones in ceramics is almost totally lacking. Moreover, recent *in-situ* observations of propagating cracks in aluminas and other R-curve

ceramics<sup>6,7</sup> (previously considered prime candidates for microcracking<sup>2</sup>) reveal no evidence whatsoever for active frontal zones: on the other hand, considerable grain-interlock bridging activity is observed at the crack interface behind the crack tips. Those observations have led some to question the very existence of microcrack clouds in ceramic materials.

In the present note, we consider this last point: what *are* the underlying conditions for the existence of a microcloud zone? For simplicity, we focus on monophase ceramics, although the principles to be outlined below extend to multiphase ceramics and, indeed, to other frontal-zone toughening processes (e.g. transformation toughening).

Consider a *monophase* ceramic material with predominantly intergranular fracture. For generality, suppose the material to be *non-cubic*, to allow for any thermal-expansion anisotropy stresses. We investigate the critical condition for microcrack initiation from the perspective of an observer at the tip of an equilibrium primary crack (P) looking outward towards potential sources (M) at  $(r, \theta)$  (Fig. 1). The stress  $\sigma^M$  acting on a particular active source, assumed to be located at a grain-boundary sub-facet, is the superposition of two contributions:

(i) The mean (hydrostatic) tensile near-tip stress,  $\bar{\sigma}_{ii} = (\sigma_{rr} + \sigma_{\theta\theta} + \sigma_{zz})/3$ , in the polar field of the primary crack, evaluated from the Irwin displacement equation for a slit-like crack<sup>8</sup> at  $K = K^P$ ,

$$\bar{\sigma}_{ii} = K^P \bar{f}_{ii}(\theta) / (2\pi r)^{1/2} \quad (1)$$

with  $\bar{f}_{ii}(\theta) = (2/3)(1+\nu)\cos(\theta/2)$ . This stress component has a maximum value  $\bar{f}_{ii}(\theta) = 0.72$  at  $\theta = 60^\circ$ .

(ii) The tensile component of the thermal-expansion anisotropy stress is given by:

$$\sigma_R = E \Delta \alpha \Delta T (1 + \nu) \quad (2)$$

with  $\Delta \alpha$  the differential expansion coefficient between adjacent grains and  $\Delta T$  the temperature range through which the material deforms elastically during the first cooling cycle. Of course,  $\sigma_R = 0$  for cubic materials.

Approximating the sources as uniformly stressed penny-shaped flaws of radius  $c_0$ , the critical stress-intensity factor for microcrack extension is:<sup>9</sup>

$$\begin{aligned} K^M &= 2\sigma^M (c_0 \pi)^{1/2} \\ &= 2(\bar{\sigma}_{ii} + \sigma_R) (c_0 \pi)^{1/2} = T_0 \end{aligned} \quad (3)$$

with  $T_0$  the intrinsic grain-boundary toughness.

Mention was made of a critical grain size,  $l_c$  say, above which non-cubic ceramics tend to general microcracking during initial cooling. It is accordingly of interest to determine the conditions for micro-

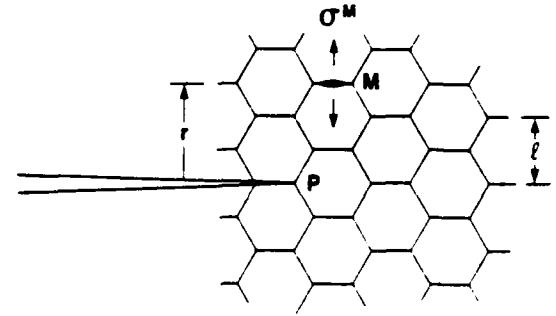


Fig. 1. Co-ordinates for evaluating microcrack initiation in polycrystalline material. Intrinsic penny-like microcrack flaw (M) at  $(r, \theta)$ , radius  $c_0$  (not shown), subjected to superposed opening stresses  $\sigma^M$  from field of primary crack (P) and thermal-expansion mismatch stresses. It is assumed that the microstructure satisfies conditions of geometrical similarity at different grain sizes  $l$ , such that  $c_0$  and  $r$  scale with  $l$ .

cracking in the absence as well as in the presence of a primary crack, to establish an upper bound to the scale of the frontal cloud. Suppose that the dimensions  $c_0$  and  $r$  in Fig. 1 scale directly with grain size  $l$ , i.e. in accordance with the principles of geometrical similitude, so that the corresponding normalised quantities

$$\mathcal{C}_0 = c_0 / l \quad (4a)$$

$$\mathcal{R} = r / l \quad (4b)$$

are scale-invariant. We may then distinguish between spontaneous and activated microcracking, as follows:

(i) *Spontaneous (general) microcracking*. In the absence of any primary crack ( $\bar{\sigma}_{ii} = 0$ ), sources M initiate at tensile sub-facets from the sole action of the internal stress ( $+\sigma_R$ ). Equation (3) is then satisfied at the critical grain size

$$l_c = (\pi/4) (T_0 / \sigma_R)^2 \quad (5)$$

Above  $l_c$ , general microcracking occurs from active sources throughout the material. Taking typical values for alumina,  $T_0 \approx 2.0 \text{ MPa m}^{1/2}$ ,  $\sigma_R \approx 250 \text{ MPa}$ ,  $\mathcal{C}_0 \approx 0.5$  (say), we obtain  $l_c \approx 100 \mu\text{m}$  in eqn (5); this is of the order of the critical grain size observed experimentally. We note that, whereas some grain facets are in tension ( $+\sigma_R$ ), others will be in compression ( $-\sigma_R$ ), so that the initiated microcracks arrest at neighbouring facets (incipient bridging sites<sup>10,11</sup>) after extending approximately 3–5 grain diameters.

(ii) *Activated (cloud) microcracking*. Now consider the grain-size domain  $l \leq l_c$ . Active microcracking is confined to a cloud around the tip of primary crack P, within a maximum radius determined by inserting  $K^P = T_0$  in eqn (1) and combining with eqn (3):

$$\mathcal{R}_c = 2\mathcal{C}_0 \bar{f}_{ii}(\theta) / (\pi [1 - (l/l_c)^{1/2}])^{1/2} \quad (6)$$

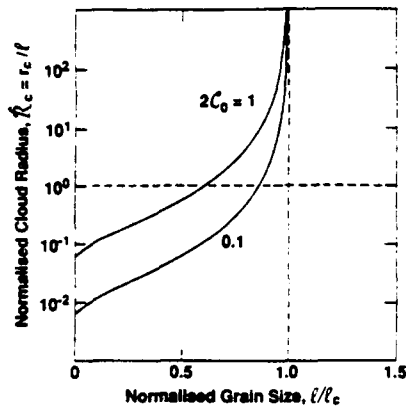


Fig. 2. Microcrack cloud radius around primary crack tip as function of grain size, for two values of penny-flaw diameter.

We plot  $\mathcal{R}_c$  as a function of  $l/l_c$  in Fig. 2, at two bounding values of  $c_0$ , with  $\bar{l}_{ii}$  evaluated at  $\theta = 60$  as above.

These calculations help to explain why microcrack clouds may not be as prevalent as generally presumed. In interpreting the plots in Fig. 2, we note that the condition  $\mathcal{R}_c = r_c/l = \infty$  indicates an upper bound for general microfracture, as described by eqn (5); and  $\mathcal{R}_c = 1$  indicates a lower level below which microcrack sources simply coalesce into the primary crack, i.e. there can be no detached cloud. With that, consider two limiting cases in eqn (6) as follows:

- $l/l_c \rightarrow 1$ ,  $\mathcal{R}_c \rightarrow \infty$ , corresponding to the limiting grain size for general microfracture
- $l/l_c \rightarrow 0$ ,  $\mathcal{R}_c \approx 0.1c_0$ , relating to materials for which  $l \rightarrow 0$  or  $l_c \rightarrow \infty$  ( $\sigma_R \rightarrow 0$  in eqn (5)). Thus, since  $c_0 < 1$  generally, it follows that  $\mathcal{R}_c < 0.1$ , so that no microcracking, spontaneous or activated, is expected in fine-grained or cubic materials. Physically, this is because the sub-facet flaws lie too far distant (one grain dimension or more) from the primary-crack tip for the near field alone to be effective: decreasing the grain size brings the sources closer (eqn (4b)), but this is more than counteracted by a diminished flaw size (eqn (4a)).

Figure 2 shows that, between these limits, the cloud radius diminishes rapidly with decreasing grain size, more so at smaller  $c_0$ . Thus, for 'well-made' ceramics (small  $c_0$ ) the 'window' of allowable grain sizes for the activation of significant clouds (at  $r_c/l > 10$ , say) may simply be too restrictive for common observation.

We are led to believe, especially in light of the

current trend for materials processors to fabricate fine-grained, flaw-free microstructures, that microcrack-cloud toughening is unlikely to be a commonplace observation in monophase ceramics. Alternative toughening modes, e.g. grain-interlock bridging,<sup>5,6</sup> are not subject to the same restrictive windows and are therefore expected to dominate over the broader range of grain sizes.

In principle, the above analysis should be extendable to multiphase ceramics, and to other frontal-zone processes, with cosmetic adjustments to the treatment. It is conceivable that the flexibility afforded by the addition of a second phase (e.g. removal of necessity to conform to the restrictions of geometrical similarity) could facilitate an expansion of the grain-size window and thereby make microcracking a more viable prospect. In this context, it is interesting to note that the best-validated observations of microcrack zones in ceramics have been reported in two-phase systems.<sup>1,2</sup>

### Acknowledgements

The author thanks S. J. Bennison, S. Lathabai and J. Rödel for comments and discussions. This work was funded by the U.S. Air Force Office of Scientific Research.

### References

- Hoagland, R. G., Embury, J. D. & Green, D. J., On the density of microcracks formed during the fracture of ceramics. *Scripta Met.*, **9** (1975) 907-9.
- Evans, A. G., On the formation of a crack-tip microcrack zone. *Scripta Met.*, **10** (1976) 93-7.
- Claussen, N., Stebb, J. & Pabst, R. B., Effect of induced microcracking on the fracture toughness of ceramics. *Amer. Ceram. Soc. Bull.*, **56** (1977) 559-62.
- Evans, A. G. & Faber, K. T., Crack-growth resistance of microcracking brittle materials. *J. Amer. Ceram. Soc.*, **67** (1984) 255-60.
- Clarke, D. R., A simple calculation of process-zone toughening by microcracking. *J. Amer. Ceram. Soc.*, **67** C15-16 (1984).
- Swanson, P. L., Fairbanks, C. J., Lawn, B. R., Mai, Y.-W. & Hockey, B. J., Crack-interface grain bridging as a fracture resistance mechanism in ceramics: I. Experimental study on alumina. *J. Amer. Ceram. Soc.*, **70** (1987) 279-89.
- Swanson, P. L., Crack-interface traction: A fracture-resistance mechanism in brittle polycrystals. In *Advances in Ceramics*, Vol. 22: *Fractography of Glasses and Ceramics*. American Ceramic Society, Columbus, Ohio, USA, 1988, pp. 135-55.
- Lawn, B. R. & Wilshaw, T. R., *Fracture of Brittle Solids*. Cambridge University Press, Cambridge, UK, 1975, Chapter 3.

9. McMeeking, R. M. & Evans, A. G., Mechanics of transformation toughening in brittle materials. *J. Amer. Ceram. Soc.*, **65** (1982) 242-6.
10. Bennison, S. J. & Lawn, B. R., Role of interfacial grain-bridging sliding friction in the crack-resistance and strength properties of nontransforming ceramics. *Acta Metall.*, **37** (1989) 2659-71.
11. Chantikul, Prapaipan, Bennison, S. J. & Lawn, B. R., Role of grain size in the strength and R-curve properties of alumina. *J. Amer. Ceram. Soc.*, **13** (1990) 2419-27.
12. Ruhle, M., Claussen, N. & Heuer, A. H., Transformation toughening and microcracking as complementary processes in  $\text{ZrO}_2$ -toughened  $\text{Al}_2\text{O}_3$ . *J. Amer. Ceram. Soc.*, **69** (1986) 195-7.

## Cyclic Fatigue from Frictional Degradation at Bridging Grains in Alumina

Srinivasarao Lathabai,<sup>\*,†</sup> Jürgen Rödel,<sup>\*</sup> and Brian R. Lawn<sup>\*</sup>

Ceramics Division, National Institute of Standards and Technology, Gaithersburg, Maryland 20899

Tension-tension cyclic loading tests have been conducted on a coarse-grained alumina ceramic that exhibits toughness-curve behavior by grain-interlock bridging. Fatigue effects are observed in the regions of both short cracks, using indentation flaws, and long cracks, using compact-tension specimens. A true mechanical fatigue effect is demonstrated by running the tests below the static fatigue limit. A custom-made device for in situ observation of crack propagation in the scanning electron microscope enables us to identify bridge degradation as a cause of the fatigue process. "Wear" debris cumulates at the sliding intergranular frictional contact points, indicating a loss of traction at the junction. The basis of a fracture mechanics model describing the effect of this frictional degradation in reducing crack-tip shielding is outlined and fitted to the data. It is suggested that the bridge degradation fatigue mechanism may be widespread in polycrystalline ceramics with pronounced toughness curves. [Key words: fatigue, friction, degradation, grains, bridging.]

### I. Introduction

A NEW breed of flaw-tolerant ceramics is emerging. Flaw tolerance is a manifestation of crack-tip shielding that cumulatively toughens the material as the crack extends, resulting in an increasing toughness curve (*R*-curve or *T*-curve).<sup>1</sup> Several shielding processes have been considered in the literature, most notably frontal-zone phase transformation and microcracking. But in monophase ceramics like aluminas the principal mode is bridging of the crack interface by interlocking grains.<sup>2-4</sup> A leading question in the potential use of such materials for structural applications is whether the elements responsible for the toughening degrade during reversed loading: do bridging materials exhibit true, mechanical cyclic fatigue, and, if so, what is the degradation mechanism?

Early studies on alumina<sup>5-8</sup> reported reduced lifetimes in cyclic relative to static loading. A fracture mechanics analysis of results on glass and porcelain (in the context of a review of some of the earlier data<sup>9</sup>) suggested that the fatigue could be explained as the integrated effect of environmentally enhanced slow crack growth.<sup>9</sup> A study on silicon carbide<sup>10</sup> showed no cyclic effect at all. However, more recent studies on aluminas,<sup>11,12</sup> zirconias,<sup>13,14</sup> silicon nitrides,<sup>15-20</sup> and fiber-reinforced ceramics<sup>21</sup> do appear to demonstrate definite mechanical cyclic fatigue.

If authentication of the *existence* of true cyclic fatigue has been slow in coming, identification of the responsible mechanisms of degradation is virtually *totally* lacking. Some authors, drawing largely from the greater knowledge of fatigue processes in metallic materials, have proposed very specific mechanisms for fatigue damage in ceramics.<sup>22-24</sup> One class of these mechanisms invokes crack "closure,"<sup>24</sup> including wedging by crack-interface asperities, debris, and the like; others invoke frontal-zone microcracking or even microplasticity. However, direct experimental evidence proving or disproving these hypothetical mechanisms is lacking. The possibility of interfacial bridge degradation has hardly been given any consideration at all in the literature.<sup>21,25</sup>

Our objective in the present study is to investigate the effect of cyclic tension-tension loading on an alumina ceramic with a demonstrably pronounced *T*-curve from bridging, in the opposite domains of "short" cracks pertinent to strength properties and "long" cracks encountered in specimens for toughness evaluations. For the short cracks we use indentation flaws, comparing lifetimes of flexure specimens under cyclic loading with those of control static specimens. In an earlier, less complete study of this kind in our laboratories<sup>26</sup> on a finer-grained alumina (i.e., with weaker *T*-curve) we were unable to detect any true degradation, over and above that due to moisture-induced slow growth, in the strength properties. For the long cracks we use a compact-tension geometry, subjecting the specimen to cyclic loading at various interruption stages in the crack extension. Evidence for modest mechanically induced cyclic fatigue is found in both crack-size domains.

In light of the hypothetical nature of previously proposed fatigue mechanisms, we use a custom-designed device<sup>27-29</sup> for in situ viewing of cracks in our material in the scanning electron microscope (SEM). *Direct observations during cyclic loading reveal the cumulation of debris at sliding grain facets along the crack interfaces.* A specific model for fatigue damage in bridging ceramics, based on frictional degradation at grain-interlock "pullout" sites, is thereby advanced. It is proposed that frictional degradation may be a dominant fatigue mechanism in a broad range of ordinary monophase and multiphase ceramics, and therefore a factor for special consideration in designing with such materials.

### II. Experiment

The material used in this study was a commercial polycrystalline alumina, with <0.1% additive.<sup>1</sup> The specimens were obtained as disks 22 mm in diameter and 2 mm thick, and plates 100 mm × 100 mm × 6 mm. This alumina was nominally the same as used in our earlier study,<sup>26</sup> except that it was subjected to a heat treatment to coarsen the mean grain size, from 23 to 35 μm, and thereby to strengthen the *T*-curve. It fractured predominantly by intergranular fracture, with some

K. Faber—contributing editor

Manuscript No. 197256. Received October 1, 1990; approved March 11, 1991.

Presented at the 92nd Annual Meeting of the American Ceramic Society, Dallas, TX, April 25, 1990 (Paper No. J-XX-90).

Supported by the U.S. Air Force Office of Scientific Research

\*Member, American Ceramic Society.

<sup>†</sup>Guest scientist from the Department of Materials Science and Engineering, Lehigh University, Bethlehem, PA.

<sup>‡</sup>Now in the Division of Materials Science, CSIRO, Clayton, Victoria 3168, Australia.

<sup>1</sup>A term coined by metallurgists to designate a residual opening on unloading.

<sup>2</sup>Vistal grade Al<sub>2</sub>O<sub>3</sub>, Coors Ceramics Co., Golden, CO.

transgranular fracture through the larger grains.<sup>2,4</sup> Fatigue tests were run in tension-tension loading, as follows.

### (1) Short-Crack Fatigue Tests

"Short-crack" tests were conducted on the disks. Vickers indentation flaws at a load of 30 N (immediate postcontact radial crack dimension  $\approx 100 \mu\text{m}$ ) were placed at the centers of the prospective tensile faces. The indented disks were mounted on a biaxial loading fixture,<sup>29</sup> using a flat circular punch of diameter 4 mm on a three-point support of diameter 19 mm. Cyclic tests were run in water, with sinusoidal loading at frequencies of 1 and 100 Hz on a digitally controlled servo-hydraulic testing machine.<sup>30</sup> The maximum tensile stress was adjusted as required, but the minimum was maintained constant at 20 MPa. Runs were discontinued if no failure occurred within 24 to 40 h. Control tests were carried out under static loading in water, at the same maximum levels as in the cyclic runs. Additional, "calibration" strength tests were run at the same indent load (30 N) at constant stressing rates in water, and at various loads in inert environment (silicone oil), to evaluate the intrinsic crack velocity and microstructural  $T$ -curve parameters for our material.<sup>30</sup>

### (2) Long-Crack Fatigue Tests

"Long-crack" tests were conducted on two plate specimens, width 44 mm (measured from the load line), in the compact-tension geometry of ASTM E399.<sup>31</sup> The viewing surfaces of these specimens were polished to 1- $\mu\text{m}$  finish, for optimal crack observation. A starter notch of length 14 mm and tip radius  $\approx 420 \mu\text{m}$  was machined into each specimen. To control pop-in, a half-chevron slot of included angle  $\approx 28^\circ$  and radius  $\approx 200 \mu\text{m}$  was sawn at the end of the machined notch, so that the slot extended just beyond the notch on the polished surface. A Vickers indentation (50 N) was placed  $\approx 200 \mu\text{m}$  in front of the half-chevron on this latter surface. This led to a precrack of length  $\approx 250 \mu\text{m}$  on loading. After subsequent incremental extensions the crack was resawn to within  $\approx 300 \mu\text{m}$  of the new crack tip.

One of the specimens was then loaded in displacement-control mode in the servo-hydraulic testing machine, in laboratory atmosphere (relative humidity 50% to 60%). A traveling microscope was used to track the crack growth. At the first sign of slow crack growth the crack was immediately unloaded, to avoid premature failure of the system. The specimen was then transferred to a transmission optical microscope, and the crack length measured. A crack-opening-displacement (COD) gauge attached to the crack notch mouth (via steel knife edges fixed to the specimen with epoxy) enabled the load at which crack growth initiated to be readily determined as the point where the load-displacement record deviates from linearity. The applied stress-intensity factor  $K_A$  at each such point of crack growth was computed from the ASTM standard formula.<sup>31</sup> This procedure was repeated at various crack growth increments in monotonic loading, to allow for determination of the quasi-static toughness curve as a function of crack extension,  $K_A(\Delta c) = T(\Delta c)$ .<sup>1</sup>

A similar procedure was adopted for the second specimen, except that now the specimen was only partially unloaded at the interruption points, and then subjected to a specified static-cyclic loading sequence. Static loading was thus run at a stress-intensity factor  $K_A = 0.8$  to 0.9 times that for quasi-static extension in monotonic loading. Cyclic loading was sinusoidal, frequency 10 Hz, at maximum  $K_A^{\text{Max}} = K_A$  and amplitude  $K_A^{\text{Min}}/K_A^{\text{Max}} = 0.1$ . In these experiments the crack length was carefully monitored via the traveling microscope, and the system once more unloaded after extensions of 500  $\mu\text{m}$  or more. After each such interval of static-cyclic loading the crack was reloaded to quasi-static extension and the toughness reevaluated.

### (3) In Situ Observations of Bridging Crack

In situ fatigue tests were conducted using a custom-designed device for incorporation in the SEM,<sup>27,28</sup> similar in design to that of Frei and Grathwohl.<sup>25</sup> Compact-tension specimens were prepared as above for the SEM in situ observations, except that the cracks were always contained within the initial chevron sawcut as an extra precaution against uncontrolled crack instability.<sup>27</sup> At the vacuum level in the SEM environmentally induced slow crack growth was almost totally eliminated, although some was occasionally observed if this vacuum was allowed to deteriorate (e.g., after switching off the diffusion pump). The viewing surfaces were again polished to 1- $\mu\text{m}$  finish, and gold coated before insertion into the SEM. After the crack was propagated to a suitable crack length, the opening force was reduced to a level  $K_A = 0.8T$  to  $0.9T$  ( $T$  the toughness at that length in monotonic loading) and the specimen subjected to an interval of cycling. This was done via a piezoelectric drive controlled remotely through a function generator outside the SEM chamber.<sup>27,28</sup> The frequency was limited to a maximum of 2 Hz. The load amplitude was also limited, thereby necessitating manual preload of the crack before insertion into the SEM. Several locations of interest along the crack interface could be monitored during the cycling interval by means of a videocassette recorder, and photographed at static load at any point.

## III. Results

### (1) Short-Crack Fatigue Tests

The lifetime data for the indentation-flaw specimens are summarized in Figs. 1 to 3. Figure 1 shows the time to failure at static stresses,  $\sigma_A = \text{constant}$ . "Survivors" are represented by arrows. We note that the lifetime varies dramatically with minute changes in the applied stress, indicating that the system is close to a static fatigue limit for this material: i.e., the cracks are growing close to a threshold in the intrinsic crack velocity function.<sup>30</sup> Thus by operating at this stress level we may conveniently minimize the role of chemically assisted slow growth in the cyclic tests. The curve through the data represents a theoretical prediction (Section IV) from the calibrated microstructural  $T$ -curve and crack velocity parameters at the prescribed indentation load.<sup>29,30</sup>

Figure 2 shows the comparative lifetime data for cyclic loading as a function of maximum applied stress,  $\sigma_{\text{Max}}$ , at the two frequencies used. A rapid variation of lifetime with applied stress is again apparent, although in this case there does appear to be some indication of a systematic if modest falloff relative to the predicted curves for kinetic crack growth

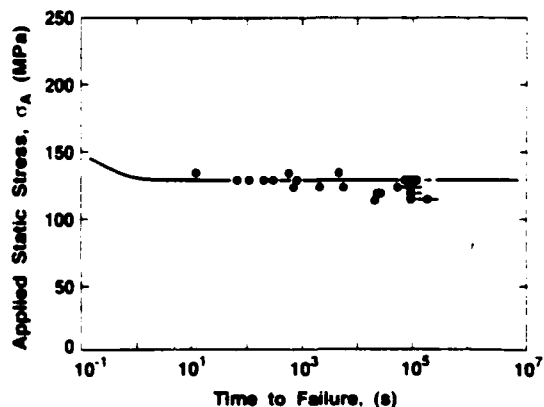


Fig. 1. Lifetimes in static loading of alumina in water. Vickers indentations ( $P = 30 \text{ N}$ ). Most data points are results of individual tests; those with arrows are means of interrupted tests for a minimum of five specimens. Solid curve is theoretical prediction. Note fatigue limit.

<sup>30</sup>Instron Digital Servo-hydraulic Testing Machine 8502, Instron Corp., Canton, MA.

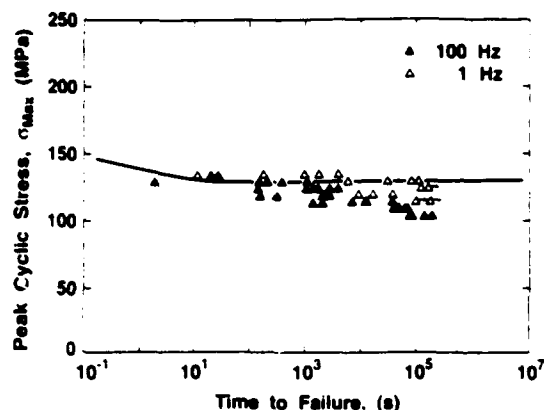


Fig. 2. Lifetimes in cyclic loading of alumina in water. Vickers indentations ( $P = 30$  N). Data points are individual tests, open symbols 1 Hz, closed symbols 100 Hz; arrows are interrupted tests, minimum of five specimens. Solid line is theoretical prediction assuming environmentally-assisted slow crack growth without mechanical degradation.

alone,<sup>26</sup> especially at the higher frequency. The falloff is seen to better effect in Fig. 3, which replots the data as a function of cycles to failure. The fact that the data fit a more universal curve in the replotted figure is further indication that the fatigue is due to a true mechanical effect.

### (2) Long-Crack Fatigue Tests

Results of the compact-tension toughness-curve tests are plotted in Fig. 4. Data for the two specimens overlap within experimental error, saturating at  $T \approx 5.3 \text{ MPa} \cdot \text{m}^{1/2}$ . We reemphasize that the toughness values in this plot are quasi-static, in that the tests are carried out in air and the crack does not extend in strict equilibrium; i.e., the configuration is located partway up the velocity curve in monotonic loading. Recalling that one of these specimens was subjected to interrupted static and cycling sequences, we conclude that any degradation of the shielding that might have occurred in reversed loading is insufficient, at least over the cyclic range covered, to be detectable in the toughness data.

At the same time, there is compelling evidence, from the measurements of crack extensions  $\delta c$  over the interruption intervals  $\delta t$ , that some such degradation *does* occur. The results of three interrupt sequences, each at specified values of  $K_A(\text{static}) = K_A^{\text{Max}}(\text{cyclic})$ , are plotted in Fig. 5. In each case  $\delta c/\delta t$  is significantly larger in cyclic relative to static loading, despite the smaller time-averaged  $K$ -field. Note in particular the first two sequences at  $K_A = 4.2 \text{ MPa} \cdot \text{m}^{1/2}$  (i.e., at 0.87): there is a total absence of crack growth in the static

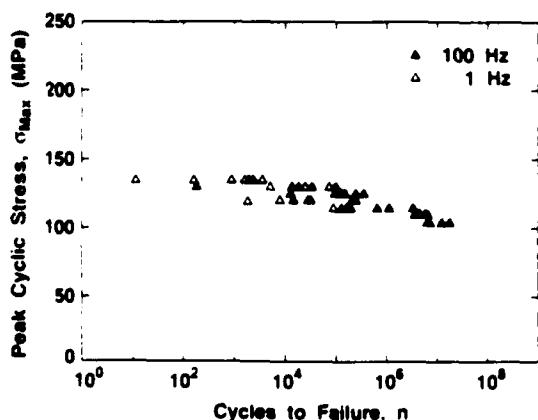


Fig. 3. Replot of data in Fig. 2 as function of cycles to failure. Symbols as in Fig. 2.

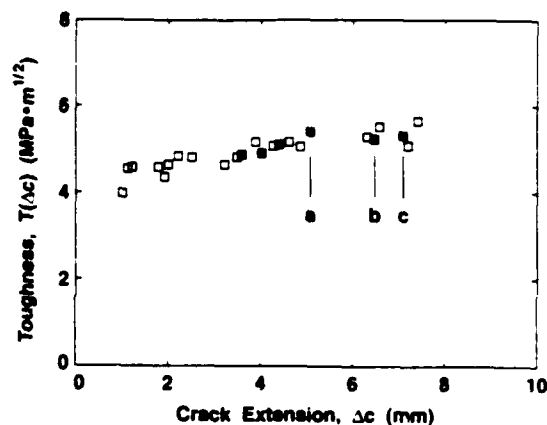


Fig. 4. Toughness curves for two alumina compact-tension specimens (distinguished by open and closed symbols) in air. Unlabeled points represent quasi-equilibrium crack extension in monotonic loading. Labeled points a, b, c represent similar extension but after interruption static-cyclic sequence (see Fig. 5 for details).

phase, indicating that at this  $K_A$  level the system lies below the crack velocity threshold; and yet there is significant extension in the ensuing cyclic phase, again implying some mechanical fatigue effect.

### (3) In Situ Observations

The in situ SEM device provided an opportunity to follow the development of bridging sites along the intergranular crack interface during cyclic loading tests. Notwithstanding the practical limitation on number of cycles, evidence for continuing bridge evolution was obtained in these tests, with and without attendant crack propagation. Selected sequences are shown in Figs. 6 to 10 (crack propagation top to bottom and applied loading horizontal in all cases). All bridging elements in these sequences are photographed at peak crack opening in the in situ cycle unless otherwise qualified, with number of cycles  $n$  and distance  $x$  behind crack tip indicated where appropriate:

(i) Figure 6: Segmentation of a bridging grain at three stages in its development. Between (a) and (b), after a few thousand cycles and minor crack propagation, the crack closes at lower right (segment P) and redirects, releasing internal stress in the intervening grain.<sup>27</sup> Between (b) and (c), the crack propagates further by virtue of an increment in the applied load, and undergoes a further closure relaxation at upper right (segment Q). This example demonstrates the general

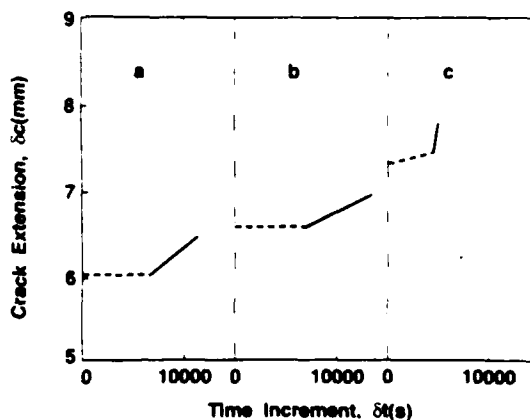


Fig. 5. Crack extensions during intervals in static-cyclic (10 Hz) interruption sequences at points labeled in Fig. 4. Measurements of c and t were made at end points of each straight line segment, so slopes are average velocities: (a)  $K_A = K_A^{\text{Max}} = 4.2 \text{ MPa} \cdot \text{m}^{1/2}$ , (b) same; (c)  $K_A = K_A^{\text{Max}} = 4.75 \text{ MPa} \cdot \text{m}^{1/2}$ .



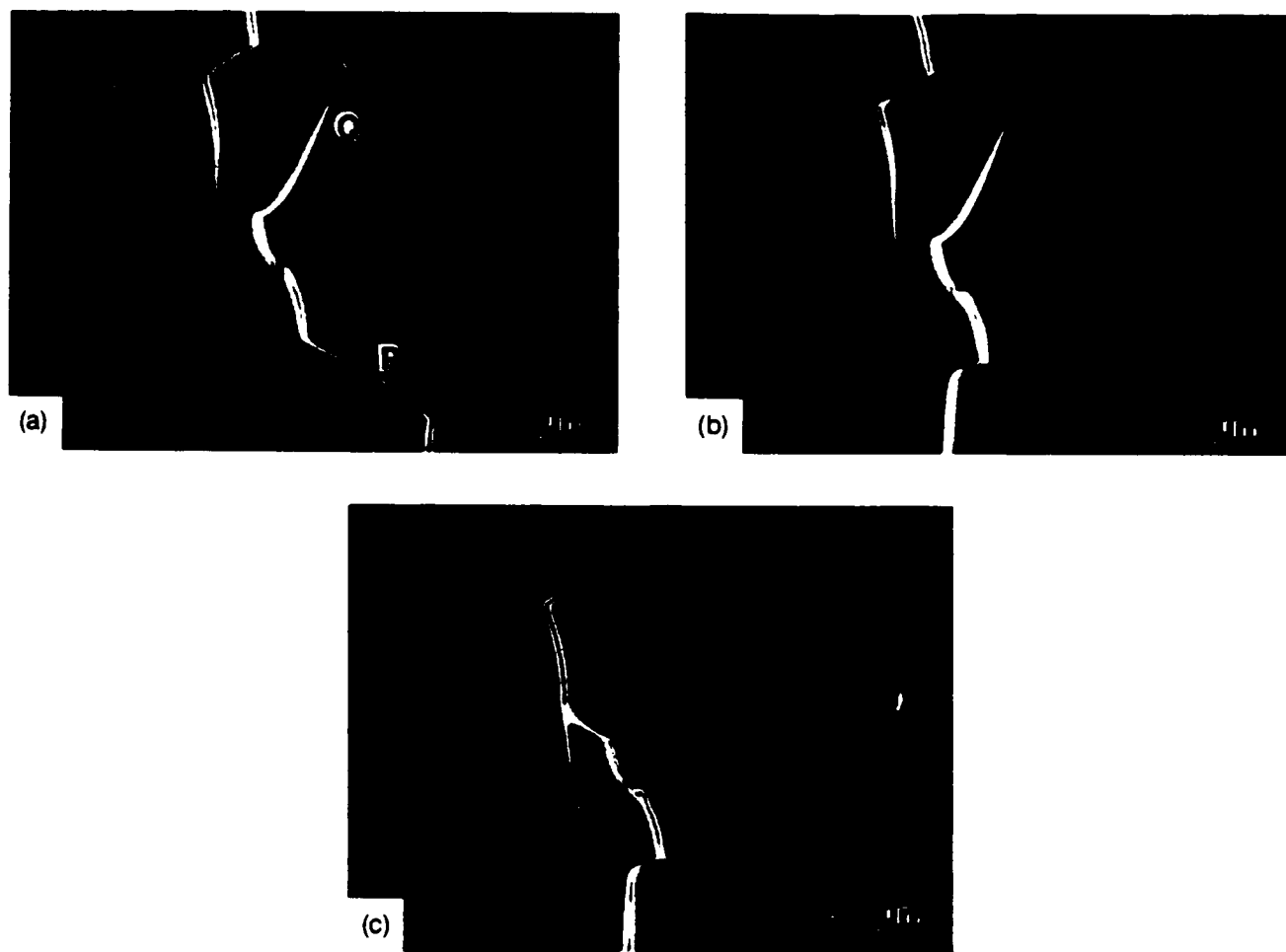


Fig. 6. SEM micrograph of crack in alumina, showing grain-bridging element: (a) after initial crack propagation (distance  $x = 860 \mu\text{m}$  behind crack tip); (b) after cycling in SEM ( $n = 7000$  at  $2 \text{ Hz}$ ,  $K_A^{\text{Max}} = 0.857$ ) and minor crack propagation ( $x = 880 \mu\text{m}$ ); (c) after increasing  $K_A$  and further propagation ( $x = 1080 \mu\text{m}$ ).

capacity of bridging sites to continue their evolution in response to load perturbations well after passage of the primary crack front.

(ii) Figure 7: Surface grain dislodgement from frictional rotation. Between (a) and (b) the primary crack advances under load and intergranular facet cracks link at the interlocking site, rotating the grain out of its "socket." On unloading, partially in (c) and almost completely in (d), the walls close but the grain protrudes from the surface. Note in (d) that the opening is small,  $\approx 0.1$  times that at full load in (b) (i.e., in proportion to the reduction in  $K_A$ ), indicating that despite the grain dislodgement there is very little residual crack-interface wedging.

These first two sequences show distinctive evidence of bridge evolution in cyclic loading, but do not unequivocally establish a true mechanical degradation effect: how much of the evolution is due to inadvertent crack propagation, however small, during the cycling? Accordingly, the next sequences contain stages in which no propagation is observed during the cycling, and yet bridge degradation is still evident:

(iii) Figure 8: Sliding grain boundary facet with apparently strong frictional traction. Cycling between (a) and (b) produces a secondary crack below the bridging grain (P), without detectable crack propagation. After further loading and propagation to (c), both primary and secondary cracks open up (the former almost to the point of disengagement of the sliding grain boundary facet). Subsequent static loading at constant load in a degraded SEM vacuum (by switching off the diffusion pump overnight) causes the crack to more than

double its length, disengaging the bridging grain facet totally in (d). We note the "flipover" of grain segment P from the right side of the interface to the left between (c) and (d) at the point of disengagement, suggesting that this segment remains permanently attached at its subsurface base to the left wall throughout the separation, like a highly sprung cantilever. The consequent release of elastic strain energy at disengagement in this case must be considerable and highly dissipative.

The following two sequences are further examples of bridge evolution in reversed loading, but with closer attention to degradation of frictional facets for extended cycling periods:

(iv) Figure 9: Degradation of frictional facet. Through cycling stages (a) to (e) there is gradual cumulation of debris from the sliding grain facet interface, even between (c) and (e), where no primary crack propagation occurs. Stage (f) is after total unload; note the residual opening at upper right, indicating some small wedging in this region.

(v) Figure 10: Another frictional facet. Similar to Fig. 9, with appearance of debris between (a) and (c) (no crack propagation between (b) and (c)). Stage (d) shows enhanced debris buildup after prolonged additional cycling *in air*.

Selective energy dispersive spectroscopy of the debris in Figs. 9 and 10 reveals strong aluminum and oxygen peaks, and trace magnesium, but no excess gold, consistent with some product from the alumina itself rather than from the surface coating or any extruded grain boundary phase.

These micrographs are representative of extensive examinations along the interfaces of three alumina specimens. The geometrical disposition of the interlocking configurations and

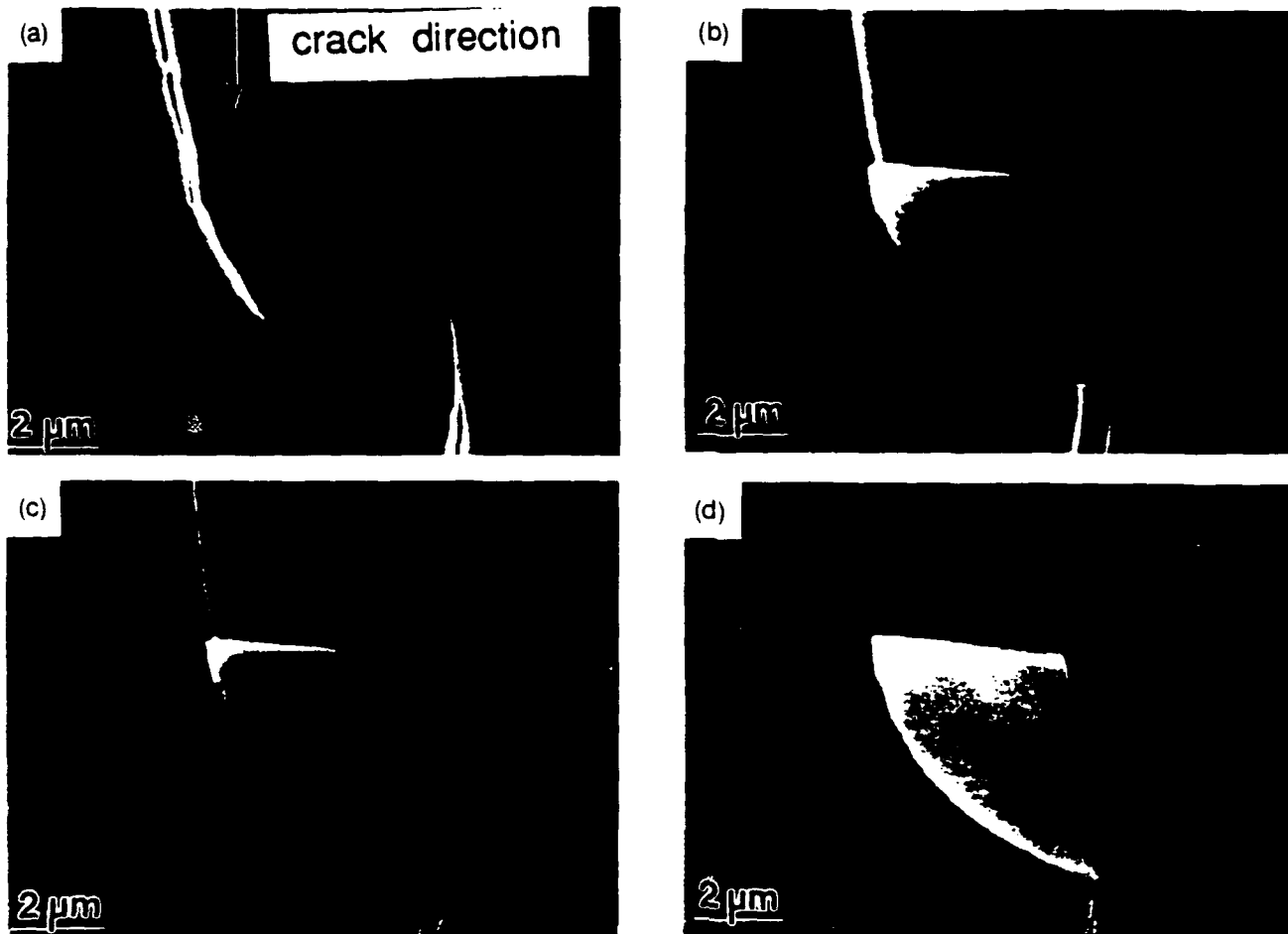


Fig. 7. SEM micrographs of grain facet: (a) after initial crack propagation ( $x = 170 \mu\text{m}$ ), showing bridge; (b) after further loading and cycling ( $n = 2200$  at  $2 \text{ Hz}$ ,  $K_{\text{max}} = 0.87$ ), with attendant propagation ( $x = 740 \mu\text{m}$ ); (c) after partial unload to  $K_{\text{A}} = 0.6T$ ; (d) at near-complete unload,  $K_{\text{A}} = 0.1T$ . Note near dislodgement of grain.

the associated frictional degradation varies considerably from point to point. We have given some indication of wedging at incompletely closed cracks, but this was never a large effect (residual opening always  $< 0.2$  that at full load).

As in earlier studies,<sup>2,27</sup> we find no evidence for detached frontal-zone microcrack clouds.

#### IV. Model

We noted from comparison of the indentation-strength data in Figs. 2 and 3 that it is the total number of cycles, rather than integrated time, that is the important independent variable in the lifetime characteristics. The reduction in strength of the specimens is modest,  $< 20\%$  in  $10^6$  cycles. In this context we may recall the apparent absence of any such effect in our earlier, preliminary study;<sup>2b</sup> here we are using an alumina with a larger grain size, hence more pronounced toughness curve, and have extended the data range. Although there was little indication of any comparable reduction in toughness in the long-crack data of Fig. 4, the same tests revealed an enhancement in crack extension in cyclic loading, Fig. 5. The apparent absence of fatigue effects in control static tests (Figs. 1 and 5) is especially pertinent, implying that the (shielded) crack-tip stress-intensity factor  $K_{\text{I}}$  in those cases must remain below the threshold in the  $v$ - $K_{\text{I}}$  curve. Taken together, these results would appear to imply a buildup of  $K_{\text{I}}$  during cyclic loading.

Several hypothetical mechanisms have been proposed to account for mechanical fatigue in cyclic loading. All may op-

erate in certain materials under certain conditions, but none have hitherto been directly confirmed. In the present study we may immediately eliminate potential contributions from frontal zones,<sup>2,14</sup> because our material is nontransforming and we see no microcracking clouds. Geometrical processes like asperity-induced secondary cracking,<sup>22</sup> and wedging by debris<sup>23,24,32</sup> and surface roughness<sup>22,24</sup> ("closure"), have also been proposed; and we do see minor secondary cracking and residual crack openings at our crack interfaces. However, whereas some of these mechanisms do allow for an increase in the mean crack-tip stress-intensity factor  $K_{\text{I}}$  in cyclic loading, none allows for an enhancement in the maximum  $K_{\text{I}}$ ,<sup>22</sup> as is necessary if the crack system is ever to rise above the velocity threshold.

The above SEM observations of frictional bridge activity suggest that the fatigue results may be due to a progressive degradation of the shielding stress-intensity factor. To quantify this, we begin by summarizing the more important elements of the toughness curve ( $T$ -curve) theory by grain-interlock bridging, referring the reader to earlier sources<sup>2b,36</sup> for greater detail. The crack-tip stress-intensity factor is

$$K_{\text{I}}(c) = K_{\text{A}}(c) + K_{\text{R}}(c) + K_{\text{B}}(c) \quad (1)$$

with  $K_{\text{A}}(c) = \psi \sigma_{\text{A}} c^{1/2}$  from the applied stress ( $\psi$  a geometry term),  $K_{\text{R}}(c) = \chi P/c^{1/2}$  from any residual contact stresses (here relevant only to indentation cracks,  $\chi$  a contact coefficient<sup>23,40</sup>), and  $-K_{\text{B}}(c)$  a microstructural shielding term (note  $K_{\text{B}} < 0$ ) from the bridging. This last term is a function of several microstructural parameters, among them the coeffi-

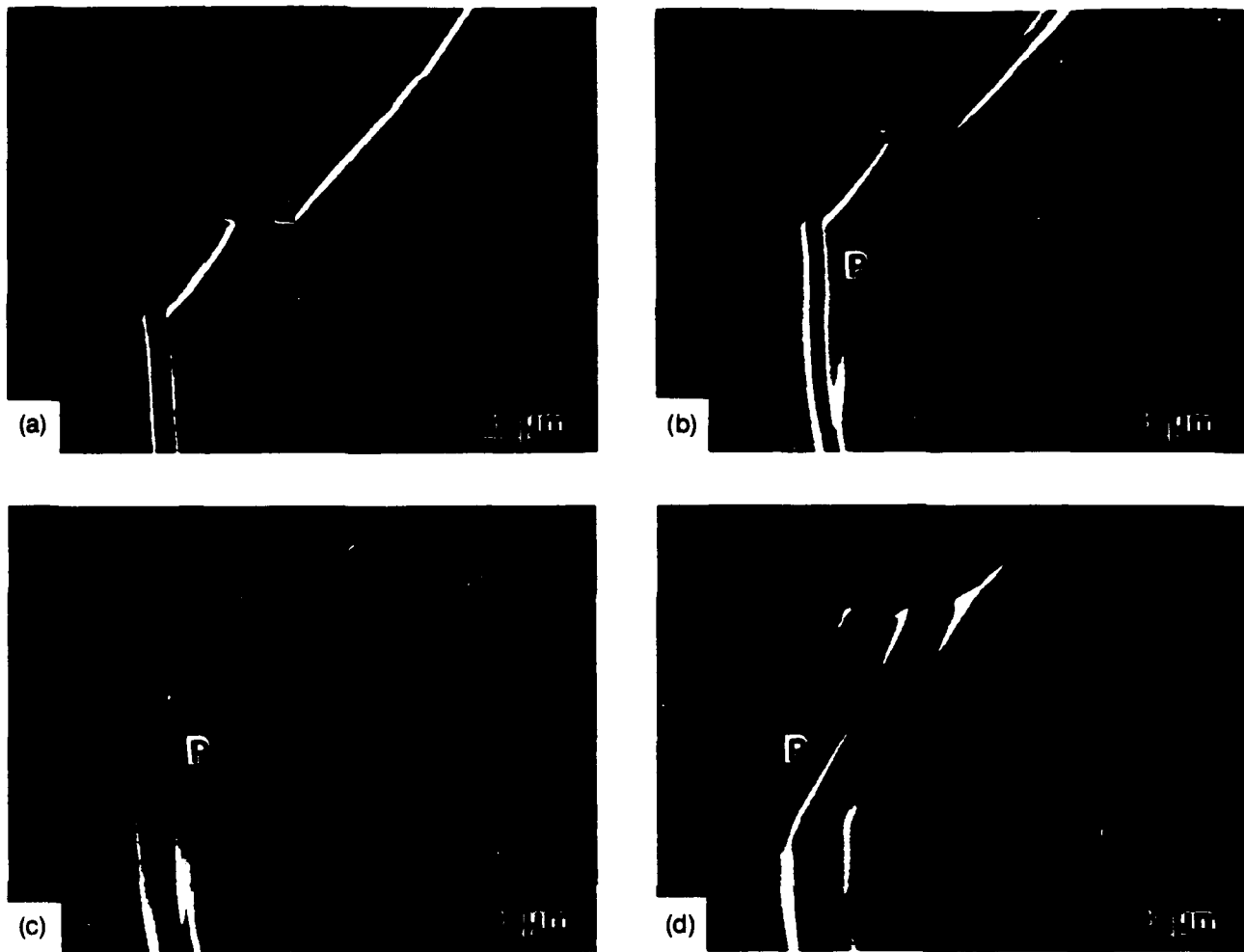


Fig. 8. SEM micrographs of frictional grain facet: (a) after initial crack propagation ( $x = 290 \mu\text{m}$ ); (b) after cycling ( $n = 7200$  at  $2 \text{ Hz}$ ,  $K_A^{\text{Max}} = 0.87$ ), with no propagation; (c) after loading and cycling ( $n = 54000$  at  $2 \text{ Hz}$ ,  $K_A^{\text{Max}} = 0.97$ ), with accompanying propagation ( $x = 850 \mu\text{m}$ ); (d) after static loading in degraded SEM vacuum for  $16 \text{ h}$  at  $K_A = 0.97$ , with further propagation ( $x = 2120 \mu\text{m}$ ). Note appearance of secondary crack at segment P in (b) as result of cycling only, and ultimate "flip" of this segment from right to left side of interface between (c) and (d).

cient of friction  $\mu$ , between sliding facets at grain interlock sites, i.e.,  $K_\mu = K_\mu(\mu, c)$ .<sup>4,30</sup> As indicated earlier, these microstructural parameters (and thence the  $T$ -curve) are calibrated from control indentation strength vs load data on our material in inert environments (Section II(1)). To accommodate environmentally-assisted slow crack growth we define a velocity function, based on thermal activation over atomically localized energy barriers<sup>33</sup>

$$v(G_*) = v_0 \sinh [(G_* - W_{\text{BEB}})/2\Gamma] \quad (W_{\text{BEB}} \leq G_* \leq W_{\text{BB}}) \quad (2)$$

with a threshold ( $v = 0$ ) at  $G_* = K^2(1 - \nu^2)/E = W_{\text{BEB}}/E$  denotes Young's modulus,  $\nu$  is Poisson's ratio, and  $W_{\text{BB}}$  and  $W_{\text{BEB}}$  are the reversible work to separate the grain boundary B-B under vacuum and in environmental species E, respectively. The adjustable parameters  $v_0$  and  $\Gamma$  are calibrated from strength data in water at constant stressing rates (Section II(1)). Equations (1) and (2) constitute the underlying basis of the theoretically generated plots for the appropriate stress vs life-time functions in Figs. 1 and 2.<sup>26</sup>

We propose that bridge degradation with increasing cycles is manifested primarily as a progressive reduction in the friction coefficient  $\mu(n)$ , hence in the magnitude of the shielding term  $-K_\mu(n)$ . Now for any given crack length  $c$  and applied stress  $\sigma_A$  we have  $\Delta K_* = \Delta K_\mu$  from Eq. (1). Then, since  $K_\mu < 0$  for bridging, we see that reduced shielding corre-

sponds to increased  $K_*(n)$ , in the manner of Fig. 11. Figure 12 is a plot of  $\mu(n)$  corresponding to the indentation cyclic data, obtained by treating  $\mu$  as an adjustable parameter and using a numerical algorithm to solve Eqs. (1) and (2) for a best fit at each point in Fig. 3.<sup>26</sup> We note that the reduction in  $\mu$  required to explain the strength degradation is not large, i.e.,  $< 25\%$  over the cycle range.

Using a smoothed function through the  $\mu(n)$  data in Fig. 12, we may now calculate  $K_\mu(n)$  from Eqs. (1) and (2) for cyclic loading in long cracks, and thence attempt to explain the data in Figs. 4 and 5. Accordingly, in Fig. 13 we plot  $-K_\mu(n)$  for the loading conditions pertaining to Figs. 5(a) and (b) (i.e., no static growth). The peak crack-tip field  $K_*^{\text{Max}}(n)$ , although starting below the threshold at  $W_{\text{BEB}}$ , attains this level after a critical interval, after which environmentally assisted slow crack growth can occur, consistent with the observations of nonzero  $\delta c/\delta t$  during the cyclic loading stages in Fig. 5. At the same time, the decrement  $\Delta K_\mu(n) = K_\mu(1) - K_\mu(n)$  is sufficiently small,  $< 0.25 \text{ MPa} \cdot \text{m}^{1/2}$ , over 150,000 cycles as to pass unnoticed at the interruption points in the  $T$ -curve plots in Fig. 4.

## V. Discussion

We have observed cyclic fatigue in an alumina ceramic which exhibits toughness-curve behavior by bridging. By

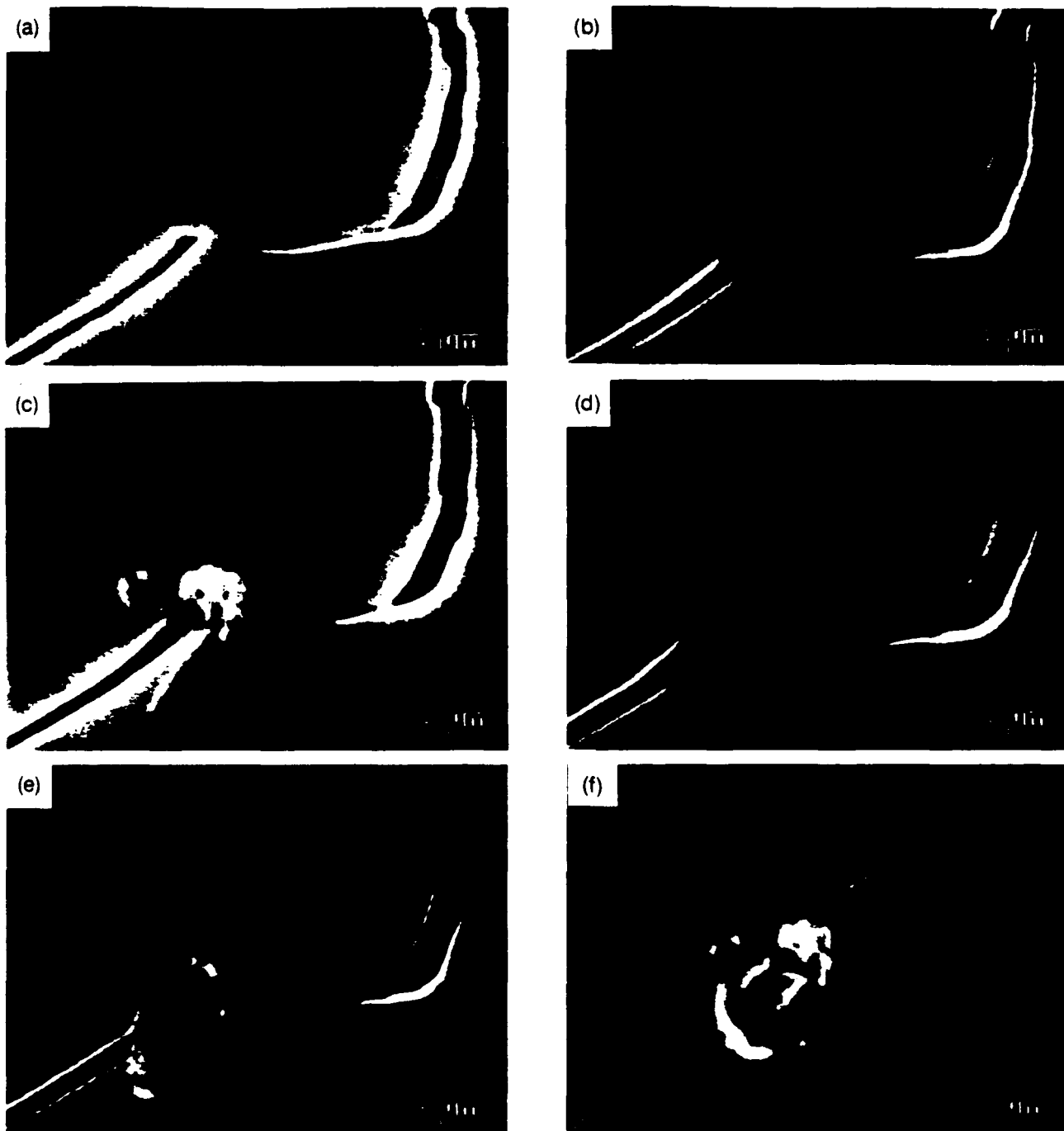


Fig. 9. SEM micrographs of frictional grain facet at various stages of cycling (all cycles at 2 Hz,  $K_{\text{I}}^{\text{Max}} = 0.857$ ): (a) after initial crack propagation ( $x = 610 \mu\text{m}$ ); (b) after  $n = 7000$ , with minor propagation ( $x = 630 \mu\text{m}$ ); (c) at  $n = 20000$  and additional propagation ( $x = 700 \mu\text{m}$ ); (d) at  $n = 27000$ , no propagation; (e) after  $n = 45000$ , no propagation; (f) total unload. Note cumulation of frictional debris at facet.

working below the static fatigue limit, i.e., below the crack velocity threshold, we are able to attribute the fatigue to true mechanical degradation of the material. On the basis of in situ observations of cracks during cyclic loading, we have proposed a new model for this degradation. Grain-interlock bridges that impart toughness can degrade in repeated unloading and reloading. The cumulation of "wear" debris at bridging sites suggests a specific mechanism of this degradation, whereby frictional tractions at sliding bridging grain boundary facets diminish progressively by persistent reversed sliding.

Notwithstanding the SEM observations, our model of a degraded frictional junction must be recognized as largely phe-

nomenological. There are some important questions that need to be answered if we are to obtain a proper understanding of the degradation process. Thus, what is the specific nature of the friction at the intergranular sliding interface? We note that the friction coefficient is of order unity in Fig. 12, not unusual for virgin interfaces in their pristine state.<sup>4</sup> What is the role of environment, particularly water, in this friction? There is evidence in the wear literature that the friction at contacting surfaces of alumina can indeed be modified by repeated sliding and, moreover, that this sliding produces debris from chemical reaction with environmental species.<sup>35</sup> Thus interfacial friction is a vital factor not only in toughness,<sup>4,36</sup> but also in lifetime.

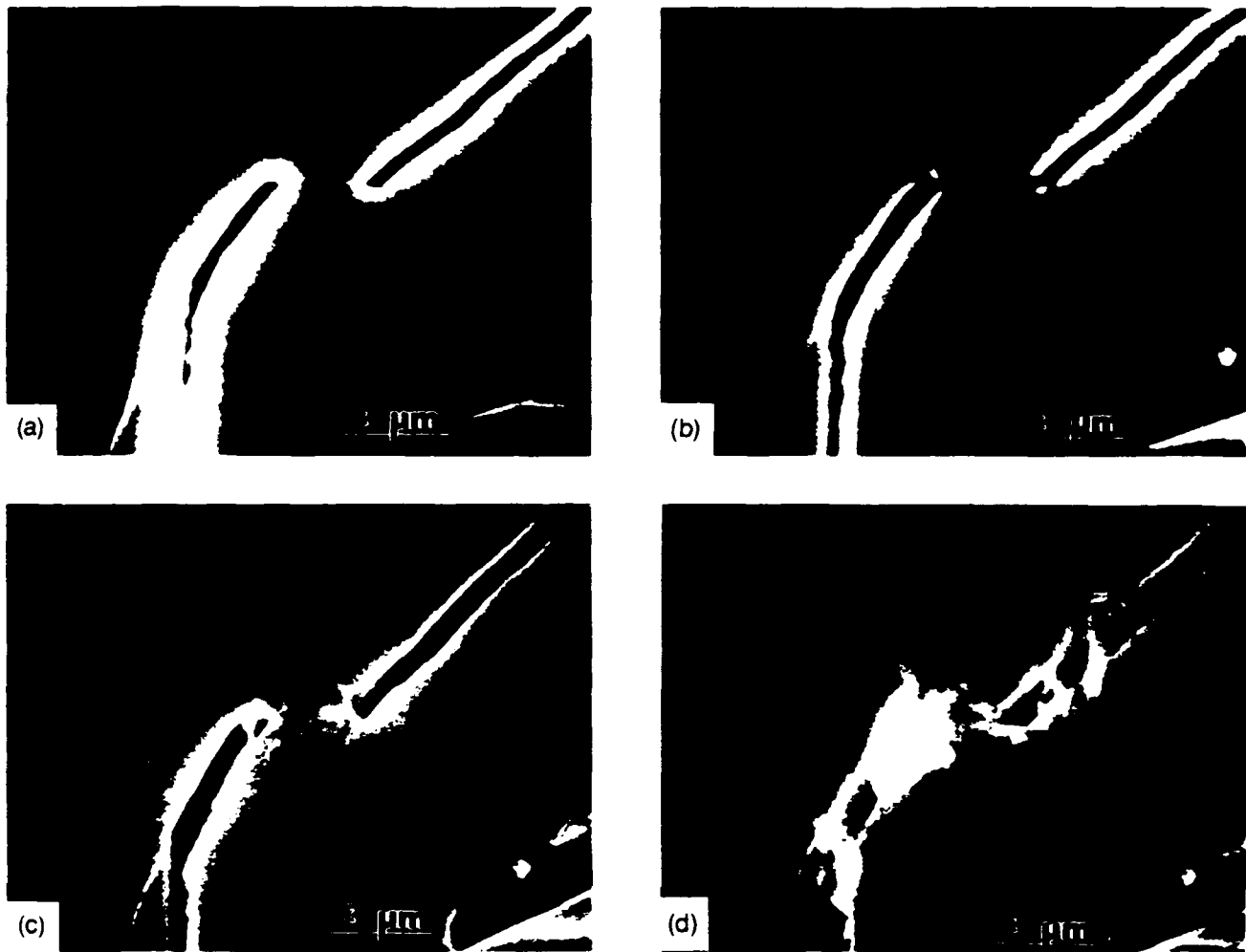


Fig. 10. SEM micrographs of another frictional grain facet at various stages of cycling (all cycles at  $K_{\text{I}}^{\text{Max}} = 0.857$ ): (a) after initial propagation ( $x = 820 \mu\text{m}$ ); (b) after  $n = 20000$  (2 Hz), crack propagation ( $x = 910 \mu\text{m}$ ); (c) after  $n = 45000$  (2 Hz), no propagation; (d) after  $n = 50000$  (10 Hz) in air, minor propagation ( $x = 930 \mu\text{m}$ ). Note debris.

The present study should be seen as a first step in identifying and modeling the mechanisms of cyclic fatigue in ceramics. The following aspects of the fatigue characterization warrant comment:

(i) *Generality of Model.* The indication is that our model, although formulated specifically from observations on alumina, may apply to nontransforming, bridging ceramics in general. Materials with more pronounced *T*-curves may therefore serve as better candidates for quantifying the degradation.

There is a need to rationalize the interrelations between short- and long-crack data; thus, a null effect in one test (e.g., Fig. 4) does not necessarily translate into a null effect in another (cf. Figs. 3 and 5), making general conclusions and extrapolations suspect in the absence of a proper degradation model.

(ii) *In Situ SEM.* Direct observations are a crucial element of any proper identification of the fatigue processes in ce-

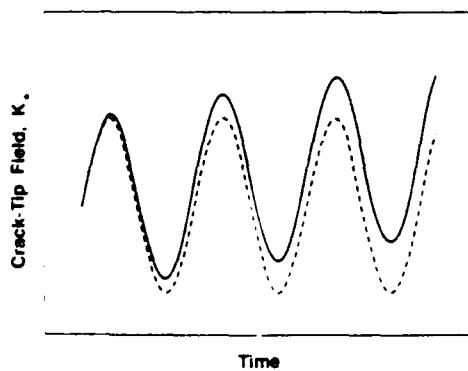


Fig. 11. Schematic illustrating possible cyclic fatigue mechanism due to frictional degradation of bridges. As shielding term diminishes with cycling, crack-tip  $K_{\text{I}}$  steadily increases (solid curve), until sufficient to take system above threshold on velocity curve.

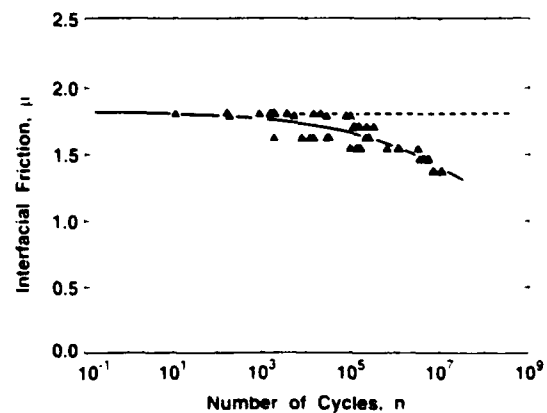


Fig. 12. Computed degradation of friction coefficient with number of cycles required to account for fatigue effect in data for alumina in Fig. 3. Dashed line is calibrated friction coefficient for monotonic loading.

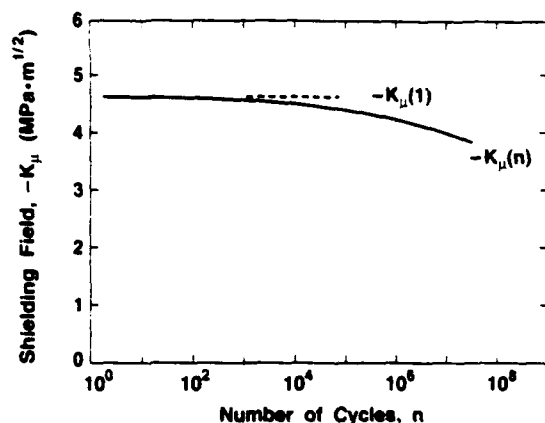


Fig. 13. Plot predicting decreasing bridging field,  $-K_u(n)$ , for cyclic loading in alumina.

ramic microstructures. This will inevitably be so in the more complex, multiphase ceramic composites, where multiple mechanisms may operate.

(iii) *Modeling.* With more positive confirmation of friction as the major microstructural variable in the degradation mechanism of cyclic fatigue, one might aim to express the model more closely in terms of documented frictional properties of interfaces, especially in regard to environmental interactions. This would open up the possibility of predetermining fatigue characteristics and tailoring interfaces for optimal resistance to degradation.

Finally, it is apparent that cyclic fatigue becomes an important design consideration in any application with moving ceramic parts. Such design will inevitably involve trade-offs. On the one hand, strong shielding is needed to promote flaw tolerance<sup>4</sup> and to enhance static fatigue limits.<sup>30</sup> It is the potential degradation of this same shielding that has important implications for fatigue.

**Acknowledgments:** We thank Y.-W. Mai for discussions, J. F. Kelly and D. E. Roberts for assistance with the experiments, and S. Derby for machining the specimens. Thanks are also due to J. Sibold of Coors Ceramics for providing the alumina.

## References

- Y.-W. Mai and B. R. Lawn, "Crack Stability and Toughness Characteristics in Brittle Materials," *Annu. Rev. Mater. Sci.*, **16** 415-39 (1986).
- P. L. Swanson, C. J. Fairbanks, B. R. Lawn, Y.-W. Mai, and B. J. Hockey, "Crack-Interface Grain Bridging as a Fracture Resistance Mechanism in Ceramics: I. Experimental Study on Alumina," *J. Am. Ceram. Soc.*, **70** [4] 279-89 (1987).
- Y.-W. Mai and B. R. Lawn, "Crack-Interface Grain Bridging as a Fracture Resistance Mechanism in Ceramics: II. Theoretical Fracture Mechanics Model," *J. Am. Ceram. Soc.*, **70** [4] 289-94 (1987).
- S. J. Bennison and B. R. Lawn, "Role of Interfacial Grain-Bridging Sliding Friction in the Crack-Resistance and Strength Properties of Non-Transforming Ceramics," *Acta Metall.*, **37** [10] 2659-71 (1989).
- L. S. Williams, "Stress Endurance of Sintered Alumina," *Trans. Br. Ceram. Soc.*, **55** [5] 287-312 (1956).
- R. Sedlacek and F. A. Halden, "Static and Cyclic Fatigue of Alumina," pp. 211-20 in *Structural Ceramics and Testing of Brittle Materials*. Edited by S. J. Acquaviva and S. A. Bortz. Gordon and Breach, New York, 1967.
- B. K. Sarkar and T. G. T. Glinn, "Fatigue Behavior of High Alumina Ceramics," *Trans. Br. Ceram. Soc.*, **69** [5] 199-203 (1970).
- D. A. Krohn and D. P. H. Hasselman, "Static and Cyclic Fatigue Behavior of a Polycrystalline Alumina," *J. Am. Ceram. Soc.*, **55** [4] 208-11 (1972).
- A. G. Evans and E. R. Fuller, "Crack Propagation in Ceramic Materials Under Cyclic Loading Conditions," *Metall. Trans.*, **5** [1] 27-33 (1974).
- S. Horibe and M. Sumita, "Fatigue Behavior of Sintered SiC: Temperature Dependence and Effect of Doping with Aluminum," *J. Mater. Sci.*, **23** [9] 3305-13 (1988).
- L. Ewart and S. Suresh, "Crack Propagation in Ceramics under Cyclic Loads," *J. Mater. Sci.*, **22** [4] 1173-92 (1987).
- M. J. Reece, F. Guu, and M. F. R. Sammur, "Cyclic Fatigue Crack Propagation in Alumina under Direct Tension-Compression Loading," *J. Am. Ceram. Soc.*, **72** [2] 348-52 (1989).
- R. H. Dauskardt, W. Yu, and R. O. Ritchie, "Fatigue Crack Propagation in Transformation-Toughened Zirconia Ceramic," *J. Am. Ceram. Soc.*, **70** [10] C-248-C-252 (1987).
- R. H. Dauskardt, D. B. Marshall, and R. O. Ritchie, "Cyclic Fatigue Crack Propagation in Ceramics: Behavior in Overaged and Partially-Stabilized MgO-Zirconia," in *Fracture Mechanics/Structural Ceramics*. Materials Research Society, Philadelphia, PA, in press.
- T. Kawakubo and K. Komeya, "Static and Cyclic Fatigue Behaviour of a Sintered Silicon Nitride at Room Temperature," *J. Am. Ceram. Soc.*, **70** [6] 400-405 (1987).
- M. Masuda, T. Soma, M. Matsui, and I. Oda, "Cyclic Fatigue of Sintered Silicon Nitride," *Ceram. Eng. Sci. Proc.*, **9** [9-10] 1371-82 (1988).
- M. Masuda, T. Soma, and M. Matsui, "Cyclic Fatigue Behaviour of Silicon Nitride Ceramics," *J. Eur. Ceram. Soc.*, **6** [4] 253-58 (1990).
- C.-W. Li, D. J. Lee, J. Yamanis, and I. Palley, "Cyclic Fatigue Properties of Silicon Nitride with Strong R-Curve Behavior," presented at the 92nd Annual Meeting of the American Ceramic Society, Dallas, TX, 1990.
- J. T. Beals and I. Bar-On, "Fracture Toughness and Fatigue Crack Propagation of Silicon Nitride with Two Different Microstructures," presented at the 14th Annual Conference on Composites and Advanced Ceramics, Cocoa Beach, FL, January 1990.
- C.-W. Li and J. Yamanis, "Super-Tough Silicon Nitride with R-curve Behavior," *Ceram. Eng. Sci. Proc.*, **10** [7-8] 632-45 (1989).
- D. Lewis, "Cyclic Mechanical Fatigue in Ceramic-Ceramic Composites—An Update," *Ceram. Eng. Sci. Proc.*, **4** [9] 874-81 (1983).
- A. G. Evans, "Fatigue in Ceramics," *Int. J. Fract.*, **16** [6] 485-98 (1980).
- S. Suresh and J. R. Brockenbrough, "Theory and Experiments of Fracture in Cyclic Compression: Single-Phase Ceramics, Transforming Ceramics and Ceramic Composites," *Acta Metall.*, **35** [6] 1455-70 (1988).
- R. O. Ritchie, "Mechanisms of Fatigue Crack Propagation in Metals, Ceramics and Composites: Role of Crack Tip Shielding," *Mater. Sci. Eng.*, **A103**, 15-28 (1988).
- H. Frei and G. Grathwohl, "The Fracture Resistance of High Performance Ceramics by In Situ Experiments in the SEM" (in Ger.), *Beitr. Elektronenmikroskop. Direktabb. Oberfl.*, **22**, 71-78 (1989).
- S. Lathabai, Y.-W. Mai, and B. R. Lawn, "Cyclic Fatigue Behavior of an Alumina Ceramic with Crack-Resistance Curves," *J. Am. Ceram. Soc.*, **72** [9] 1760-63 (1989).
- J. Rödel, J. F. Kelly, and B. R. Lawn, "In Situ Measurements of Bridged Crack Interfaces in the SEM," *J. Am. Ceram. Soc.*, **73** [11] 3313-18 (1990).
- J. Rödel, J. F. Kelly, M. R. Stoudt, and S. J. Bennison, "A Loading Device for Fracture Testing of Compact Tension Specimens in the SEM," *Scanning Microsc.*, in press.
- D. B. Marshall, "An Improved Biaxial Flexure Test for Ceramics," *Am. Ceram. Soc. Bull.*, **59** [5] 551-53 (1980).
- S. Lathabai and B. R. Lawn, "Fatigue Limits in Noncyclic Loading of Ceramics with Crack-Resistance Curves," *J. Mater. Sci.*, **24** [12] 4298-306 (1989).
- Annual Book of ASTM Standards*, Vol. 3.01, E-399-83. American Society for Testing and Materials, Philadelphia, PA, 1989.
- C. J. Beevers, K. Bell, R. L. Carlson, and E. A. Starke, "A Model for Fatigue Crack Closure," *Eng. Fract. Mech.*, **19** [1] 93-100 (1984).
- K.-T. Wan, S. Lathabai, and B. R. Lawn, "Crack Velocity Functions and Thresholds in Brittle Solids," *J. Eur. Ceram. Soc.*, **6** [4] 259-68 (1990).
- D. H. Buckley, *Surface Effects in Adhesion, Friction, Wear, and Lubrication*. Ch. 6. Elsevier, Amsterdam, Netherlands, 1981.
- X. Dong, S. Jahanmir, and S. M. Hsu, "Tribological Characteristics of  $\alpha$ -Alumina at Elevated Temperatures," *J. Am. Ceram. Soc.*, **74** [5] 1036-44 (1991).
- D. B. Marshall and A. G. Evans, "Failure Mechanisms in Ceramic-Fiber/Ceramic-Matrix Composites," *J. Am. Ceram. Soc.*, **68** [5] 225-31 (1985).

**MICROSTRUCTURE, TOUGHNESS CURVES AND MECHANICAL PROPERTIES  
OF ALUMINA CERAMICS**

**Stephen J. Bennison, Jürgen Rödel, Srinivasarao Lathabai,  
Prapaipan Chantikul, Brian R. Lawn**

**Ceramics Division  
National Institute of Standards and Technology  
Gaithersburg, MD 20899**

**September 1990**

**NATO Advanced Research Workshop on Toughening Mechanisms  
in Quasi-Brittle Materials, July 16-20, 1990, Northwestern  
University. To be published by Kluwer Academic  
Publishers, Dordrecht, The Netherlands.**

## MICROSTRUCTURE, TOUGHNESS CURVES AND MECHANICAL PROPERTIES OF ALUMINA CERAMICS

STEPHEN J. BENNISON, JÜRGEN RÖDEL, SRINIVASARAO LATHABAI,  
PRAPAIPAN CHANTIKUL, BRIAN R. LAWN  
Ceramics Division  
National Institute of Standards and Technology  
Gaithersburg, MD 20899, USA

**ABSTRACT.** The microstructural variables that determine the toughness (T-curve) characteristics of alumina and other structural ceramics are considered. Alumina ceramics gain their toughness from shielding by grain-interlock bridging at the interface behind the cra tip. A general fracture mechanics formalism for describing the bridging is outlined in terms of desirable microstructural elements, such as weak internal boundaries, high internal stress, coarse microstructure. The T-curve imparts the quality of flaw tolerance to the strength properties. We examine this quality, under both inert and interactive environmental conditions, monotonic and cyclic loading, using indentation flaws. In situ observations of bridging sites during loading in the scanning electron microscope provide insight into the bridge degradation micromechanisms. Finally, short-crack properties, spontaneous microcracking and wear degradation, are examined in light of the bridging model. It is concluded that design with ceramics may require certain tradeoffs, long vs short cracks, high toughness vs flaw tolerance, etc. The key to optimal performance in ceramics rests with microstructural processing for specific properties.

### 1. INTRODUCTION

It is now well established that many monophase ceramics exhibit the property of rising fracture resistance or toughness with crack extension (R-curve or T-curve) [1-14]. The magnitude of the toughness increase can be respectable, in some cases approaching a factor of five or so over extensions of several millimeters or hundreds of grain dimensions.

Toughness-curve characteristics dictate mechanical behavior. For example, the associated stabilizing effect on crack growth confers the



quality of "damage tolerance" [5,9,12-14], i.e. insensitivity of strength to flaw size. This leads to the highly appealing prospect of a well-defined, flaw-insensitive stress for engineering design. However, the cost of gaining flaw tolerance is inevitably the sacrifice of toughness in the domain of "short" cracks, where properties like thermal shock and wear resistance are decided. Specifying the T-curve for optimal performance of ceramics involves certain tradeoffs.

A substantial body of evidence now exists to demonstrate that the principal mechanism of T-curve behavior in alumina and other ceramics is grain-localized bridging at the crack interface behind the advancing tip [1-14]. Bridging grains exert frictional closure forces across the crack walls and thereby shield the tip from the applied stress-intensity field [9,13,14]. The cumulation of bridging tractions over the crack interface with continued propagation leads to a rising toughness curve.

The magnitude and shape of the resultant T-curve are sensitive to the microstructure: grain size and shape [4,5,13,15]; internal residual stresses (e.g. thermal expansion anisotropy) in noncubic materials [13], especially as they may be intensified by incorporation of a second phase [16]; grain boundary energy [13]; all these are important players in the toughness. This strong influence of microstructure leads to the potential for manipulation of crack-resistance properties through controlled processing. Opportunities for the development of improved structural ceramics thereby rest with the development of novel microstructures and fabrication strategies that exploit the operative toughening micromechanisms.

In the present paper we review the toughness-curve phenomenon in ceramics, with alumina as a model system. First a microstructure-based model for grain bridging is discussed. Second, we examine the role of the T-curve in determining different mechanical properties. Primary consideration is given to strength properties [9,12,13,15,17,18], in both inert and interactive environments, and under quasistatic and (cyclic) fatigue loading. This is the domain of "intermediate" crack sizes (corresponding to the rising portion of the T-curve). Additional consideration is given to microfracture-induced wear properties [19], the domain of "short" cracks. Noting further that most conventional toughness evaluations are made in specimens with "long" cracks, we emphasize the importance of identifying any specific mechanical property with the proper crack-size domain. Then we present results of more recent, in situ observations of grain bridging in the scanning electron microscope [20]. Measurements of crack profiles demonstrate directly the nature of the closure forces exerted by the bridges on the cracks, and reveal details of fatigue processes. Finally, the prospects of innovative microstructural processing for optimizing toughness properties of ceramics, including composite systems, is discussed.

## 2. MICROSTRUCTURAL FRACTURE MECHANICS MODEL

### 2.1 GENERAL EQUILIBRIUM REQUIREMENTS

Begin by defining a net crack-tip stress-intensity factor condition for a crack subject to a superposed tensile loading field,  $K_A(c)$ , flaw-localized residual nucleation field,  $K_r(c)$ , and microstructure-associated field,  $K_\mu(c)$  [14]:

$$K_* (c) = K_A (c) + K_r (c) + K_\mu (c). \quad (1)$$

Equilibrium obtains when  $K_*$  just balances the intrinsic toughness associated with the creation of crack surfaces:

$$K_* = T_0. \quad (2)$$

This last requirement can be restated by considering  $K_A$  and  $K_r$  in Eq. 1 as part of the net effective applied mechanical field,  $K_A$ , and  $K_\mu = -T_\mu$  as part of the internal toughness, i.e.

$$\begin{aligned} K_A (c) &= K_A (c) + K_r (c) \\ &= T_0 + T_\mu (c) = T(c). \end{aligned} \quad (3)$$

The net toughness function  $T(c)$  constitutes the so-called T-curve, the K-field equivalent of the R-curve.

An alternative formulation for the crack-tip conditions may be given in terms of the mechanical-energy-release rates [14]. Write, in analogy to Eq. (3),

$$G_A (c) = R_0 + R_\mu (c) = R(c) \quad (4)$$

with  $R$  the crack-resistance energy. The Griffith requirement for equilibrium is then

$$G_* = R_0 = 2\gamma_b \quad (5)$$

where  $\gamma_b$  is the fracture surface energy of the body in inert atmospheres. For intergranular fracture  $\gamma_b$  incorporates the grain boundary energy. By defining the connecting relations [14]

$$K_A = (G_A E')^{1/2} \quad (6a)$$

$$K_* = (G_* E')^{1/2} \quad (6b)$$

with  $E' = E/(1 - \nu^2)$  in plane strain,  $E$  Young's modulus and  $\nu$  Poisson's ratio, we identify the intrinsic toughness  $T_0 = (R_0 E')^{1/2}$  in Eq. 2.

## 2.2 MICROSTRUCTURAL STRESS-INTENSITY FACTOR

Microstructural properties are introduced into the formalism in Sect. 2.1 via  $T_\mu(c)$  in Eq. 3. For materials that toughen by bridging we need to determine the micromechanics of grain interlock and subsequent pullout [13]. A subsidiary element of the process is the segmentation of the primary crack front at incipient bridging grains, driven by conflicting tendencies to follow weak intergranular or interphase boundaries and local thermal expansion anisotropy tensile stresses. For the present we focus on simplistic, idealized structures in monophase, noncubic ceramics.

Consider a half-penny crack, radius  $c$ , evolving in a rectangular microstructure, Fig. 1. The submicroscopic crack is assumed to begin its life as a flaw in a region of most favorable internal tension,  $+\sigma_R$ , and thereafter to intersect bridging grains as it expands radially outward. The grains which act as bridges are assumed to be those with compressive components of the residual stress field,  $-\sigma_R$ , at transverse facets. The problem is then to determine the closure stresses exerted by the bridges in terms of crack-wall separation.

These stresses are governed by Coulombic friction that restricts the separation of bridging grain facets. At initial separation the bridging grains debond along the constrained facets and then "pull out" until final "rupture" at some critical rupture strain. The debond stage consumes relatively little energy, so the constitutive relation between closure stress  $p$  and (half-) crack-opening displacement  $u$  for a single bridge may be written exclusively in terms of a simple tail-dominated pullout relation [8,13]:

$$p(u) = p_M(1 - u/u_\ell) \quad (7)$$

where  $p_M$  is the maximum resistance stress (at  $u = 0$ ) and  $u_\ell$  is the wall-wall half-displacement at bridge-matrix disengagement (at  $p = 0$ ). The essential material quantities in Eq. 7 are contained in the parameters [13]:

$$u_\ell = \epsilon_\ell \ell / 2 \quad (8a)$$

$$p_M = (\bar{\alpha}_\lambda \alpha_L \epsilon_\ell \mu \sigma_R) (1 - 1/2\alpha_d^2) \quad (8b)$$

with  $\ell$  grain size,  $\mu$  friction coefficient,  $\sigma_R$  internal residual stress. The  $\alpha$  and  $\epsilon$  terms are dimensionless constants for geometrically similar microstructures:

$$\alpha_\lambda = \lambda / \ell \quad (9a)$$

$$\alpha_L = L / \ell \quad (9b)$$

$$\alpha_d = d / \ell \quad (9c)$$

$$\epsilon_\ell = 2u_\ell / \ell \quad (9d)$$

with  $\lambda$  the bridge cross-sectional perimeter,  $L$  the embedded grain length,  $d$  the bridge spacing. In Eq. 8 only the pullout distance  $u_\ell$  depends on the grain size; the closure stress  $p_M$  is scale-invariant.

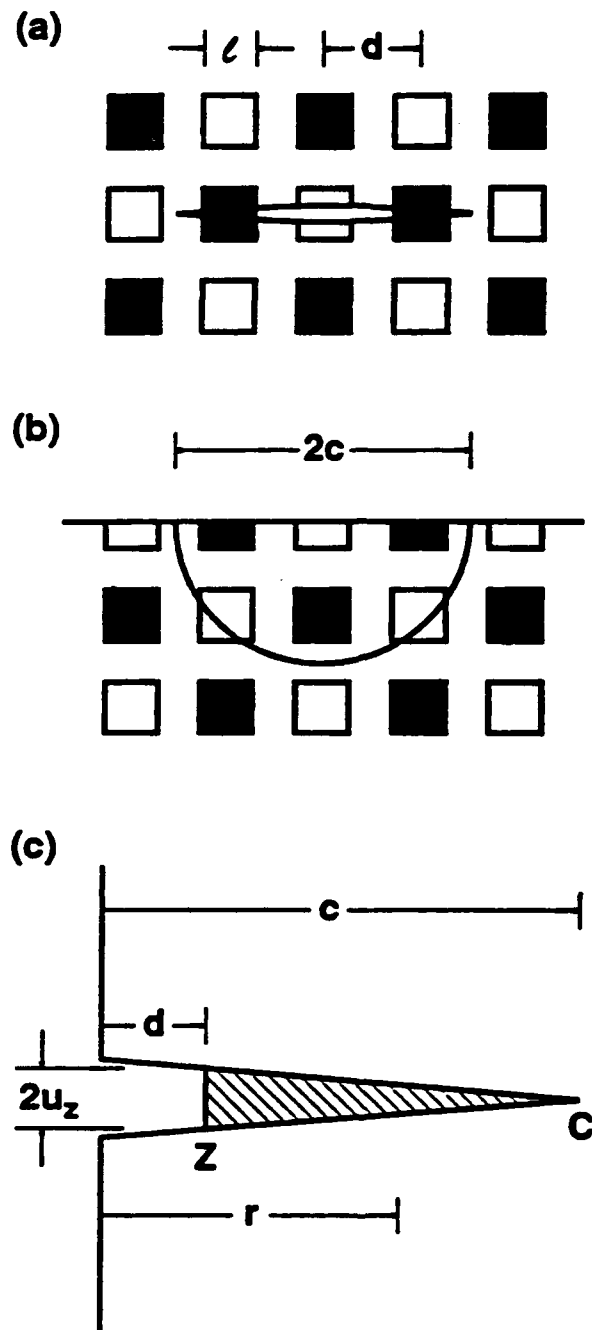


Figure 1. Microstructural model of grain bridging for penny crack in microstructure with bridging grains (squares): (a) in-plane view; (b) out-of-plane view. (c) Coordinate system for bridging zone. Crack initiates in residual tensile field at  $c \leq d$ , and thereafter extends into bridging field.

The toughening associated with the bridging is calculated according to crack-size domain, as follows [8,9,13,17]:

(i) Small Cracks ( $c \leq d$ ), no bridge intersections. Within this region the crack experiences only the matrix tensile stress,  $+\sigma_R$ . Assuming this field to be uniform, we obtain

$$T_\mu(c) = -K_\mu(c) = -\psi\sigma_R c^{1/2} \quad (10)$$

where  $\psi$  is a geometry dependent coefficient. This  $K_\mu$  term is not expected to be present in straight cracks, where tensile and compressive facets average to zero stress along the crack front.

(ii) Intermediate Cracks ( $c \geq d$ ,  $0 \leq u \leq u_p$ ), bridges intersected. There are two contributions to the toughness in this region,  $T_\mu(c) = T'_\mu(c) + T''_\mu(c)$ . The first is an opening post-intersection component from the persistent residual tensile stress field from (i) above,

$$T'_\mu(c) = -\psi\sigma_R c^{1/2} [1 - (1 - \alpha_d^2 \ell^2 / c^2)^{1/2}]. \quad (11)$$

The second is a countervailing closing component from the bridging tractions, Eq. 7. This contribution is most readily evaluated as a J-integral,

$$\begin{aligned} R'_\mu(u) &= 2 \int_0^{u_z} p(u) du \\ &= 2p_H u_z (1 - u_z / \epsilon_p \ell). \end{aligned} \quad (12)$$

The displacement  $u_z = u_z(c)$  at the edge of the bridging zone (i.e. first bridge intersection at  $c = d$ , Fig. 1c) may be evaluated approximately from the Sneddon crack profile relation ("weak shielding" approximation)

$$u_z(c) = (\psi K_A / E') [(c^2 - \alpha_d^2 \ell^2) / c]^{1/2}. \quad (13)$$

The toughness  $T''_\mu(c)$  may be determined from the crack resistance  $R'_\mu(c)$  by eliminating  $G_A$  and  $K_A$  from Eqs. 2-5:

$$T''_\mu(c) = E'^{1/2} ([R'_\mu(c) + G_*]^{1/2} - G_*^{1/2}). \quad (14)$$

This relation is implicit in  $T''_\mu$ , so Eqs. 3, 11-14 must be solved simultaneously.

(iii) Long Cracks ( $c \gg d$ ,  $u_z \geq u_p$ ), bridging zone now of constant size and translating with the advancing crack. In this limit,  $T'_\mu \rightarrow 0$  and the steady-state toughening increment is evaluated from Eq. 14 with  $R'_\mu = p_H \epsilon_p \ell / 2$  from Eq. 12.

## 2.3 ENVIRONMENTALLY-ENHANCED KINETIC CRACK GROWTH

Environmentally-assisted "slow" crack growth in ceramics manifests itself as a finite "lifetime" at sustained stress. The slow crack growth is characterized by a crack velocity function,  $v(K)$  or  $v(G)$ . The fundamental form of the  $v(G)$  function is [17]

$$v(G_*) = v_0 \sinh[(G_* - 2\gamma_{BE})/2\Gamma] \quad (2\gamma_{BE} \leq G_* \leq 2\gamma_B) \quad (15)$$

where  $\gamma_{BE}$  is the fracture surface energy in the presence of the reactive environment, and  $v_0$  and  $\Gamma$  are intercept and slope parameters. This function has provision for a threshold at  $G_* = 2\gamma_{BE}$ , and dynamic velocity at  $G_* = 2\gamma_B$ .

Combining  $v = dc/dt$  in Eq. 15 with the relations in Sects. 2.1 and 2.2 then yields a differential equation in  $c(t)$  for any specified time-dependent applied stress.

## 3. STRENGTH: INDENTATION FLAWS

Now let us examine the influence of the T-curve on strength properties. We reemphasize that strength pertains specifically to cracks in the intermediate-crack domain, i.e. to the rising portion of the T-curve. To place this into proper context, we again point out that most traditional toughness evaluations are made in long-crack specimens. Later we shall address short-crack properties, viz. spontaneous microcracking and wear.

### 3.1 INERT STRENGTH

The inert strength of a ceramic material is determined by the condition for instability under essentially equilibrium conditions:  $dK_*(c)/dc \geq 0$  at  $K_*(c) = T_0$  in Eq. 2 or, alternatively,  $dK_A(c)/dc \geq dT(c)/dc$  at  $K_A(c) = T(c)$  in Eq. 3 [14]. The latter defines the familiar "tangency" construction for toughness curves. The form of  $K_*$  and  $K_r$  in Eq. 1 is determined by the relevant testing geometry and flaw type.

In this section we consider controlled indentation radial cracks formed at contact load  $P$  and subsequently subjected to uniform tensile stress  $\sigma_*$ :

$$K_r = \chi P/c^{3/2} \quad (16a)$$

$$K_A = \psi \sigma_* c^{1/2} \quad (16b)$$

with  $\chi$  a parameter defining the intensity of the residual contact field [22] and  $\psi$  as defined in Eq. 10. Indentation cracks enable one to "calibrate" T-curve parameters with maximum efficiency and, moreover, take us close to the crack-size realm of natural flaws [12,13,23].

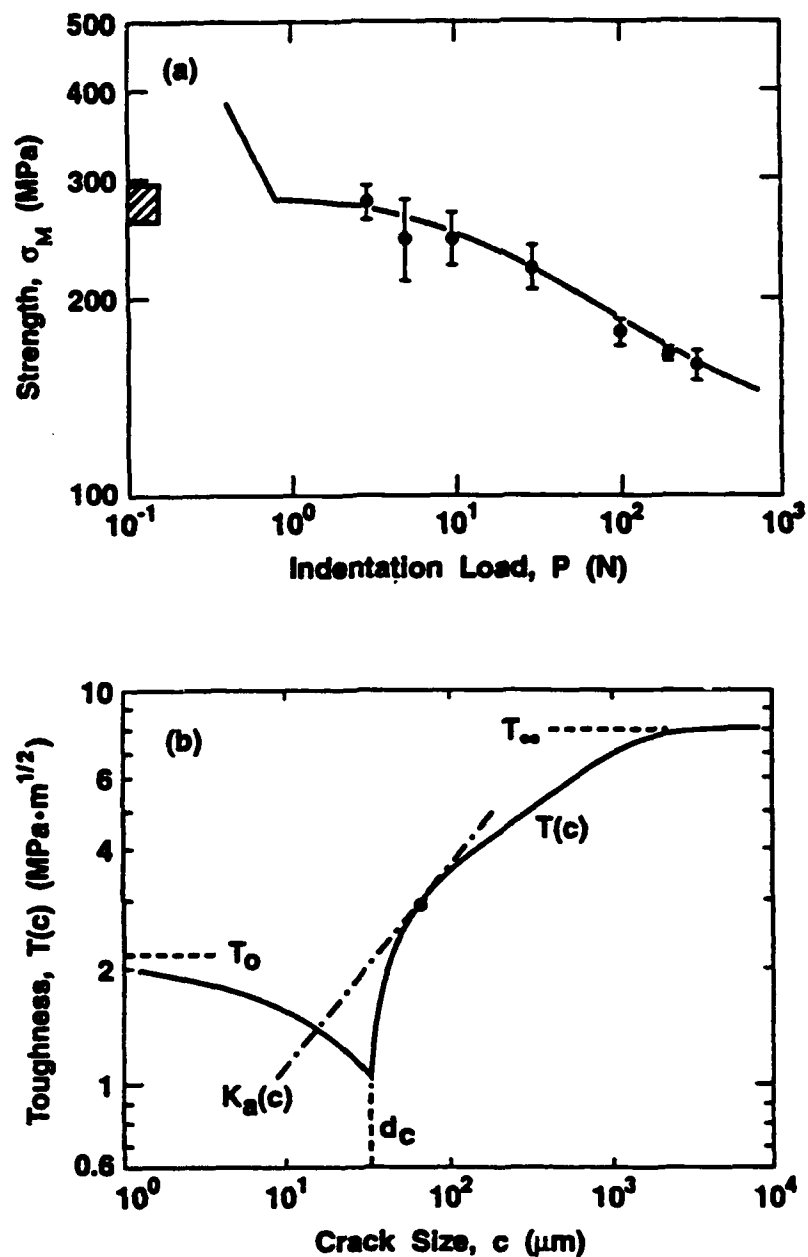


Figure 2. (a) Inert strength as function of Vickers indentation load for a reference single-phase polycrystalline alumina, grain size  $l = 23 \mu\text{m}$ , tested in dry silicone oil. Shaded region at left represents breaks from natural flaws. Solid curve is fit of bridging T-curve formalism. (b) Deconvoluted T-curve. Dashed line is  $K_a(c)$  tangency condition for failure from natural flaw ( $\chi = 0$ ).

Fig. 2a shows inert strength vs indentation load data for a "reference" alumina with single phase and equiaxed microstructure, grain size  $l = 23 \mu\text{m}$ . We note the strong tendency to a plateau at low  $P$ . These data reflect the quality of flaw tolerance alluded to earlier. The solid curve is a data fit obtained by adjusting the microstructural parameters  $\mu$ ,  $\sigma_R$ ,  $\epsilon$ , and  $\alpha$  terms in Eq. 8, using a numerical algorithm [13,17]. From this fit we deconvolute the T-curve shown in Fig. 2b, using Eqs. 10-14. Note that the intrinsic material toughness initially diminishes from  $T = T_0$  with crack size, due to the action of the residual tensile field at  $c \leq d$  (Fig. 1). After the first bridge intersection the toughness rises sharply as a result of dominant frictional restraining stresses from the grain pullout. This rise continues as the bridging zone expands with crack extension, until the first bridge ultimately ruptures. At this point the bridging zone translates with the crack, and a steady state obtains at  $T = T_\infty$ .

The T-curve strongly stabilizes the crack growth en route to failure. For simplicity, consider a natural flaw without any residual stress ( $\chi = 0$ ). Then  $K_A = K_\infty \propto c^{1/2}$  in Eqs. 3, 16a. We show this applied loading function at the tangency condition in Fig. 2b. Suppose the initial size of the flaw lies to the right of the dashed line somewhere on the diminishing branch of the T-curve. Then at a certain point in the loading the flaw "pops in" and arrests on the rising branch of the T-curve. Further load is needed to extend the crack in stable equilibrium up the T-curve, until the configuration at  $dK_A(c)/dc \geq dT(c)/dc$  is attained, whence the specimen fails. It is this precursor stability characteristic that is responsible for the flaw tolerance characteristic in Fig. 2a: the critical failure condition depends on the final, not the initial, flaw size.

The "calibrated" T-curve contains all the necessary ingredients to predict the effects of variations in microstructural characteristics on the toughness characteristics. We return to this prospect in Sect. 5.

### 3.2 RATE-DEPENDENT STRENGTH

Now let us consider the deleterious, rate-dependent influence of water-containing environments on strength, in accordance with the  $v(G)$  velocity function of Eq. 15. We again focus on indentation flaws.

Strength data for the same alumina as in Fig. 2, but now tested in water at a fixed indentation load, are shown in Fig. 3 as a function of stressing rate. The solid curve through the data is a best fit from numerical solutions of the differential equation embodied in Eq. 15 for the time to grow the crack from its initial (stable) state to final instability, the "lifetime". This is done using the T-curve calibration from Sect. 3.1 and adjusting the crack velocity parameters  $v_0$  and  $\Gamma$  [17]. Note the asymptotic limits: at fast stressing rates to the inert strength; at slow rates to a "fatigue limit".

This fitting procedure allows us to deconvolute velocity functions from the strength data. We plot the results from such deconvolutions in Fig. 4 [17]. The dashed curve at left represents the fundamental



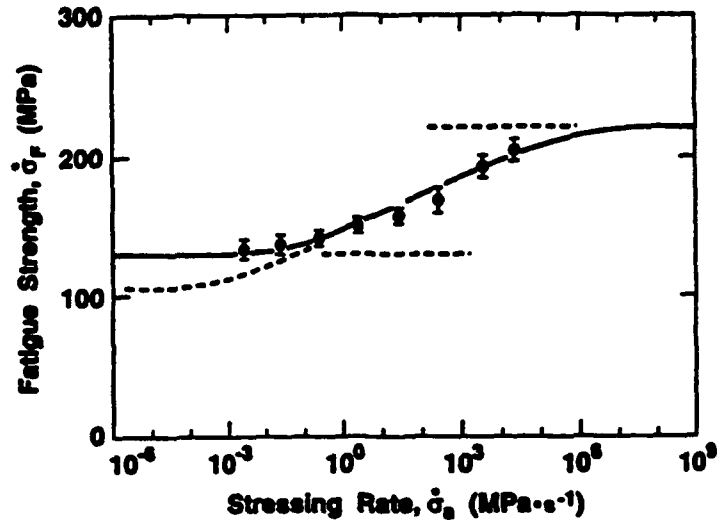


Figure 3. Strength of same alumina as Fig. 2, but as function of stressing rate for tests in water, Vickers indentations at  $P = 30$  N. Upper horizontal line is inert strength limit from Fig. 2, lower line is fatigue limit. Dashed curve is equivalent response for hypothetical material without crack velocity threshold.

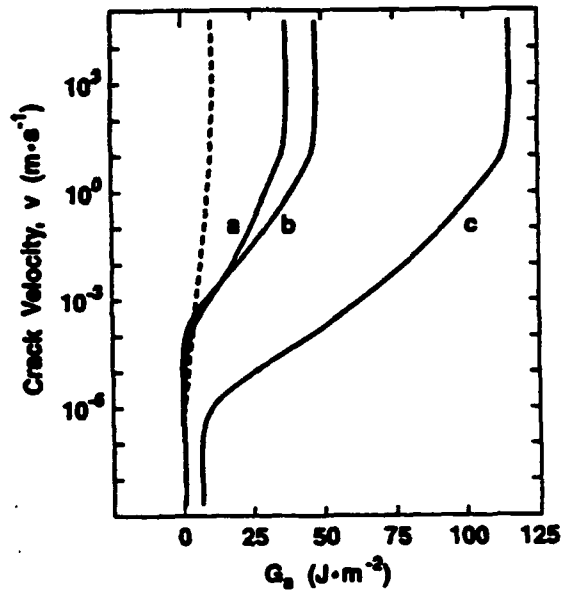


Figure 4. Velocity functions, deconvoluted from Fig. 3. Dashed curve is intrinsic, invariant crack-tip function,  $v(G_s)$ . Solid curves are history-dependent global functions  $v(G_A)$ , as monitored via the applied loading: (a)  $P = 3$  N,  $\dot{\sigma}_A = 10^3$  MPa $\cdot$ s $^{-1}$ ; (b)  $P = 30$  N,  $\dot{\sigma}_A = 10^3$  MPa $\cdot$ s $^{-1}$ ; (c)  $P = 30$  N,  $\dot{\sigma}_A = 10^{-1}$  MPa $\cdot$ s $^{-1}$ .

$v$ - $G$ , relation of Eq. 15, equivalent to the curve that a "global" observer at the load points would measure for a material with no shielding ( $K_2 = 0 = K_u$ ). The solid curves are the corresponding  $v(G_A)$  curves for indentation flaws with shielding present. We see that the global velocity curve is history dependent, i.e. is a function of the residual contact field and stressing rate. The curves shift because the shielding contribution to the toughness is no longer a unique function of crack size, but depends also on the subcritical path [17]. Such curve shifts are regularly reported in the ceramics literature.

These results have a special relevance to fatigue. Many ceramics exhibit a static fatigue stress limit (analogous to the lower stress limit apparent in Fig. 3) below which the lifetime is effectively infinite. A fatigue limit is usually considered to be a direct manifestation of the crack velocity threshold, the crack-tip stress intensity below which all propagation ceases. But this is not the whole story. A strong T-curve enhances the fatigue limit, and can even generate an effective limit in materials with no detectable natural velocity threshold. To illustrate, we include as the dashed curve in Fig. 3 the computed strength vs stressing rate function for a hypothetical material with the same velocity function as our alumina but with its threshold shifted to zero  $G_*$ . A fatigue limit is still apparent, albeit at a somewhat reduced stress level. Mathematically, the existence of this limit is possible because the bridging closure term  $-K_u$  can negate the effective applied loading term  $K_A = K_s + K_2$  in Eq. 1, giving rise to a zero velocity state  $K_* = 0 = G_*$  in Eq. 15.

### 3.3 CYCLIC FATIGUE

We have just referred to fatigue in static loading. Taking the metals literature as a guide, we might suspect some additional reduction in the fatigue limit in cyclic loading, due to some hysteresis in the crack-tip shielding. Specifically, we might anticipate mechanical degradation from deterioration of bridging ligaments in repeated loading.

Cyclic fatigue tests are most conveniently conducted with the indentation flaw configuration [18]. Results of such tests at two frequencies on alumina (this time on a coarser material than in Figs. 2 and 3) are shown in Fig. 5. Theoretical curves, obtained once more by solution of the crack velocity differential equation in Sect. 2 (but for the new grain size), exhibit a similar fatigue limit to that in Fig. 3. The data do appear to fall systematically below this predicted limit at long lifetimes, suggesting a real mechanical degradation of the microstructure.

The modest level of this degradation in Fig. 5 is not necessarily discouraging if one regards a million cycles as a reasonable service limit. Nevertheless, the potential exists for stronger effects in other configurations, e.g. long cracks and materials with more pronounced T-curves. For this reason it is proper that one should attempt to understand the underlying causes of the degradation.

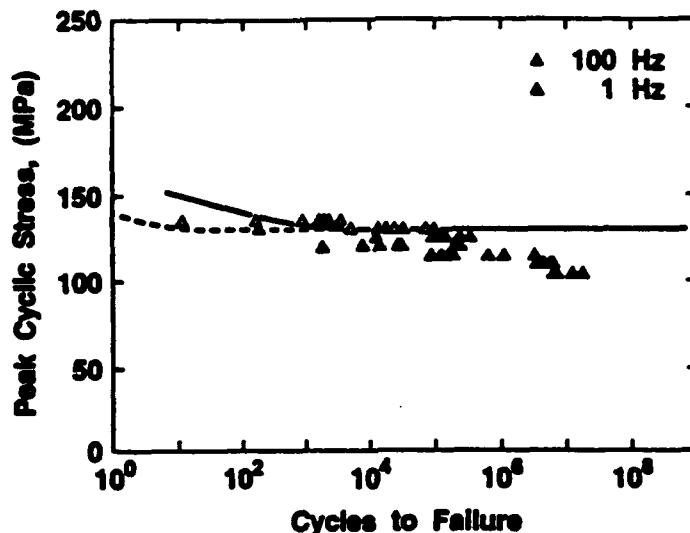


Figure 5. Cyclic fatigue plot for polycrystalline alumina,  $l = 35 \mu\text{m}$ , in water, Vickers indentations at  $P = 30 \text{ N}$ , as function of number of cycles. Open symbols are for 1 Hz, closed symbols 100 Hz. Curves are predictions for 1 Hz (dashed) and 100 Hz (solid) assuming slow crack growth without mechanical degradation.

#### 4. IN-SITU SCANNING ELECTRON MICROSCOPY OBSERVATIONS

##### 4.1 OBSERVATIONS OF BRIDGE EVOLUTION

In situ observations of crack microstructure interactions using optical microscopy have played a pivotal role in identifying grain bridging as an important toughening mechanism in ceramics [7,10]. The development of miniature straining devices for operation within the scanning electron microscope (SEM) have opened the possibility for more detailed observation and quantitative analysis of bridging mechanisms [20,21].

Fig. 6 presents SEM surface views of a crack-interface bridging site in an alumina, grain size  $l = 11 \mu\text{m}$ , at two stages in monotonic loading [20]. The bridge has continued to evolve between the two stages, during which the crack front has undergone an incremental extension of  $\approx 600 \mu\text{m}$ . Persistent frictional contact points P and S are indicated. In the interval between (a) and (b) secondary fractures have been initiated in the bridging grain adjoining P by the frictional tractions. During this same interval a single secondary fracture in the large grain to the right of S has closed significantly, indicating a falloff in the frictional tractions. This latter is indicative of a tail-dominated constitutive stress-separation function, as assumed in Eq. 7.

Fig. 7 presents analogous views of a frictional site in the alumina used in Fig. 5, at various stages of cyclic loading [18]. There is gradual cumulation of debris from repeated load reversal at the sliding

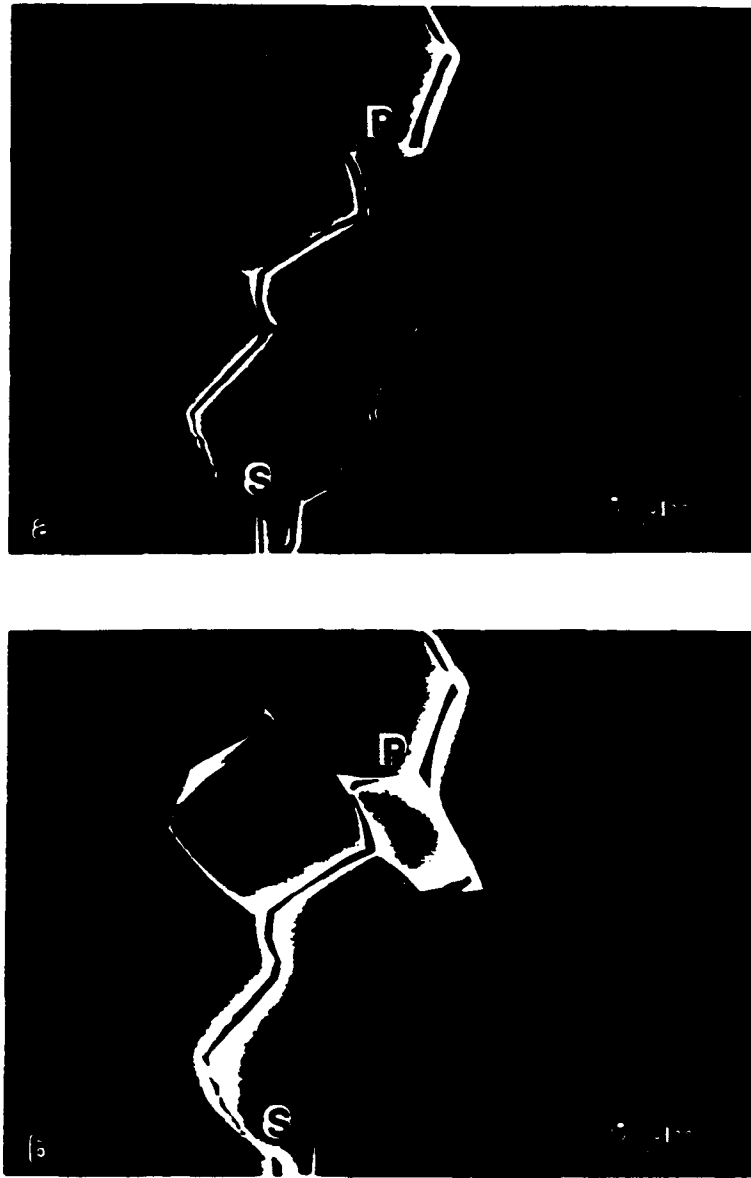


Figure 6. SEM micrographs showing evolution of grain-bridging ligament at a crack interface in alumina,  $l = 11 \mu\text{m}$ , at distances (a)  $600 \mu\text{m}$  and (b)  $1190 \mu\text{m}$  behind the advancing crack tip. P and S denote frictional contact points.

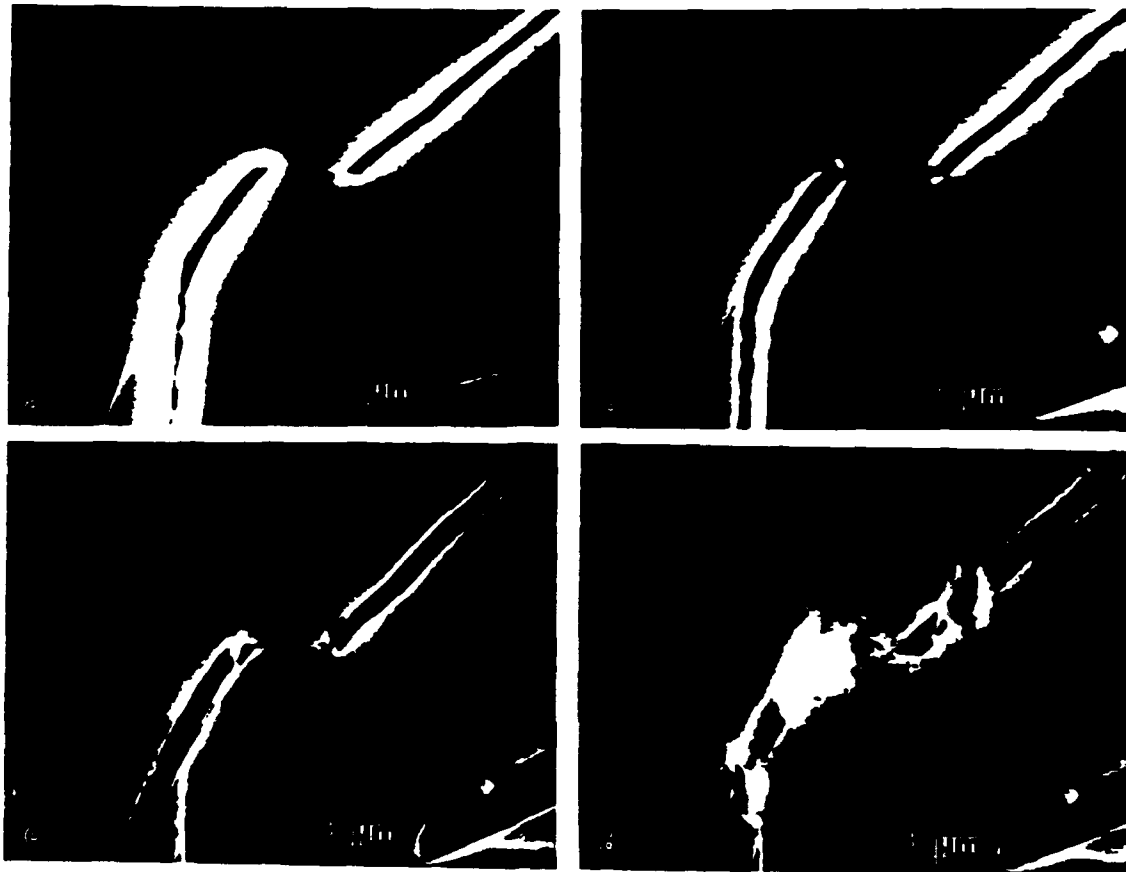


Figure 7. SEM micrographs of frictional grain facet in same alumina as Fig. 5, at various stages of cycling loading (vacuum, 2 Hz, unless otherwise indicated): (a) after initial propagation; (b) after 20000 cycles, with accompanying crack propagation 90  $\mu\text{m}$ ; (c) after 45000 cycles, no propagation; (d) after 50000 cycles (air, 10 Hz), propagation 20  $\mu\text{m}$ . Note debris at friction facet.

grain facet, even between (b) and (c) where no primary crack growth occurs. Stage (d) shows strongly enhanced buildup of the debris after prolonged additional cycling in air. The debris may be taken as direct evidence for degradation of the interface at the sliding facet. Analysis using the bridging formulation in Sect. 2 indicates that the reduction in friction coefficient needed to account for the mechanical fatigue effect in Fig. 5 is modest, from  $\mu = 1.8$  to 1.4 [18].

#### 4.2 QUANTITATIVE CRACK PROFILE MEASUREMENTS

The quantitative capability afforded by the SEM is demonstrated in Fig. 8 with measurements of crack-opening displacement (COD)  $2u$  as a function of distance  $x$  behind the crack tip, for the alumina in Fig. 6. The crack profile is seen to be closer to linear than the usual Irwin-parabola for stress-free walls [20], reflecting the closure effect of bridging tractions. In the limit of small bridging zones, as pertains to small extensions  $\Delta c$  from a long notch, the profile may be approximated by the Barenblatt relation

$$u(x) = (8x/\pi)^{1/2} K_A / E' - (2/\pi E') \int_0^{\Delta c} p(x') \ln[(x'^{1/2} + x^{1/2}) / (x'^{1/2} - x^{1/2})] dx' \quad (16)$$

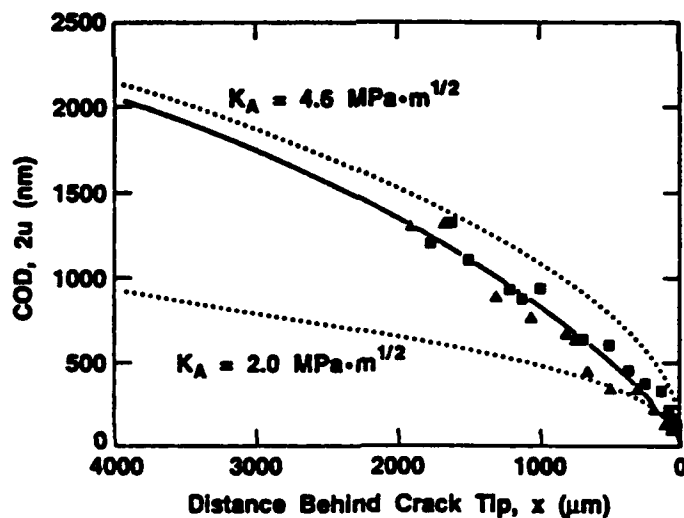


Figure 8. Measured crack-opening displacement at crack interface in same alumina as Fig. 6, compact-tension specimen, extended crack length  $\Delta c = 1.9$  mm. Solid curve is fitted profile from Eq. 16. Dashed curves are enveloping Irwin parabolas for  $K_A = 4.6 \text{ MPa} \cdot \text{m}^{1/2}$  and  $K_A = T_0 = 2.0 \text{ MPa} \cdot \text{m}^{1/2}$ .

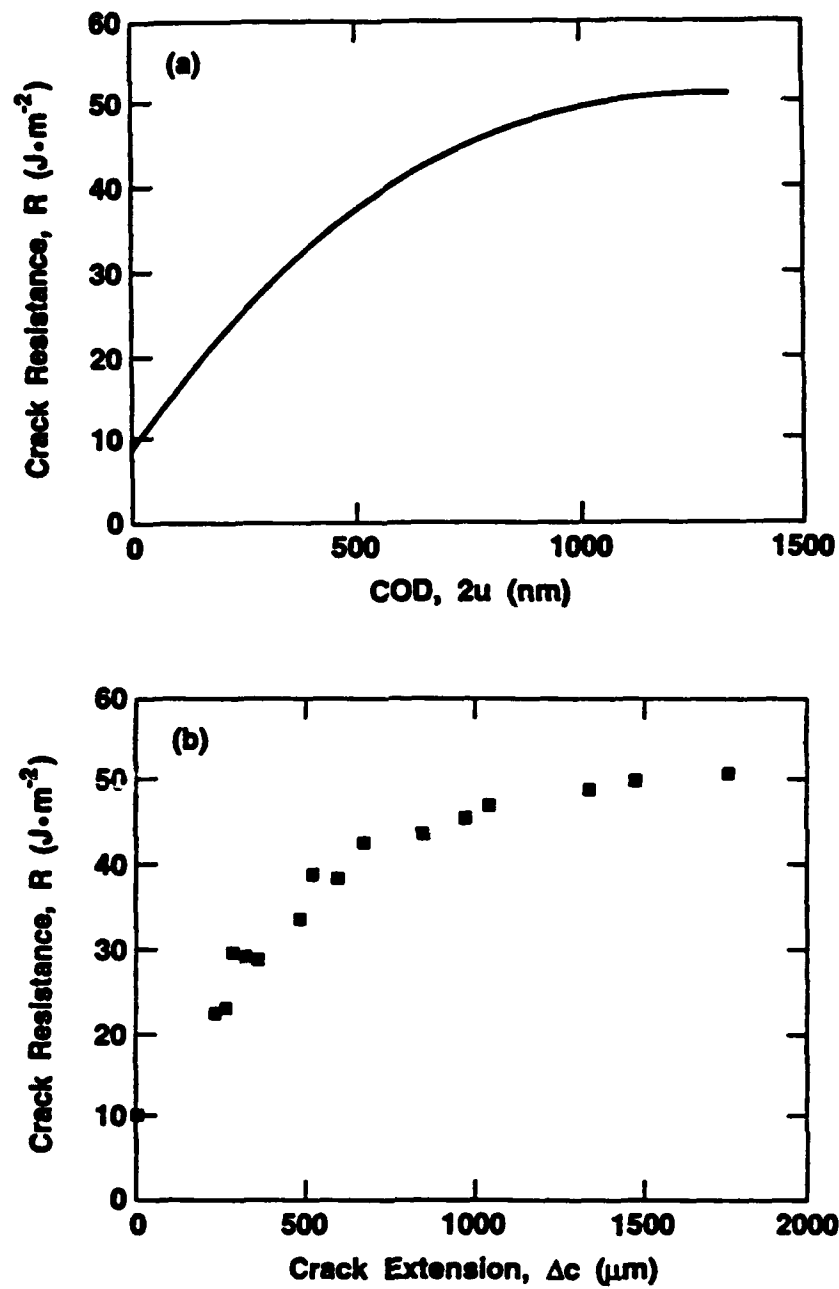


Figure 9. Crack-resistance curves corresponding to constitutive functions evaluated from crack profile in Fig. 8, (a)  $R(u)$ , and (b)  $R(\Delta c)$ .

with  $x$  now a field point at which the displacement is to be evaluated and  $x'$  a source point for the closure stresses. The problem is to find a solution for  $p(x')$ , thence  $p(u)$ , self-consistent with the measured  $u(x)$ . Eq. 16 is a nonlinear integral equation, for which there is no analytical solution. The solid curve in Fig. 8 is a best fit obtained by numerical iteration.

Once  $p(u)$  is known the crack-resistance curves are readily evaluated using the J-integral in Eq. 12 (recall that the contribution from Eq. 10 is negligible for straight cracks), identifying  $2u_2$  with the notch-tip COD. The resulting  $R(u)$  curve for the alumina is shown in Fig. 9a. We assert that  $R(u)$  is a material property, since it is uniquely dependent on the intrinsic function  $p(u)$ . On the other hand, the corresponding  $R(\Delta c)$  curve in Fig. 9b, evaluated in conjunction with the geometry-sensitive profile  $u(\Delta c)$ , is a function of test configuration.

## 5. MICROSTRUCTURAL CONTROL OF TOUGHNESS PROPERTIES

We have indicated the strong influence of microstructural variables on toughness-curve characteristics, and the associated potential for manipulating mechanical properties through controlled processing. Two examples serve to illustrate the point:

### 5.1 GRAIN-SIZE EFFECTS

The role of grain size on the strength characteristics of alumina has been systematically investigated in an indentation-strength study [15]. Fig. 10a plots indentation-strength data for selected grain sizes. The solid curves correspond to predictions from the calibrated bridging theory from Sect. 3. Fig. 10b plots the deconvoluted T-curves. Observe the effect of coarsening the microstructure: the strengths tend to more pronounced, low-load plateaus, hence greater flaw tolerance; reductions of strength and toughness in the short-crack domain are compensated by increases in the long-crack domain.

The bridging model also provides insights into the nature of flaw states in strength-grain size characteristics. Fig. 11 is an "Orowan-Petch" plot of strength data for failures from natural flaws ( $K_{Ic} = 0$ ) in our aluminas as a function of inverse square-root grain size [15]. Included as the solid and dashed curves are the predicted responses for intrinsic (processing) grain-facet flaws ( $c_f \approx d = \alpha_d l$ ) and extrinsic (surface) flaws ( $c_f$  specified). Note that the solid and dashed curves merge in the large grain-size (Orowan) region. The insensitivity of the strength to any assumptions concerning type or initial size of flaw in this region indicates an instability condition controlled by material properties: failure is determined by a single point, the tangency point, on the T-curve. (We point out that the solid curve is not strictly linear in this region, as would obtain if ideal Griffith



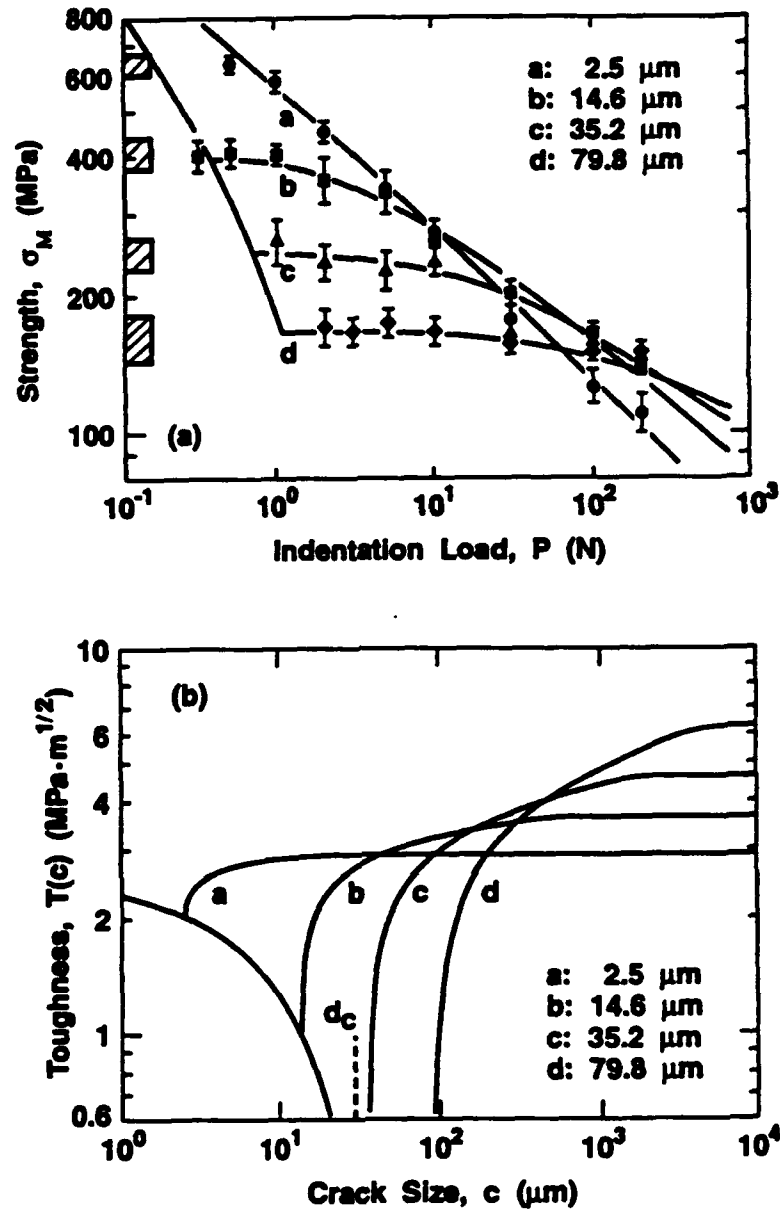


Figure 10. (a) Vickers indentation-strength data for four single-phase aluminas of differing grain size. Solid curves are predictions using calibrated bridging stress-intensity factor from Sect. 3. Note enhanced plateau behavior at larger grain sizes. Curves are theoretical fits from bridging model. (b) Corresponding deconvoluted T-curves. Vertical dashed line denotes intersection point of curve with crack-size axis at  $T = 0$  for  $l = 30 \mu\text{m}$ , corresponding to onset of spontaneous microcracking. Note tendency for curves to cross in both (a) and (b).

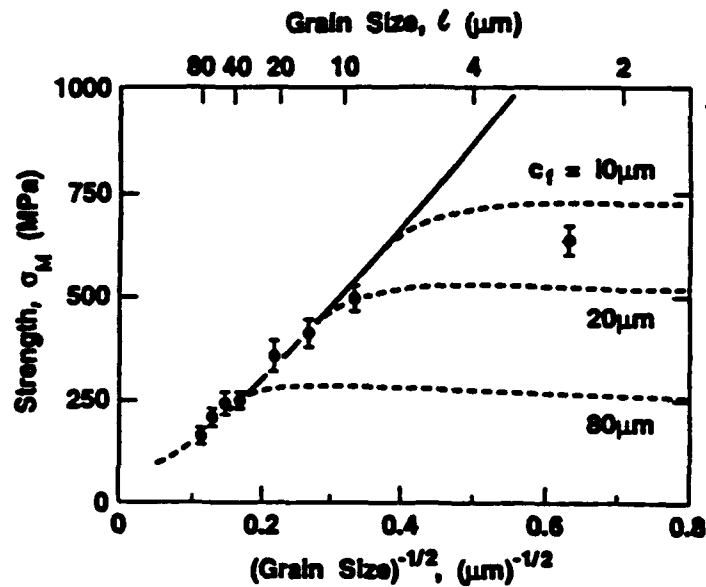


Figure 11. Strength versus inverse square-root grain size for alumina. Data are failures for polished, unindented specimens. Solid curve is prediction from bridging model for intrinsic flaws. Dashed curves are predictions for extrinsic flaws of specified initial size  $c_f$ . Note insensitivity of strength to flaw size in large grain-size domain.

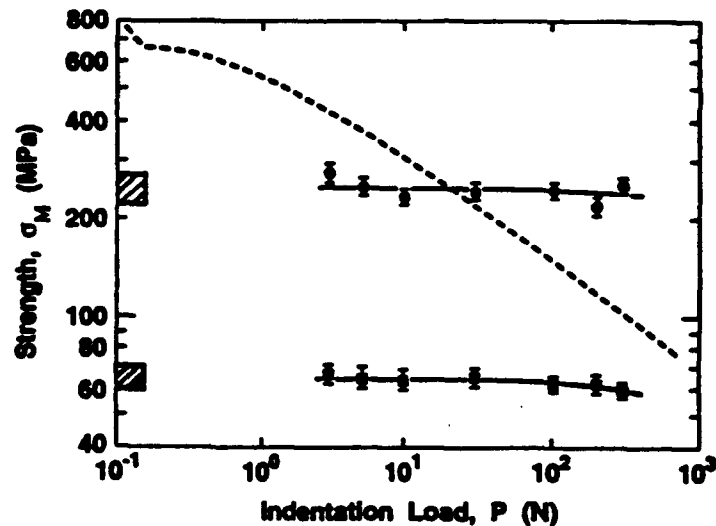


Figure 12. Inert strength as function of Vickers indentation load for an alumina matrix composite, grain size  $l = 6 \mu\text{m}$ , with 20 vol.% second-phase aluminum titanate particles. Lower data are for degraded material with  $l = 14 \mu\text{m}$ , above the critical grain size for spontaneous microcracking. Included as the dashed curve is prediction for equivalent monophase alumina ( $l = 6 \mu\text{m}$ ).

behavior, i.e. flaw scaling with grain size, single-valued toughness  $T = T_0$ , were to prevail.) However, the curves diverge in the small grain-size (Petch) region, reflecting the sensitivity to flaw size usually associated with ceramics. On passing into this region the extrinsic flaws begin to dominate their microstructural counterparts, and traverse the tangency points on the T-curves (Fig. 10b) beyond which precursor stable crack growth prior to failure no longer occurs. Only one of the data points in Fig. 11, that of the finest grain size, appears to fall into the extrinsic region.

## 5.2 SECOND-PHASES

A second illustrative example demonstrates the importance of microstructural parameters other than grain size. We consider a model composite ceramic in which aluminum titanate has been added as a particulate second phase to an alumina matrix, grain size  $6 \mu\text{m}$  [16]. Aluminum titanate was selected because of its unusually strong thermal expansion mismatch relative to alumina. An aging heat treatment promoting grain growth to  $l = 14 \mu\text{m}$  caused general microcracking (see Sect. 6.1) in the composite.

Results of indentation-strength tests on the as-fabricated material are shown as the upper set of data points in Fig. 12. Included for comparison is a predicted curve for single-phase alumina of the same grain size ( $l = 6 \mu\text{m}$ ). It is immediately apparent that the composite has greatly exaggerated flaw tolerance relative to the alumina, although at the expense of short-crack strength. Also included is a data set for the heat-treated composite. The strength level for this latter material is severely reduced, as expected for an overaged microstructure.

A proper understanding of the bridging micromechanisms responsible for the striking changes in Fig. 12 is yet to be attained. Is the main role of the enhanced mismatch one of intensifying the frictional tractions at compressive bridging facets, or to enhance the formation of bridges by providing favorable tensile paths for deflection? In situ studies may help to provide answers. Once the micromechanisms are identified, the challenge will be to modify the model in Sect. 2.

These results demonstrate the capacity for improved strength properties in ceramic composites, particularly in the long-crack domain. Potential pitfalls in fabrication strategies are also apparent. The line between ultra-high toughness and unacceptable weakness may be very fine indeed.

## 6. SHORT-CRACK PROPERTIES: SPONTANEOUS MICROCRACKING AND WEAR

What is good for properties that pertain to long or intermediate cracks may not be so for short cracks. The very ingredients responsible for

flaw tolerance, notably internal residual stresses, can be detrimental to general microcracking and wear resistance.

## 6.1 SPONTANEOUS MICROCRACKING

It is well known that noncubic polycrystals tend to general microcracking above a critical grain size. Such microcracking is attributable to the action of residual thermal expansion stresses. In terms of our shielding model, the critical condition is that processing flaws at tensile grain boundary facets should be unstable in the absence of any extraneous driving force. Seen from the perspective of Fig. 10b, a minimum requirement for such spontaneous instability is that the unstable branch of the toughness curve should intersect the abscissa ( $K_A = T = 0$ ) at the flaw size  $c_L$ . Beyond this point instability ensues, and the microcrack arrests on the stable branch. Writing  $c_L = \beta l$ , with  $\beta$  a dimensionless constant (geometrical scaling), the critical grain size may be determined directly from Eq. 10 at equilibrium,  $K_{II}(c) = \psi \sigma_R (\beta l_C)^{1/2} = T_0$ : thus [19]

$$l_C = (1/\beta \psi^2) (T_0/\sigma_R)^2. \quad (17)$$

From Fig. 10b we estimate  $l_C \approx 30 \mu\text{m}$  for our alumina, which accords with experimental observations of spontaneous microcracking in the same series of aluminas [15]. Fig. 13 is a micrograph of an individual microcrack in a coarse-grained alumina.

## 6.2 MICROFRACTURE-WEAR PROCESSES

The earliest theories of surface removal by contact-induced cracking in brittle surfaces suggested that the least severe wear rates should occur in those materials with the highest toughness [24]. Such theories presume that the toughness is single-valued. The question arises as to the behavior in ceramics with strong T-curves.

Fig. 14 presents wear data on aluminas at three grain sizes [19]. Of these aluminas, the coarser have the higher conventional (long-crack) toughness. Yet it is the coarser aluminas here that show the greater susceptibility to wear degradation. Wear is quantified in Fig. 14 by the diameter of a scar generated by a rotating hard ( $\text{Si}_3\text{N}_4$ ) sphere at specified contact time. The scar diameter increases monotonically with time for each material, initially slowly and subsequently, after an "incubation" period, abruptly. Whereas the initial increase is microstructure-invariant, the transition shifts to smaller times at the larger grain sizes.

Hence the "toughest" aluminas exhibit the most rapid degradation. A qualitative resolution to the apparent anomaly is once more to be found in the T-curve construction of Fig. 10b. The coarser microstructures indeed show greater long-crack toughness. However, it is the short-crack domain that is relevant to wear; and, as we have

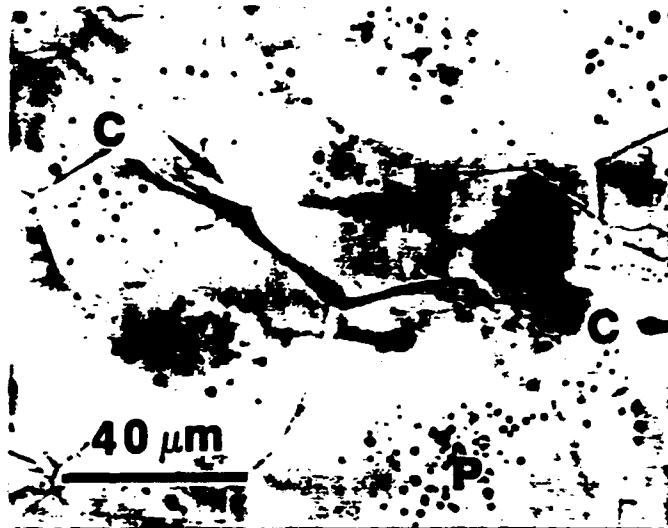


Figure 13. Optical micrograph showing extended microcrack (C-C) in alumina,  $l = 80 \mu\text{m}$ . Note that, contrary to "conventional wisdom", grain-size microcracks are quite visible, here in transmitted light, by virtue of residual opening associated with release of internal tensile stress. Some processing pores (P) are also visible.

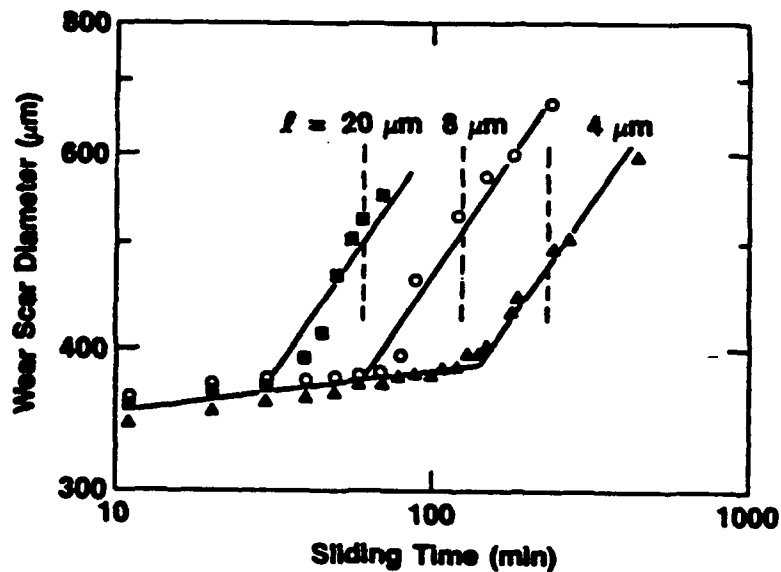


Figure 14. Wear data for aluminas at three grain sizes. Note initially slow increase of scar diameter, abrupt transition to severe microfracture-controlled wear after critical sliding time. Transition time diminishes at increasing grain size.

remarked before, the T-curves cross each other.

Microscopy reveals the initial wear to be slight, with indications of dislocation activity [19]. The abrupt increase is marked by the sudden incidence of gross chipping and grain removal. The results may therefore be interpreted in terms of a deformation-fracture transition, in which tensile stresses  $\sigma_D$  from the deformation augment those from the thermal expansion anisotropy, i.e.  $\sigma_R' = \sigma_R + \sigma_D$ . Suppose that these deformation stresses cumulate monotonically with time, i.e.  $\dot{\sigma}_D = \sigma_D/t = \text{const.}$  Then replacing  $\sigma_R$  by  $\sigma_R'$  in Eq. 17 allows us to solve for the time to induce microcracking [19]

$$t_* = (\sigma_R/\dot{\sigma}_D)[(l_C/l)^2 - 1] \quad (l \leq l_C). \quad (18)$$

Observe that  $t_* = 0$  at  $l = l_C$ , as required. As  $l$  decreases below  $l_C$ ,  $t_*$  diminishes, in qualitative accord with observation. The shifts in Fig. 14 are quantitatively consistent with a stress cumulation rate  $\dot{\sigma}_D = 5 \text{ MPa} \cdot \text{s}^{-1}$ .

The implications concerning optimization of microstructures for maximum resistance to spontaneous microcracking and microfracture-induced wear are clear in this case - refine the grain size and, if possible, avoid internal residual stresses. It is reiterated that such measures may run entirely counter to the requirements for maximum large-crack toughness and flaw tolerance.

## CONCLUSIONS

We have described toughness-curve phenomena in terms of a grain-interlocking bridging model. Essential microstructural ingredients for strong T-curves are weak boundaries, high internal stresses, and coarse grains. Our model has been illustrated with data from alumina, but a wider applicability to ceramics in general is asserted.

The T-curve has positive implications in strength. These include flaw tolerance and an enhanced fatigue limit. However, such benefits could be countered to some extent by possible bridge degradation in cyclic loading.

In situ observations of bridging sites in the scanning electron microscope provide insight into the degradation micromechanisms, and allow for quantitative evaluation of the crack-interface tractions.

Short-crack properties, spontaneous microcracking and abrasive wear, may be exacerbated in materials with strong T-curves.

## ACKNOWLEDGEMENTS

The authors wish to thank colleagues S-J. Cho, E.R. Fuller Jr., B.J. Hockey, J.F. Kelly, Y-W. Mai and J.L. Runyan for many valuable contributions to this work. Funding was provided by the U.S. Air Force Office of Scientific Research and E.I. duPont de Nemours & Co. Inc. S.J.B., J.R., S.L. are Guest Scientists on leave from the Department of Materials Science and Engineering, Lehigh University, Bethlehem, PA, USA; P.C. is Guest Scientist on leave from Department of Physics, Chulalongkorn University, Bangkok, Thailand. S.L. is now at Division of Materials Science, CSIRO, Clayton, VIC, Australia.

## REFERENCES

- [1] H. Hübner and W. Jillek (1977) "Sub-Critical Crack Extension and Crack Resistance in Polycrystalline Alumina", J. Mater. Sci. 12 117-25.
- [2] R. Knehans and R.W. Steinbrech (1982) "Memory Effect of Crack Resistance During Slow Crack Growth in Notched  $\text{Al}_2\text{O}_3$  Bend Specimens", J. Mater. Sci. Lett. 1 327-29.
- [3] R.W. Steinbrech, R. Knehans and W. Schaarwächter (1983) "Increase of Crack Resistance During Slow Crack Growth in  $\text{Al}_2\text{O}_3$  Bend Specimens", J. Mater. Sci. 18 265-70.
- [4] R. Knehans and R.W. Steinbrech (1984) "Effect of Grain Size on the Crack Resistance Curves of  $\text{Al}_2\text{O}_3$  Bend Specimens"; in Science of Ceramics, Vol. 12, pp. 613-19, ed. P. Vincenzini. Ceramurgia, Imola, Italy.
- [5] R.F. Cook, B.R. Lawn and C.J. Fairbanks (1985) "Microstructure-Strength Properties in Ceramics: I. Effect of Crack Size on Toughness", J. Am. Ceram. Soc. 68 604-15.
- [6] M.V. Swain (1986) "R-Curve Behavior in a Polycrystalline Alumina Material", J. Mater. Sci. Lett. 5 1313-15.
- [7] P.L. Swanson, C.J. Fairbanks, B.R. Lawn, Y-W Mai and B.J. Hockey (1987) "Crack-Interface Grain Bridging as a Fracture Resistance Mechanism in Ceramics: I. Experimental Study on Alumina", J. Am Ceram. Soc. 70 279-89.
- [8] Y-W. Mai and B.R. Lawn (1987) "Crack-Interface Grain Bridging as a Fracture Resistance Mechanism in Ceramics: II. Theoretical Fracture Mechanics Model", J. Am. Ceram. Soc. 70 289-94.
- [9] R.F. Cook, C.J. Fairbanks, B.R. Lawn and Y-W. Mai (1987) "Crack Resistance by Interfacial Bridging: Its Role in Determining Strength Characteristics", J. Mater. Research 2 345-56.
- [10] P.L. Swanson (1988) "Crack-Interface Traction: A Fracture-Resistance Mechanism in Brittle Polycrystals"; in Advances in Ceramics, Vol. 22, pp. 135-55, Fractography of Glasses and Ceramics. American Ceramic Society, Columbus, OH.

- [11] R.W. Steinbrech and O. Schmenkel (1988) "Crack-Resistance Curves of Surface Cracks in Alumina", J. Am. Ceram. Soc. 71 C271-73.
- [12] S.J. Bennison and B.R. Lawn (1989) "Flaw Tolerance in Ceramics With Rising Crack-Resistance Characteristics" J. Mater. Sci. 24 3169-75.
- [13] S.J. Bennison and B.R. Lawn (1989) "Role of Interfacial Grain-Bridging Sliding Friction in the Crack-Resistance and Strength Properties of Nontransforming Ceramics", Acta Metall. 37 2659-71.
- [14] Y-W. Mai and B.R. Lawn (1986) "Crack Stability and Toughness Characteristics in Brittle Materials", Ann. Rev. Mat. Sci. 16 415-39.
- [15] P. Chantikul, S.J. Bennison and B.R. Lawn, "Role of Grain Size in the Strength and R-Curve Properties of Alumina", J. Am. Ceram. Soc., in press.
- [16] J.L. Runyan and S.J. Bennison, "Fabrication of Flaw-Tolerant Aluminum-Titanate-Reinforced Alumina", J. Europ. Ceram. Soc., in press.
- [17] S. Lathabai and B.R. Lawn (1989) "Fatigue Limits in Noncyclic Loading of Ceramics with Crack-Resistance Curves", J. Mat. Sci. 24 4298-4306.
- [18] S. Lathabai, J. Rödel and B.R. Lawn, "Cyclic Fatigue from Frictional Degradation at Bridging Grains in Alumina", J. Mater. Sci., in press.
- [19] S-J. Cho, B.J. Hockey, B.R. Lawn and S.J. Bennison (1989) "Grain-Size and R-Curve Effects in the Abrasive Wear of Alumina", J. Am. Ceram. Soc. 72 1249-52.
- [20] J. Rödel, J.F. Kelly and B.R. Lawn, "In Situ Measurements of Bridged Crack Interfaces in the SEM", J. Am. Ceram. Soc., in press.
- [21] J. Rödel, J.F. Kelly, M.R. Stoudt and S.J. Bennison, "A Loading Device for Fracture Testing of Compact Tension Specimens in the SEM," Scanning Microscopy, in press.
- [22] B.R. Lawn, A.G. Evans and D.B. Marshall (1980) "Elastic/Plastic Indentation Damage in Ceramics: The Median/Radial Crack System", J. Am. Ceram. Soc. 63 574-81.
- [23] B.R. Lawn, D.B. Marshall, P. Chantikul and G.R. Anstis (1980) "Indentation Fracture: Applications in the Assessment of Strength of Ceramics", J. Aust. Ceram. Soc. 16 4-9.
- [24] A.W. Ruff and S.M. Wiederhorn (1979) "Erosion by Solid Particle Impact", in Treatise on Materials Science and Technology, Vol. 16, pp. 69-126, ed. C.M. Preece. Academic, New York.



## FLAW TOLERANT $\text{Al}_2\text{O}_3$ - $\text{Al}_2\text{TiO}_5$ COMPOSITES

Nitin P. Padture,<sup>1</sup> Stephen J. Bennison,<sup>2</sup> Julie L. Runyan,<sup>2</sup> Jürgen Rödel,<sup>2</sup> Helen M. Chan,<sup>1</sup> Brian R. Lawn<sup>2</sup>

<sup>1</sup> Department of Materials Science & Engineering, Lehigh University  
Bethlehem, PA 18015

<sup>2</sup> Ceramics Division, National Institute of Standards & Technology  
Gaithersburg, MD 20899

### ABSTRACT

Fabrication of particulate-reinforced  $\text{Al}_2\text{O}_3$ - $\text{Al}_2\text{TiO}_5$  composites, with controlled homogeneous and heterogeneous microstructures, is described. The degree of flaw-tolerance in these composites, as determined by indentation-strength testing, is enhanced by the strong thermal expansion anisotropy stresses associated with the  $\text{Al}_2\text{TiO}_5$  particles and by the scale of the microstructure. In situ scanning electron microscope observations of bridging grains at propagating cracks in the microstructure are analyzed. The role of key microstructural elements in the underlying toughness-curve behavior responsible for the flaw-tolerance is discussed.

### INTRODUCTION

Researchers in recent years have demonstrated R-curves, i.e. an increasing crack resistance with crack size, in  $\text{Al}_2\text{O}_3$ -based ceramics [1-3]. A most important manifestation of this property is "flaw tolerance", i.e. near-invariance in strength over a broad range of flaw sizes. The major toughening mechanism responsible for R-curve behavior in  $\text{Al}_2\text{O}_3$  ceramics has been identified as grain-localized bridging of the crack-wake interface [2,4]. The bridging grains are "clamped" in the matrix by internal compressive stresses from thermal expansion anisotropy (TEA), which augment frictional closure tractions from pullout during crack propagation [5]. Microstructural scaling parameters appear as additional important variables in the ensuing toughness equation [5].

The present paper reports on processing strategies to optimize the effect of TEA stresses and microstructural scaling on

the R-curve. TEA in monophase  $\text{Al}_2\text{O}_3$  is relatively small, but can be enhanced by the incorporation of a suitable second phase.  $\text{Al}_2\text{TiO}_5$  was chosen in this study because it has large TEA; it also has low solubility in  $\text{Al}_2\text{O}_3$ , and does not form intermediate phases [6-8]. Estimates of the internal stress in  $\text{Al}_2\text{O}_3$ - $\text{Al}_2\text{TiO}_5$  yield  $\approx 3$  GPa [8], greater than in  $\text{Al}_2\text{O}_3$  by a factor  $\approx 10$ .

The simplest way to scale up ceramic microstructures is by heat treatments [8,9,11]. However, coarsening of ceramics containing  $\text{Al}_2\text{TiO}_5$  is severely restricted by an enhanced tendency to spontaneous microcracking [8]. To circumvent this problem scaling was achieved through controlled additions of large  $\text{Al}_2\text{O}_3$  grains within an otherwise fine-grained  $\text{Al}_2\text{O}_3$ - $\text{Al}_2\text{TiO}_5$  matrix.

It will be seen in the subsequent sections that the tailored  $\text{Al}_2\text{O}_3$ - $\text{Al}_2\text{TiO}_5$  composites show profoundly enhanced flaw tolerance, hence stronger R-curves.

## EXPERIMENTAL

Conventional ceramic processing routes were used to fabricate 80/20 vol%  $\text{Al}_2\text{O}_3$ / $\text{Al}_2\text{TiO}_5$  composites. Powders<sup>1</sup> of high purity  $\alpha$ - $\text{Al}_2\text{O}_3$  (0.5  $\mu\text{m}$ ) and  $\beta$ - $\text{Al}_2\text{TiO}_5$  (crystallites 1-5  $\mu\text{m}$ , agglomerates 10-20  $\mu\text{m}$ ) were mixed in a class A-100 clean-room, dispersed in methanol and stir-dried. Three batches were prepared: A, homogeneous, with a pre-drying ball-milling stage (Y-TZP balls, 24 hr in methanol) to remove the agglomerates; B, heterogeneous, with spray-dried  $\text{Al}_2\text{O}_3$  agglomerates (25  $\mu\text{m}$ ) added to the ball-milled mix before drying; C, heterogeneous, similar to A but without ball milling, to retain  $\text{Al}_2\text{TiO}_5$  agglomerates (10-20  $\mu\text{m}$ ).

Disks 4 mm thick were uniaxially pressed at 50-60 MPa followed by wet-bag isostatic pressing at 350 MPa. These disks were calcined at 1050°C for 12 hr, then sintered at 1550-1600°C for 1-17 hr. Microstructures were examined in the SEM and characterized using routine ceramographic procedures.

Prospective tensile sides of 20 mm diam. disks were polished to 1  $\mu\text{m}$ , followed by indentation at the face center with a Vickers diamond at loads from 3 to 300 N. The indented specimens were then broken in biaxial flexure and the strengths determined. Details of this method are described elsewhere [3].

Compact-tension geometry fracture specimens were machined from 50 mm diameter disks for crack-interface examinations. These examinations were made in situ using a mechanical loading fixture housed in an SEM [10].

---

<sup>1</sup>  $\alpha$ - $\text{Al}_2\text{O}_3$ , Sumitomo AKP-HP;  $\beta$ - $\text{Al}_2\text{TiO}_5$ , Trans-Tech.

## RESULTS

Figure 1 shows the microstructures of materials A, B and C. The base size of the matrix  $\text{Al}_2\text{O}_3$  grains is consistently  $\approx 6 \mu\text{m}$ . In material A, fig. 1a, the  $\text{Al}_2\text{TiO}_5$  grains are homogeneously distributed, but are about half the size of the  $\text{Al}_2\text{O}_3$  grains. In material B and C, figs. 1b and 1c, distributions of relatively large heterogeneities are evident:  $\text{Al}_2\text{O}_3$  agglomerates in B;  $\text{Al}_2\text{O}_3$  and  $\text{Al}_2\text{TiO}_5$  agglomerates in C. Densities in all cases exceed 98% of the theoretical limit.

Figure 2 shows data for strength against indentation load for the three composites, together with a comparative curve computed for  $6 \mu\text{m}$  pure  $\text{Al}_2\text{O}_3$  from an earlier study [11]. The composites show significantly lower strength sensitivity to starter flaw size, i.e. greater flaw tolerance, than the base  $\text{Al}_2\text{O}_3$ . Further, the sensitivity decreases in the composite sequence A→B→C, i.e. with more pronounced heterogeneity.

Figure 3 shows SEM micrographs of a bridging site taken at two stages of monotonic loading, in material B. Grain-facet frictional contacts at points P and Q act on the large (alumina) grain. Highly active bridge sites of this kind were significantly more prevalent in the composites than in the base  $\text{Al}_2\text{O}_3$ .

## DISCUSSION AND CONCLUSION

We conclude from the above results that  $\text{Al}_2\text{O}_3$ -based composites can show considerably enhanced flaw tolerance relative to base  $\text{Al}_2\text{O}_3$ . This enhanced tolerance is a manifestation of a more pronounced R-curve [4], resulting in turn from stronger grain-interlock bridging.

Specifically, it is evident that high residual TEA stresses and heterogeneity are key factors in the increased flaw tolerance. Simplistically, internal stresses contribute by augmenting the frictional tractions at sliding grain facets during pullout [5]. Heterogeneity increases the pullout distance at the larger individual grains. Predictive modelling of the resultant enhanced bridging in two-phase ceramics should provide useful guidelines for improved microstructural design of structural ceramics [5,12].

We note finally that the approach advocated here of including controlled heterogeneous stress centers to augment bridging is in strong violation of conventional ceramics processing wisdom, where one seeks to produce ultra-fine, defect-free microstructures. Ours is a philosophy of containing cracks, not of eliminating them. In the same context, it may be pointed out that those very same internal stress sources that enhance long-crack toughness also may lead to deleterious short-crack properties like wear, spontaneous microcracking and fatigue [12].

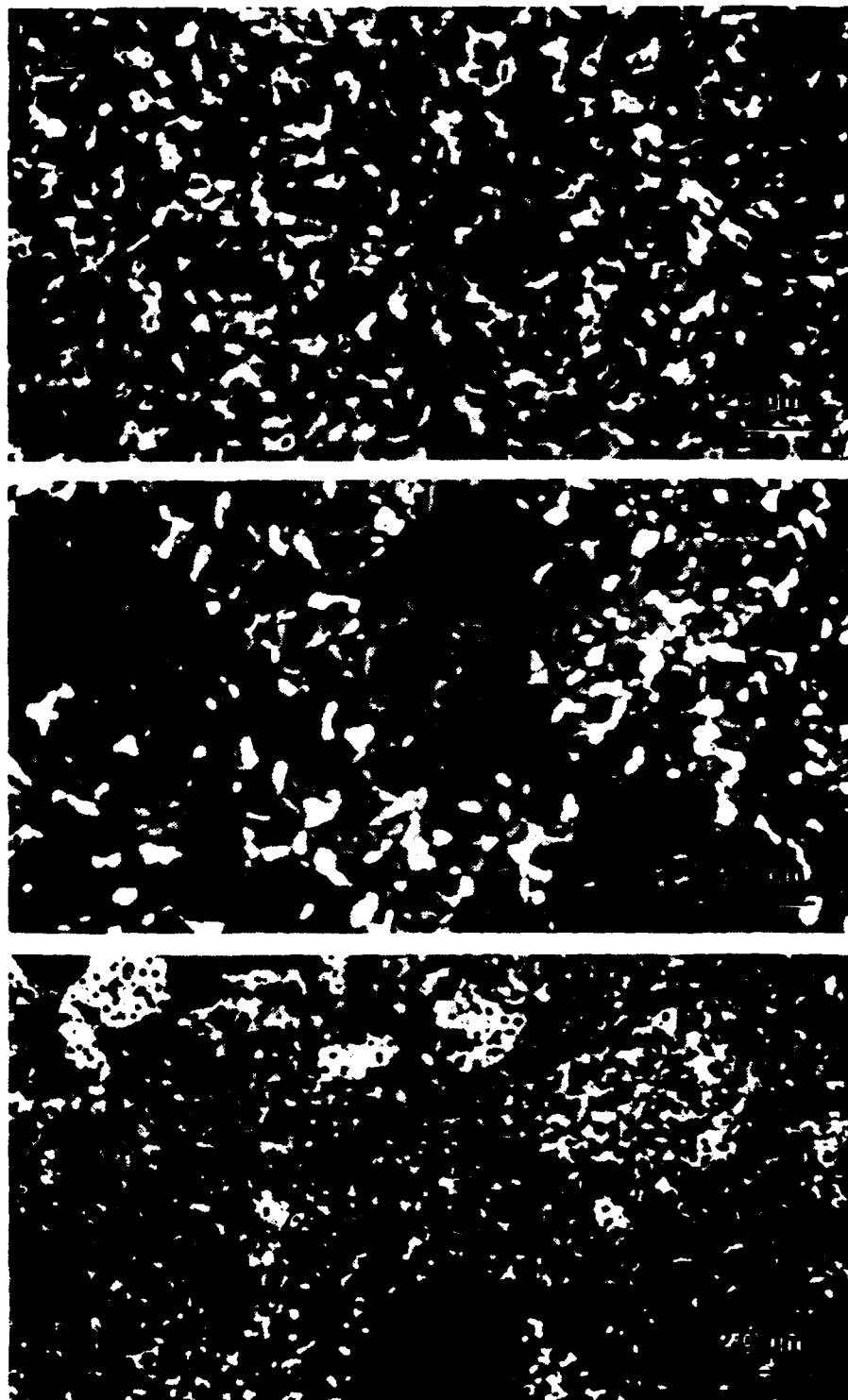


Figure 1. SEM microstructures of composites of 80%  $\text{Al}_2\text{O}_3$  (dark grains) and 20%  $\text{Al}_2\text{TiO}_5$  (light grains): (a) homogeneous material A, (b) heterogeneous material B; (c) heterogeneous material C. Samples polished to  $1\text{ }\mu\text{m}$  and thermally etched.

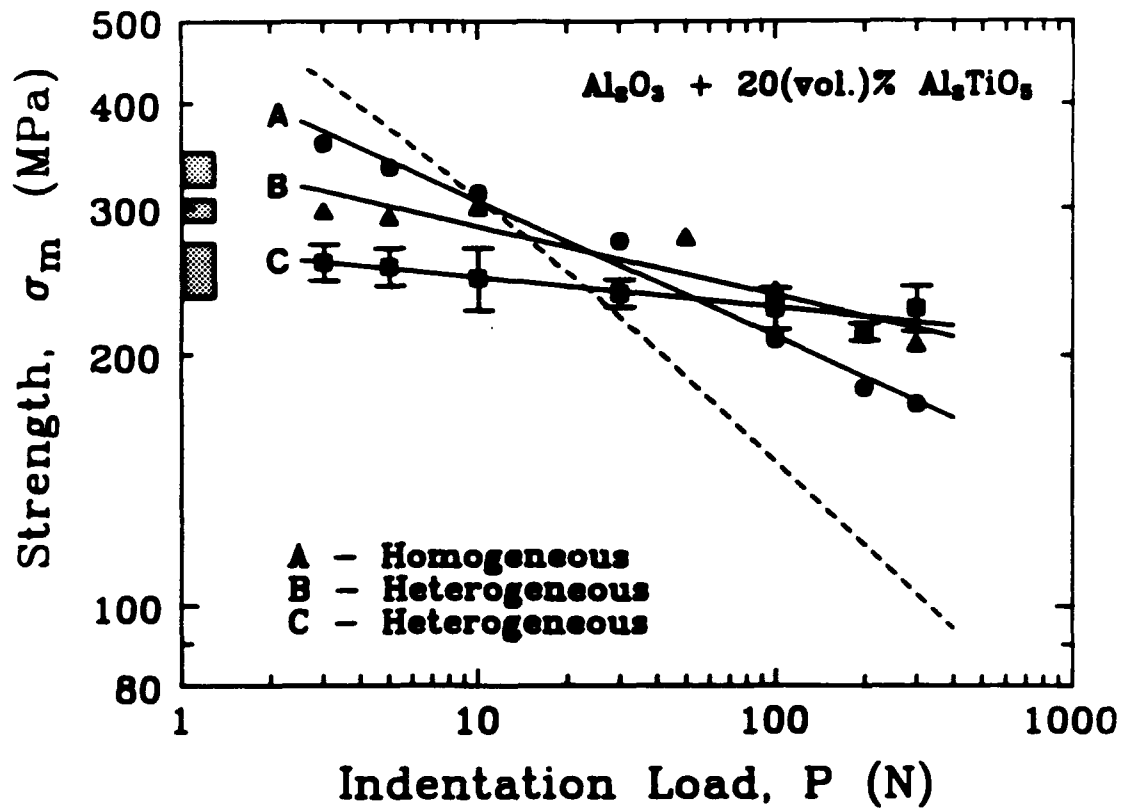


Figure 2. Indentation load versus strength plots. Data with solid curves for composite materials A, B and C. Error bars omitted from A and B data for clarity. Shaded area to left represents failures from natural flaws. Comparative dashed curve for  $\text{Al}_2\text{O}_3$  of same grain size.

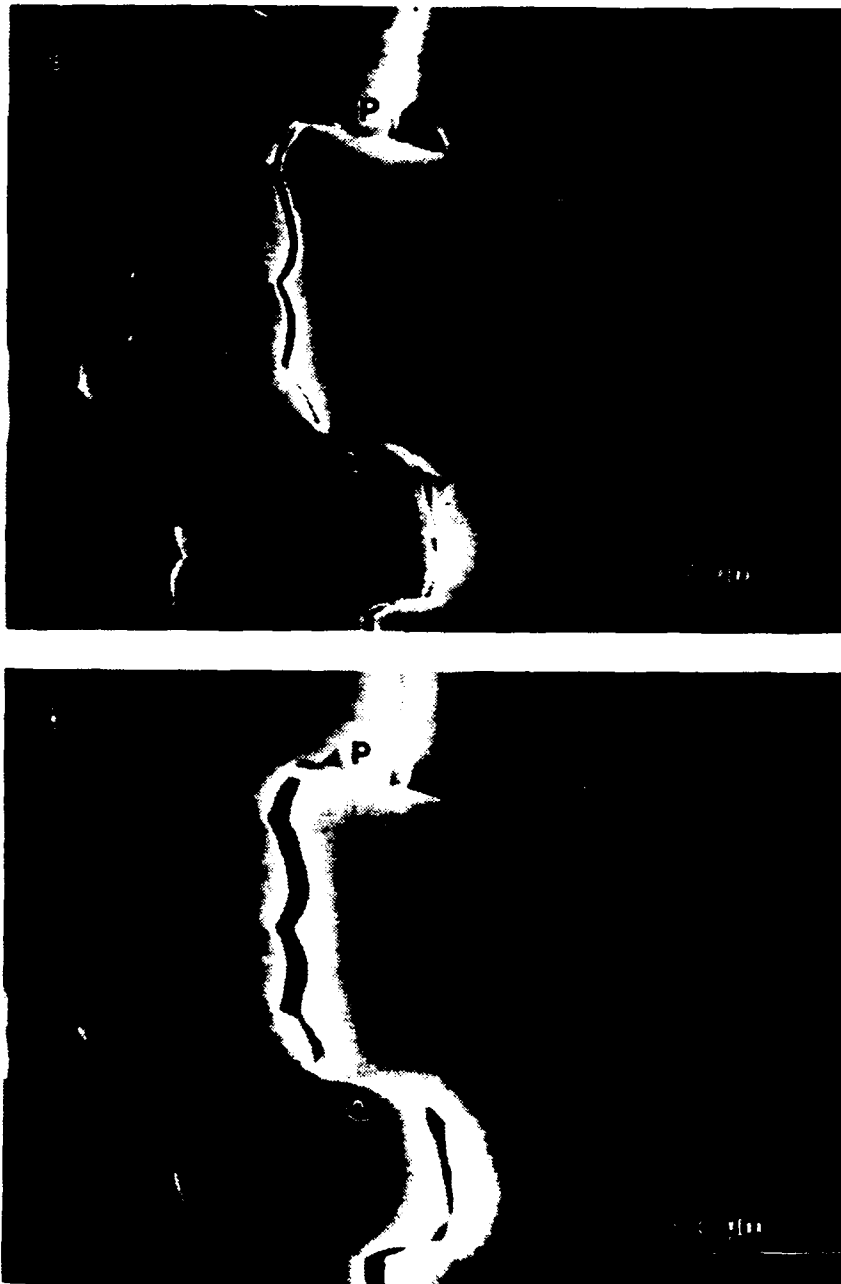


Figure 3. Bridging site at large alumina grain in composite B, showing frictional contact points at P and Q. Micrographs (a) and (b) taken in situ at successive increasing loads in SEM.

## ACKNOWLEDGEMENTS

Funding for this work was provided by the Air Force Office of Scientific Research and E.I. duPont de Nemours and Co. Inc.

## REFERENCES

1. H. Hübner and W. Jillek, "Sub-Critical Crack Extension and Crack Resistance in Polycrystalline Alumina", *J. Mater. Sci.* 12[1] 117-25 (1977).
2. R. Knehans and R.W. Steinbrech, "Memory Effect of Crack Resistance During Slow Crack Growth in Notched  $\text{Al}_2\text{O}_3$  Bend Specimens," *J. Mater. Sci. Lett.* 1[8] 327-29 (1982).
3. R.F. Cook, B.R. Lawn and C.J. Fairbanks, "Microstructure-Strength Properties in Ceramics: I. Effect of Crack Size on Toughness," *J. Amer. Ceram. Soc.* 68[11] 604-15 (1985).
4. P.L. Swanson, C.J. Fairbanks, B.R. Lawn, Y-W. Mai and B.J. Hockey, "Crack-Interface Bridging as a Fracture Resistance Mechanism in Ceramics: I. Experimental Study on Alumina," *J. Amer. Ceram. Soc.* 70[4] 279-89 (1987).
5. S.J. Bennison and B.R. Lawn, "Role of Interfacial Grain-Bridging Sliding Friction in the Crack-Resistance and Strength Properties of Non-transforming Ceramics," *Acta Metall.* 37[10] 2659-71 (1989).
6. G. Bayer, "Thermal Expansion Anisotropy of Oxide Compounds," *Proc. Br. Ceram. Soc.* [22] 39-53 (1973).
7. S. M. Lange, C. L. Fillmore and L. H. Maxwell, "The System Beryllia-Alumina-Titania: Phase Relations and General Properties of Three-Component Porcelains," *J. Res. Natl. Bur. Stds.* 48[4] 298-301 (1952).
8. J.L. Runyan and S.J. Bennison, "Flaw Tolerance Properties of Aluminum Titanate reinforced Alumina Ceramics," *J. Europ. Ceram. Soc.*, in press.
9. S.J. Bennison, H.M. Chan and B.R. Lawn, "Effect of Heat Treatment on Crack-Resistance Curves in Liquid-Phase-Sintered Alumina," *J. Amer. Ceram. Soc.* 72[4] 677-79 (1989).
10. J. Rödel, J.F. Kelly and B.R. Lawn, *J. Amer. Ceram. Soc.* "In Situ Measurements of Bridged Crack Interfaces in the SEM," *J. Amer. Ceram. Soc.*, in press.
11. P. Chantikul, S.J. Bennison and B.R. Lawn, *J. Amer. Ceram. Soc.*, "Role of Grain Size in the Strength and R-curve Properties of Alumina," *J. Amer. Ceram. Soc.* 73[8] 2419-27 (1990).
12. S.J. Bennison, J. Rödel, S. Lathabai, P. Chantikul, B.R. Lawn "Microstructure, Toughness Curves and Mechanical Properties of Alumina Ceramics," *Toughening Mechanisms in Quasi-Brittle Materials*, Kluwer Academic Publishers, Dordrecht, The Netherlands, in press.

# Fabrication of Flaw-tolerant Aluminum-titanate-reinforced Alumina

Julie L. Runyan\* & Stephen J. Bennison†

Ceramics Division, National Institute of Standards and Technology, Gaithersburg, MD 20899, USA

(Received 18 June 1990; accepted 23 October 1990)

## Abstract

*The fabrication and the flaw tolerance behavior of particulate aluminum-titanate-reinforced alumina composites have been studied. High-density (~99% theoretical) composites with controlled microstructures are readily produced via a conventional ceramics processing scheme using starting powders of  $\alpha$ -alumina and  $\beta$ -aluminum titanate. Indentation-strength measurements demonstrate that these composites are highly flaw tolerant. Direct observations of crack evolution from Vickers indentations during loading reveal a strong crack-stabilization with pre-failure extensions of a millimeter or more. This stabilization gives rise to the flaw tolerance properties and results from pronounced crack-resistance (*R*-curve) behavior. Grain-localized crack bridging is active in these materials and is believed to be a contributor to the *R*-curve properties.*

*In dieser Arbeit wurde die Herstellung und die Anfälligkeit gegenüber Gefügefehlern eines  $\text{Al}_2\text{TiO}_5$ -Teilchen verstärkten  $\text{Al}_2\text{O}_3$ -Verbundwerkstoffs untersucht. Aus  $\alpha$ - $\text{Al}_2\text{O}_3$ - und  $\beta$ - $\text{Al}_2\text{TiO}_5$ -Ausgangspulvern konnten mittels keramiktypischer Verfahrungsweise Verbundwerkstoffe mit hoher Dichte (99% th.) und mit kontrollierten Gefügen auf einfache Weise gesintert werden. Härteeindruck- und Festigkeitsmessungen konnten zeigen, daß diese Verbundwerkstoffe eine sehr geringe Anfälligkeit gegenüber Gefügefehlern besitzen. Die in-situ Beobachtung der durch Vickers-Eindrücke hervorgerufenen Rißaus-*

*breitung während der Belastung zeigt eine hohe Rißstabilisierung mit Rißlängen von über 1 mm vor dem Versagen des Materials. Diese Stabilisierung vermindert die Anfälligkeit gegenüber Gefügefehlern und ist die Folge eines ausgeprägten *R*-Kurven-Verhaltens dieses Werkstoffs. Rißflankenüberbrückung durch Reibungsflächen an einzelnen Körnern kommt in diesen Materialien vor und wird als eine der Ursachen für das *R*-Kurven-Verhalten gesehen.*

*On a étudié l'élaboration et la tolérance aux défauts de composites d'alumine renforcée par des particules de titanate d'aluminium. On a pu ainsi produire des composites de haute densité (~99% de la densité théorique) à microstructure contrôlée, et ceci par un procédé d'élaboration conventionnelle mettant en jeu des poudres de départ d'alumine  $\alpha$  et de titanate d'aluminium  $\beta$ . Des mesures de résistance à la rupture par indentation ont montré que ces composites sont hautement résistants aux défauts. Les observations directes d'évolution sous charge de fissures induites par indentation Vickers ont révélé une forte stabilisation des fissures avec des extensions de pré-fissuration d'un millimètre ou plus. Cette stabilisation entraîne les propriétés de tolérance aux défauts et est la conséquence d'une haute résistance à la fissuration (courbe *R*). On suppose que le pontage des fissures observé pour les grains contribue également aux propriétés des courbes *R*.*

## 1 Introduction

One of the more important consequences of an increasing crack resistance with increasing crack length (*R*-curve, *T*-curve) behavior<sup>1-9</sup> in ceramics is the reduced sensitivity of the strength to the size of any processing or service-induced defects, viz. the

\* Present address: Department of Materials Engineering, Virginia Polytechnic Institute and State University, Blacksburg, VA 24061, USA.

† To whom correspondence should be addressed at: Department of Materials Science and Engineering, Lehigh University, Bethlehem, PA 18015, USA.



quality of 'flaw tolerance'.<sup>5,10,11</sup> The resulting improvements in reliability as reflected in greater Weibull moduli<sup>12-16</sup> and enhanced fatigue limits<sup>17</sup> make flaw tolerance a desirable property for brittle materials in structural applications.

A variety of phenomena can give rise to *R*-curves in ceramics.<sup>18</sup> For non-transforming materials with relatively simple microstructures and with predominantly intergranular fracture, grain-localized crack bridging has been identified as a primary mechanism.<sup>19,20</sup> In this case, intact grains bridge the crack walls and apply closure forces that shield the crack tip from the applied stress intensity field.<sup>21,22</sup> These bridging grains are assumed to be 'locked' into the microstructure by local thermal expansion anisotropy stresses.<sup>8,23</sup> The important microstructural and material parameters include grain size and shape, the intensity of the residual stress, grain boundary toughness and friction at the sliding grain-matrix interface.<sup>23</sup> A proper understanding of the role of these parameters opens the way to tailoring the *R*-curve and flaw-tolerance properties through controlled processing.<sup>24</sup>

In the present study, improvements in the *R*-curve and flaw-tolerance characteristics of alumina are sought through enhancement of the local residual stress levels. The approach is to incorporate a second phase  $\beta$ -aluminum titanate into the  $\alpha$ -alumina matrix. Aluminum titanate exhibits extremely high thermal expansion anisotropy;<sup>25</sup> when added to alumina it is expected to raise the maximum levels of residual stress by approximately one order of magnitude. This estimate is determined from  $\sigma_R \approx \frac{1}{2}E\Delta\alpha\Delta T$  and the most severe misorientation of alumina and aluminum titanate; ( $\sigma_R$  = residual stress;  $E$  = Young's modulus,  $\Delta\alpha$  = thermal expansion difference,  $\Delta T$  = temperature range over which stresses develop).

The fabrication of aluminum titanate and alumina-aluminum titanate is usually accomplished via a reaction-sintering route with starting powders of alumina and titania.<sup>26-29</sup> However, unless careful control of the powder characteristics is maintained during processing<sup>30</sup> the resulting microstructures generally display low as-fired densities (<90% theoretical) and abnormal grain growth, making them weak and, therefore, generally unsuitable for structural applications.

In the present work a conventional ceramics processing scheme using starting powders of alumina and aluminum titanate is developed whereby composites of high fired density and controlled grain structure are readily manufactured. The *R*-curve and flaw-tolerance properties are investigated

using the indentation-strength technique in which the strength is determined as a function of indentation load.<sup>5,9,11,22</sup> The interaction of cracks with the microstructure is studied using a statically loaded biaxial flexure device mounted either in an optical or scanning electron microscope (SEM). It will be shown that certain composites of  $\alpha$ -alumina reinforced with  $\beta$ -aluminum titanate demonstrate pronounced flaw tolerance resulting from the crack-stabilizing effect of a strong *R*-curve. The unusual flaw-tolerance properties coupled with the ease of fabrication make these composites attractive for applications where components are subjected to damage during service.

## 2 Experimental

### 2.1 Composite fabrication

All powder processing was carried out in class A-100 clean room conditions. A stable colloidal suspension of high-purity  $\alpha$ -Al<sub>2</sub>O<sub>3</sub> (Sumitomo AKP-HP grade (99.995% pure, 0.5  $\mu$ m crystallites), Sumitomo Chemical America Inc., New York, USA) in water containing the desired volume fraction of  $\beta$ -Al<sub>2</sub>TiO<sub>5</sub> (99.9%, 1-5  $\mu$ m particle size, Trans-Tech Inc., Adamstown, USA) was prepared by adjusting the pH to  $\approx 3$  with additions of HNO<sub>3</sub>. Drying was carried out using a hot-plate while stirring continuously and the resulting cake was subsequently broken down by crushing in a polyethene bag. Disc-shaped test specimens, 25 mm diameter and 5 mm thickness, were fabricated by uniaxial pressing at 63 MPa using a high-purity graphite die, punch and spacer assembly. Removal of any defects associated with die pressing was achieved by subsequent wet-bag isostatic pressing at 350 MPa. A green density of  $\approx 55\%$  of the theoretical limit was attained using this procedure.

Green discs were packed in loose alumina powder in high-purity alumina crucibles for firing using a two-stage heat treatment. The first stage consisted of heating at a rate of 50°C/h to a calcining temperature of 1050°C with a 12 h soak. The second stage consisted of heating at a rate of 500°C/h from the calcining temperature to a sintering temperature of 1600°C with hold times of 1 h and 16 h. Specimens were cooled at  $\approx 500^\circ\text{C/h}$ . All heat treatments were carried out in air using a MoSi<sub>2</sub> resistance-heated furnace.

Sample specimens from each batch were subjected to microstructural characterization. Densities were measured by the Archimedes method using water as the immersion medium.<sup>31</sup> Surfaces were prepared,

where possible, for optical and scanning electron microscopy (SEM) by diamond-polishing to a 1  $\mu\text{m}$  finish. Microstructures were revealed by thermal etching (air, 1500 C, 6 min) and grain sizes were determined by a linear intercept technique.<sup>32</sup> Where polishing was found to be impractical due to localized spontaneous microfracture, approximate grain sizes were determined from fracture surfaces examined by SEM. Phases present in the composite were identified by X-ray diffraction.

## 2.2 Indentation-strength testing

Prior to testing, each fired disc was machined to a thickness of 2.5 mm and the prospective tensile face diamond-polished to a 1  $\mu\text{m}$  finish. Care was taken to ensure that polishing removed the majority of the surface damage introduced during the preliminary machining operation. Most specimens were indented at their face centers with a Vickers diamond pyramid at contact loads between 3 and 300 N; some discs were left unindented as controls. All indentations were made under ambient laboratory conditions and allowed to stand for 10 min. Biaxial strength tests were then made using a flat circular punch (4 mm diameter) and a three-point support (15 mm diameter).<sup>33</sup> A drop of dry silicone oil was placed on each indentation prior to testing and the failure times were kept below 20 ms to minimize possible effects from moisture assisted non-equilibrium crack growth. Inert strengths were calculated from the breaking loads and specimen dimensions using thin-plate formulas.<sup>34</sup> Special effort was made to examine all specimens after testing using optical microscopy to verify that the indentation contact site acted as the origin of failure. Unsuccessful breaks were incorporated into the data pool of unindented controls.

Direct observations of crack extension from indentations during loading were made on selected specimens using a biaxial flexure device mounted on an optical microscope.<sup>19</sup> Crack-microstructure interactions were also investigated using this fixture mounted in an SEM.

## 3 Results

Table 1 lists the salient characteristics of the two composites (20 vol.% aluminum titanate) prepared in this study.

Figure 1 shows the microstructure of composite A (alumina grain size = 5.8  $\mu\text{m}$ ). The aluminum titanate phase is primarily distributed as isolated particles both at grain boundaries and within grains.

**Table 1.** Microstructural characteristics of the two composites studied

Composite	Volume % $\text{Al}_2\text{TiO}_5$	Grain size $\text{Al}_2\text{O}_3$ ( $\mu\text{m}$ )	Density ( $\text{mg m}^{-3}$ )	Phases present
A	20	5.8	3.88 (98.9%)	$\alpha\text{-Al}_2\text{O}_3$ $\beta\text{-Al}_2\text{TiO}_5$
B	20	$\approx 14$	3.89 (99.0%)	$\alpha\text{-Al}_2\text{O}_3$ $\beta\text{-Al}_2\text{TiO}_5$

Local concentrations of aluminum titanate are occasionally observed. These islands typically consist of 5–10 grains and are probably remnants of hard agglomerates in the base powder. The alumina matrix shows no sign of abnormal grain growth although faceted grain shapes are evident. The microstructure is of high density ( $\sim 99\%$ ), as confirmed by direct measurements (Table 1), with angular pores resulting from grain pullout during polishing constituting the prominent surface defect population. Microcracks are seen in this composite and are predominantly associated with the islands of aluminum titanate.

Figure 2 shows the microstructure of composite B (alumina grain size  $\approx 14 \mu\text{m}$ ). The primary distinctions between composites A and B are the increased scale of the microstructure in the latter and the widespread occurrence of microcracking in this coarser material. The difficulty in preparing quality polished sections for microscopy implies that the majority of the microcracks form spontaneously on cooling from the sintering temperature.

Figure 3 presents the measured inert strengths as a function of indentation load for both materials. Each datum point represents the mean and standard

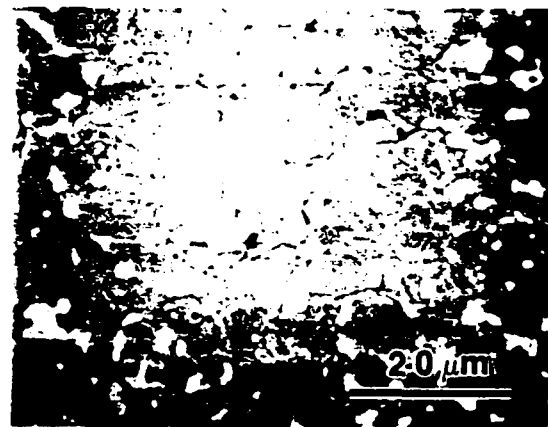


**Fig. 1.** SEM micrograph (back-scattered electron image) of a polished and etched section from composite A (20 vol.%  $\text{Al}_2\text{TiO}_5$ ,  $\text{Al}_2\text{O}_3$  grain size = 5.8  $\mu\text{m}$ ). The lighter phase is  $\text{Al}_2\text{TiO}_5$ , the gray phase is  $\text{Al}_2\text{O}_3$  and the black phase is porosity.

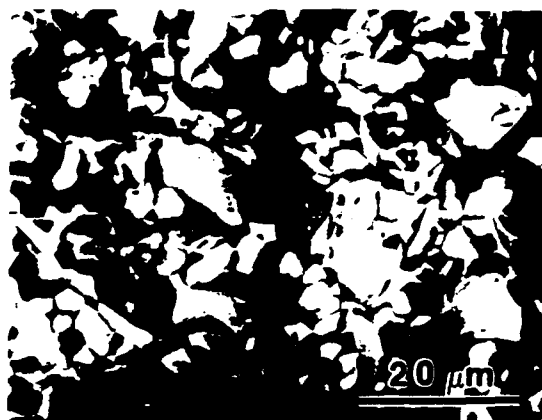


Fig. 2. SEM micrograph (back-scattered electron image) of a fracture surface from composite B (20 vol.%  $\text{Al}_2\text{TiO}_5$ ,  $\text{Al}_2\text{O}_3$  grain size  $\approx 14 \mu\text{m}$ ).

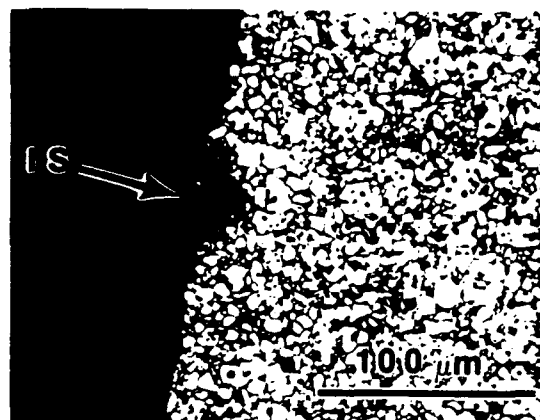


Fig. 4. Optical micrograph (reflected light) of fracture path (*post mortem*) in composite A. The 30 N indentation site (IS) is clearly included in the fracture path.

deviation of, on average, four indentation-flaw failures: the boxes at the far left represent failures from natural flaws. Figure 4 is a post-mortem micrograph showing the fracture path in one specimen tested: the fracture clearly includes the indentation site and is assumed to have initiated from it. Great care was taken to ensure the indentation site was the source of the critical flaw for *all* data reported.

Both materials show *unusually* pronounced flaw tolerance behavior with little dependence of the strength on indentation load. The strengths of specimens containing 300 N indentations are only slightly degraded ( $\approx 8\%$ ) in comparison to the unindented controls. Composite B is considerably weaker, by a factor of  $\approx 5$ , than composite A for a relatively small ( $\approx 2.5$ ) increase in grain size.

Observations of crack evolution from an indent-

ation during static loading are presented in Figs 5 and 6. Figure 5 shows the crack pattern from a 30 N indentation during subsequent biaxial tensile loading. The radial cracks have extended stably from an initial size of the order of  $100 \mu\text{m}$  to sizes in the millimeter range. Note that the cracks are in equilibrium with the applied tensile field. Figure 6 shows interactions of the primary radial crack with features of the microstructure. The failure mode is predominantly intergranular and active bridging can be readily observed. The primary crack is heavily deflected on the scale of the grain size and tends to be attracted to the matrix-second-phase interface.

Figure 7 shows a secondary crack of 5–20 grain dimensions in size formed during the loading of composite A. Such secondary cracks are seen on the tensile surface of the test specimen within the zone of

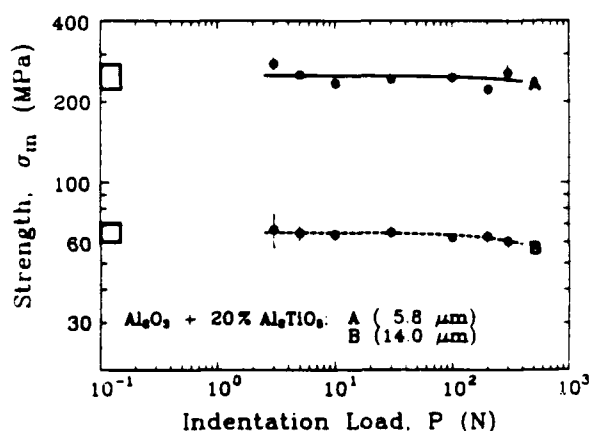


Fig. 3. Plot of inert strength,  $\sigma_m$ , versus indentation load,  $P$ , for the two composites. The curves are empirical linear fits to the data and serve only as a guide to the eye. Note the pronounced flaw tolerance of these materials.

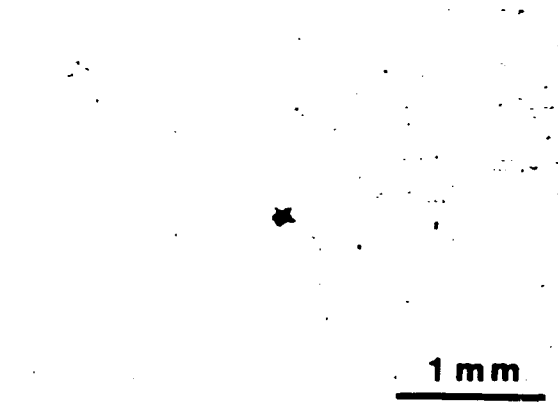


Fig. 5. Optical micrograph (reflected light) of a 30 N indentation loaded in equibiaxial flexure (composite A). The radial cracks have grown *stably* from the initial size ( $\sim 100 \mu\text{m}$ ) produced by indentation and are in equilibrium with the applied tensile field.

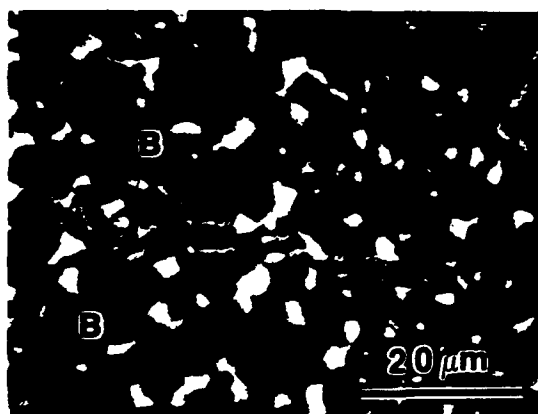


Fig. 6. SEM micrograph (back-scattered electron image) showing details of crack-microstructure interactions. Evidence for bridging grains can be seen (e.g. at B-B).

constant equibiaxial tension. The location of these cracks does not appear to correlate with the position and evolution of the primary cracks developing from the indentation site.

Figure 8 displays the load versus displacement of the testing machine cross-head responses for the two composites each containing 200 N Vickers indentations. The finer material (A) shows predominantly linear (Hookean) behavior during loading with slight non-linear characteristics just prior to peak load. The composite fails abruptly at peak load. The coarser material (B) shows very pronounced non-linear behavior with greater strain to a lower maximum in load. Failure then proceeds in a stable manner until final rupture at very large displacements (strains). Widespread secondary cracking is observed on the tensile face of composite B during testing. Note that a finite force,  $P'$ , is required to separate the crack walls of composite B after large displacements.



Fig. 7. Optical micrograph (reflected light) of a secondary crack (C-C) located on the tensile face of one test specimen within the equibiaxial tensile zone.

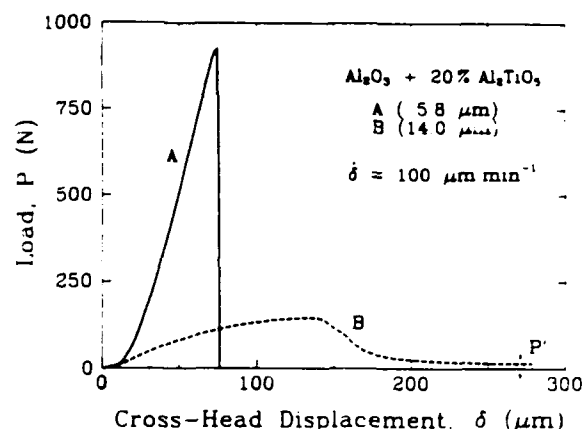


Fig. 8. Load versus cross-head displacement traces for composites A and B each containing 200 N Vickers indentations. Material A displays unstable fracture at a critical displacement and evidence of slight non-linearity prior to reaching peak load. Material B shows stable fracture and very pronounced non-linear behavior. Note material B shows some load bearing capacity well after peak loading (denoted by  $P'$ ).

#### 4 Discussion

Two important conclusions may be drawn from these experiments: (i) high-density alumina-aluminum-titanate composites with controlled microstructures can be readily fabricated via a processing route using starting powders of alumina and aluminum titanate; (ii) reinforcement of alumina with aluminum titanate results in composites with pronounced flaw tolerance.

The microstructures developed in the present work display several improvements over those generally produced by reaction sintering between alumina and titania.<sup>26-29</sup> The first clear improvement is the absence of abnormal grain growth and associated pore-grain boundary separation. Addition of the aluminum titanate phase prior to the start of sintering is thought to suppress the initiation of abnormal grains by a pinning mechanism similar to that suggested for other two-phase systems.<sup>35</sup> The second improvement is the attainment of high ( $\sim 99\%$  theoretical) fired densities. The high density results from the avoidance of pore-grain boundary separation associated with abnormal grain growth<sup>36</sup> and the indirect enhancement of densification with respect to coarsening resulting from grain growth inhibition.<sup>37</sup> Also, it is possible that the aluminum titanate enhances densification processes directly in a fashion analogous to the function of titania additions to alumina.<sup>38,39</sup>

The indentation-strength properties of the composites may be compared with those of unreinforced aluminas of varying  $R$ -curve and flaw tolerance

characteristics. Figure 9 presents the behavior of composite A together with trends for aluminas with grain sizes of 5.8 and 80  $\mu\text{m}$ . (The trends for the aluminas were calculated from a 'calibrated' grain-bridging model used previously to interpret the effect of grain size on  $R$ -curve behavior.<sup>23,24</sup>) It can be seen that composite A has superior flaw tolerance to the 80  $\mu\text{m}$  alumina (D), i.e. it is stronger and displays less degradation in strength with increasing contact load. The remaining alumina (C), with comparable grain size to composite A, shows higher strengths at lower indentation loads but the strength degrades rapidly with increasing contact load and eventually falls well below composite A at the highest loads. Composite A is, therefore, a better choice of material than monophase alumina for applications where the component is subjected to in-service damage.

The composites may also be compared to pure aluminum titanate ceramics. It is generally difficult to fabricate aluminum titanate with sufficiently fine grain size to avoid spontaneous microcracking on cooling from the sintering temperature.<sup>26-29</sup> As such, it is damage tolerant and shows strong  $R$ -curve behavior but at the same time is weak (strengths  $\approx 20$  MPa for optimum load-displacement characteristics).<sup>40</sup> Composite B displays similar load versus cross-head displacement properties to pure aluminum titanate, is equally damage tolerant but is stronger by approximately a factor of three. Composite B may, therefore, be considered a contender for applications where pure aluminum titanate is presently used.

The unusual flaw tolerance of the aluminum-titanate-reinforced alumina composites results from strong stabilization of incipient critical flaws; *this stabilization is a manifestation of pronounced  $R$ -curve*

*behavior*. The underlying physical mechanism(s) giving rise to the flaw-tolerance properties observed are yet to be unequivocally identified. Evidence for grain bridging is presented in the form of in-situ observations of loaded cracks (Fig. 6). The ability of composite B to support a finite load even after what is normally considered catastrophic failure (Fig. 8) further suggests the presence of intact grain bridges across the crack-wall interfaces. These preliminary observations imply that grain bridging is a contributor to the  $R$ -curve and flaw-tolerance properties of the composites.

The subsidiary cracking observed on the tensile faces of the test specimens is also expected to contribute to the damage tolerance of the composites. One consequence of the subsidiary cracking is a non-linear stress-strain response as reflected in the load-deflection traces recorded (Fig. 8). Such non-linear behavior influences the strength properties by reducing the applied stress-intensity field.<sup>41,42</sup> The mechanism through which the composites tolerate widespread damage evolution is presently unclear. However, considering the potential benefits of such unusual damage-tolerant characteristics further investigation is warranted. It is worth noting that the behavior observed in the present work is similar to damage phenomena reported for some continuous fiber-reinforced composites.<sup>43</sup>

It is anticipated that the strength and damage-tolerance properties of alumina-aluminum titanate composites can be further tailored through microstructure adjustment. When manipulating the toughness behavior in this manner there is a compromise between the component strength and flaw tolerance. Potential applications will ultimately depend on a foreknowledge of the degree of damage a component is likely to experience and the stresses to be supported. It is recommended that  $\text{Al}_2\text{O}_3$ - $\text{Al}_2\text{TiO}_5$  composites are given full consideration for components where damage tolerance and reliability are the primary design requirements.

#### Acknowledgements

The authors wish to thank E. P. Butler, B. R. Lawn, N. P. Padture and J. Rödel for useful discussions. J. F. Kelly contributed to the SEM work. J. Cline assisted with the X-ray diffraction characterization and S. Darby machined the test specimens. The work was supported by the US Air Force Office of Scientific Research and E. I. DuPont de Nemours & Co. Inc.

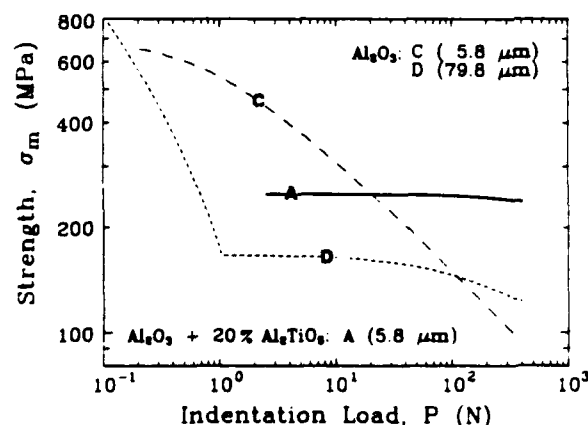


Fig. 9. Strength,  $\sigma_m$ , versus indentation load,  $P$ , characteristics. Results for composite A compared to trends calculated for aluminas of grain sizes C, 5.8  $\mu\text{m}$ ; D, 79.8  $\mu\text{m}$  using a bridging model.<sup>23,24</sup>

# References

1. Hübner, H. & Jillek, W., Sub-critical crack extension and crack resistance in polycrystalline alumina. *J. Mater. Sci.*, **12** (1977) 117-25.
2. Knehan, R. & Steinbrech, R. W., Memory effect of crack resistance during slow crack growth in notched  $\text{Al}_2\text{O}_3$  bend specimens. *J. Mater. Sci. Lett.*, **1** (1982) 327-9.
3. Steinbrech, R. W., Knehan, R. & Schaarwachter, W., Increase of crack resistance during slow crack growth in  $\text{Al}_2\text{O}_3$  bend specimens. *J. Mater. Sci.*, **18** (1983) 265-70.
4. Knehan, R. & Steinbrech, R. W., Effect of grain size on the crack-resistance curves of  $\text{Al}_2\text{O}_3$  bend specimens. In *Science of Ceramics*, Vol. 12, ed. P. Vincenzini. Ceramurgia, Imola, Italy, 1984, pp. 613-19.
5. Cook, R. F., Lawn, B. R. & Fairbanks, C. J., Microstructure-strength properties in ceramics. I. Effect of crack size on toughness. *J. Am. Ceram. Soc.*, **68** (1985) 604-15.
6. Cook, R. F., Lawn, B. R. & Fairbanks, G. J., Microstructure-strength properties in ceramics: II. Fatigue relations. *J. Am. Ceram. Soc.*, **68** (1985) 616-23.
7. Rose, L. R. F. & Swain, M. V., Two *R*-curves for partially stabilized zirconia. *J. Am. Ceram. Soc.*, **69** (1986) 203-7.
8. Swain, M. V., *R*-curve behavior in a polycrystalline alumina material. *J. Mater. Sci. Lett.*, **5** (1986) 1313-15.
9. Krause, R. F., Fuller, E. R. & Rhodes, J. F., Fracture resistance behavior of silicon carbide whisker-reinforced alumina composites with different porosities. *J. Am. Ceram. Soc.*, **73** (1990) 559-66.
10. Lawn, B. R. & Fairbanks, C. J., Toughness and flaw responses in nontransforming ceramics: implications for NDE. In *Review of Progress in Quantitative NDE*, Vol. 6B, ed. D. O. Thompson & D. E. Chimenti. Plenum, NY, USA, 1987, pp. 1023-30.
11. Bennison, S. J. & Lawn, B. R., Flaw tolerance in ceramics with rising crack-resistance behavior. *J. Mater. Sci.*, **24** (1989) 3169-75.
12. Kendall, K., McN. Alford, N., Tan, S. R. & Birchall, J. D., Influence of toughness on Weibull modulus of ceramic bending strength. *J. Mater. Res.*, **1** (1986) 120-3.
13. Cook, R. F. & Clarke, D. R., Fracture stability, *R*-curves and strength variability. *Acta Metall.*, **36** (1988) 555-62.
14. Shetty, D. K. & Wang, J.-S., Crack stability and strength distribution of ceramics that exhibit rising crack-growth-resistance (*R*-curve) behavior. *J. Am. Ceram. Soc.*, **72** (1989) 1158-62.
15. Evans, A. G., New opportunities in the processing of high reliability structural ceramics. In *Ceramic Transactions*, Vol. 1, ed. G. L. Messing, E. R. Fuller, Jr & H. Hausner. American Ceramic Society, Westerville, OH, USA, 1989, pp. 989-1010.
16. Li, C.-W. & Yamanis, J., Super-tough silicon nitride with *R*-curve behavior. *Ceramic Engineering and Science Proceedings*, ed. R. E. Barks. The American Society, Westerville OH, USA, **10** (1989) 632-45.
17. Lathabai, S. & Lawn, B. R., Fatigue limits in noncyclic loading of ceramics with crack-resistance curves. *J. Mater. Sci.*, **24** (1989) 4298-306.
18. Evans, A. G., Perspectives on the development of high-toughness ceramics. *J. Am. Ceram. Soc.*, **73** (1990) 187-206.
19. Swanson, P. L., Fairbanks, C. J., Lawn, B. R., Mai, Y.-W. & Hockey, B. J., Crack-interface grain bridging as a fracture resistance mechanism in ceramics. I. Experimental study on alumina. *J. Am. Ceram. Soc.*, **70** (1987) 279-89.
20. Swanson, P. L., Crack-interface traction: A fracture-resistance mechanism in brittle polycrystals. In *Advances in Ceramics*, Vol. 22, American Ceramic Society, Westerville, OH, USA, 1988, pp. 135-55.
21. Mai, Y.-W. & Lawn, B. R., Crack-interface grain bridging as a fracture resistance mechanism in ceramics. II. Theoretical Fracture Mechanics Model. *J. Am. Ceram. Soc.*, **70** (1987) 289-94.
22. Cook, R. F., Fairbanks, C. J., Lawn, B. R. & Mai, Y.-W., Crack resistance by interfacial bridging: Its role in determining strength characteristics. *J. Mater. Res.*, **2** (1987) 345-56.
23. Bennison, S. J. & Lawn, B. R., Role of interfacial grain-bridging sliding friction in the crack-resistance and strength properties of nontransforming ceramics. *Acta Metall.*, **37** (1989) 2659-71.
24. Chantikul, P., Bennison, S. J. & Lawn, B. R., Role of grain size in the strength and *R*-curve properties of alumina. *J. Am. Ceram. Soc.*, **73** (1990) 2419-27.
25. Bayer, G., Thermal expansion characteristics and stability of pseudobrookite type compounds.  $\text{M}_2\text{O}_3$ . *J. Less Common Met.*, **24** (1971) 129-38.
26. Cleveland, J. J. & Bradt, R. C., Grain size microcracking relations for pseudobrookite oxides. *J. Am. Ceram. Soc.*, **61** (1978) 478-81.
27. Hamano, K., Ohya, Y. & Nakagawa, Z.-E., Microstructure and mechanical strength of aluminum titanate ceramic prepared from mixture of alumina and titania. *Yogyo-Kyokai-Shi*, **91** (1983) 95-101.
28. Ohya, Y., Hamano, K. & Nakagawa, Z.-E., Microstructure and mechanical strength of aluminum titanate ceramics prepared from synthesized powders. *Yogyo-Kyokai-Shi*, **91** (1983) 289-97.
29. Qian, D.-F., Ohya, Y., Hamano, K. & Nakagawa, Z.-E., Effects of excess alumina on microstructure of aluminum titanate ceramics prepared from mixture of alumina and titania. *Yogyo-Kyokai-Shi*, **93** (1985) 315-21.
30. Okamura, H., Barringer, E. A. & Bowen, H. K., Preparation and sintering of narrow-sized  $\text{Al}_2\text{O}_3$ - $\text{TiO}_2$  composites. *J. Mater. Sci.*, **24** (1989) 1867-80.
31. Pennings, E. C. M. & Grellner, W., Precise nondestructive determination of the density of porous ceramics. *J. Am. Ceram. Soc.*, **72** (1989) 1268-70.
32. Wurst, J. C. & Nelson, J. A., Lineal intercept technique for measuring grain size in two-phase polycrystalline ceramics. *J. Am. Ceram. Soc.*, **55** (1972) 109.
33. Marshall, D. B., An improved biaxial flexure test for ceramics. *Am. Ceram. Soc. Bull.*, **59** (1980) 551-3.
34. De With, G. & Wagemans, H. H. M., Ball-on-ring test revisited. *J. Am. Ceram. Soc.*, **72** (1989) 1528-41.
35. Brook, R. J., Controlled grain growth. In *Treatise on Materials Science and Technology*, Vol. 9, ed. F. F. Y. Wang. Academic Press, NY, USA, 1976, pp. 331-64.
36. Coble, R. L. & Burke, J. E., Sintering in ceramics. *Progr. Ceram. Sci.*, **3** (1963) 197-251.
37. Harmer, M. P., Use of solid-solution additives in ceramic processing. In *Advances in Ceramics*, Vol. 10, ed. W. D. Kingery. American Ceramic Society, Westerville, OH, USA, 1984, pp. 679-96.
38. Bagley, R. D., Cutler, I. B. & Johnson, D. L., Effect of  $\text{TiO}_2$  on initial sintering of  $\text{Al}_2\text{O}_3$ . *J. Am. Ceram. Soc.*, **53** (1970) 136-41.
39. Morgan, P. E. D. & Koutsoutsis, M. S., Phase studies concerning sintering in aluminas doped with  $\text{Ti}^{4+}$ . *J. Am. Ceram. Soc.*, **68** (1985) C156-C158.
40. Hamano, K., Ohya, Y. & Nakagawa, Z.-E., Crack propagation resistance of aluminum titanate ceramics. *Int. J. High Technol. Ceram.*, **1** (1985) 129-37.
41. Marshall, D. B., Strength characteristics of transformation-toughened zirconia. *J. Am. Ceram. Soc.*, **69** (1986) 173-80.
42. Chuang, T.-J. & Mai, Y. W., Flexural behavior of strain-softening solids. *Int. J. Solids Structures*, **25** (1989) 1427-43.
43. Roach, D. A., Damage evolution in ceramic matrix composites. Paper 101-SIV-90 presented at the 92nd Annual Meeting of the American Ceramic Society, Dallas, TX, USA, 1990.

**Crack Closure Forces in Ceramics:  
Characterization and Formation**

**Jürgen Rödel**

**Ceramics Division  
National Institute of Standards and Technology  
Gaithersburg, MD 20899**

***For: J. European Ceramic Society***

## Abstract:

In situ crack propagation studies in the scanning electron microscope (SEM) on seven materials are used to define three general categories for crack bridging elements: intact (elastic) bridges, frictionally sliding (plastic) bridges and mechanically interlocked (elastic-plastic) bridges . A number of examples are provided, some including sequences detailing bridge formation and bridge evolution. Failure modes of all these restraining elements, their interrelations and synergistic effects are discussed.

A simple fracture mechanics model attempts to provide the criteria for bridge formation. The relevant microstructural parameters are: grain size and shape, intra- or intercrystalline fracture energy, residual stress and Young's modulus.

In situ Rissausbreitung an sieben verschiedenen Materialien im Rasterelektronenmikroskop (REM) dient als Grundlage um drei allgemeine Klassen von Elementen die der Rissüberbrückung dienen, zu definieren. Diese sind: intakte (elastische) Brücken, Reibungsbrücken (plastische Brücken) und mechanisch verhakte (elastisch - plastische) Brücken. Eine Anzahl von Beispielen, z.T. Folgen, erläutern Brückenbildung und Brückenentwicklung.

Ein einfaches Modell aus der Bruchmechanik versucht, Kriterien zur Brückenbildung zu geben. Als entscheidende Gefügeparameter werden Korngrösse und Kornform, inter - oder intrakristalline Bruchenergie, Restspannungen und E - modul identifiziert.



## 1. Introduction

Ceramic materials still find only limited application because of their brittleness. A sound approach to increase the fracture toughness in these materials is therefore the delocalization of the fracture process. This allows a participation of the crack interfaces and the surrounding areas in the energy absorption process and thereby shielding of the crack tip from the externally applied load. These mechanisms are divided into dilation (transformation toughening<sup>1</sup> and microcrack toughening<sup>2</sup>) and crack bridging<sup>3-6</sup> (use of crack closure forces to limit a further opening of the crack). Both mechanisms lead to R-curve behaviour, an increase in crack resistance with increasing crack length. Our focus here will be on crack closure forces with sole emphasis on brittle restraining elements.

To avoid confusion we start by giving some simple definitions: Crack closure force (also crack interface traction): Closure traction which is applied perpendicular to the crack interfaces, thereby reducing the crack opening displacement (COD). Closure forces can be combined (for restrictions, see discussion by Smith<sup>7</sup>) and be taken as a smeared out closure stress ( $p$ ) as a function of crack opening ( $2u$ ). They are then represented as  $p(u)$  function.

Bridge (also: bridging element, restraining element): Any microstructural element which provides a closure force in the crack wake.

Primary crack (also: main crack): Crack system providing continuous (at least one-dimensional) link between crack mouth and crack tip, not necessarily continuous in two dimensions.

Secondary crack: Connected to primary crack; opening of secondary crack is derived from closure force across primary crack. Secondary cracks close therefore when closure force subsides.

Microcrack: Small crack (with respect to the microstructure), not usually connected to primary crack. Opening arises from residual stress, therefore persistent.

While a number of discrete bridging elements have been studied in detail, e.g. fibers<sup>8</sup>, whiskers<sup>6</sup>, particular grain configurations<sup>9</sup>, a more general picture has not yet emerged. The attempt here is therefore to step back and develop a fundamental characterization and classification of crack closure forces in different types of materials which could include fibers, whiskers, elongated grains, etc. The hope then is to give general guidelines to the processing community to help in the quest for tougher materials.

The study was conducted in two parts. Firstly, an in depth characterization of bridge configurations: what kind of bridges can be found, in what situation do they occur, how is energy absorbed and how do they fail. For this part, an in situ straining stage<sup>10,11</sup>, custom designed for the SEM, was used. Secondly, a simplistic theoretical analysis is given, describing the formation of closure forces. This model describes generation of a single microcrack at the crack tip and is based on detailed crack propagation studies.

Four classes of materials were investigated:

- a) materials with a modest thermal expansion anisotropy (two aluminas),
- b) materials containing strong reinforcements (two silicon carbide whisker reinforced aluminas),

- c) materials with strong internal residual stresses (two  $\text{Al}_2\text{TiO}_4$  /  $\text{Al}_2\text{O}_3$  composites),
- d) a more complex, metal- and particulate reinforced alumina-based composite ( $\text{SiC}/\text{Al}/\text{Al}_2\text{O}_3$ ).

## 2. Experiment

All microstructural observations were obtained with an in situ custom-designed straining stage built into an SEM chamber<sup>10,11</sup>. Extension of a piezoelectric translator delivers a finely tuneable load (measured through a load cell) to the specimen. Crack propagation is quasi-static and recorded on videotape with intermittent periods of static loading to allow for closer observation and micrographic recording. Details concerning the design of the fracture stage can be found elsewhere<sup>11</sup>. Similar devices for different crack geometries are also described by Frei and Grathwohl<sup>12</sup>. All micrographs shown are taken from specimen held at  $\approx 95\%$  of the equilibrium load for crack extension.

Crack-microstructure interactions were recorded using compact tension specimen. This sample geometry offers the advantage of extensive stable crack propagation. A large sample area is therefore intersected by the primary crack with an accompanying large number of microstructural sites being activated as elements applying closure forces in the crack wake. Observations were specifically made at the crack tip, to determine how and when bridges are formed but also in the crack wake to observe evolution of already identified bridging elements. Cracks are driven in either half-chevron geometry<sup>10</sup> or in a regime with constant sample thickness.

Bridging elements are characterized by their distance to the crack tip,  $x$ , and their accompanying local crack opening displacement,  $2u$ . Our prime goal was the observation of microstructural elements close to the crack tip ( $x < 1$  mm), in a regime where penny-shaped cracks might still be in a stable mode of crack propagation. Compact tension specimen are tempting since bridges far behind the crack tip ( $x > 1$  mm) can be characterized, yet these observations are somewhat irrelevant as cracks originating from surface flaws experience closure forces from these bridges only while they are already in an unstable mode of crack propagation. The local crack opening,  $2u$ , finally is the relevant parameter which enters into the stress displacement function  $p(u)$ . Knowledge of the  $p(u)$  relationship allows computation of a geometry and stress field invariant R-curve as a function of crack opening ( $R(u)$ )<sup>10</sup>.

The materials chosen for this study were:

- a hot pressed alumina (average grain size,  $\bar{G} = 11 \mu\text{m}$ ),
- a commercial alumina ( $\bar{G} = 35 \mu\text{m}$ , Vistal grade alumina, Coors Ceramics Co., USA),
- a hot pressed  $\text{SiC}_w/\text{Al}_2\text{O}_3$  with 30 vol. % large SiC whiskers (TWS-400, Tokai Carbon Ltd., Japan), referred to as 30SiC<sub>w</sub>/Al<sub>2</sub>O<sub>3</sub>.
- a hot pressed  $\text{SiC}_w/\text{Al}_2\text{O}_3$  with 20 vol. % small SiC whiskers (TWS-100, Tokai Carbon Ltd., Japan), referred to as 20SiC<sub>w</sub>/Al<sub>2</sub>O<sub>3</sub>,
- an  $\text{Al}_2\text{TiO}_4/\text{Al}_2\text{O}_3$  composite<sup>13</sup> (containing 20 vol. %  $\text{Al}_2\text{TiO}_4$ ) with  $\bar{G} = 6 \mu\text{m}$  for  $\text{Al}_2\text{O}_3$  and  $\bar{G} = 3 \mu\text{m}$  for the  $\text{Al}_2\text{TiO}_4$ .
- an  $\text{Al}_2\text{TiO}_4/\text{Al}_2\text{O}_3$  composite<sup>14</sup> (as above, but also containing large ( $\bar{G} = 25 \mu\text{m}$ ) alumina grains,
- as well as an Al/Al<sub>2</sub>O<sub>3</sub>/SiC composite material (Alanx FGS, Alanx

Products L.P. Newark, DE, USA) .

### 3. Characterization of Crack Closure Forces

Again, a broad view is chosen, where results are presented irrespective of material investigated. Microscopical observations are classified in terms of bridge categories. General guidelines are sought and will be discussed.

Based on our observations in the SEM we establish three bridge categories: intact bridge, frictionally sliding bridge and mechanically interlocked bridge. A select number of examples together with discussion of salient features of the three types follow:

#### 3.1. Intact bridges:

This type of restraining element relies on intact, unbroken microstructural elements.

Fig. 1: A sequence describes the evolution of intact micro-bridges in an  $\alpha$ -SiC grain (grain size  $\approx 30 \mu\text{m}$ ) embedded in an  $\text{Al}_2\text{O}_3$ -Al matrix. We might borrow a term from the geological society<sup>15</sup> and call this crack a "right stepping crack", since the crack shifted about  $0.5 \mu\text{m}$  to the right during crack advancement thereby creating each of the four restraining elements. In Fig. 1a only one bridge is broken while only one remains intact in Fig. 1b.

Fig. 2: An unbroken micro-bridge in the commercial alumina ( $\bar{G} = 35 \mu\text{m}$ ) is shown. A very picturesque description of this type of reinforcement is "handshake".

Fig. 3: Intact ligament (a) as it fails (breaks) and simultaneously transforms into a frictionally sliding bridge (b). Images are taken from the commercial alumina investigated.

Fig. 4: Bridging SiC whisker close to the crack tip in a  $30\text{SiC}_w/\text{Al}_2\text{O}_3$  matrix. Debonding did not occur close to the interface, but in the alumina, about 100 nm away from the interface itself. This particular whisker broke at a total COD of 300 nm, when situated 120  $\mu\text{m}$  behind the crack tip.

Fig. 5: Three intact whisker reinforcements ( $30\text{SiC}_w/\text{Al}_2\text{O}_3$ ) are closely lined up. The very peculiar whisker shape might have aided bridge formation.

Fig. 6: Two multi-grain intact ligaments are set up in an  $\text{Al}_2\text{TiO}_4/\text{Al}_2\text{O}_3$  composite.

Intact bridges occur in different sizes; the here called micro-bridges (Fig. 1,2) are of a ligament width of  $< 1 \mu\text{m}$ , which is much smaller than the grain size. These bridges therefore show transgranular failure. Restraining elements as in Fig. 1 have not been observed before, which is understandable, since it is very hard to detect them by optical microscopy alone. Their deformation behaviour (Fig. 1) allows us to expect huge stresses and strains

along the ligament (which, however does not necessarily translate into a large closure stress perpendicular to the crack interfaces).

Bridges as in Fig. 3 might arise from part intergranular, part intragranular failure and are in the size range of the grain size. Reinforcements as seen in Fig. 4 and 5 are mainly determined by the scale of the second phase. Bridging on a scale larger than the grain size<sup>13</sup> as in Fig. 6 involves intergranular failure and leads to unbroken reinforcements with ligaments several grains wide and tens of grains long.

This type of reinforcement is found particularly close to the crack tip (where closure forces weigh in strongest<sup>16</sup>), but - as was demonstrated - are effective in cracks with COD's of about 0.5  $\mu\text{m}$ , which translates (depending on material, crack geometry etc.) into cracks = 0.5 mm long.

### 3.2. Frictionally sliding bridge

This restraining element relies on an element of friction which transforms a stress parallel to the general crack direction into a stress normal to the crack direction (closure stress).

Fig. 7: In this case the primary crack shifted right and left an almost invisible crack segment perpendicular to the crack direction.

Repeated sliding with resultant abrasion<sup>17</sup> allowed verification that the crack interfaces were indeed in contact while sliding across each other.

Fig. 8: A frictional element at point P in a) is released by connecting a secondary crack at point A with the main crack (b). The poor visibility of the crack at P gives an indication for the possible existence of a frictionally sliding bridge. The fact that the crack is redirected (presumably to release a closure stress) is good evidence for the presence of the restraining element nearby.

Static micrographic observations of bridging elements alone appear insufficient to verify the existence of a frictionally sliding bridge. Further evidence, like debris accumulation or crack redirection, as come from in situ observations are therefore very helpful. This type of restraining element can occur in all possible geometries but embodies usually one segment of the crack interfaces which lies close to perpendicular to the crack direction.

### 3. Mechanically interlocking bridge

Here we consider a microstructural element, which - though broken - remains wedged and applies a restraint to a further increase of the local crack opening displacement. This occurs at positions where a crack segment forms an acute angle with the crack plane (in other words, the crack retracted for a short distance).



Fig. 9: A mechanically interlocking grain appears in (a) at point P. To reduce the restraint (b), it tries to rotate out of its socket, but also causes secondary cracking (note also frictionally sliding bridge at point S).

Fig. 10: A mechanically interlocking grain can be seen as a cantilever, which, if stressed at point P by a closure force will lead to a bending of the grain segment (arrow), visible through the opening of the secondary crack b.

Fig. 11: Primary crack appears to retract at P, leading to mechanical interlocking of a large alumina grain in (a). Surface roughness at Q leads to additional mechanical restraint. Increased COD in (b) highlights critical contact points P and Q.

Fig. 12: Whisker in  $30\text{SiC}_w/\text{Al}_2\text{O}_3$  is shown slightly inclined to the applied stress axis (a), thereby providing a mechanical restraint to pull-out, which has still not completely subsided at b).

Fig. 13: This case of whisker pull-out is similar to the description in Fig. 12. In distinction, the whisker angle to the crack plane is smaller, the restraining force is thereby higher (a-c), which leads to fracture of the restraining alumina matrix in d) before the whisker has pulled out completely.

Mechanical interlocking occurs, where - particularly elongated - microstructural elements are wedged and apply a mechanical restraint to pull-out. Stress release was seen to occur through either ligament rotation or fracture of the restraining matrix. Ligament fracture may also be possible.

#### 4. Formation of Crack Closure Forces

An understanding of how restraining elements are set up is a key element in the attempt of tailoring microstructure aimed at producing tougher ceramics.

Bridge formation is governed by events occurring at the crack tip and is influenced by microstructural parameters influencing the crack path. Crack propagation itself is discontinuous with intermittent jumps equivalent to 1 - 100 grain lengths. Crack arrest can in some cases be related to strong reinforcements<sup>18</sup> or might be connected to compressive zones. These crack arrest sites might serve - after corresponding crack translation - as bridging elements, manifesting themselves in the discrete and bumpy nature of the R - curve . Other smaller bridging elements are set up without necessary crack arrest at the particular site.

In focussing on the repropagation step (and thereby the selection of crack path), we resort to in - situ observations recorded during the experiments performed in the SEM chamber. Quite frequently, particularly noticeable in the alumina materials, in  $\text{Al}_2\text{TiO}_4/\text{Al}_2\text{O}_3$  and  $\text{SiC}_w/\text{Al}_2\text{O}_3$ , crack propagation occurs in two steps: a) opening of a microcrack ahead of the crack tip and b) joining of the microcrack to the primary crack (which could be restricted to the subsurface area, giving an elastic bridge at the surface). This step is distinct from deflection, where the crack remains continuous but changes direction in encountering a suitable reinforcement. Both events are governed by the same microstructural parameters. Since recent focus has been on the later step (fiber debonding<sup>8</sup> etc.), but

microscopical observation points at least to an equal degree to the first event, we model the opening of a microfacet in front of the crack tip and give the characteristics under which a bridge is formed. This model is related to the known microcracking model<sup>19,20</sup>, a consequence which will be discussed later.

Let us assume a crack tip in a microstructure as given in Fig. 14. Though the schematic represents a case of intergranular fracture, the argument can be expanded to intragranular fracture as well. Take the event where crack translation occurs by either first opening a microfacet 'a' or 'd' with 'b' and 'c' remaining closed during that step. An opening of facet 'a' with facet 'b' opening subsequently would lead to a mechanically interlocked bridge, an elastic bridge if 'b' does not open. An opening of facet 'd' would not lead to a local crack retraction and therefore would not favour bridge formation.

The condition, in general terms for a distinct microcrack source (which might see a local stress field,  $\sigma_{res}$ , to open under the local crack tip stress field  $\sigma(r)$  is given by<sup>21</sup>:

$$T_0 = \frac{Y}{\sqrt{c}} \int_0^c \frac{(\sigma(r) + \sigma_{res}) r dr}{\sqrt{c^2 - r^2}} \quad \text{Eq. 1}$$

with  $T_0$  the grain boundary toughness (alternatively: an intragranular fracture toughness),  $Y$  a geometrical parameter determined by the crack shape,  $c$  the length of a grain boundary defect, taken as a fixed fraction of the grain boundary facet length<sup>22</sup>, and  $r$  the distance to the crack tip. Eq. 1 is equally valid for microfacet 'a' and 'd' and

might be also written with subscripts 'a' or 'd'. Let us now simply inspect each of the microstructural parameters given in Eq. 1 in turn. If we assume all other parameters for both cases (a or d) equal, then the opening of a microcrack at 'a' (always in comparison to 'd') is favoured if

- a) the grain facet at 'a' is larger, leading to a larger value for  $c$ .
- b) the grain shape at 'a' leads to a larger crack parameter  $Y$ .
- c) a smaller grain boundary toughness  $T_0$  at 'a' obtains.
- d) the residual stress term,  $\sigma_{res}$ , is larger at 'a'.
- e)  $\sigma(r)$  is larger at 'a', which occurs if 'a' is closer to the crack tip than 'd' (trivial), or if a stress field asymmetry occurs. In this later case a mixed - mode induces a disruption of the crack plane (seen as a local deflection) in order to seek a mode II (or III) = 0 criterion<sup>23</sup>. This can arise through a difference in Young's moduli (different phases) in the region in front of the crack tip. A second possibility obtains when the bridging zone itself (e.g. through geometrical interlocking and pull-out) creates a local mode II or III.

## 5. Discussion

### 5.1. Characterization of Closure Forces

We have presented a general classification scheme for closure forces. Intact bridges, frictionally sliding bridges and mechanically interlocking bridges (see Fig. 15) can be distinguished. Comparable attempts to shed some light on the various distinct closure force mechanisms are rarely found in the literature. Swanson<sup>15</sup> in his work on alumina and glass ceramics finds two bridge categories: a)

frictional or geometrical interlocking and b) ligamentary bridging by intact islands. Venkinis et al.<sup>24</sup> propose a similar classification scheme as presented here for alumina with elastic bridges, frictionally sliding bridges and rotation of an angled bridging grain against restraining material. The latter is exemplified in Fig. 9, closure force at P, but is viewed here only as a subcategory of the mechanically interlocked bridge. This restraining element, namely, might fail through rotation, cracking of the matrix (also in Fig. 9, closure force at P, or Fig. 13) or even failure of the restraining element.

If we focus on intact bridges only (Fig. 15a), we can find further subcategories depending either on bridge size or fracture path. Micro-bridges, for example, exhibit transgranular failure mode with restraining elements much smaller than the grain size (Fig. 1,2). Bridges of a size comparable to the grain size can show inter- or intragranular fracture (Fig. 3,4) and multi-grain ligaments usually exhibit intergranular fracture (Fig. 6). A more mechanistic classification of intact bridges, however, distinguishes between restraining elements with fixed or no (Fig. 15a) or continued debonding (Fig. 15b). Intact bridges are essentially elastic in their deformation behaviour (or spring - like<sup>25</sup>). We therefore set intact reinforcement synonymous with elastic reinforcement. The  $p(u)$  function is linearly rising, except for the case where continued debonding occurs and the compliance of the element changes with the local crack opening. Then the terminology elastic (no permanent deformation) strictly does not hold, since the debonding mechanism is not completely reversible. Nevertheless, the essentially elastic deformation implies complete resistance against cyclic loading: energy is not dissipated during loading (as in frictionally sliding

bridges but simply stored. A small degree of friction is only embodied in an elastic bridge if no concurrent bending moment is applied and the bridge pulls out of its socket perpendicular to the crack plane. Elastic restraining elements occur primarily close to the crack tip (but can be effective up to COD's of about 500 nm, see Fig 1 etc.). They fail catastrophically under release of acoustic energy with the closure force either dropping to zero or transform into a bridge of one of the two other categories, thereby retaining part of the crack interface traction. Their existence in whisker-reinforced materials has been documented by SEM and TEM<sup>26</sup>. Venkinis et al.<sup>24</sup> observe elastic bridges in alumina, but only with small COD ( $2u < 100 \text{ nm}$ ).

The frictionally sliding bridge has been recognized and discussed by various groups<sup>5,15,24,27</sup>. The friction coefficient serves as a proportionality constant required to transform stresses parallel to the crack direction (residual stresses or locally as well as externally applied shear stresses - Fig. 15c,d) to stresses perpendicular to the crack direction (closure stresses). They store elastic energy in accordance with the locally applied closure stress  $p$  and the crack opening  $2u$ . While the crack opening increases, this elastic energy is, however, continuously dissipated. Accordingly, the  $p(u)$  function is continuously decreasing. Frictionally sliding bridges can fail catastrophically or simply slide out of their respective sockets until no surface contact remains. Crack interface tractions can be active in regions with COD's  $> 1 \text{ }\mu\text{m}$  and therefore might be to a large degree responsible for long crack  $R$  - curve behaviour. Frictionally sliding bridges are, however, difficult to characterize, since it is unclear whether crack interfaces are locally in frictional

contact or form a narrow gap only. Subsidiary elements, like secondary cracks (Fig. 9) or subsequent performance (debris accumulation during cyclic fatigue<sup>17</sup>) or crack redirection (Fig. 8) are therefore helpful indicators of their true existence.

Deformation, since energy has been dissipated, is essentially permanent. In analogy to elastic bridges we therefore set frictionally sliding bridges synonymous with plastic bridges. This implies strong susceptibility to cyclic fatigue<sup>17</sup>.

Mechanical interlocking appears to occur preferably in microstructures containing platelets or acicular elements and for example, could not occur in a hexagonal network. It usually relies on intergranular fracture. Failure of this type of restraining element occurs mostly through fracture of the restraining matrix (see Fig. 9, 13), grain rotation (Fig. 8) or possibly fracture of the reinforcement. In cases where the angle  $\alpha$  (Fig. 15e,f) is close to 90°, complete pull-out (Fig. 12) might occur.

In distinction to the frictionally sliding bridge, residual stresses or shear stresses are not required to create a closure stress. In contrary, pull-out of a misaligned element can generate a local shear stress (Fig. 15 c). The absorbed energy is to an increasing degree stored elastically (in reinforcement and restraining matrix) but also dissipated during frictional sliding. The elastically stored energy may build up until fracture of the restraining matrix occurs, where the  $p(u)$  function will drop to zero. Mechanically interlocked bridges are therefore termed synonymous with elastic-plastic bridges and can be seen as an intermediate form of the two other categories. The part of the elastic-plastic restraining element,

which relies on a component of friction, is susceptible to mechanical fatigue.

A distinction between the three bridging elements can be somewhat diffuse or their behaviour can be mixed. Frictionally sliding bridges with small misalignment can turn into mechanically interlocked bridges where the energy is then stored to a large degree elastically. One bridge type can also fail and thereby transform into another type, as Fig. 3 proves where the elastic bridge turns into a frictionally sliding bridge. In general, depending on misalignment angle  $\alpha$ , an elastic bridge can (but need not) turn into a plastic or elastic-plastic bridge. Synergistic processes can be observed as in Fig. 9 where a mechanically interlocked bridge at P creates a local mode II, which pins the frictionally sliding bridge at S.

At this juncture we attempt to clarify a point which caused confusion in several discussions leading to this work. The fact that all the energy once stored in the restraining elements is finally lost in an irreversible manner, may lead to the conclusion that the R-curve is continuously and forever rising, since ever more energy is required to drive the crack with increasing crack length. The crack resistance at steady state, however, is at its peak value. The energy to drive the crack further indeed has to be increased (increasing load displacement); the energy absorbed per increment of crack advancement, however, remains constant, once the steady state bridging zone is reached. Energy is continuously absorbed by the restraining elements as well as by the crack tip region to create new surface energy. Were this not the case, the crack would advance with constant velocity in a constant K-specimen under constant load (no further energy input).



## 5.2 Formation of Crack Closure Forces

We have based our discussion on bridge formation solely on the discussion of the opening of a suitably positioned microcrack source in front of the crack tip. While this mechanism is based on microscopical *in situ* observation, it nevertheless forms a restriction. A microcrack, as it appears on the surface, might be connected to the primary crack subsurface. Also, bridge formation during continuous crack propagation will have to be described by a different model. However, the same ideas based on  $T_0$ ,  $\sigma_R$  etc. will be raised. In reviewing the separate points leading to bridge formation we might note:

A variation in grain size and grain shape had not been discussed before as leading to bridge formation; the dependence of closure stress (bridge performance, not bridge formation) on grain size and grain shape had been established for the case of alumina by Bennison and Lawn<sup>9</sup>. Both parameters (besides  $\sigma_{res}$ ) are essential in the description of microcrack formation and give a microcrack zone size, depending on grain facet size and shape.<sup>20</sup> The beneficial effect of a slight degree of inhomogeneity has been realized with the  $Al_2TiO_4/Al_2O_3$  composite<sup>14</sup>. The rather strong R-curve of somewhat heterogeneous commercial aluminas<sup>17</sup> might also be rationalized under this aspect.

There are no recipes for adjusting the grain boundary toughness. In fact this parameter is the one which is clearly most difficult to work with from the ones mentioned above. A partial reduction in  $T_0$  at select grain facets would enhance bridge formation, but also reduce the average grain boundary toughness of the material, thereby reducing the base level of the crack resistance from where an R-

curve could be built. Materials with non-cubic crystallographic structure (e.g.  $\alpha$ -SiC, see Fig. 1) and an anisotropy in fracture energies are thought to be candidates for the formation of elastic bridges (aided by local mode II, III, see Fig. 1, 2, 3).

Local adjustment of residual stresses has been proven effective<sup>13,14,28</sup> in terms of producing materials with strong R-curve. This approach might lead to the formation of large elastic bridges, mechanically interlocking and frictionally sliding elements. It can bring a synergistic effect with microcrack toughening, but excessive residual stress might lead to microcrack growth and coalescence, rendering the material susceptible to environmentally influenced static fatigue.

A stress field asymmetry arises where either an external mode II is applied (trivial) or the bridging zone (e.g. through mechanical interlocking) creates a mode II at the crack tip or the crack tip senses a difference in Young's moduli. In the later case the crack prefers to extend into the lower modulus material<sup>29</sup> and will drive towards a mode II = 0 condition and therefore a deviation from the straight crack path. A difference of Young's moduli has been demonstrated effective in that sense in experiments where pores ( $E = 0$ ) were shown to cause a crack deviation towards the pore<sup>30</sup> (lower modulus phase). Distortion of the crack tip stress field has been discussed by Swanson<sup>15</sup> and can be related to resultant fracture surface markings. It is also well known, that a combined mode I mode II (or III) loading leads to increased fracture energy both at interfaces<sup>31</sup> and monoliths<sup>32</sup>. Quantitative statements of mixed-mode stress induced disruption of the crack plane due to either tractions in the bridging zone, or microstructural variation in front of the crack tip are not available as yet.

We remarked in establishing Eq. 1, that the model for generation of a microcrack zone is closely related to our approach. With this in mind it comes as no surprise that microcrack toughening and bridge formation are related phenomena and rely - in part - on adjusting the same set of microstructural parameters. Materials which show microcrack toughening might therefore also be prone to show bridge formation. In other words, in searching for new materials which provide good toughening through crack bridging, materials which exhibit microcracking might be good candidates (the reverse is not necessarily true, since bridge formation does not rely solely on residual stresses). In this context the discussion over the last years, whether microcrack toughening or crack bridging is the dominant mechanism in a given material appears in a different light. Both processes can be seen as related where the formation is concerned, with one process the extreme form of a common parent. The parent in this case is the formation of a microcrack in front of the crack tip, which subsequently links up to the primary crack or does not. While this might be a somewhat oversimplistic view, considering our assumptions we made during the discussion on crack formation, it might help to bring the proponents for both mechanisms closer together.

We should emphasize, that bridge formation should not be confused with bridge performance or with the prediction of actual closure forces. In considering the closure stress obtainable in a given material, both processes, bridge formation (leading to a parameter for the bridge density) and actual closure stress of a given singular bridging element have to be combined to give the average, smeared-out closure stress for a given crack-microstructure system.

## 6. Conclusions

We have proposed a classification scheme for crack bridging elements in brittle solids, based on appearance and deformation behaviour. The three types are:

A) intact (or elastic) bridges, which:

- store an increasing amount of elastic energy with increasing crack opening.
- are represented by an increasing  $p(u)$  function.
- fail catastrophically under release of acoustic energy, thereby possibly turning into a bridge of one of the two other categories.
- are - by definition of their reversible nature - resistant to cyclic loading.

B) frictionally sliding (or plastic) bridges:

- continuously dissipate energy, which is stored elastically, with increasing crack opening.
- are represented by a decreasing  $p(u)$  function.
- rely on an element of friction to transform a clamping or shear stress into a closure stress.
- can fail catastrophically or simply slide out of their respective sockets.
- are susceptible to cyclic loading.

C) mechanically interlocked (or elastic-plastic) bridges, which:

- combine an element of storing elastic energy with a mechanism of continued dissipation of frictional energy.
- are represented by a  $p(u)$  function, which strongly depends on the inclination angle  $\alpha$ .

- can fail through fracture of the restraining matrix, bridging element or rotation of the reinforcing component.
- are to a certain degree susceptible to cyclic loading.

Bridge formation has been related to the formation of a microcrack ahead of the crack tip, an event which has been observed repeatedly. The parameters influencing bridge formation are grain size and shape, crack resistance of a grain boundary or an intergranular fracture plane, residual stresses and stress field asymmetry at the crack tip, the latter derived from both a difference of Young's moduli of different phases ahead of the crack as well as from tractions in the bridging zone. Very simply, small (not excessive) degrees of heterogeneity, anisotropy in interfacial fracture energies, thermal expansion anisotropy leading to residual stresses (or phases with different thermal expansion coefficient) and/or different Young's moduli are expected to increase bridge formation.

## 7. Acknowledgements

For either help in sample preparation or many fruitful discussions I am indebted to Steve Bennison, Linda Braun, Nils Claussen, Ed Fuller, Rolf Janssen, Ralph Krause, Srinivasarao Lathabai, Brian Lawn and Manfred Sindel. The experimental part of this work was supported by the U.S. Air Force, Office of Scientific Research. The theoretical part of this study was supported by the Volkswagen Foundation under contract number I/66 790.

## References

1. McMeeking, R.M. & Evans, A.G. Mechanics of transformation toughening in brittle materials. J. Am. Ceram. Soc. **65** (1982) 242-46.
2. Rühle, M., Evans, A.G., McMeeking, R.M., Charalambrides, P.G. & Hutchinson, J.W. Microcrack toughening in alumina/zirconia. Acta metall. **35** (1987) 2701-10.
3. Hübner, H. & Jillek, W. Sub-critical crack extension and crack resistance in polycrystalline alumina. J. Mat. Sci. **12** (1977) 117-25.
4. Knehans, R. & Steinbrech R. Memory effect of crack resistance during slow crack growth in notched  $\text{Al}_2\text{O}_3$  bend specimens. J. Mat. Sci. Let. **1** (1982). 327-329.
5. Swanson, P.L., Fairbanks, C.J., Lawn, B.R., Mai, Y.-W. & Hockey, B.J. Crack-interface grain bridging as a fracture resistance mechanism in ceramics: I, Experimental study on alumina. J. Am. Ceram. Soc. **70** (1987) 279-289.
6. Becher, P.F. Microstructural design of toughened ceramics. J. Am. Ceram. Soc. **74** (1991) 255-69.
7. Smith, E. Estimating the toughening effect of crack-bridging particles in a brittle matrix. Int. J. Fract. **45** (1990) 283-98.
8. Budiansky, B., Hutchinson, J.W. & Evans, A.G. Matrix fracture in fiber-reinforced ceramics. J. Mech. Phys. Solids. **34** (1986) 167-89.
9. Bennison, S.J. & Lawn, B.R. Role of interfacial grain-bridging sliding friction in the crack-resistance and

- strength properties of nontransforming ceramics. Acta metall. **37** (1989) 2659-2671 .
10. Rödel, J., Kelly, J.F. & Lawn, B.R. In situ measurements of bridged crack interfaces in the scanning electro microscope. J. Am. Ceram. Soc. **73** (1990) 3313-18.
  11. Rödel, J., Kelly, J.F., Stoudt, M.R. & Bennison, S.J. A loading device for fracture testing of compact tension specimen in the SEM. Scanning Microscopy, in print.
  12. Frei, H. & Grathwohl, G. Development of a piezotranslator-based bending device for in situ SEM investigations of high performance ceramics. J. Phys. E. **22** (1989) 589-93.
  13. Runyan, J.L. & Bennison, S.J. Fabrication of flaw-tolerant aluminumtitanate - reinforced alumina. J. Eur. Ceram. Soc. **7** (1991) 93-99.
  14. Padture, N.P., Bennison, S.J., Runyan, J.L., Rödel, J., Chan, H.M. & Lawn, B.R. Flaw tolerant  $\text{Al}_2\text{O}_3\text{-Al}_2\text{TiO}_4$  composites. To appear In Ceramic Transactions, **19** Symposium on Composites. (ed. M.D. Sacks) American Ceramic Society, Westerville, OH (1991).
  15. Swanson, P.L. Crack-interface traction: a fracture-resistance mechanism in brittle polycrystals. In Advances in Ceramics, **22** Fractography of Glasses and Ceramics. American Ceramic Society, Westerville, OH (1988) 135-155.
  16. Lawn, B.R. & Wilshaw, T.R. Fracture of brittle solids. Cambridge University press, London, 1975, pp. 46-73.
  17. Lathabai, S., Rödel, J. & Lawn, B.R. Cyclic fatigue from frictional degradation at bridging grains in alumina. J. Am. Ceram. Soc. in print.

18. Rödel, J., Lawn, B.R. & Fuller, E.R. Crack propagation in silicon carbide whisker-reinforced alumina. to be submitted to J. Am. Ceram. Soc.
19. Fu, Y. & Evans, A.G. Microcrack zone formation in single phase polycrystals. Acta metall. **30** (1982) 1619-1625.
20. Lawn, B. R. Fundamental condition for existence of microcrack clouds in monophasic ceramics. J. Eur. Ceram. Soc. **7** (1991) 17-20.
21. Sih, G.C., Handbook of stress intensity factors. Lehigh University Press, Bethlehem, PA, 1973.
22. Tvergaard, V. & Hutchinson, J.W. Microcracking in ceramics induced by thermal expansion or elastic anisotropy. J. Am. Ceram. Soc. **71** (1988) 157-166.
23. Atkins, A.G. & Mai, Y-W. Elastic and plastic fracture. John Wiley & Sons, New York, 1985, pp. 198-219.
24. Venkinis, G., Ashby, M.F. & Beaumont, P.W. R. R-Curve behaviour of  $\text{Al}_2\text{O}_3$  ceramics. Acta metall. mater. **38** (1990) 1151-1162 .
25. Rose, L.R.F. Crack reinforcement by distributed springs. J. Mech. Phys. Solids **35** (1987) 383-405 .
26. Rühle, M., Dalgleish, B.J. & Evans, A.G. On the toughening of ceramics by whiskers. Scr. Met. **21** (1987) 681-86.
27. Knehans, R. & Steinbrech R. Effect of grain size on the crack resistance curves of  $\text{Al}_2\text{O}_3$  bend specimens. Sci. of Ceram. **12** (1983) 613-619.
28. Lutz, E.H., Claussen, N. & Swain, M.V.  $\text{K}_\text{R}$ -Curve behavior of duplex ceramics. J. Am. Ceram. Soc. **74** (1991) 11-18.



29. Evans, A.G., Dalgleish, B.J., He, M. & Hutchinson, J.W. On crack path selection and the interface fracture energy in bimaterial systems. Acta metall. **37** (1989) 3249-54.
30. Penugonda, M.R., Virkar, A.V. & Shetty, D.K. Prediction of crack paths in particulate composites using electrical analog. J. Am. Ceram. Soc. **73** (1990) 340-45.
31. Cao, H.C. & Evans, A.G. An experimental study of the fracture resistance of bimaterial interface. Mechanics of Materials. **7** (1989). 295-305.
32. Suresh, S. & Tschegg, E.K. Combined mode I - mode III fracture of fatigue - precracked alumina. J. Am. Ceram. Soc. **70** (1987) 726-33.

### Figure captions

1. Evolution of intact micro-bridges in  $\alpha$ -SiC grain embedded in Al/Al<sub>2</sub>O<sub>3</sub> matrix; crack propagation is in all micrographs from top to bottom; a)  $x$  (distance from the crack tip) = 410  $\mu\text{m}$ ,  $2u$  (total crack opening) = 540 nm, b)  $x$  = 530  $\mu\text{m}$ ,  $2u$  = 750 nm.
2. Unbroken micro-bridge (or handshake) in Al<sub>2</sub>O<sub>3</sub>; a)  $x \approx 700$   $\mu\text{m}$ ,  $2u \approx 600$  nm.
3. Intact bridge in commercial alumina (a) transforms into frictionally sliding bridge (b); a)  $x$  = 170  $\mu\text{m}$ ,  $2u$  = 140 nm; b)  $x$  = 740  $\mu\text{m}$ ,  $2u$  = 560 nm.
4. Unbroken whisker provides restraining element in a 30SiC<sub>w</sub>/Al<sub>2</sub>O<sub>3</sub> composite;  $x$  = 10  $\mu\text{m}$ ,  $2u$  = 80 nm.
5. Three intact SiC whisker elements in a 20SiC<sub>w</sub>/Al<sub>2</sub>O<sub>3</sub> composite;  $x$  = 40  $\mu\text{m}$ ,  $2u$  = 140 nm.
6. Intact multi - grain ligaments in Al<sub>2</sub>TiO<sub>4</sub>/Al<sub>2</sub>O<sub>3</sub> composite;  $x \approx 700$   $\mu\text{m}$ ,  $2u \approx 1000$  nm.
7. Frictionally sliding bridge in commercial alumina;  $x$  = 290  $\mu\text{m}$ ,  $2u$  = 450 nm.

8. Frictionally sliding bridge (a) breaks as shown in (b) in a commercial alumina; a)  $x = 880 \mu\text{m}$ ,  $2u \approx 750 \text{ nm}$ ; b)  $x = 1080 \mu\text{m}$ ,  $2u \approx 900 \text{ nm}$ .
9. Mechanically interlocking bridge at P and frictionally sliding bridge at S in hot pressed alumina; a)  $x = 600 \mu\text{m}$ ,  $2u \approx 500 \text{ nm}$ ; b)  $x = 1190 \mu\text{m}$ ,  $2u \approx 860 \text{ nm}$ .
10. Mechanically interlocking grain applies closure force at P in hot pressed alumina, thereby pulling ligament to the right (arrow) and opening secondary crack 'b';  $x = 810 \mu\text{m}$ ,  $2u = 600 \text{ nm}$ .
11. Large alumina grain is mechanically interlocked with bridging tractions at P and Q in  $\text{Al}_2\text{TiO}_4/\text{Al}_2\text{O}_3$  composite; a)  $x = 110 \mu\text{m}$ ,  $2u = 200 \text{ nm}$ ;  $x = 370 \mu\text{m}$ ,  $2u = 600 \text{ nm}$ .
12. Whisker pull-out in  $30\text{SiC}_w/\text{Al}_2\text{O}_3$ ; a)  $x = 80 \mu\text{m}$ ,  $2u = 250 \text{ nm}$ , b)  $x = 170 \mu\text{m}$ ,  $2u = 500 \text{ nm}$ .
13. Whisker pull-out in  $20\text{SiC}_w/\text{Al}_2\text{O}_3$ , a)  $x = 100 \mu\text{m}$ ,  $2u = 200 \text{ nm}$ ; b)  $x = 110 \mu\text{m}$ ,  $2u = 400 \text{ nm}$ ; c)  $x = 330 \mu\text{m}$ ,  $2u = 570 \text{ nm}$ ; d)  $x = 830 \mu\text{m}$ ,  $2u = 860 \text{ nm}$ .
14. Schematic for bridge formation model. Creation of microcrack at either 'a' or 'd' ahead of the crack tip is considered. Facets 'c' and 'd' are assumed closed.

15. Schematic for possible bridge configurations; a,b) intact (elastic)bridges with no further debonding (a) and further debonding (b), c,d) frictionally sliding (plastic) bridges with different geometries and e,f) mechanically interlocked (elastic-plastic) bridges.

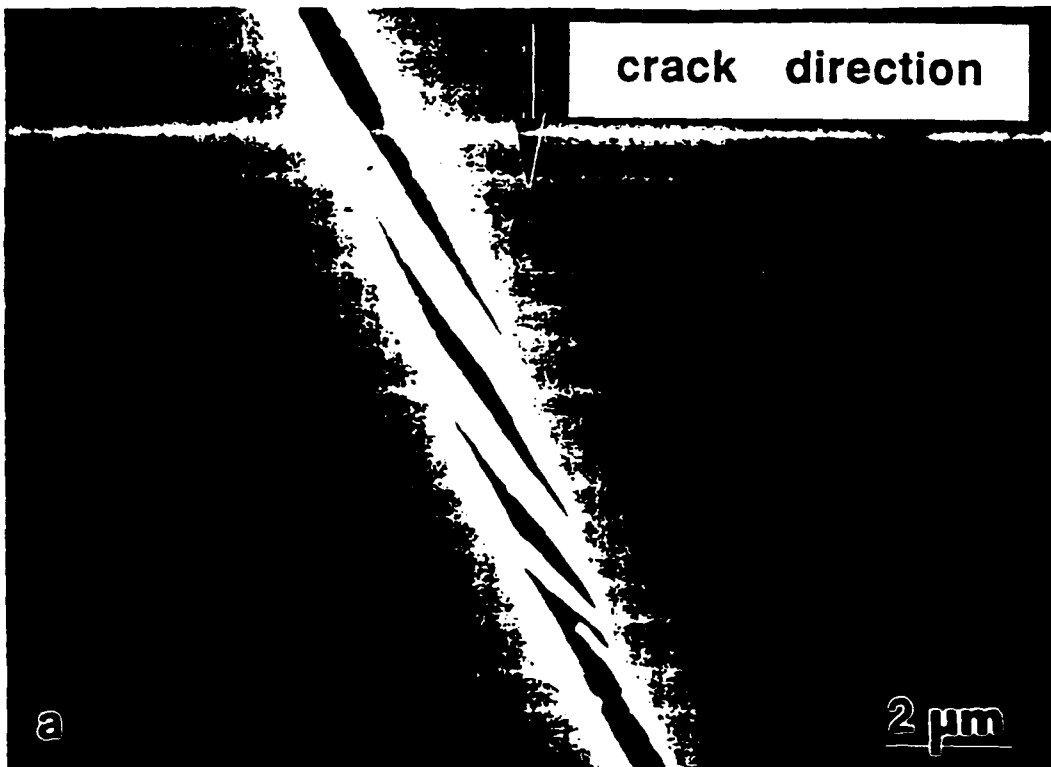


Fig. 1



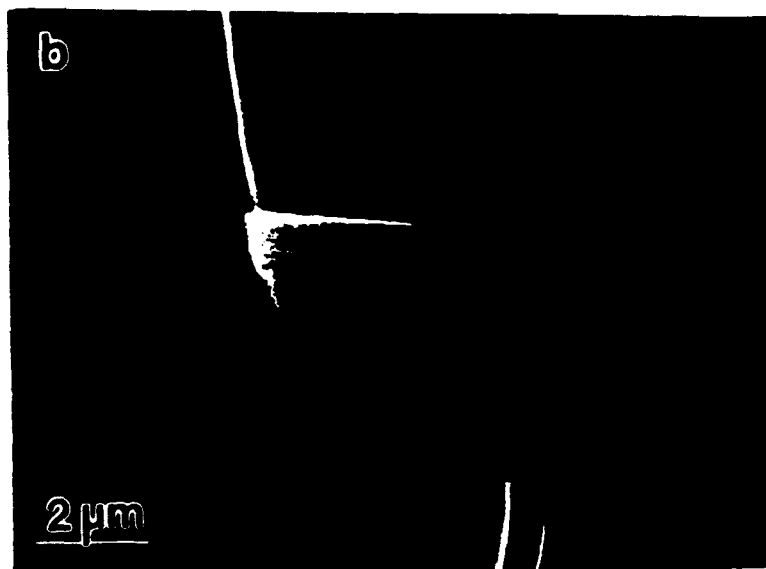
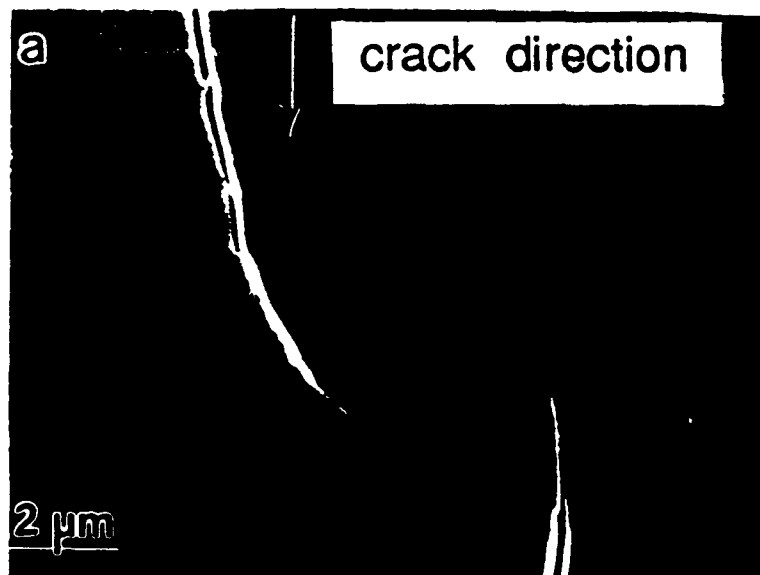




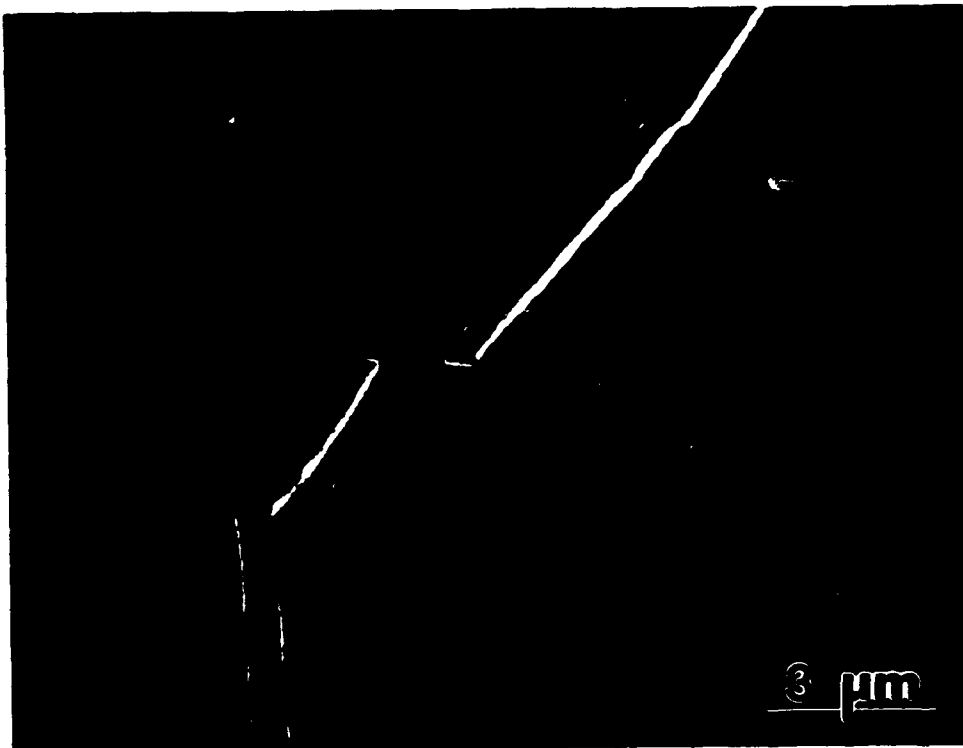
Fig. ④

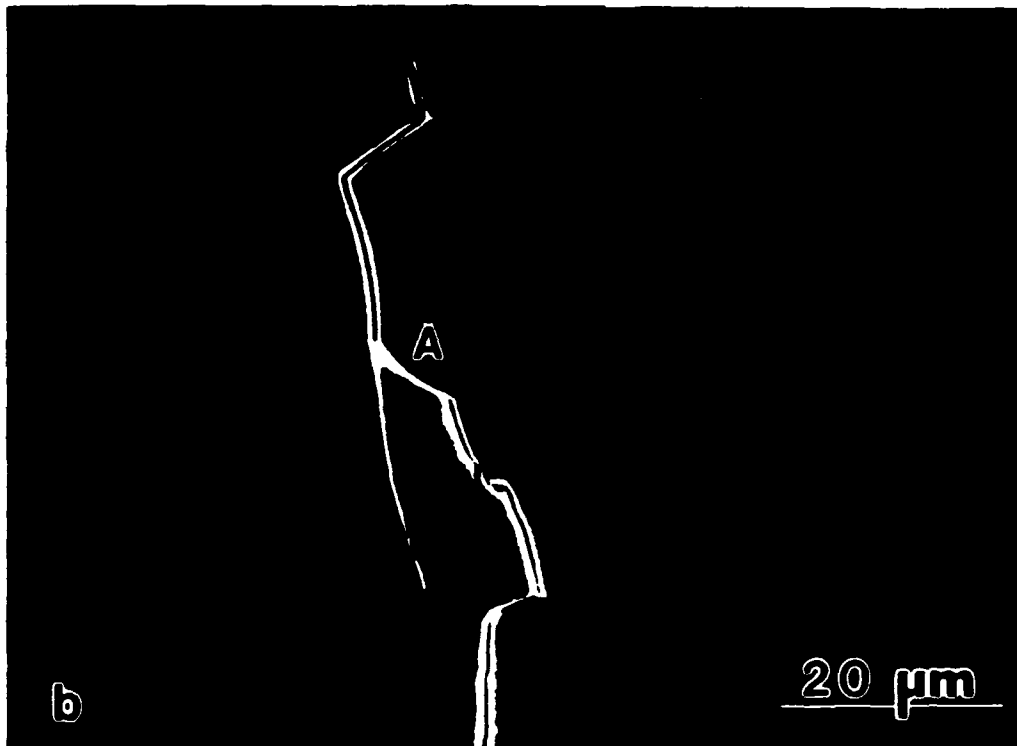
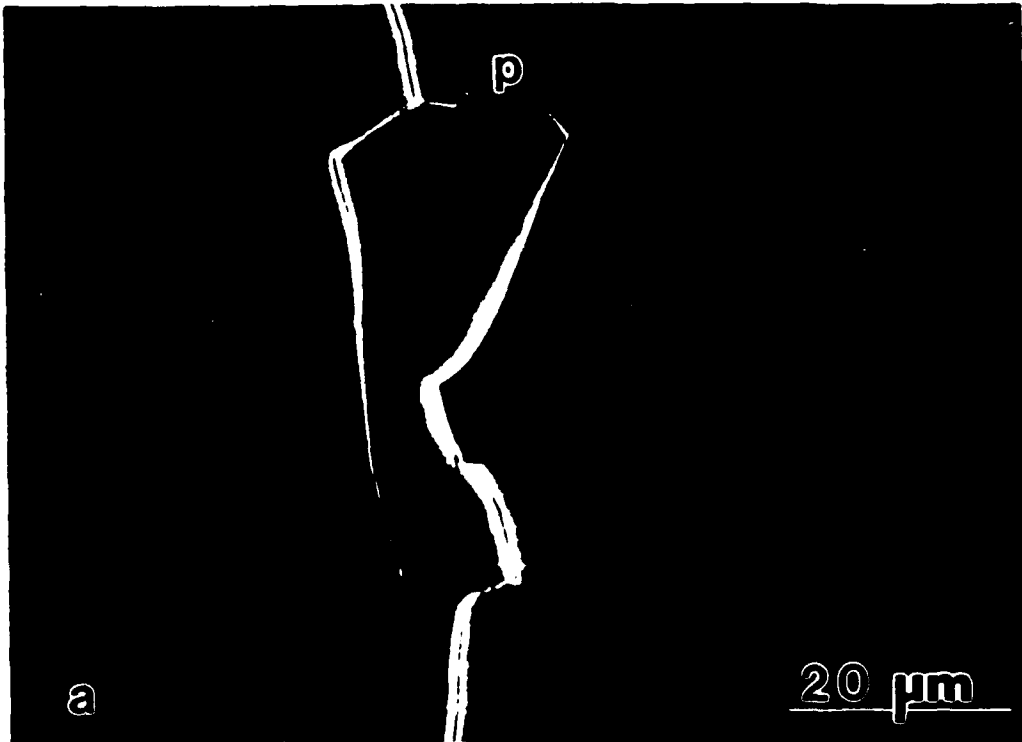




Fig. 5







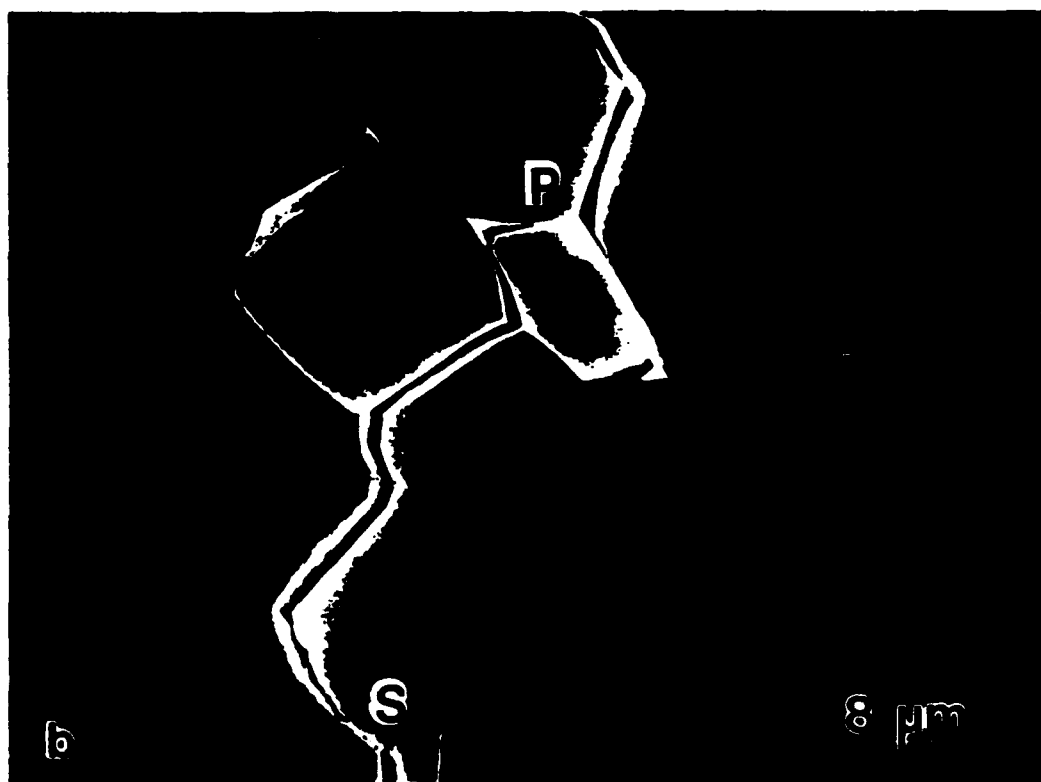
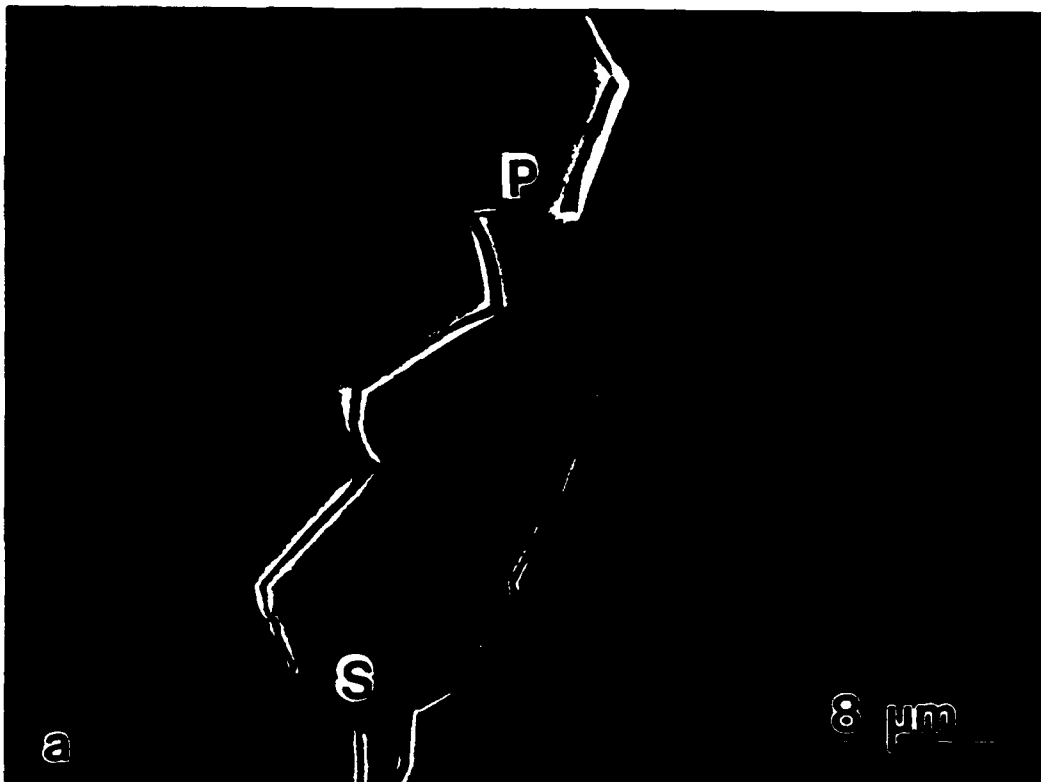
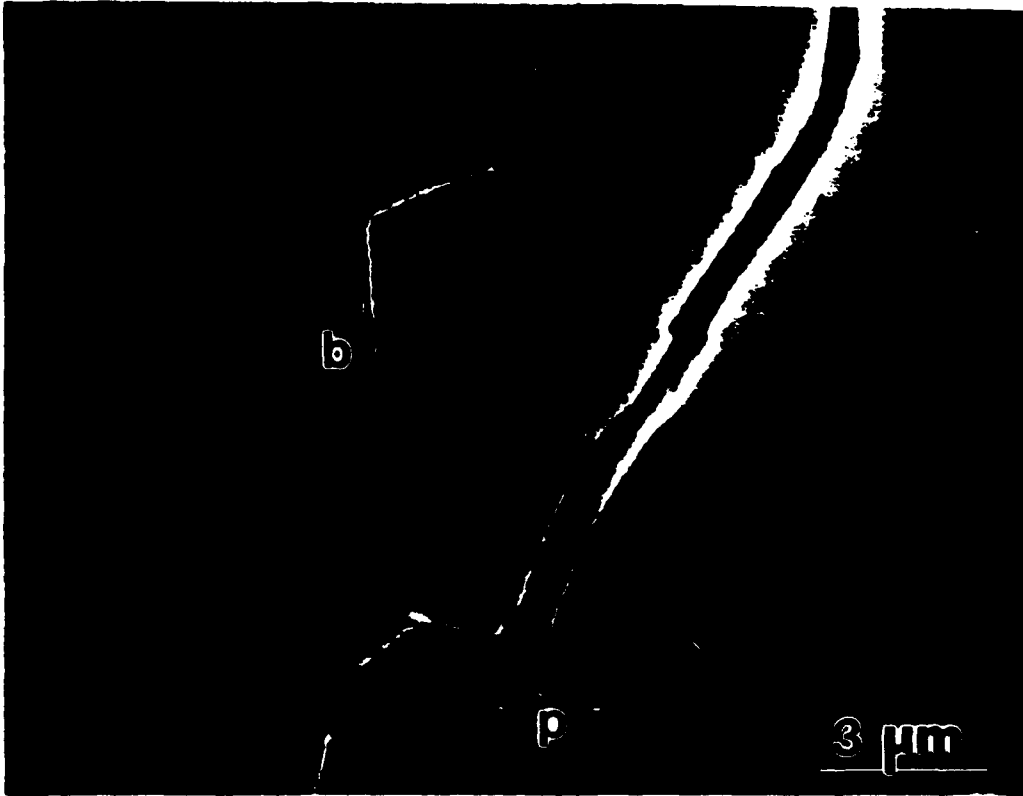


Fig ⑨



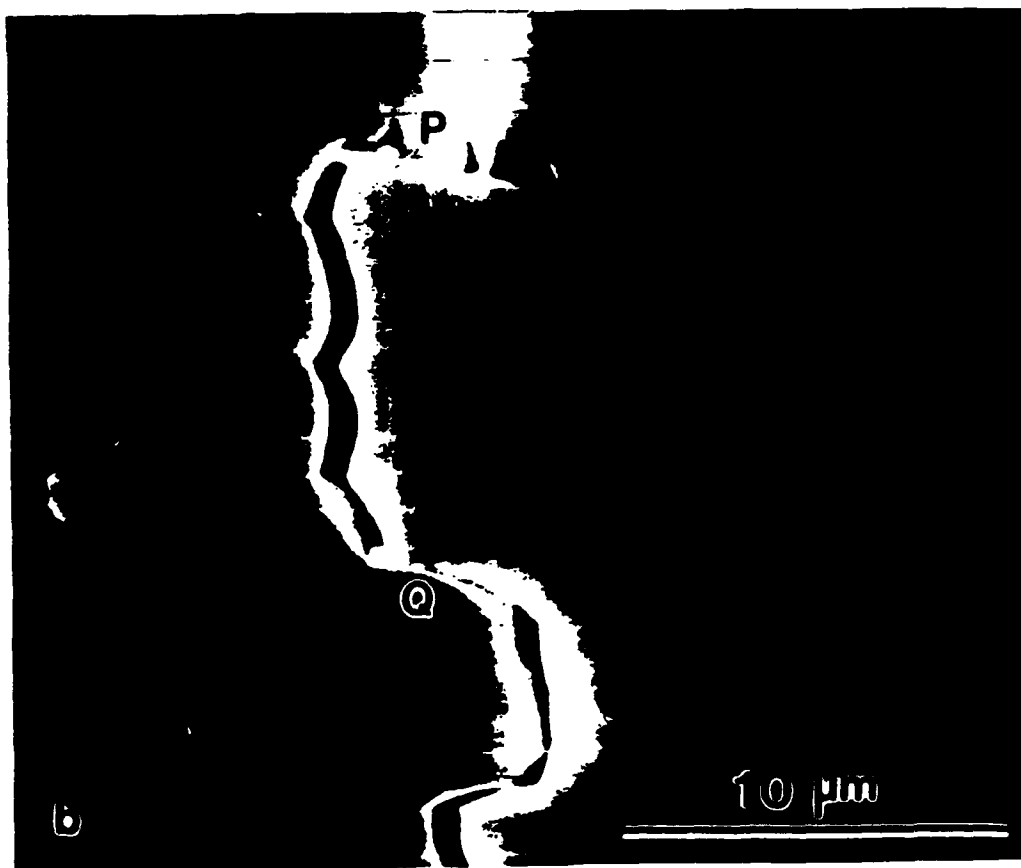
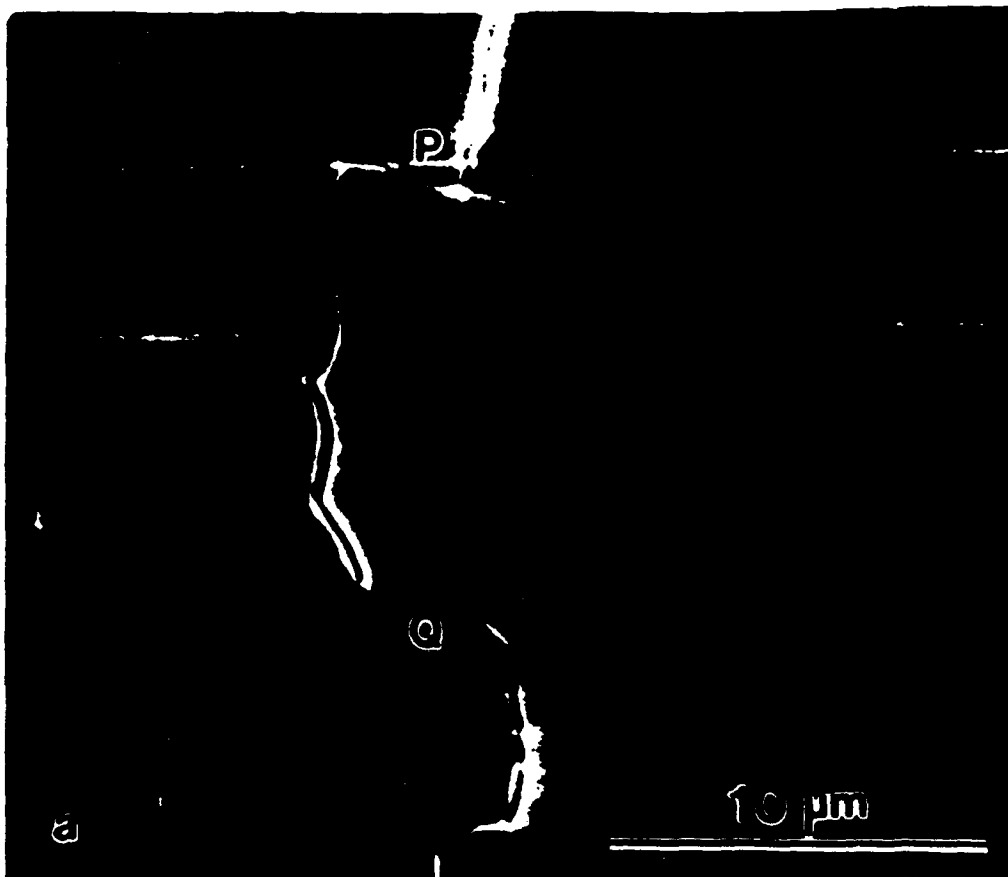
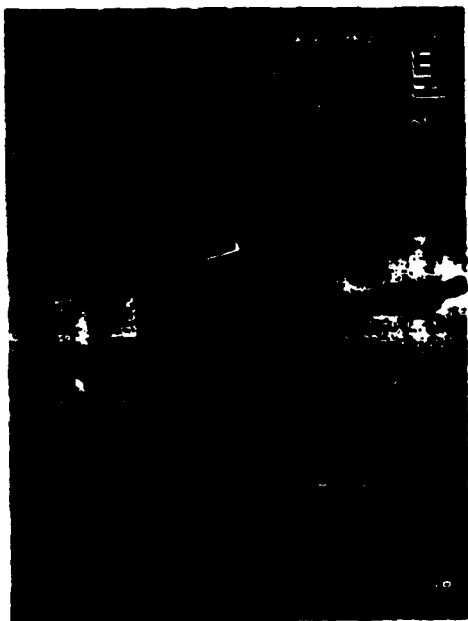
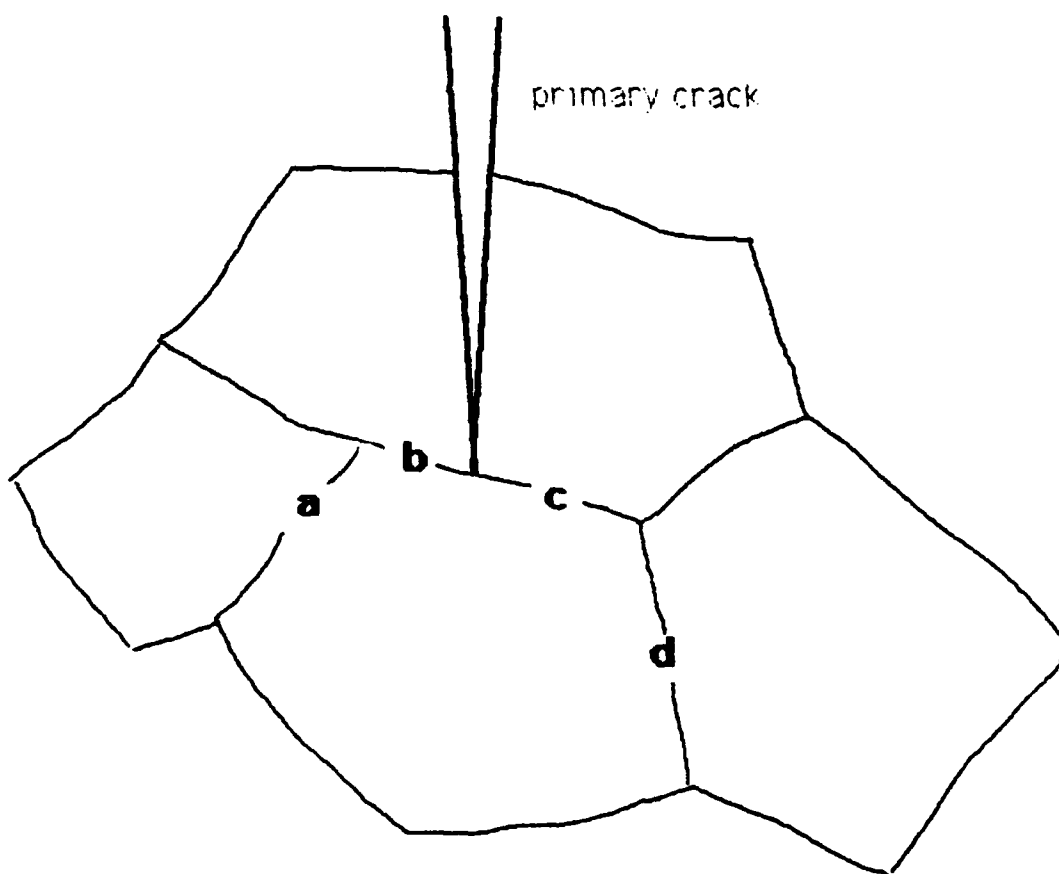


Fig 11









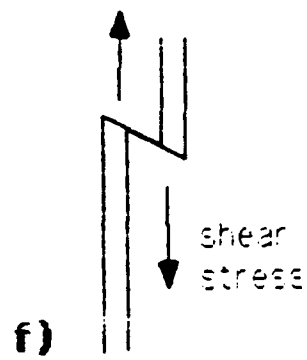
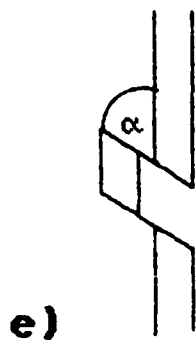
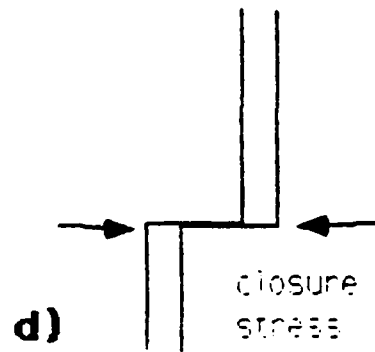
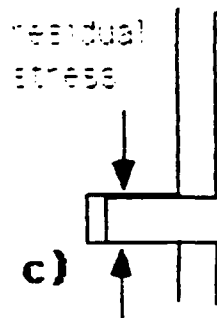
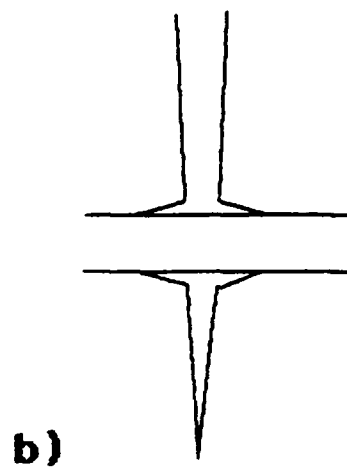


Fig. 15

# Influence of grain size and degree of crystallization of intergranular glassy phase on the mechanical behaviour of a debased alumina

N. P. PADTURE, H. M. CHAN

Department of Materials Science and Engineering, Lehigh University, Bethlehem, PA 18015, USA

The influence of microstructure on the crack resistance (*R*-curve) behaviour of a commercial debased alumina containing large amounts of glassy phase (28 vol %) has been studied by strength measurements at controlled flaw sizes produced by indentation. Both the individual and combined effects of (a) grain size, and (b) intergranular second phase (glassy or crystalline) were evaluated. Enhancement of the *R*-curve behaviour was observed when the average grain size was increased from 3–18  $\mu\text{m}$  by thermal treatment. However, no effect of the degree of crystallinity of the intergranular second phase on the *R*-curve behaviour, in either small- or large-grained materials, was observed. These results are discussed with reference to the influence of grain-boundary residual stresses on grain bridging across the crack interface.

## 1. Introduction

In recent years there has been increasing evidence that non-transforming ceramics such as aluminas can exhibit so-called *R*-curve behaviour, i.e. they show increasing toughness with increase in crack size [1–6]. The enhancement of *R*-curve behaviour yields several tangible benefits. Firstly, the ceramic exhibits a range of flaw sizes over which the strength is near-invariant. In turn, this “flaw tolerance” enables the engineer to work with a single (flaw-size independent) design stress. The advantage from the ceramics processing standpoint is that the strength of a ceramic with strong *R*-curve behaviour is relatively insensitive to processing defects. In addition, it has recently been postulated that enhanced *R*-curve behaviour results in an increase in the Weibull modulus [7–9].

Because it has been clearly demonstrated that the extent of the *R*-curve behaviour is influenced by microstructure [3], it would seem highly feasible to modify *R*-curve characteristics through control of microstructural variables. The microstructural parameters evaluated in this study were (a) grain size, and (b) degree of crystallinity of the intergranular phase. The selection of these particular parameters was based on the consideration of a model which assumes grain-localized bridging in the crack wake [1, 5, 10]. In the above model, represented schematically in Fig. 1, the grains bridging the crack are “clamped” in the matrix by compressive residual stresses arising from thermal expansion anisotropy [11]. These grains thereby exert a restraint across the crack walls, giving rise to increased toughness in a manner analogous to that

of fibre-reinforced composites. Without going into the details of the stress-displacement relation for the bridge elements [11, 12], it can be appreciated that the degree of enhanced toughening will depend both on the grain size (which determines the length over which the grains must be pulled out), and the residual stresses (which control how tightly the grains are clamped).

A limited number of systematic experimental investigations of these predictions have been carried out, and these confirm a strong dependence on grain size. A study on nominally single-phase aluminas showed that coarsening the microstructure results in a stronger *R*-curve [3]. Similar results were obtained for a debased alumina (containing 18 vol % intergranular phase) [13]. The influence of the intergranular second phases, however, is less well documented, and different studies have produced somewhat conflicting results. Thus several researchers [14–18] have reported significant increases in the toughness values of liquid-phase-sintered aluminas containing 10–30 vol % intergranular glass. The toughness improvements resulted from simple heat treatments, and were attributed to crystallization of the glass. However, it should be noted that the toughness measurements in those studies were performed at a single crack length. In contrast to this, work by Bennison *et al.* [13] showed that for fine-grained aluminas containing 18 vol % second phase, crystallization of the second phase had very little effect on the crack resistance curve. Powell-Doğan and Heuer [19] also showed that for 96% alumina, crystallization of the second

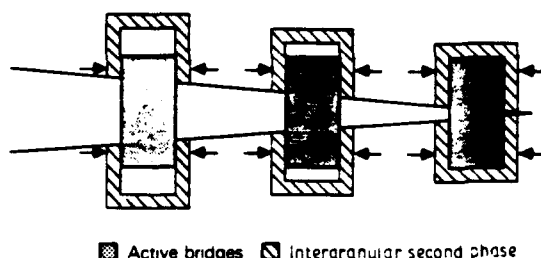


Figure 1 Schematic representation of grain-localized bridging of the crack.

phase had no effect on either the mechanical properties, or the mode of fracture.

The purpose of this study was to determine experimentally the relative influence of these two variables, grain size and second phase, on the *R*-curve behaviour of a debased alumina. This work differs from that of previous researchers in that both the individual and combined influence of grain size, and crystallinity of the second phase, are determined.

## 2. Experimental procedure

Some 300 specimens of a commercial debased (liquid-phase sintered) alumina (AD 85) in the form of discs (25 mm diameter  $\times$  3 mm) were obtained. A series of heat treatments was carefully devised to produce four sets of specimens of differing microstructures. Table I shows the details of the heat treatments and the resulting microstructures. The notation S or L refers to "small" or "large" grain size, respectively, and C or G refers to crystalline or glassy second-phase, respectively.

Specimens for transmission electron microscopy (TEM) were prepared following standard procedures for ceramic materials. Discs (3 mm) were ultrasonically cut from thin sections of the above samples. The discs were then dimpled to a thickness of 20  $\mu$ m in the centre and ion-beam milled until perforation. Subsequent investigation on the transmission electron microscope was carried out at an accelerating voltage of 120 keV. The chemical composition of the intergranular glass was determined using energy dispersive spectroscopy of X-rays (EDS) on the same instrument. A "standard" glass (SRM 2063) of known composition was used to provide the necessary *k*-factors for compositional analysis. Samples were prepared for scanning electron microscopy (SEM) by polishing sections

to 1  $\mu$ m grade followed by thermal etching at 1500  $^{\circ}$ C for 15 min.

Mechanical testing of AD85-S-G, AD85-S-C, AD85-L-G and AD85-L-C was carried out as follows. About 50 disc specimens of each batch were polished to 1  $\mu$ m grade on the prospective tensile side. A Vickers indentation was made at the centre of the polished surface with loads varying from 2–300 N. Some samples were left unindented. All indentations were made in air and the samples allowed to stand for 10 min. A drop of vacuum grease was then placed on the indentation sites. The specimens were broken in biaxial flexure using the three-point support and punch fixture [20], and failure times were kept below 20 ms to minimize effects from static fatigue. Strength values were calculated from the breaking loads and specimen dimensions using thin-plate and beam formulas [21]. Care was taken to examine all specimens after fracture to verify the indentation site as the origin of failure. The specimens that did not fracture from indentations were incorporated into the data pool for unindented controls. Details of this particular method of mechanical testing have been described elsewhere [3].

Preliminary experiments revealed that crystallization of the intergranular glass produced predominantly anorthite ( $\text{CaO} \cdot \text{Al}_2\text{O}_3 \cdot 2\text{SiO}_2$ ). To obtain a comparison between the high-temperature mechanical properties of anorthite and alumina, the hardness of bulk anorthite was determined as a function of temperature from 20–1200  $^{\circ}$ C. Bulk anorthite was made by first melting anorthite composition glass from reagent grade  $\text{SiO}_2$ ,  $\text{Al}_2\text{O}_3$  and  $\text{CaCO}_3$  raw materials in a Pt–Rh crucible at 1600  $^{\circ}$ C for 24 h. This was followed by crystallization at 1200  $^{\circ}$ C for 30 min.

## 3. Results

### 3.1. Microstructure

Table II shows the composition of the intergranular glass of AD85-S-G samples after homogenization heat treatment, as determined by X-ray EDS. The values represent an average of ten different spectra obtained from different regions of the sample. The compositions were observed to be consistent within  $\pm 5\%$ , implying that the glassy phase is homogeneous. In addition, the glass composition obtained was found to agree within  $\pm 5\%$  of the values determined by Wiederhorn *et al.* [22] for AD85 with the same heat treatment. Using this composition as a basis, the heat treatment

TABLE I Heat-treatment schedules and microstructures

Material	Heat treatment	Purpose	Resulting microstructure	
			Grain size ( $\mu$ m)	Intergranular phase
AD85-S-G	As-received		3	Glassy
AD85-S-C	(a) 1400 $^{\circ}$ C for 6 h (quenched)	Homogenize intergranular glass	3	Partially crystalline
	(b) 1150 $^{\circ}$ C for 130 h	Crystallize intergranular glass		
AD85-L-G	(a) 1550 $^{\circ}$ C for 250 h	Increase grain size	18	Glassy
AD85-L-C	(a) 1550 $^{\circ}$ C for 250 h	Crystallize inter-granular glass	18	Partially crystalline
	(b) 1200 $^{\circ}$ C for 130 h	with large grain size		

TABLE II Average composition (wt %) of the intergranular glass in AD85

SiO <sub>2</sub>	Al <sub>2</sub> O <sub>3</sub>	MgO	CaO	BaO
56.5	27.5	2.1	8.6	5.3

given in Table I was devised in order to obtain anorthite as the major crystalline phase [23].

Fig. 2 shows scanning electron micrographs of AD85-S-G (grain size  $\approx 3 \mu\text{m}$ ) and AD85-L-G (grain size  $\approx 18 \mu\text{m}$ ). Qualitative visual comparison of the two micrographs shows that the heat treatment results in a scaling up of the grain structure as a whole, and that there is no significant change in the distribution of grain sizes about the mean. Fig. 3a and b show transmission electron micrographs of AD85-S-G and AD85-S-C depicting glassy and crystalline intergranular phases respectively. The grain size has not changed appreciably during crystallization heat treatment. The crystalline intergranular phase in AD85-S-C is observed to be mostly anorthite. With this composition it was not possible to achieve 100% crystallinity; thus pockets of residual glassy phase were observed at many triple points. From TEM examination, the overall degree of crystallinity was estimated to be  $\approx 80\%$ .

### 3.2. Mechanical behaviour

Fig. 4 shows indentation load versus failure stress for the four sets of samples. Consider firstly the behaviour of the fine-grained material. It can be seen that the data points for AD85-S-G and AD85-S-C lie essentially on the same line. The results for the coarse-grained specimens (AD85-L-G and AD85-L-C), on the other hand, fall on a distinctly separate curve.

The results of the hot-hardness measurements obtained from the bulk anorthite samples are shown in Fig. 5. Data for alumina [24] are also plotted for comparison. Although the hardness of anorthite at

room temperature is significantly lower than that of alumina, its rate of decrease with increasing temperature is lower. Consequently, at temperature around 1000 °C, the hardness values of the two phases are similar.

### 4. Discussion

The results depicted in Fig. 4 clearly show that *R*-curve behaviour, as evinced by the flattening of the data in Fig. 4 at low indentation loads, is enhanced with increasing grain size. This behaviour is consistent with the observations of other researchers obtained on both single-phase [3, 25] and two-phase aluminas [3, 13]. It confirms grain size as a significant parameter in determining the extent of increased toughening with crack extension.

However, the effect of crystallization of the intergranular phase on the *R*-curve properties of these materials appears to be insignificant. In terms of the grain-bridging model, this null effect may seem surprising, because the bridging processes are thought to be sensitive to residual stresses,  $\sigma_r$ , in the grain-boundary regions. To explore the validity of this reasoning further, the magnitude of these grain-boundary stresses due to thermal expansion anisotropy between the alumina (A) and the intergranular anorthite (An) can be estimated from the following relation for a spherical inclusion embedded in a matrix [26, 27]

$$\sigma_r = [(x_A - x_{An})\Delta T] [(1 - \nu_A)/2E_A + (1 - 2\nu_{An})/E_{An}] \quad (1)$$

where  $x$  is the linear thermal expansion coefficient,  $\nu$  is Poisson's ratio,  $E$  the elastic modulus and  $\Delta T$  is the difference between heat treatment and ambient temperatures. Although the inclusion problem represents an oversimplification of the experimentally observed

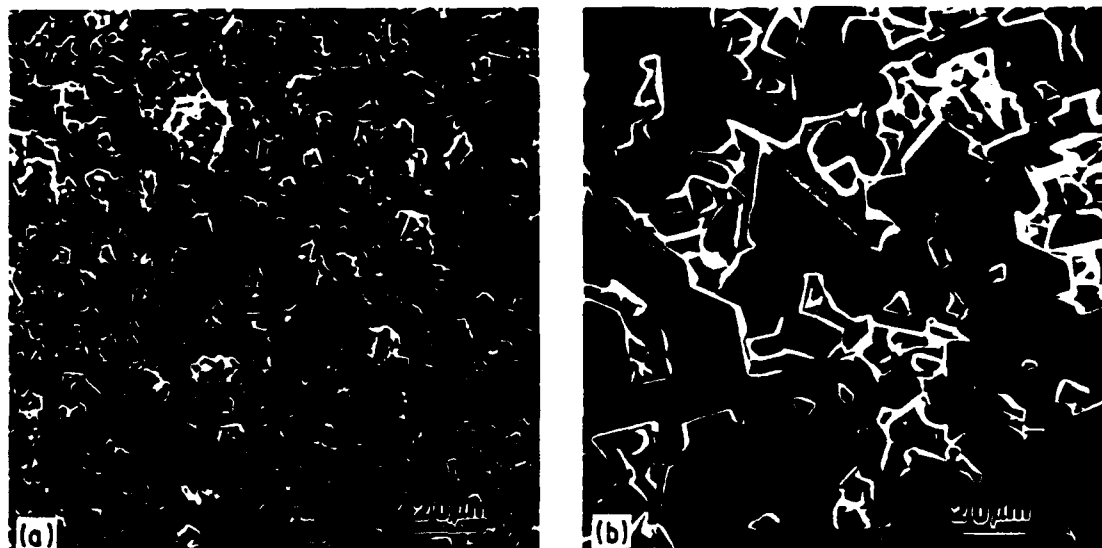


Figure 2 SEM secondary electron images of polished and etched sections of AD85 aluminas (a) AD85-S-G (fine-grained material), (b) AD85-L-G (coarse-grained material).

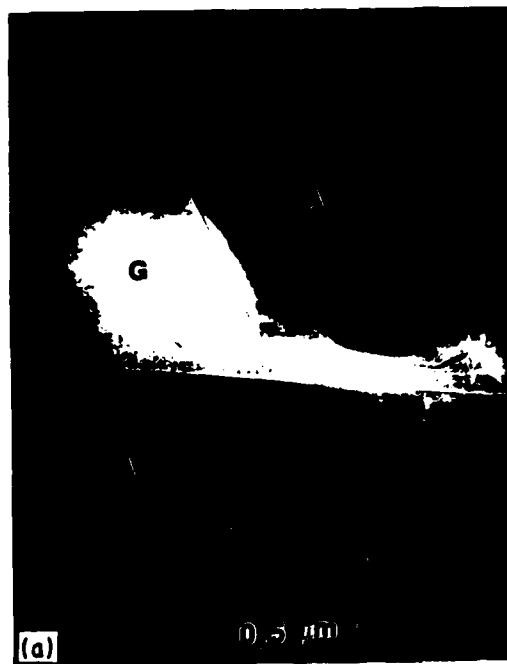


Figure 3 TEM bright-field images of AD85 aluminas (a) AD85-S-G showing intergranular glassy pockets (A, alumina; G, glass). (b) AD85-S-C showing crystalline intergranular phase (A, alumina; An, anorthite; G, residual glass).

morphology, it is believed that this relation gives a useful indication of the magnitude of the residual stresses. Taking  $\alpha_A = 9.0 \times 10^{-6} \text{ } ^\circ\text{C}^{-1}$  [28],  $\alpha_{An} = 3.7 \times 10^{-6} \text{ } ^\circ\text{C}^{-1}$  [29]\*,  $E_A = 390 \text{ GPa}$  ( $\nu_{Al} = 0.2$ ) [3],  $E_{An} = 250 \text{ GPa}$  ( $\nu_{An} = 0.25$ ) [30] and  $\Delta T = 1000 \text{ } ^\circ\text{C}$ , we obtain  $\sigma_r = 1.5 \text{ GPa}$  for the alumina/anorthite system. For a single-phase alumina, taking  $\alpha_{Al} = 8.6 \times 10^{-6} \text{ } ^\circ\text{C}^{-1}$  and  $\alpha_{Al} = 9.6 \times 10^{-6} \text{ } ^\circ\text{C}^{-1}$  [28], we ob-

\* It should be noted that alumina and anorthite are non-cubic materials and possess thermal expansion anisotropy along  $a$  and  $c$  axes. Because the thermal expansion anisotropy within these individual crystals is much less than that between the two phases, the values mentioned here are average and represent the thermal expansion coefficients of polycrystalline materials.

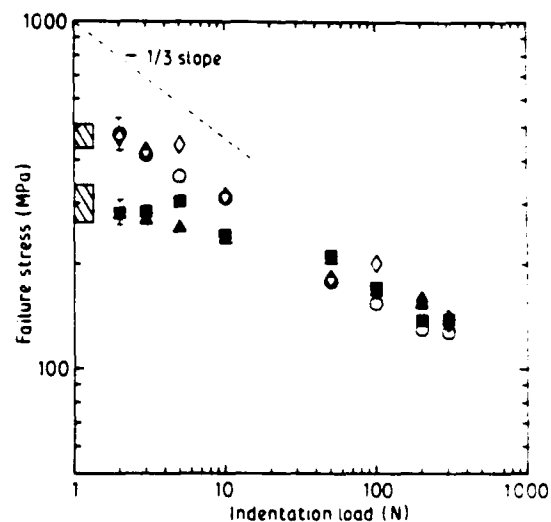


Figure 4 Plot of indentation load versus failure stress for four different materials, derived from AD85. The hatched region represents failures from natural flaws. (Representative error bars are included on the end data points.) (□) AD85-S-G, (○) AD85-S-C, (■) AD85-L-G, (▲) AD85-L-C.

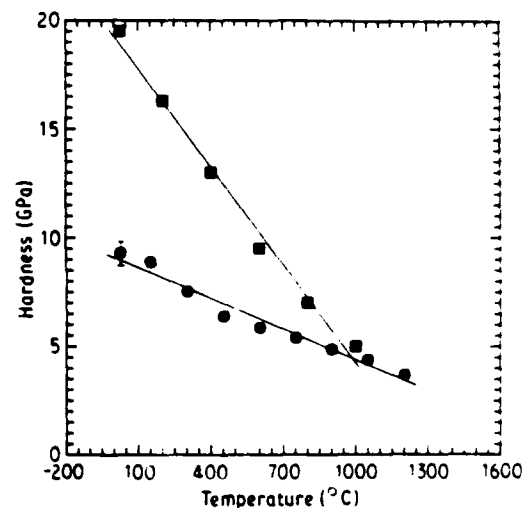


Figure 5 Comparison of hardness as a function of temperature between (■) alumina [24] and (●) anorthite (present work). (A representative error bar is shown on the end data point.)

tain  $\sigma_r = 0.35 \text{ GPa}$ . Thus the residual stresses induced in the two-phase alumina are greater, by about a factor of four, than in the single-phase material.

One could therefore argue that the  $R$ -curve in single-phase alumina should be further enhanced in the two-phase alumina with the crystalline second phase. That this was not observed experimentally, suggests that the residual stresses must be at least partially relaxed in AD85-S-C and AD85-L-C. As described previously, TEM examination of these samples revealed that the anorthite was highly twinned. In addition, residual glass was often observed in the

intergranular pockets. It is arguable, therefore, that relaxation of the grain-boundary residual stresses is taking place at the treatment temperature by deformation of either the anorthite or glassy phase. Because no dislocation activity was observed in the alumina grains, deformation of the alumina grains was disregarded as a possibility. Consideration of Fig. 5 shows that deformation of the anorthite appears less likely, because at elevated temperatures the hardness values of alumina and anorthite become comparable, so it is difficult to see why the anorthite would deform in preference to the alumina.

This essentially leaves the role of the residual glass to be considered. Because the approximate composition of the glass is known, it is possible to estimate the value of the glass viscosity from standard data [31]. For comparable glass compositions, the softening temperature, i.e. the temperature at which the glass will deform appreciably under its own weight, is 900 °C. Thus at the level of stresses which have been calculated, the glass would be expected to flow readily. It is therefore suggested that the expected change in mechanical properties does not occur because of relaxation of the induced stresses by viscous flow of the residual glass.

The above discussion represents a highly simplified picture of the deformation processes which take place on cooling of the crystallized AD85 to ambient temperatures. Nonetheless, the postulate that the induced stresses are being relaxed is consistent with the experimental data. Ideally, it would have been desirable to estimate the stress distribution within the microstructure more accurately, by taking into account the morphology of the various phases. Unfortunately, the complexity of the microstructure of the commercial materials studied rendered such analysis intractable. It is envisaged that laboratory-processed specimens with controlled microstructures will be more amenable to theoretical modelling. Work is thus currently under way to process two-phase aluminas where the glass composition is controlled so that virtually 100% crystallinity can be achieved.

## 5. Conclusions

For the commercial liquid-phase-sintered aluminas examined in this study, the effect of grain size on the *R*-curve behaviour predominates. Crystallization of the intergranular glass had relatively little to no effect on the *R*-curve behaviour. Although significant residual stresses would be expected to be induced due to the differences in thermal expansion between the alumina and the crystallized intergranular phase, these appear to be relaxed by flow of residual glass. The results have interesting implications with respect to the applications of these materials, because they show that prolonged heat-treatment cycles up to 1200 °C do not affect the room-temperature mechanical properties.

## Acknowledgements

The authors thank S. J. Bennison, B. R. Lawn and M. J. Readey for many stimulating and useful discussions, and B. R. Lawn for valuable suggestions regarding the manuscript. The authors also thank M. J. Readey, Coors Ceramics Co., for providing the starting materials. This work was funded jointly by Coors Ceramics Company and Air Force Office of Scientific Research.

## References

1. R. KNEHANS and R. W. STEINBRECH, *J. Mater. Sci. Lett.* **1** (1982) 327.
2. R. W. STEINBRECH, R. KNEHANS and W. SCHAAR-WACHTER, *J. Mater. Sci.* **18** (1983) 265.
3. R. F. COOK, B. R. LAWN and C. J. FAIRBANKS, *J. Amer. Ceram. Soc.* **68** (1985) 604.
4. M. V. SWAIN, *J. Mater. Sci. Lett.* **5** (1986) 1313.
5. A. REICHL and R. W. STEINBRECH, *J. Amer. Ceram. Soc.* **71** (1988) C299.
6. S. J. BENNISON and B. R. LAWN, *J. Mater. Sci.* **24** (1989) 3169.
7. K. KENDAL, N. McN ALFORD, S. R. TAN and J. D. BIRCHALL, *J. Mater. Res.* **1** (1986) 120.
8. R. F. COOK and D. R. CLARKE, *Acta Metall.* **36** (1988) 555.
9. D. K. SHETTY and J. S. WANG, *J. Amer. Ceram. Soc.* **72** (1989) 1158.
10. P. L. SWANSON, C. J. FAIRBANKS, B. R. LAWN, Y.-W. MAI and B. J. HOCKEY, *ibid.* **70** (1987) 279.
11. S. J. BENNISON and B. R. LAWN, *Acta Metall.* **37** (1989) 2659.
12. Y.-W. MAI and B. R. LAWN, *J. Amer. Ceram. Soc.* **70** (1987) 289.
13. S. J. BENNISON, H. M. CHAN and B. R. LAWN, *ibid.* **72** (1989) 677.
14. N. A. TRAVITZKY, D. G. BRANDON and E. Y. GUTMANAS, *Mater. Sci. Engng* **71** (1985) 65.
15. *Idem.*, *ibid.* **71** (1985) 77.
16. Y. YESHURUN, Z. ROSENBERG, N. A. TRAVITZKY and D. G. BRANDON, *ibid.* **71** (1985) 71.
17. W. A. ZDANIEWSKI and H. P. KIRCHNER, *Adv. Ceram. Mater.* **1** (1986) 99.
18. H. TOMASZEWSKI, *Ceram. Int.* **14** (1988) 93.
19. C. A. POWELL-DOĞAN and A. H. HEUER, *J. Amer. Ceram. Soc.*, *J. Amer. Ceram. Soc.* **73** (1990) 3684.
20. D. B. MARSHALL, *Amer. Ceram. Soc. Bull.* **59** (1980) 551.
21. R. J. ROARK, in "Formulas for Stress and Strain" (McGraw-Hill, New York, 1965) Ch. 7.
22. S. M. WIEDERHORN, B. J. HOCKEY and R. F. KRAUSE Jr., in "Ceramic Microstructures '86", edited by J. Pask and A. G. Evans (Plenum, New York, 1988) p. 795.
23. L. KLEIN and D. R. UHLMANN, *J. Geophys. Res.* **79** (1974) 4869.
24. C. P. ALPERT, H. M. CHAN, S. J. BENNISON and B. R. LAWN, *J. Amer. Ceram. Soc.* **71** (1988) C371.
25. P. CHANTIKUL, S. J. BENNISON and B. R. LAWN, *ibid.* **73** (1990) 2419.
26. D. WEYL, *Ber. Deut. Keram. Ges.* **36** (1959) 319.
27. J. SELSING, *J. Amer. Ceram. Soc.* **44** (1961) 419.
28. G. BAYER, *Proc. Brit. Ceram. Soc.* **22** (1973) 39.
29. M. CZANK and H. SCHULZ, *Naturwiss.* **54** (1971) 94.
30. J. V. SMITH and W. L. BROWN, in "Feldspar Minerals", Vol. 1 (Springer-Verlag, Berlin, 1988) Ch. 12.
31. N. BANSAL and R. H. DOREMUS, in "Handbook of Glass Properties" (Academic Press, Orlando, 1986) Ch. 9.

Received 20 March  
and accepted 5 July 1990



ON THE CONSTRAINED CRYSTALLIZATION OF SYNTHETIC  
ANORTHITE ( $\text{CaO} \cdot \text{Al}_2\text{O}_3 \cdot 2\text{SiO}_2$ )

NITIN P. PADTURE and HELEN M. CHAN

Department of Materials Science and Engineering  
Lehigh University, Bethlehem, Pennsylvania 18015

March 1991

For: Journal of Materials Research

ON THE CONSTRAINED CRYSTALLIZATION OF SYNTHETIC  
ANORTHITE ( $\text{CaO} \cdot \text{Al}_2\text{O}_3 \cdot 2\text{SiO}_2$ )

ABSTRACT

To determine the influence of volume constraint, the crystallization behavior of bulk anorthite glass was compared to that of anorthite glass situated at intergranular pockets in an alumina ceramic. Near-100% crystallization of the glass was obtained in both cases. Examination of the crystallized microstructures using SEM and TEM revealed several interesting features. The resulting microstructures, together with the very high degree of crystallization are discussed with reference to a thermodynamic model for the constrained crystallization of glass.

## 1. INTRODUCTION

Over a period of the last 40 years or so, the development of glass-ceramics in which select glass compositions are fabricated in the glassy state and subsequently crystallized, has proven to be of great scientific and technological importance [for reviews see references 1 and 2]. More recently, interest has developed in the area of crystallization of glassy phases present as intergranular pockets within liquid-phase-sintered (LPS) ceramics [3-10]. In both these cases, the major goal has been to achieve very high degrees of crystallinity. As will be seen from the following, the importance of this topic lies in the fact that the degree of crystallinity can have a significant influence on the mechanical properties.

Silica-based oxides are used as sintering-aids during the processing of many LPS ceramics; these oxides form a liquid at the sintering temperature, which upon cooling is retained as a glassy phase at the grain boundaries [11]. The volume percent of the residual glass may be significant, and can be as high as 30 vol% in some commercial aluminas. The presence of such intergranular residual glass is known to degrade the high temperature creep resistance of LPS alumina [12] and silicon nitride [13]. However, crystallization of the intergranular glass, (either during creep or through post-sintering heat-treatments) results in improved mechanical properties at elevated temperatures [12,14-16]. Unfortunately, in many glass-ceramic

systems, complete crystallization of the glass cannot be achieved. One explanation for this behavior lies in the volume constraint of the surrounding grains.

It has been known for a some time that the complete crystallization of a glassy phase is very difficult when it is constrained within intergranular pockets surrounded by crystalline grains. Note that such glassy intergranular pockets can arise during the final stages of crystallization of a bulk glass, as well as in LPS ceramics (as described earlier). Raj and Lange [17] have proposed a thermodynamical model in order to explain the lack of complete crystallization of constrained glass. Figure 1a shows a schematic illustration of an intergranular pocket, which has been approximated by a sphere surrounded by a rigid crystalline body (figure 1b). The essence of the Raj-Lange model is as follows. Consider the growth of a crystal nucleus within an intergranular pocket; as the glass transforms into crystalline material, its volume decreases. Since the crystallizing phase is physically bonded to the surrounding glass, strain is generated in the glass setting up hydrostatic tension. As the crystal grows, the magnitude of the strain energy increases, thus offsetting the corresponding decrease in chemical free energy (which is the driving force for crystal growth). At some critical crystal size, therefore, it is possible for a balance to occur between the opposing energy terms. At this point, the crystal ceases to grow, resulting in a

partially crystallized intergranular pocket. It follows that the actual degree of crystallinity achieved depends on several parameters, the values of which are particular to the geometry and the system in question.

Perhaps surprisingly, there has been very little detailed work aimed at studying the influence of volume constraint on the crystallization behavior of glass. Isolated observations exist on constrained-crystallization in commercial LPS aluminas, however in these systems there is the added consideration that the composition of the intergranular glass is different from that of the crystallizing phase [6-9,18]. This lack of control over the composition of the intergranular glass further complicates the constrained-crystallization problem, invariably leading to incomplete crystallization in commercial materials [6-9,18,19]. A notable exception is in the case of silicon nitride ceramics, commonly referred to as SiAlON materials (solid-solutions), where 100% crystallization of the intergranular glass has been reported [10]. This has been attributed to the dissolution of the constituent oxides of the residual glass in the SiAlON constraining grains [10].

The purpose of the present study was to compare the crystallization behavior of anorthite ( $\text{CaO} \cdot \text{Al}_2\text{O}_3 \cdot 2\text{SiO}_2$ ), a feldspar mineral, crystallized from the same composition glass present in two different physical situations, viz: a) bulk glass

and b) glass constrained within intergranular pockets of LPS alumina. Anorthite was chosen for this study for the following reasons. Firstly, anorthite composition glass is relatively easy to form, also the glass-formation behavior, structure and properties of anorthite glass have been documented by several researchers [20,21]. Anorthite has the additional advantage that its nucleation [22] and crystal growth [23,24] behavior from the bulk anorthite glass is relatively well-understood. Finally, anorthite is of some practical significance in that it has been reported to be the major crystallizing phase in several commercial LPS aluminas [8,9,18]. Our aim in this paper, therefore, was to determine the crystallization behavior of anorthite glass in both bulk anorthite and alumina-anorthite, and to examine the results in the light of the Raj-Lange model.

## **2. EXPERIMENTAL**

### **2.1 Materials Processing**

#### **Bulk Anorthite**

Reagent grade (Fisher Scientific Company)  $\text{CaCO}_3$ ,  $\text{Al}_2\text{O}_3$  and  $\text{SiO}_2$  were mixed in appropriate proportions and dry-blended for 12 hours. This batch was then melted at 1600 °C for 24 hours in a covered platinum crucible heated by an electrical resistance furnace. The resulting glass was then quenched, crushed and remelted. (To ensure good chemical homogeneity, the preceding steps were repeated several times) Next, the glass was cast into a steel mold and subsequently annealed at 800 °C for 1 hour and

cooled very slowly. This base glass will be referred to as specimen BULK-G (G refers to Glassy)<sup>1</sup>. Crystallization of the bulk glass was carried out by heat-treating at 1200 °C for 30 minutes in a platinum enclosure (1200 °C corresponds to the temperature at which Klein and Uhlmann [23] reported a maximum in the crystallization rate). A short heat-treatment duration was chosen to avoid excessive grain growth and hence prevent severe microcracking of the crystallized specimen. This specimen will be referred to as specimen BULK-C (C refers to Crystalline).

#### Alumina-Anorthite

Some of the above glass was crushed and ball-milled into a glass-frit (< 1.0  $\mu\text{m}$  particle size as classified by sedimentation [25]). This glass-frit was mixed with high-purity  $\alpha$ -alumina powder (Sumitomo Chemical Company) in the volumetric proportion of anorthite glass-frit : alumina, equal to 1 : 3. This mixture was then wet-ball-milled in methanol using zirconia ball-grinding media for 24 hours. The resulting slurry was subsequently transferred to a teflon beaker where it was continuously stirred during drying, and deagglomerated by crushing. A disk 10 mm in diameter and 2 mm thickness was fabricated from this powder by uniaxial pressing at 50 MPa followed by wet-bag isostatic pressing at 350 MPa. The green disk was packed in loose alumina

---

<sup>1</sup> For similar melting procedure of anorthite glass the deviation of the composition of the glass from the starting batch was reported to be less than 0.2 wt% of any of the principal constituents [23].

powder in a high purity alumina crucible, and calcined at 800 °C for 12 hours, followed by sintering at 1600 °C for 60 minutes. This sintered specimen will be referred to as INTER-G (since anorthite is in the form of an INTERgranular Glass). Note that because of the short sintering duration the composition of the intergranular glass is assumed to be unchanged from that of anorthite. A piece of the sintered specimen was heat-treated at 1200 °C for 25 hours in order to crystallize the intergranular glass. The relatively long crystallization heat-treatment used in this case was to try and overcome any kinetic effects. This specimen will be referred to as specimen INTER-C (C refers to Crystalline INTERgranular phase).

## 2.2 Materials Characterization

Specimens BULK-C and INTER-C were subjected to x-ray powder diffraction analysis and the product of crystallization was confirmed to be anorthite (triclinic, space group  $P\bar{1}$ , at room temperature). The densities of all the specimens were measured using the Archimedes method with water as the immersing medium [25]. Sections of specimens BULK-C and INTER-C were polished to 1  $\mu\text{m}$  grade using standard ceramographic techniques for microstructural observations in the scanning electron microscope (SEM). The microstructures of the specimens were revealed by thermal etching (BULK-C at 1300 °C for 30 minutes, and INTER-C at 1500 °C for 30 minutes). All SEM specimens were sputter-coated with Au-Pd to avoid charging in the microscope. Transmission



electron microscopy (TEM) specimens were prepared from disks (diameter  $\approx$  3 mm, thickness  $\approx$  100  $\mu$ m), cut ultrasonically from polished sections of BULK-C and INTER-C. The centers of the disks were dimpled to 20  $\mu$ m followed by ion-beam milling until perforation. Prior to examination in the TEM<sup>2</sup>, specimens were coated with amorphous carbon.

### 3. RESULTS

Table I gives the nomenclatures, heat treatments and densities for the materials fabricated. The theoretical densities of the specimens were calculated taking the density of anorthite glass to be 2.700 g/cm<sup>3</sup>, and the theoretical densities of crystalline anorthite and  $\alpha$ -alumina to be 2.763 g/cm<sup>3</sup> [27] and 3.987 g/cm<sup>3</sup> respectively [28].

#### Bulk Anorthite

Figure 2 shows the microstructure of the specimen BULK-C as seen in the SEM. The grain size distribution in this material was found to be very broad with grain diameters ranging from 0.5  $\mu$ m to 25  $\mu$ m. The most novel feature in this microstructure was the wavy and jagged nature of the grain boundaries. Consistent with this was the large amount of surface relief exhibited by the fracture surface of the BULK-C specimen (figure 3). TEM examination of BULK-C showed that the degree of crystallinity was close to 100%. Furthermore, it was observed that the anorthite

---

<sup>2</sup> Philips 400T at 120 keV, Philips 430 at 250 keV

grains were highly twinned (figure 4). It was also found that the twin density within a single grain increased with a decrease in the grain size. However, no attempt was made to establish a detailed quantitative relationship between twin density and grain size in this material.

Figure 5 shows a high resolution TEM (HRTEM) image of (010) twin boundaries (indicated by the arrows) in anorthite taken from specimen BULK-C. These boundaries were confirmed to be twin boundaries by optical (LASER) diffraction. No evidence of any imperfections along the twin boundaries was observed. The inset in figure 5 shows the corresponding selected area electron diffraction pattern (SAEDP) ([001] beam direction); spot splitting (indicated by the arrow) due to the numerous twin planes within the selected area aperture is clearly visible.

#### Alumina-Anorthite

In the alumina-anorthite specimen INTER-C the average grain size of the alumina was estimated to be  $\approx 5 \mu\text{m}$ , whereas the average size of the intergranular pockets was  $\approx 1 \mu\text{m}$ . An SEM micrograph depicting the microstructure of specimen INTER-C is given in figure 6. An anorthite grain (which was identified by the presence of strong Ca and Si peaks in the x-ray energy dispersive spectrum) is shown situated at an alumina multi-grain junction. The corresponding TEM image of an intergranular pocket of crystalline anorthite is shown in figure 7. The highly

twinned nature of anorthite, and the near-100% crystallinity is clearly evident from this micrograph. The twinned phase was identified to be anorthite by SAEDP and x-ray energy dispersive spectroscopy (XEDS).

#### 4. DISCUSSION

Grain boundary waviness is clearly evident in the SEM micrograph of bulk crystalline anorthite (figure 2). The distribution of the microstructural scale of the waviness (facet length) is seen to be wide, ranging from several nm (figure 4) to several  $\mu\text{m}$  (figure 2). Such waviness is believed to be due to the intersection of the numerous twins within each grain with the grain boundaries. The wide distribution of the scale of the waviness is consistent with the variation in the width of the twin bands. It is postulated that the existence of such wavy grain boundaries may be partially responsible for the excellent high temperature hardness behavior of anorthite [9].

The observation of extensive twinning in anorthite is consistent with the results of previous workers. Anorthite is known to twin readily during crystal growth and/or mechanical deformation [29]. Twinning in anorthite follows the albite twinning law in which the twin operation is given by a reflection across the (010) (twin) plane [29]. Confirmation that the twin plane in anorthite is indeed the (010) is clearly shown in figure 5. The aforementioned twinning operation is equivalent to

rotation of  $180^\circ$  about  $b^*$ , the normal to (010). It is perhaps worth mentioning that in anorthite, the angle,  $\phi$ , between  $b$  and  $b^*$  is equal to  $3.7^\circ$ , hence the deviation in crystallographic directions across the twin boundary is relatively small [29].

As mentioned earlier near-100% crystallinity occurs in specimens BULK-C and INTER-C<sup>3</sup>. Such high degrees of crystallinity are quite uncommon in glass-ceramics due to the strain energy considerations embodied in the Raj-Lange model mentioned in section 1. For an in-depth analysis of the problem in question, the reader is referred to the original paper by Raj and Lange [17]. Here, our aim is simply to apply the Raj-Lange model to the problem of anorthite crystallizing from severely constrained glass in a LPS alumina. The following assumptions are made in this analysis: a) the intergranular pocket is spherical, b) nucleation of the crystallizing phase occurs homogeneously, c) the constraining crystalline grains are rigid and chemically inert, d) the crystallizing phase is also rigid and e) the compositions of the glass and the crystallizing phase are identical. The expression derived by Raj and Lange [17] for the normalized free energy change,  $\Delta g$ , during constrained crystallization is as follows:

$$\Delta g = a\rho^{15} + b\rho^{12} - \rho^3 + 3/2\rho_0\rho^2 \quad \dots(1)$$

---

<sup>3</sup> It should be noted that we refer to degree of crystallization as "near-100%", since very thin glassy films may be present at the grain boundaries.

where  $a$ ,  $b$ ,  $\rho$  and  $\rho_0$  are non-dimensional parameters. After substituting suitable values for the parameters pertinent to the alumina-anorthite system, we can arrive at the following expression for  $\Delta g$  (the details of the calculations entailed in this analysis are deferred to the APPENDIX):

$$\Delta g = 0.221\rho^{15} + 0.083\rho^{12} - \rho^3 + 0.0075\rho^2 \quad \dots(2)$$

Figure 8 plots  $\Delta g$  as a function of  $\rho$ , where  $\rho = r/R$ . As seen from figure 1b,  $\rho$  is a measure of the crystal size relative to the pocket size. It can be seen that the minimum in this curve occurs at  $\rho = 0.97$ . The prediction, therefore, is that the crystallizing phase will grow to 97% of the pocket size. This compares very favorably with the experimental observations of near-100% crystallinity, especially given the simplifying assumptions made in the analysis, and the possible errors in the values of the physical parameters. It should be emphasized, however, that prediction of such a high degree of crystallinity is very specific to the anorthite system. This is primarily because the densities of glassy and crystalline anorthite do not differ to a great extent, rendering the value of  $\delta V$  to be very small ( $\delta V = 0.023$ ). As indicated by the dashed lines in figure 8 the  $\Delta g$ - $\rho$  function appears to be quite sensitive to  $\delta V$ ; thus minima in the dashed curves for  $\delta V = 0.05$  and  $0.10$  occur at  $0.85$  and  $0.74$  respectively. This comparison reinforces the argument that a small  $\delta V$  value plays a significant role in the high degree

of crystallinity in anorthite.

Some other factors, again specific to the anorthite system, may also be contributing to the high degree of crystallinity observed. Firstly, in violation of one of the assumptions of the Raj-Lange model, the crystallizing phase anorthite is not perfectly rigid. As pointed out earlier, profuse twinning has been observed in anorthite in both specimens BULK-C and INTER-C. Although it is not possible to distinguish between deformation twins and growth twins purely by observation, it is reasonable to assume that deformation twinning does occur. This would partially relieve the elastic strain energy and hence enhance the degree of crystallization. Next, let us consider the assumption that the crystalline matrix surrounding the intergranular pocket is completely rigid. Clarke [30] has discussed the existence of very thin intergranular glassy films in ceramics which may be thermodynamically stable. If such films were to exist in the alumina-anorthite, it is plausible that they would facilitate creep of matrix grains, thus allowing accommodation of the volume change during crystallization. Such accommodation would be expected to lead to an increase in density after crystallization. An attempt was made to correlate the measured densities of INTER-G and INTER-C with their respective theoretical densities (see table I). However, due to the very small difference in the densities of glassy and crystalline anorthite, and the large fraction of porosity in the bulk alumina specimen, the results

were inconclusive.

Finally, we wish to emphasize that achieving a high degree of crystallinity in glass-ceramics and LPS ceramics is of great technological value in terms of their improved physical properties. Our study of the anorthite system has clearly shown that near-100% crystallinity can be achieved in both bulk anorthite and alumina-anorthite. Further, the applicability of existing models for constrained crystallization to real systems, has been demonstrated.

## 5. CONCLUSIONS

It can be concluded that near-100% crystallinity can be achieved when anorthite is crystallized from the same composition glass in a) bulk form, and b) situated in an intergranular pocket constrained by four or more alumina grains in a LPS alumina. Such a high degree of crystallinity can be attributed to the following reasons:

- i) The composition of the glass was the same as the crystallizing phase.
- ii) The density of crystalline anorthite is very close to that of glassy anorthite.

Other reasons which also possibly contributed are strain energy relief due to twinning of anorthite, and creep of the constraining matrix (anorthite grains in BULK-C and alumina grains in INTER-C) at the crystallization temperature.

## APPENDIX

The expression derived by Raj and Lange for the normalized free energy change during constrained crystallization is given by [17]:

$$\Delta g = a\rho^{15} + b\rho^{12} - \rho^3 + 3/2\rho_0\rho^2 \quad \dots (A1)$$

The constituent terms are defined as follows [17]:

1)  $\rho$  is a measure of the crystal size relative to the pocket size, (see figure 1b) and is given by:

$$\rho = r / R \quad \dots (A2)$$

2)  $\rho_0$  is related to the critical radius of the crystal ( $r_0$ ) by:

$$\rho_0 = r_0 / R \quad \dots (A3)$$

Assuming homogeneous nucleation,  $r_0$  is given by:

$$r_0 = 2\gamma / \Delta G_v \quad \dots (A4)$$

where  $\gamma$  is the interfacial energy between the crystal and the glass, and  $\Delta G_v$  is the decrease in the free energy per unit volume of the crystallized glass [31].

3) "a" is a measure of the strain energy per unit volume in the



crystallizing phase relative to the chemical free energy during the transformation, and is given by:

$$a = \delta V^2 K_c / 2\Delta G_v \quad \dots (A5)$$

where  $\delta V$  is the change in the volume during transformation per unit volume of the crystal, and  $K_c$  is the bulk modulus of the crystallizing phase.

4) "b" is a measure of the strain energy per unit volume in the glass phase relative to the chemical free energy during the transformation, and is given by:

$$b = \delta V^2 K_g / 2\Delta G_v \quad \dots (A6)$$

where  $K_g$  is the bulk modulus of the glass.

By substituting reasonable values for the aforementioned variables, we may now obtain  $\Delta g(\rho)$ . The value of  $\Delta G_v$  can be estimated using the following relation:

$$\Delta G_v = \Delta H_f (\Delta T \cdot T / T_m^2) \quad \dots (A7)$$

where  $\Delta H_f$  is the heat of fusion per unit volume of the crystallizing phase,  $T$  is the crystallization temperature,  $T_m$  is the equilibrium melting temperature of the crystallizing phase,

and  $\Delta T$  is the undercooling ( $T_m - T$ ) [32]. Taking  $T_m = 1826$  K [29],  $T = 1473$  K ( $\Delta T = 353$  K) and  $\Delta H_f = 1.04 \times 10^9$  J/m<sup>3</sup> [23], we obtain  $\Delta G_v = 1.62 \times 10^8$  J/m<sup>3</sup>. Using this value of  $\Delta G_v$  and  $\gamma = 0.19$  J/m<sup>2</sup> [22] we obtain  $r_o = 2.3 \times 10^{-9}$  m (23 Å) (equation A4). Taking  $R = 0.5 \times 10^{-6}$  m ( $\approx 1$   $\mu$ m pocket size) we may now obtain  $\rho_o = 0.005$  (equation A3). From values for the density of anorthite composition glass and the theoretical density of crystalline anorthite, we obtain  $\delta V = 0.023$ . Finally, taking values from the literature for the bulk moduli ( $K_c = 139$  GPa [29],  $K_g = 52$  GPa [26]) and substituting in equations A5 and A6 respectively, we obtain  $a = 0.221$  and  $b = 0.083$ . Equation A1 can now be rewritten as:

$$\Delta g = 0.221\rho^{15} + 0.083\rho^{12} - \rho^3 + 0.0075\rho^2 \quad \dots (A8)$$

#### ACKNOWLEDGEMENTS

The authors would like to thank V. P. Dravid for his help with the HRTEM work and A. Owens for his help with the SEM work. Funding for this work was provided by U.S. Air Force Office of Scientific Research and Coors Ceramics Company.

## REFERENCES

1. P. W. McMillan, Glass-Ceramics (Academic Press, London, 1979).
2. Z. Strnad, Glass Science and Technology, vol. 8: Glass-Ceramic Materials (Elsevier, New York, 1986).
3. N. A. Travitzky, D. G. Brandon and E. Y. Gutmanas, Mater. Sci. Engng. **71** 65 (1985).
4. H. Tomaszewski, Ceram. Intl. **14** 93 (1988).
5. W. A. Zdaniewski and H. P. Kirchner, Adv. Ceram. Mater. **1** 99 (1986).
6. S. J. Bennison, H. M. Chan and B. R. Lawn, J. Amer. Ceram. Soc. **72** 677 (1989).
7. C. A. Powell-Doğan and A. H. Heuer, J. Amer. Ceram. Soc. **73** 3677 (1990).
8. C. A. Powell-Doğan and A. H. Heuer, J. Amer. Ceram. Soc. **73** 3684 (1990).
9. N. P. Padture and H. M. Chan, J. Mater. Sci. **26** (1991) in press.
10. D. A. Bonnell, T-Y. Tien and M. Rühle, J. Amer. Ceram. Soc. **70** 460 (1987).
11. W. D. Kingery, H. K. Bowen and D. R. Uhlmann, Introduction to Ceramics (John Wiley & Sons, New York, 1976).
12. S. M. Wiederhorn, B. J. Hockey and R. F. Krause Jr., Ceramics Microstructures '86, edited by J. Pask and A. G. Evans (Plenum, New York, 1988) p. 795.
13. F. F. Lange, J. Amer. Ceram. Soc. **61** 53 (1978).
14. R. A. Page and K. S. Chan, J. Mater. Sci. Lett. **8** 938 (1989).
15. A. Tsuge, K. Nashida and M. Komatsu, J. Amer. Ceram. Soc. **67** 323 (1984).
16. D. S. Wilkinson, J. Amer. Ceram. Soc. **71** 562 (1988).
17. R. Raj and F. F. Lange, Acta Metall. **29** 1993 (1981).
18. Y. Yeshurun, Z. Rosenberg, N. A. Travitzky and D. G. Brandon, Mater. Sci. Engng. **71** 71 (1985).

19. C. A. Powell-Doğan and A. H. Heuer, J. Amer. Ceram. Soc. 73 3684 (1990).
20. M. Cukierman and D. R. Uhlmann, J. Geophys. Res. 78 4920 (1973).
21. M. Yamane and M. Okuyama, J. Non-Crystalline Solids 52 217 (1982).
22. D. Cranmer, R. Salomaa, H. Yinnon and D. R. Uhlmann, J. Non-Crystalline Solids 45 127 (1981).
23. L. Klein and D. R. Uhlmann, J. Geophys. Res. 79 4869 (1974).
24. M. S. Y. Bhatti, J. A. Gard and F. P. Glasser, Miner. Mag. 37 780 (1970).
25. J. S. Reed, Introduction to Principles of Ceramics Processing (John Wiley & Sons, New York, 1988).
26. N. Bansal and R. H. Doremus, Handbook of Glass Properties (Academic Press, Orlando, 1986).
27. W. F. Cole, H. Sørum and W. H. Taylor, Acta Cryst. 4 20 (1951).
28. National; Bureau of Standards Circular 3 1 (1959).
29. J. V. Smith and W. L. Brown, Feldspar Minerals, vol. 1 (Springer-Verlag, Berlin, 1988).
30. D. R. Clarke, J. Amer. Ceram. Soc. 70 15 (1987).
31. D. Turnbull, Solid State Physics, vol. 3 (Academic Press, New York, 1956).
32. J. Hoffman, J. Chem. Phys. 29 1192 (1958).

#### **CAPTION FOR TABLE**

- I. Heat-treatments and properties of the anorthite and alumina-anorthite materials investigated.

#### **CAPTIONS FOR FIGURES**

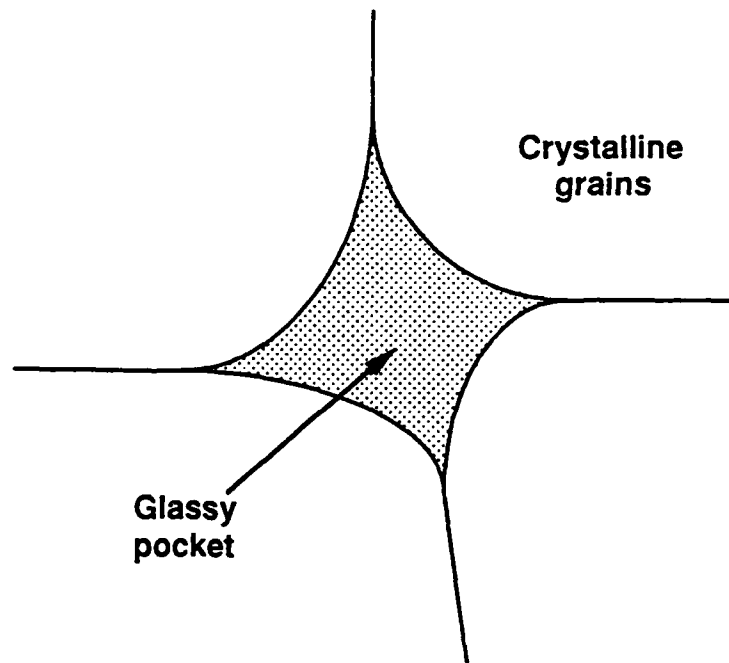
1. Schematic illustrations of a) an intergranular pocket containing glass surrounded by crystalline grains and b) spherical representation of the above intergranular pocket.  $R$ , represents the radius of the pocket and  $r$ , represents the radius of the crystallizing phase. Reproduced with modifications from reference 17.
2. SEM secondary electron image of a polished and etched section of anorthite (specimen BULK-C).
3. SEM secondary electron image of the fracture surface of anorthite (specimen BULK-C).
4. TEM bright field image of anorthite (specimen BULK-C). The arrows indicate the wavy nature of the grain boundaries.
5. HRTEM image of (010) twin boundaries in anorthite (specimen BULK-C) indicated by arrows. Inset: Corresponding SAEDP ([001] beam direction); arrows indicate streaking due to twins.

6. SEM secondary electron image of a polished and etched section of LPS alumina containing anorthite (specimen INTER-C). AL represents alumina and AN represents anorthite.
7. TEM bright field image of anorthite within LPS alumina (specimen INTER-C). AL represents alumina and AN represents anorthite.
8. A plot of  $\Delta g$  as a function of  $\rho$ , using equation 2 for different values of  $\delta V$ .

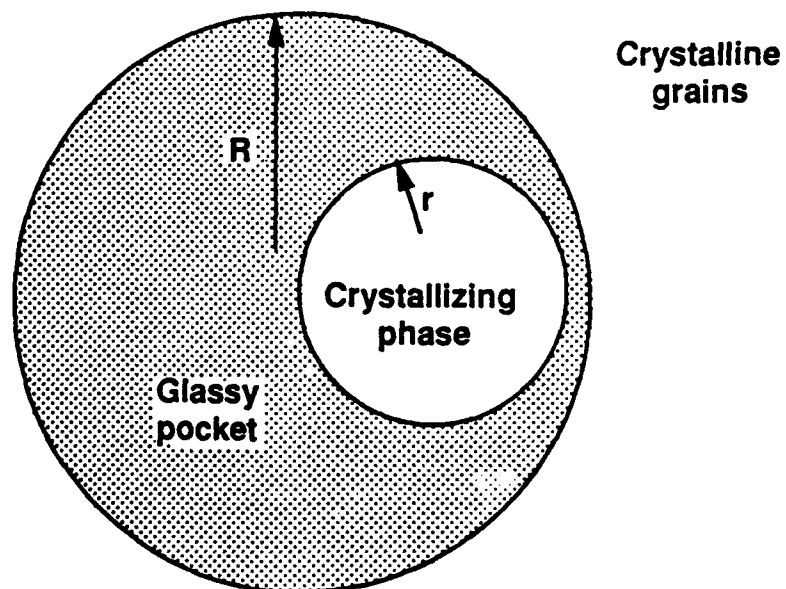
TABLE I

<u>Specimen</u>	<u>Composition and heat-treatments</u>	<u>Measured densities</u> $\frac{\text{g}}{\text{cm}^3}$	<u>Theoretical densities</u> $\frac{\text{g}}{\text{cm}^3}$
BULK-G	Anorthite composition base-glass	2.700*	-
BULK-C	Crystalline anorthite crystallized at 1200 °C for 0.5 h	2.730	2.763
INTER-G	Alumina with 25 vol% anorthite glass as the intergranular phase, as-fired at 1600 °C for 1 h	3.385	3.664
INTER-C	Alumina with crystalline anorthite as the intergranular phase, crystallized at 1200 °C for 25 h	3.387	3.680

-----  
 \* A value of 2.704 g/cm<sup>3</sup> has been reported in the literature for the density of anorthite glass [26].

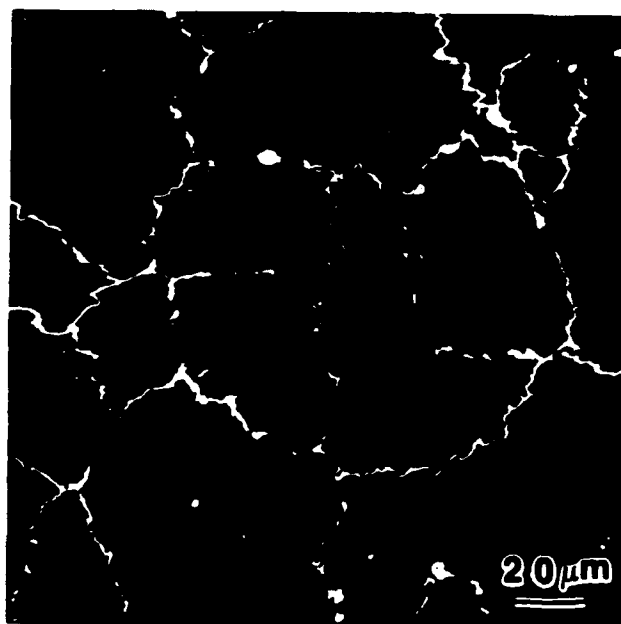


(a)



(b)





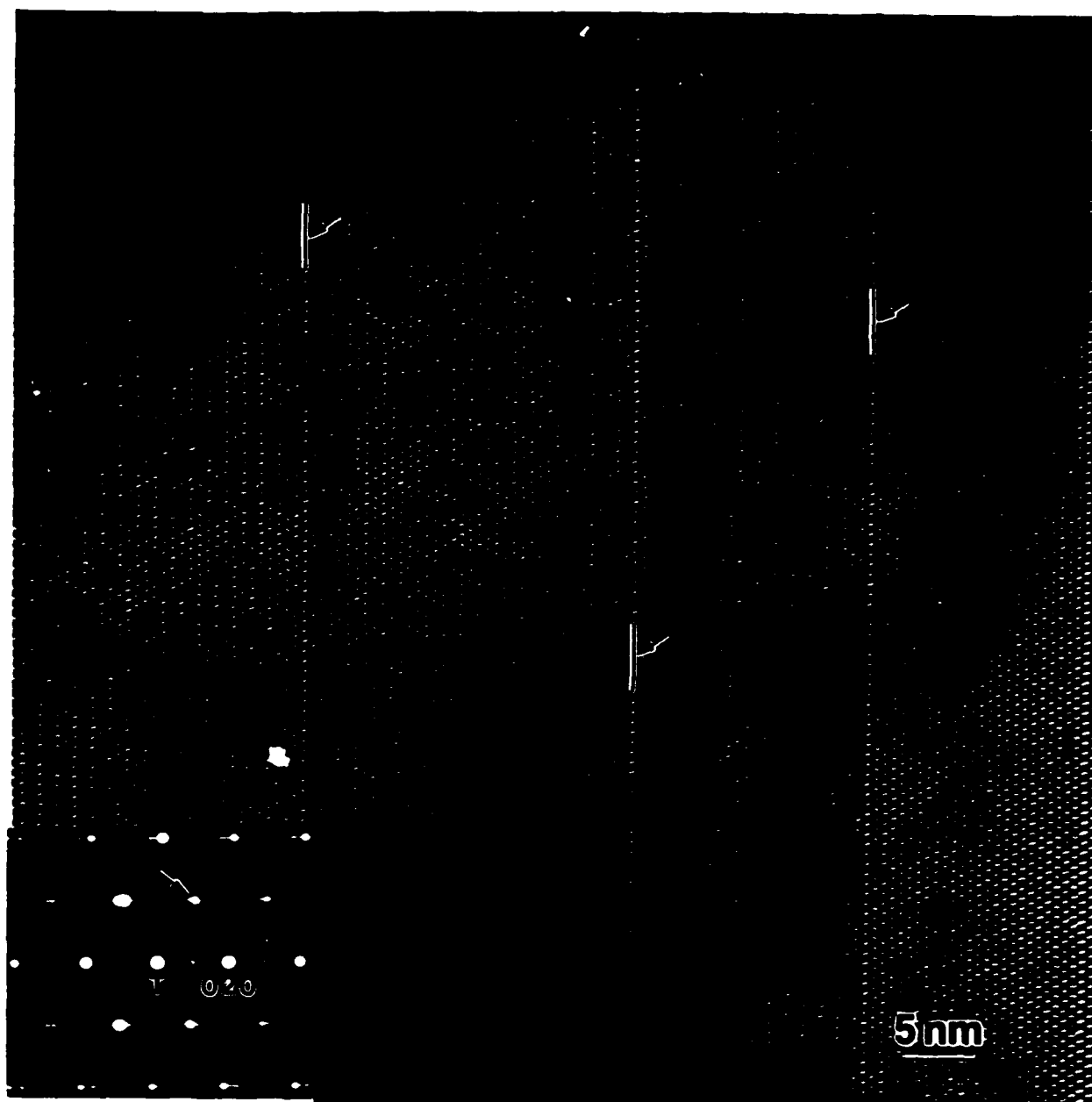
N.P. PADTURE  
& H.M. CHAN  
FIGURE 2

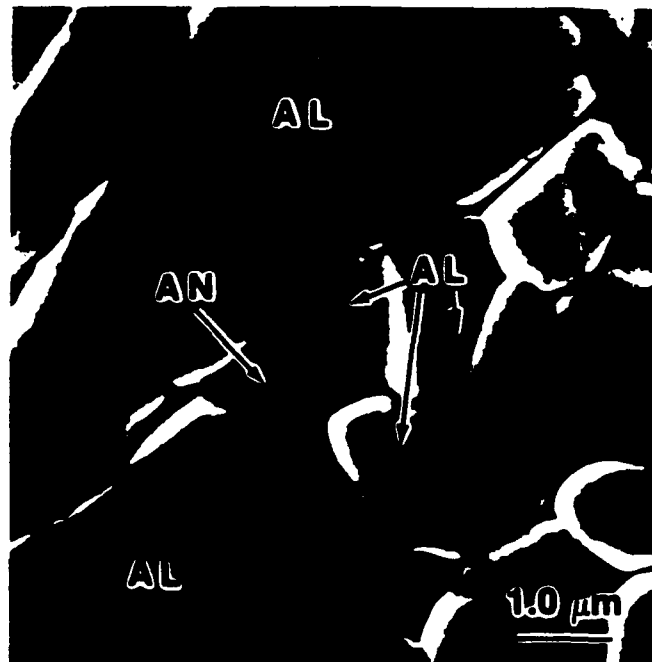


N.P. PADTURE  
& H.M. CHAN  
FIGURE 3



N.P. PADTURE  
& H.M. CHAN  
FIGURE 4





N.P. PADTURE  
& H.M. CHAN  
FIGURE 6



N.P. PADTURE  
& H.M. CHAN  
FIGURE 7

